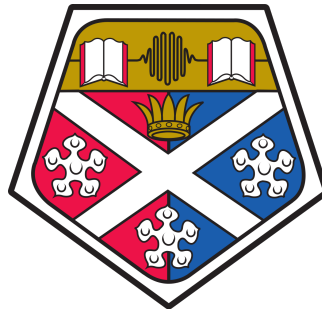A thesis submitted in partial fulfilment
of requirments for the degree of
Doctor of Philosophy

Adiabatic Processes, Noise, and Stochastic Algorithms for Quantum Computing and Quantum Simulation

Guanglei Xu

May 2018

UNIVERSITY OF STRATHCLYDE
Department of Physics and SUPA

This thesis is the result of the author's original research. It has been composed by the author and has not been previously submitted for examination which has led to the award of a degree.

The copyright of this thesis belongs to the author under the terms of the United Kingdom Copyright Acts as qualified by University of Strathclyde Regulation 3.50. Due acknowledgement must always be made of the use of any material contained in, or derived from, this thesis.

Signed:

Date: 26/09/2018

Abstract

Rapid developments in experiments provide promising platforms for realising quantum computation and quantum simulation. This, in turn, opens new possibilities for developing useful quantum algorithms and explaining complex many-body physics. The advantages of quantum computation have been demonstrated in a small range of subjects, but the potential applications of quantum algorithms for solving complex classical problems are still under investigation. Deeper understanding of complex many-body systems can lead to realising quantum simulation to study systems which are inaccessible by other means.

This thesis studies different topics of quantum computation and quantum simulation. The first one is improving a quantum algorithm in adiabatic quantum computing, which can be used to solve classical problems like combinatorial optimisation problems and simulated annealing. We are able to reach a new bound of time cost for the algorithm which has a potential to achieve a speedup over standard adiabatic quantum computing. The second topic is to understand the amplitude noise in optical lattices in the context of adiabatic state preparation and the thermalisation of the energy introduced to the system. We identify regimes where introducing certain type of noise in experiments would improve the final fidelity of adiabatic state preparation, and demonstrate the robustness of the state preparation to imperfect noise implementations. We also discuss the competition between heating and dephasing effects, the energy introduced by non-adiabaticity and heating, and the thermalisation of the system after an application of amplitude noise on the lattice. The third topic is to design quantum algorithms to solve classical problems of fluid dynamics. We develop a quantum algorithm based around phase estimation that can be tailored to specific fluid dynamics problems and demonstrate a quantum speed up over classical Monte Carlo methods. This generates new bridge between quantum physics and fluid dynamics engineering, can be used to estimate the potential impact of quantum computers and provides feedback on requirements for implementing quantum algorithms on quantum devices.

Acknowledgements

Here, I would like to look back and thank everyone through this journey.

First of all, I would like to express my greatest gratitude to my advisor Andrew Daley for his continuous support of my study and life. His enthusiasm, kindness and knowledge have always helped me throughout my research and the writing of my thesis.

I would like to thank my viva committee: Dieter Jaksch and John Jeffers for their comments, suggestions and hard questions. They really broaden my view of related topics and physics.

So many thanks to our collaborators: Hao-Tien Chiang, Rolando Somma, Peyman Givi. It is my honour to work with you and the bonds are beyond the physics.

My close friends from both US and UK have given me strength and confidence from the beginning of my adventure. Ningyuan, Yaofu, you guys made Chicago one of my favourite cities and helped me start the journey. It was a great time in Pittsburgh with my friends: Jianan, Hunter, Binbin, Lu, Zhuoni, Junmou, Lin, Peng, Azarin, Dritan, Simone, Kevin, Sumit. You put up a family and I am honoured to be part of it. The people make Glasgow: Anton, Saubhik, Jorge, Araceli, Rosaria, Liviu, Jennifer, Matteo, Enrico, Tristan, Jacopo Surace, Gione, Liam, David, Andreas, Alex, Suzanne, both Francois. Thank you, thank you so much. Friends at the westend: Gaolian, Hang, Li, Ying, Qian, Ying, Yiqiao, Lin, Jinhua, Chao, Zhaowei, both Yang. We had so much fun together and hope to see you soon.

Last but not least, I would like to thank my family and my girlfriend Zihan for supporting me go through this phase transition. You were always there for me. Your patience, support, encourage and love are the main reasons that I could overcome difficulties in the tough period. I couldn't make it without you.

Contents

Chapter 1

Introduction

1.1 Background and overview

The spirit of discovery is deeply rooted within the human heart. In order to continue pushing the frontiers of our knowledge in computational sciences across many subject areas, there is a need for new algorithms, numerical methods and computational instruments. Since the 1980s, the development of quantum computing, quantum information and quantum simulation has been undergoing fast expansion. Quantum computing uses quantum mechanical phenomena such as superposition and entanglement to perform computing. A quantum computer, which is the device that performs quantum computing, has the potential to efficiently solve problems that intractable by classical computers [1, 2]. Quantum simulation [3, 4], on the other hand, is to study specific quantum systems that are hard in the laboratory, by controlling other quantum systems that easy to access [5]. Quantum simulators, implementing quantum simulation, are designed to solve specific physics problems [6, 7]. The research on such subjects is helping build towards realising quantum computers and quantum simulators, developing quantum algorithms and also discussing their many potential applications. During the last decades, a particular interest for studying quantum many-body systems in the context of atomic, molecular, and optical physics (AMO) has arisen, particularly with neutral atoms in optical lattices [8]. Indeed, in such experiments, quantum many-body systems of atoms can be isolated from their environment and studied with microscopic understanding. Almost all the parameters of the systems can be controlled, allowing us to explore a broad range of many-body effects. [9]. These systems can be used to implement certain quantum emulations or can act as quantum computers that are able to solve complex classical problems which are intractable by other means. The continued interests

in quantum computing arises from the potential of quantum computers to solve certain complex problems much faster than can be done classically. This advantage of quantum computing over corresponding "classical" calculations, is also know as a quantum speedup. For example, Shor's algorithm for performing large number prime factorisation [10] takes a number of steps polynomial in the number of digits of the integer to be factored. This is exponentially faster than the best known classical algorithm which takes an exponential steps in the number of digits. Our interest in developing quantum algorithms is to achieve quantum speedups in broader contexts and to identify potential applications.

1.1.1   Cold atoms in optical lattices

The Bose-Einstein condensate (BEC) [11, 12], named after Satyendra Nath Bose and Albert Einstein, was first observed in dilute atomic gases in 1995 [13]. One of the key requirements for realising BEC in dilute gases is to achieve very low temperatures. The experiments can reach BEC in dilute gases at a temperature lower than 500 picokelvin [14] with the help of laser cooling [15] and evaporative cooling [16]. The interactions between atoms in such a dilute environment have a very weak effect on the condensation. In the limit of low temperature, the interatomic interactions reach a universal low-energy regime within scattering theory, so that the interaction strength is usually proportional to the scattering length. The fine tuning of the scattering length provides an important way to control the system. For example, using magnetic and optical Feshbach resonances [17, 18], the scattering length can be tuned continuously, which for some atomic species makes it possible to achieve attractive and repulsive interactions in the same experimental set-up.

The proposal of cold atoms as a toolbox to reach strong correlated regimes for particles in a lattice was developed by Jaksch *et al.* in 1998 [19]. Counter-propagating coherent lase beams form a periodic potential to confine neutral atoms with an energy shift of the ground state. The energy shift is proportional to the intensity of the laser field, so the atoms are confined in the optical lattices in the form of standing waves [15, 20–22]. The toolbox of Bose-Einstein condensation can then be used for fine tuning of properties of the atoms. We refer Chap. 3 for a detailed introduction of cold atoms in optical lattices. Several years after experiments with cold atoms in optical lattices were first proposed, a major experimental breakthrough was made [23], with observation of low-temperature properties of the Bose-Hubbard model in such systems. The experimental control of the depth of the optical potential can change both the interaction strength U between the atoms and the tunnelling rate J of the atoms from site to site through the lattice. Feshbach resonances can also be used to tune the interaction strength U. With

these controls, a wide range of the ratio U/J can thus be implemented. The continuous changing of U/J can realise a phase transition of the system between the superfluid phase and the Mott insulator phase.

The theory of phase transitions stands for a key concept for the characterization of equilibrium matter. A phase transition indicates a nonanalytic change in the properties of a large system [24]. In classical models, phase transitions are driven by thermal fluctuations. If the temperature is zero, $T = 0$, classical systems usually sit into a ground state which is fluctuationless, and therefore, no phase transition occurs. On the contrary, for quantum systems, the Heisenberg uncertainty principle provides the fluctuations that can drive interesting phase transitions at $T = 0$ even in the ground state. Quantum phase transitions (QFTs) occur as a result of competing ground state phases, where the ground-state properties undergo a nonanalytic change as a function of a control parameter [23–27]. One of the challenges to realise nonequilibrium quantum phase transition is to keep the system in the ground state throughout the processing. In Chap. 6, we introduce a new approach to realise the QPT from Mott insulator to superfluid phase by suppressing coherent process due to the change of the control parameter.

Besides orthogonal laser beam configurations producing cubic optical lattices, the experimental setups provide a more flexible geometry of optical lattices. Different geometries (triangular [20], Kagome [28], honeycomb [29]) can be realised by changing the directions of laser beams generating the optical potential. Two pairs of laser beams that form two independent 1D lattices with different frequencies can generate a superlattice geometry [30]. Also with the interplay of polarisations of two counterpropagating laser beams, a spin-dependent optical lattice can be formed to control the spin-dependent transport of neutral atoms [31]. Recent developments of quantum gas microscope techniques for Bosons [32, 33] and later for Fermions [34, 35] made it possible to detect strongly correlated states of matter directly via single-atom and single-site-resolved fluorescence imaging, and to produce arbitrary potential landscapes with spatial light modulations. In the experiments, atoms in optical lattices are cooled to a very low temperature of the order of one nanokelvin, where characteristic interaction frequencies are of the order of 10-10^4 Hz, and can be traced precisely.

Cold atoms in optical lattices thus construct a realisable platform for quantum simulations. For example, the experimental insight of high-temperature superconductors can be obtained by the simulations of phase diagrams for certain classes via cold atoms as a general quantum simulator of lattice models. The control of the parameters of the system and precise measurements provide access to out-of-equilibrium dynamics after a parameter quench [23, 36, 37] and the study of ground state properties [38, 39]. The long coherence time, secured by isolation of the system from its environment, provides the probabilities to simulate the

system with much shorter times of interaction and tunnelling. The high fidelity of state preparation and single-atom manipulation makes it possible to realise quantum simulations where this level of control is necessary.

The cold atoms in optical lattice is more than a platform of quantum simulation that we are interested, is also a promising platform of quantum computing. The basic requirements of a physical system to perform quantum computing were proposed by DiVincenzo [40]. Many of the requirements are fulfilled for cold atoms in optical lattices. An optical lattice can provide a well-defined set of qubits, which is also scalable. The long coherent time of the system grants the performing of single-qubit or two-qubit quantum gates realised by Raman laser and controlled interactions between particles [41–45]. For now, the main technical difficulty of addressing individual atoms is the disadvantage of cold atoms in optical lattices as a platform. However, proposals on quantum computing utilising global system control [46] and on using marker qubits [47] have the potential to solve that problem in the future.

1.1.2 Quantum algorithms and their applications

Quantum algorithms are designed to provide feasible solutions to problems which require enormous resources on a classical computer. The power of quantum computation comes, partly, from the access to enormous Hilbert spaces, which grow exponentially with the number of qubits. Quantum algorithms are commonly described in circuit models of quantum computation, as well as some other model like measurement-based quantum computing [48] and Hamiltonian oracle model [49, 50] which is the continuum limit of the standard unitary quantum oracles. The quantum circuit consists of initial qubits in certain well prepared quantum states, subsequent unitary quantum gates acting on a finite number of qubits, and in the end, a series of measurements in certain bases. The outcomes of measurements can generate the answer to chosen problems. Similar to classical algorithms, some basic quantum techniques are widely used in many quantum algorithms. There are two main techniques, amplitude amplification techniques [51, 52] and quantum Fourier transform (QFT) [4]. The amplitude amplification technique utilises the superposition principle of quantum mechanics. To reach a quantum state where the answer is encoded, the technique increases its amplitude to dominant so that it is the superposition. Thus we can obtain the target state from an initial state of a superposition of all the finite configurations. Based on this technique, Grover's algorithm for performing quantum searching on an unstructured database [53] provides a quadratic speedup over classical algorithms. The quantum Fourier transform is the quantum analogue of the discrete

Fourier transform, performing linear transformations on quantum bits. This unitary transform is the core to many well known algorithms like the Deutsch-Jozsa algorithm [54, 55], the Quantum phase estimation algorithm [4] and Shor's algorithm [56]. The quantum Fourier transform can be implemented efficiently on a quantum computer, and implies an exponential speedup over the classical Fourier transform [4, 57]. In recent decades, the applications of digital quantum algorithms have been extended to more general and complex subjects, like solving linear differential equations [58–60], element distinctness problems [61–63], and simulating sparse Hamiltonians [64].

Besides the quantum circuit model of quantum algorithms, analog quantum computation can also provide a speedup to solve complex problems [65]. We focus part of our research interests on adiabatic quantum computing (AQC) [66]. This form of quantum computing can provide a quantum state (usually the ground state of complex Hamiltonian) with designated answer encoded, starting with a well prepared state and implementing adiabatic evolution of time-dependent Hamiltonian. According to the adiabatic theorem, if the initial state and the target state are well connected by a time-dependent Hamiltonian, and the ramping speed is slow enough, the evolving system can be arbitrarily close to the target state. It has been shown to be equivalent to conventional quantum computing in the circuit model [67]. Within desired error, the time cost depends on the minimal energy gap of the Hamiltonian along the time evolution [68, 69]. The applications of AQC cover many of science subjects. Depending on the information encoded in the final state, the AQC can be implemeted to find the global optimum of discrete optimization problems [70, 71], to simulate quantum annealing [65, 72, 73], and to revisit the Grover search problem [74] and quantum simulation in other subjects [75–77].

To summarise, we are interested in both digital quantum computation and analogue quantum computation. The rapid developments of quantum hardware make it opportune to identify the potential applications of quantum computers in broader fields, including in engineering. By doing so, we would raise attention in different communities and provide feedback on requirements for practical quantum computing. We revisit the Phase Estimation Algorithm in Chap. 2 and apply this to develop a quantum algorithm to solve fluid dynamics problems in Chap. 8. For adiabatic quantum computing, we would like to improve the time cost of AQC in terms of gap dependence (Chap. 5). For adiabatic state preparation, we discuss adiabatic dynamics with presence of classical noise in Bose-Hubbard model (Chap. 6 & 7) to gain understanding of noise effects and identify possible optimisations of adiabatic ramping.

1.1.3 Computational methods

In the study of quantum many-body systems, it is generally hard to find analytical solutions to problems involving Hamiltonian dynamics. In a large complex quantum many-body system, the size of Hilbert space also grows exponentially with system size, which results in memory issues storing the quantum state and exponentially growing timescales for computations. For example, the Hilbert space of the one-dimensional spin $1/2$ chain with N sites has a size of 2^N. The configuration of one quantum state with 100 spins requires approximately 1.3 mega tera tera bytes of RAM to store which is impossible even for supercomputers. In the case of N Bosons confined in an optical lattice with M sites, the dimension of the Hilbert space is $(N + M - 1)!/N!(M-1)!$, which is also undertakes a exponential growth with the system size N, M at a fixed density of particles per site (N/M).

When we do not need to know all the properties of the system but only focus on a few of them, one approach is to consider only a subspace of the entire Hilbert space to approximate the properties. In other words, within certain approximation errors, considering only the most relevant quantum states can significantly reduce the dimension of Hilbert space that needs to be studied. As an example of this idea, Density Matrix Renormalization Group (DMRG) methods were proposed by S. R. White [78, 79]. These methods with a tensor network approach can reduce the computational resources required to capture the physics of quantum many-body systems. In the original proposal, DMRG methods were used for time independent calculations, like finding the ground state for one-dimensional system. Later on, it was shown that the form of matrix product states (MPS) can represent the ground state obtained from DMRG calculations [80]. Later research [81] quantified the performance of MPS representations approximating exact ground states of one-dimensional quantum spin systems. This result gave a theoretical justification of DMRG methods to achieve high accuracy even in the cases of critical systems. The extension of DMRG to study time-dependent dynamics was established in Ref. [82–84]. Behind the equivalence between the Time Evolving Block Decimation (TEBD) algorithm and t-DMRG, is the idea that adaptive change of basis, and truncation of a Hilbert space that provides advantages for exploring time evolution of complex system.

Now, the DMRG methods are widely used to study ground state properties and dynamics of complex quantum many-body systems in one dimension. They are compatible with many other computational methods like quantum trajectories methods [85] and master equation methods for studying dynamics in open quantum systems. These methods develop stochastic evolutions of quantum states to approximate master equations, which further reduces the computational resources needed. The understanding of open quantum systems can provide potential experimental tools to prepare important quantum states in strongly interacting systems

and reach the regimes necessary to realise quantum simulators. In the original research presented in this thesis, the time evolution and the ground state search of Bose-Hubbard model with large system size are computed utilising TEBD methods in Chap. 6. For small systems where exact diagonalisation methods are possible, the master equation approach is used to compute the stochastic average of a noisy time evolution and is covered in Chap. 6 & 7.

1.2   Outline of thesis

This thesis is arranged as follows. The introductory chapters consist of three parts including the physics and numerical background knowledge of our research. The original research results in the rest of this thesis are discussed in the context presented in the first part.

In Chap. 2, we start with the fundamental concepts of quantum computation and quantum metrology. In this part, we give a brief overview of quantum states and the transformations on the one-qubit system in the Bloch sphere, essential two-qubit gates that form a universal gate set, and controlled operations on $n+1$-qubits. In the following parts, we assemble universal quantum gates to form quantum circuits and demonstrate the basic structure of quantum algorithm. We discuss one method to mimic the behaviour of stochastic processes in classical algorithms by implementation of specific controlled gates. Later, we provide an overview of the phase estimation algorithm (PEA) and one method to estimate the expectation value of unitary operators. In the second half of this chapter, we revisit adiabatic quantum computing and adiabatic state preparation. In the end, we introduce the concept of eigenpath, which is essential to the discussion in Chap. 5.

In Chap. 3, we review the background of cold atoms in optical lattices, and the Hamiltonian of bosonic systems. Later, we discuss the amplitude noise introduced by the fluctuation of laser intensity, and how the parameters of the system behave accordingly in the context of the deep lattice regime. In the last part, we introduce a method to engineer amplitude noise, the dressed lattice scheme, which provides fine control on relative changes of the tunnelling parameter and the on-site interaction parameter. This scheme will be used to realise assisting noise to improve fidelity in Chap. 6 and to study thermalisation of energy introduced by amplitude noise in optical lattices in Chap. 7.

In Chap. 4, we introduce two main computational methods that we used in our research on quantum many-body system, the TEBD method and the Lindblad form of the master equation which represents an effective equation of motion for

adiabatic state transformation in the presence of classical noise. We show how the TEBD method works in the reduced Hilbert space. Later, we show how the dynamics of noisy adiabatic process can represented in master equations of Lindblad form in the limit of white noise. These methods are mainly used in simulations to obtain numerical results in Chap. 6.

In Chap. 5, we extend the idea of randomisation method, which is designed to achieve better fidelity in adiabatic state transformation by random time evolution in each discrete time step. The dephasing introduced by this stochastic average effect simulates projective measurements on an instantaneous eigenspace during a time evolution. We investigate improved bounds on eigenpath length by considering the second derivative of the Hamiltonian, and provide detail error analysis considering imperfect implementations of projective measurements to obtain the lower bound of the final fidelity of state preparation. These improved results can achieve better bounds for the time cost of adiabatic state transformation in terms of dependence relation of minimal gap during the state transformation. Thus, a potential speed up over previous research is observed.

In Chap. 6, we adapt the idea of randomised time evolution to the context of adiabatic state preparation in the presence of classical noise. By taking the one-dimensional Bose Hubbard system as an example, we identify the regime in which introducing certain type of noise can improve the final fidelity of state preparations, if the noise is approximately proportional to the instantaneous Bose Hubbard Hamiltonian. Later, we consider the adiabatic process with imperfect implementations of this noise. A study of a two-level system under certain theoretical assumptions is conducted to provide deeper understanding of this phenomenon. This study of white noise can provide insight into how classical noise acts during the adiabatic state preparation and provides a potential method to achieve high fidelity when time and resources are limited.

In Chap. 7, we extend our research of the classical noise in optical lattices and discuss further effects that classical noise induces in the dynamics of the system. We first investigate the total energy of the system after the adiabatic state preparation with the presence of classical noise. From our research, we identify a regime of minimum total energy as the evolution time grows with constant noise strength. Then we focus on the thermalisation of the system described by the Bose-Hubbard model after the application of noise pulses. The system in the superfluid phase tends to thermalise after the noise pulse, while in the Mott insulator phase, relaxation to a thermal state is not observed.

In Chap. 8, we develop a quantum algorithm to solve a stochastic mixing problem for classical fluid dynamics. The conventional Monte Carlo method to estimate properties with high precision of physical system of many particles and grids is

expensive in terms of computational resources and time-consuming. Using our quantum algorithm for turbulent mixing problems and reacting flow problems, a quadratic speed-up over classical methods is demonstrated, in terms of number of repetitions required to achieve designated precision. In this section,we both implement a classical MC method and simulate our quantum algorithm on binary scalar mixing process and reacting flow described by a coaslescence/dispersion model as examples. By illustrating comparisons of statistical error scaling of the two algorithms, we are able to demonstrate a quantum speedup. We expect this work to initiate discussions about potential applications of the quantum algorithm and requirements of corresponding quantum hardware, to thus estimate timescales of practical quantum computers.

In the final Chap. 9, we summarise the main results of our original research in this thesis, and give an outlook of future projects related to this thesis.

1.3 Contributions during my PhD

1.3.1 Publications

- Hao-Tien Chiang, Guanglei Xu, and Rolando D. Somma, "Improved bounds for eigenpath traversal", *Phys. Rev. A* 89, 012314, 2014

  The author of this thesis performed the analysis of final fidelities in this work

- Guanglei Xu, Andrew J. Daley, Peyman Givi, Rolando D. Somma, "Turbulent Mixing Simulation via a Quantum Algorithm", *AIAA journal*, pp. 1-13, 2017/12/13 2017

  The author of this thesis performed all of the numerical calculations, analytical calculations of the error of quantum algorithm, wrote the sections on numerical calculations, and produced all of the plots

1.3.2 Manuscripts in preparation

- Guanglei Xu, Andrew J. Daley, "Adiabatic dynamics with classical noise in optical lattice", *In preparation* 2017

- Guanglei Xu, Andrew J. Daley, "Thermalisation of strongly interacting bosons after amplitude noise pulse", *In preparation* 2017

- Guanglei Xu, Andrew J. Daley, Peyman Givi, Rolando D. Somma "A Quantum Algorithm for Modelling of Reactant Conversion Rate in Homogeneous Turbulence", *In preparation* 2017

1.3.3 Conference presentations

- Guanglei Xu, Andrew Daley, Peyman Givi, Rolando Somma, "Turbulent Mixing Simulation via Quantum Algorithm" in *Pittsburgh Quantum Institute Conference: Quantum Revolutions*, (Pittsburgh, PA, USA), 2017

- Guanglei Xu, Andrew Daley, Peyman Givi, Rolando Somma, "Quantum speed-up for Turbulent Mixing Simulation" in *APS DFD meeting*, (Portland, OR, USA), 2016

- Guanglei Xu, Andrew Daley, "Adiabatic dynamics with Classical Noise in Optical Lattice" in *Workshop on Many-body Dynamics and Open Quantum Systems*, (Glasgow, UK), 2016

- Guanglei Xu, Andrew Daley, "Adiabatic dynamics with classical noise in optical lattice" in *APS DAMOP meeting* (Providence, RI, USA), 2016

- Guanglei Xu, Andrew Daley, "Adiabatic dynamics with classical noise in optical lattice" in *Pittsburgh Quantum Institute Conference: Quantum challenges*, (Pittsburgh, PA, USA), 2016

- Guanglei Xu, Andrew Daley, "Adiabatic state preparation in a noisy optical lattice" in *SUSSP71*, (Glasgow, UK) 2015

- Guanglei Xu, Andrew Daley, "Adiabatic state transformation in the presence of classical noise" in *The 24th International Conference on Atomic Physics*, (Washington, D.C., USA), 2014

Chapter 2

Quantum computation

In this chapter, we present the background of techniques and concepts of quantum computation that we will use in our original research. This chapter consists of two sections: quantum algorithms and quantum metrology, and adiabatic quantum computing. Studying basic principles of quantum computation can provide us the building blocks for developing quantum algorithms. Full understanding of quantum operations can be used to improve existing quantum algorithms.

We start with an overview of quantum computation and algorithms for quantum metrology, with the basics of quantum state transformations and the phase estimation algorithm. Then, we revisit adiabatic quantum computing and the core background of that, the adiabatic theorem of quantum mechanics. After that, we introduce the concept of the eigenpath of adiabatic processes that has been used in many eigenpath transversal methods to bound the time cost of adiabatic quantum computation.

2.1 Quantum computation and quantum metrology

In this section, we provide a brief overview of quantum computation and the quantum phase estimation algorithm for quantum metrology. For more details, we would refer to Refs. [4, 86]. The Dirac bra-ket notation we use here [4, 86, 87] is that a state $|\phi\rangle$ can be associated with a column vector ϕ in the complex and finite-dimensional Hilbert space $\mathbb{C}^N$, and $\langle\phi|$ can be associated with $\phi^\dagger$, the conjugate transpose of ϕ.
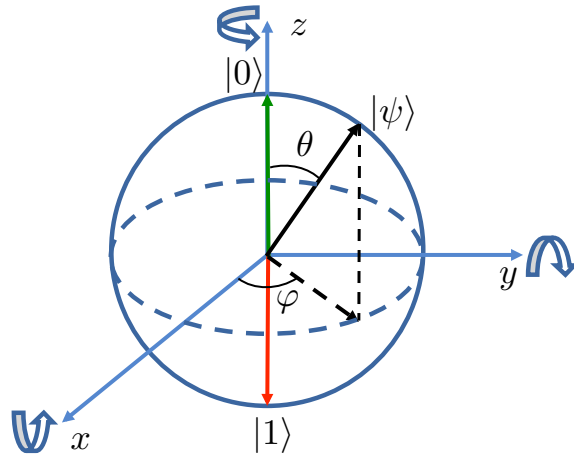
FIGURE 2.1: A Bloch sphere diagram of single-qubit unitary transformations. In the eigenbasis of σ_z, the $|0\rangle$ state (green) is defined along the north pole and $|1\rangle$ (red) is at the south pole. Up to a global phase factor, single qubit states can be represented as $|\Psi\rangle = \cos(\theta/2)\,|0\rangle + e^{i\varphi}\sin(\theta/2)\,|1\rangle$, where ϕ is the azimuthal angle, and θ is the polar angle. The curved arrows on each axis indicate rotations around axis ν.

2.1.1   Quantum states and transformations

The qubit is the fundamental unit in the circuit model of quantum computation. The state of a qubit can be represented as a linear superposition of $|0\rangle$ and $|1\rangle$ ($|\Psi\rangle = a_0\,|0\rangle + a_1\,|1\rangle$), and the complex coefficients a_0 and a_1 are normalized to unity: $|a_0|^2 + |a_1|^2 = 1$. For convenience we also define another possible basis of single qubit, $|+\rangle = (|0\rangle + |1\rangle)/\sqrt{2}$ and $|-\rangle = (|0\rangle - |1\rangle)/\sqrt{2}$. Assigned to each qubit are the Pauli (unitary) matrices σ_i. In general, $\mathbb{1}_D$ denotes the identity matrix with dimension D. Operations on a single qubit can be implemented by a sequence of unitary transformations. For example, the operation $R(\nu,\theta) = e^{-i\theta\sigma_\nu/2}$, with $\nu = x, y, z$ can be interpreted as a rotation operation around the ν axis (rotations in the Bloch sphere as in Fig. 2.1). Another useful and standard single-qubit operation used in quantum computing is the Hadamard gate H, which can transform states as $H\,|0\rangle = |+\rangle$ and $H\,|1\rangle = |-\rangle$. The matrix representation of the Hadamard gate in the eigenbasis of σ_z is,

$$H = \frac{1}{\sqrt{2}} \begin{pmatrix} 1 & 1 \\ 1 & -1 \end{pmatrix} . \tag{2.1}$$

A state of n qubits can be represented as

$$|\Psi\rangle = \sum_{l=0}^{N-1} a_l \, |l\rangle = a_0 \, |0\ldots00\rangle + a_1 \, |0\ldots01\rangle + \ldots + a_{N-1} \, |1\ldots11\rangle \ . \qquad (2.2)$$

The dimension of the Hilbert space is $N = 2^n$. In this representation, $|l\rangle$ is a state in the computational basis, which stands for the corresponding binary representation of a number l. The complex coefficients a_l satisfy the normalization condition $\sum_{l=0}^{N-1} |a_l|^2 = 1$. The position of each number $0, 1$ in the computational basis vectors represents the label of each qubit, $|00\ldots\rangle = |0\rangle_1 \, |0\rangle_2 \ldots |0\rangle_n$.

A state which can be described by a single ket vector is called a pure state, like $|0\rangle$ and Eq. (2.2). The density operator of a pure state is $\rho_{\text{pure}} = |\psi\rangle \, \langle\psi|$. On the other hand, a quantum system in one of a number of states $|\psi_i\rangle$ with certain non-zero probabilities p_i has the density operator

$$\rho_{\text{mix}} \equiv \sum_i p_i \, |\psi_i\rangle \, \langle\psi_i| \ , \qquad (2.3)$$

with $\sum_i p_i = 1$, and $0 < p_i < 1$. This density operator describe a mixed state. The trace of ρ^2 of a pure state and a mixed state is different.

$$\text{tr}(\rho_{\text{pure}}^2) = 1 \qquad (2.4)$$
$$\text{tr}(\rho_{\text{mix}}^2) < 1 \qquad (2.5)$$

The state vector of a pure state is on the Bloch sphere and the state vector of a mixed state is inside of the Bloch sphere.

An operation on the $j-$th qubit in a system of n qubits can be generated by tensor products of Pauli matrices, that is,

$$\sigma_\nu^j = \sigma_0 \otimes \cdots \otimes \underbrace{\sigma_\nu}_{j\text{th position}} \otimes \cdots \otimes \sigma_0 \ , \qquad (2.6)$$

where σ_0 is the 2-by-2 identity matrix. Here, $\nu = 0, x, y, z$ and $j = 1, \ldots, n$. In quantum computing, many-qubit operations can be performed by a sequence of gates drawn from a universal gate set. A set of gates is said to be universal for quantum computation, if any unitary operation can be approximate to arbitrary accuracy by a quantum circuit constructed only using those gates. We refer Sec.4.5 of Ref. [4] for more details. These gate sets of transformations usually act on one or two qubits, for example,

$$R_j(\nu, \theta) = e^{-i\theta\sigma_\nu^j/2} \ , \ R_{j,k}(\omega) = e^{-i\omega\sigma_z^j\sigma_z^k} \ . \qquad (2.7)$$

Other universal sets of quantum gates can be constructed using the $R_j(\nu, \theta)$ and controlled operations such as the controlled NOT gate (CNOT). The CNOT gate represents a two-qubit unitary operation that changes only the state of the target qubit according to the state of the control qubit. If we represent a two-qubit state as $|a\rangle_1 |b\rangle_2$, where the subscripts 1 and 2 represent the two qubits and $|a\rangle$ and $|b\rangle$ represent quantum states, $|a\rangle, |b\rangle \in \{|0\rangle, |1\rangle\}$. When the first qubit is the control qubit, and the second qubit is the target qubit, the CNOT gate performs the transformations as follows, $|0\rangle_1 |0\rangle_2 \to |0\rangle_1 |0\rangle_2$, $|0\rangle_1 |1\rangle_2 \to |0\rangle_1 |1\rangle_2$, $|1\rangle_1 |0\rangle_2 \to |1\rangle_1 |1\rangle_2$, $|1\rangle_1 |1\rangle_2 \to |1\rangle_1 |0\rangle_2$

For an arbitrary n-qubit unitary operation U, we can define a $n+1$-qubit unitary transformation ^cU, which is controlled by the state of an ancillary qubit noted as $|0\rangle_a$ or $|1\rangle_a$, and transforms as follows:

$$^cU |0\rangle_a |\Psi\rangle = |0\rangle_a |\Psi\rangle \quad , \quad {}^cU |1\rangle_a |\Psi\rangle = |1\rangle_a U |\Psi\rangle \ . \tag{2.8}$$

In quantum mechanics, all measurable observables have an associated Hermitian operator. In our case, we are only concerned about simple measurements of qubits in the computational basis $|0\rangle$ and $|1\rangle$, where the measurement operators are the σ_z. If the quantum state is described as in Eq. (2.2), the probability that we find the state projected into $|l\rangle$ after measurement of all qubits is $|a_l|^2$ [88].

2.1.2 Quantum algorithms and quantum circuits

In quantum computing, a general quantum algorithm often consists of three parts. The first part is the preparation of an initial state, such as a simple state $|0 \ldots 0\rangle$ or a more general initial state $|\psi\rangle$. The second part is a sequence of instructions, implementing gates from a universal gate set to approximate a desired unitary operation on all qubits. The final part is to perform projective measurements to extract classical information. The number of simple operations needed for each of the three steps gives the cost of a quantum algorithm. Typically, the complexity of a quantum algorithm (how the cost scales with n) is dominated by the preparation of the initial state and the second step, since the complexity of simple measurements from the final part is assumed to be linear in n. Quantum circuits are commonly used to represent quantum algorithms. A quantum circuit is a sequence of elementary unitary gates applied to an initial state, and one convention of diagrams is the time goes from left to right. An example of a quantum circuit is shown in Fig. 2.2, which describes the quantum phase estimation algorithm (PEA). The quantum Fourier transform F that the PEA uses is also given in Fig. 2.2 (b). Suppose the unitary operator U has an eigenvector $|u\rangle$ with eigenvalue $e^{2\pi i\phi}$, where ϕ is the eigenphase. The PEA outputs an estimate of an
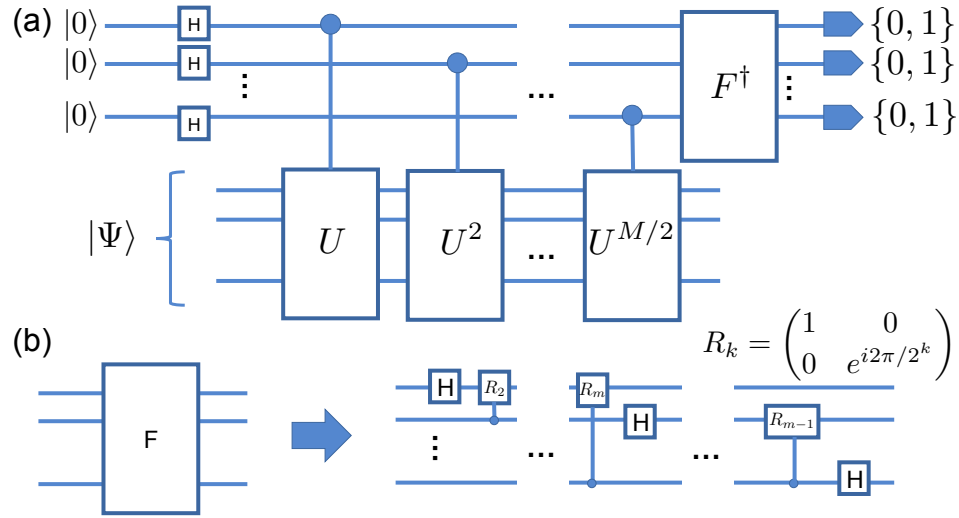
FIGURE 2.2: (a) The diagram of a quantum circuit for the phase estimation algorithm (PEA). The circles denote a controlled operation (e.g., a controlled U^k) on the corresponding state of an ancilla qubit in 2.8. The outcome $\{0,1\}$ of each measurement provides one digit of the binary representation of an estimate of an eigenphase of U (Sec. 2.1.4). $F^\dagger$ is the inverse of the quantum Fourier transform. (b) Quantum circuit for the quantum Fourier transform in terms of elementary gates on one or two qubits. For simplicity, this diagram for F does not show trivial swap operations at the end which reverse the order of the qubits [4]

eigenphase or eigenvalue of a unitary U [89]. We will provide more details of this algorithm in Sec. 2.1.4.

2.1.3   Simulating classical probabilistic problem

In computational complexity theory, the class of problems that can be solved efficiently in polynomial time with a quantum computer is referred to as BQP; on the other hand, the class of problems that can be solved in polynomial time with a classical probabilistic computer is called BPP. The relation between this two classes is that BPP $\subseteq$ BQP. Every classically solvable problem can be solved on a quantum machine. One way to simulate a classical probabilistic algorithm efficiently on a quantum computer, is that each classical random bit can be simulated by introducing a new ancilla qubit. The ancilla qubit is in the state $|p\rangle_\text{a}$, which is a random bit that has probability p of being in $|0\rangle$, e.g., $|p\rangle_\text{a} = \sqrt{p}\,|0\rangle_\text{a} + \sqrt{1-p}\,|1\rangle_\text{a}$. We can then construct a controlled gate acting on the state of the ancilla and

the qubit where the probabilistic implementation acts. We can then disregard all the ancilla qubits at the end of the quantum computation. In more detail, assume that the state of a classical computer $\phi \in \{0,1\}^n$. We introduce a random ancillary bit and depending on the value of the random bit we transform the state to $\phi_0 \in \{0,1\}^n$ or $\phi_1 \in \{0,1\}^n$ with certain probability p. In quantum computation, we can implement a controlled unitary transformation on a random ancillary qubit and the qubits representing the classical state as follows:

$$|p\rangle_a |\phi\rangle \rightarrow \sqrt{p} |0\rangle_a |\phi_0\rangle + \sqrt{1-p} |1\rangle_a |\phi_1\rangle \ . \tag{2.9}$$

It follows that a simple measurement of the ancilla qubit in Eq. (2.9) provides the outcome 0 or 1, which simulates the classical probabilistic process. In either case, the state of the quantum computer is projected into $|\phi_0\rangle$ or $|\phi_1\rangle$ with classical probability p or $1-p$.

2.1.4 Phase estimation algorithm

Quantum-enhanced metrology (QM), an important example of quantum processing of information (c.f., [90] and references therein), seeks to obtain properties of quantum states as precisely as possible within the available resources. Take the problem of obtaining the probability p by making measurements on the single qubit state $|\Psi\rangle = \sqrt{p} |0\rangle + \sqrt{1-p} |1\rangle$ as an example. The outcome after the measurement in the computational basis is either 0 or 1, representing the quantum state after the measurement becomes $|0\rangle$ or $|1\rangle$ depends on the outcome. One possible way is to repeat state preparation and measurements and count the frequency of that outcome is 0 (which means the state is in $|0\rangle$ after the measurement). According to Chebyshev's inequality, the statistical error ε_c in the estimation of p scales as $\varepsilon_c \propto 1/\sqrt{N_r^c}$, after N_r^c repetitions. However, applying certain quantum algorithms [91–93] on quantum computers, the same precision in the estimation of p can be achieved by preparing $|\Psi\rangle$ for N_r^q times. Since the error of the quantum algorithm ε_Q is proportional to $1/N_r^q$, when $\varepsilon_C = \varepsilon_Q$, N_r^q is of the order of $\sqrt{N_r^c}$, which is known as the QM limit.

We would like to introduce one method to achieve the QM limit in the following part of this section. Considering the same problem as in the previous paragraph, estimating the value of p, we can construct $U = e^{-i\theta\sigma_z/2}$ for state preparation, where $\theta = 2\arccos(\sqrt{p})$. The precision $\epsilon > 0$ of the quantum algorithm estimating θ can be translated to an uncertainty to estimating of p with the same order of

precision. We note the estimate of θ as $\hat{\theta}$ in binary form using m bits as

$$\begin{aligned}
\hat{\theta} &= 2\pi[.b_1', b_2', \ldots b_m'] \\
&= \pi(b_1' + b_2'/2 + \ldots b_m'/2^{m-1}) \, .
\end{aligned} \tag{2.10}$$

Here, $b_i' \in \{0, 1\}$ specifies the bits of the number in the binary representation, and we choose $m = O(\log_2(1/\epsilon))$ according to achieve the desired precision, ϵ. The quantum algorithm can be implemented in m basic steps. In each step $1 \leq j \leq m$, it generates the outcome b_{m-j+1}'. In the beginning, we start by estimating the least significant bit and move towards the most significant ones using previous outcomes. This algorithm is referred to as the single-qubit PEA.

Input: A single-qubit unitary $U = e^{-i\theta\sigma_z/2}$ and a precision parameter $\epsilon > 0$.

1. Obtain the smallest integer m such that $M \geq 2\pi/\epsilon$, with $M = 2^m$.
2.
    2.1 Prepare the single-qubit state $|+\rangle$ and apply U, $M/2$ times.
    2.2 Apply a Hadamard transformation and measure the qubit in the computational basis.
        Let $b_m' \in \{0, 1\}$ be the measurement outcome.

3. Do the following for each $k = (m-1), \ldots, 1$:
    3.1 Prepare the single qubit state $|+\rangle$ and apply U, 2^{k-1} times.
    3.2 Compensate the phase of $|1\rangle$ by $e^{-i\pi[.b_{k+1}'...b_m']}$.
    3.3 Apply a Hadamard transformation and measure the qubit in the computational basis.
        Let $b_k' \in \{0, 1\}$ be the measurement outcome.

Output: An estimate of θ as $\hat{\theta} = 2\pi[.b_1' \ldots b_m']$.

In general, the probability of an m-bit estimate $\hat{\theta}$ of θ is [94],

$$\Pr(\hat{\theta}) = \frac{1}{4^m} \left| \frac{e^{i2^m\theta} - 1}{e^{i(\theta-\hat{\theta})} - 1} \right|^2 \, . \tag{2.11}$$

If θ can be exactly represented just using $m-1$ bits as in Eq. (2.10), this quantum algorithm provides an exact estimate

$$\Pr(\hat{\theta} \to \theta) = \frac{1}{4^m} \left| \frac{\frac{d}{d\theta}(e^{i2^m\theta} - 1)}{\frac{d}{d\theta}(e^{i(\theta - \hat{\theta})} - 1)} \right|^2$$

$$= \frac{1}{4^m} \left| \frac{i2^m}{i} \right|^2 = 1$$

In other cases, let $\tilde{\theta}$ denote the best m-bit estimate of θ, and $\theta = \tilde{\theta} + \delta$, where $0 < |\delta| \leq \frac{2\pi}{2^{m+1}}$. From Eq. (2.11), the probability of the best estimate is

$$\Pr(\tilde{\theta}) = \frac{1}{4^m} \left| \frac{e^{i2^m\delta} - 1}{e^{i\delta} - 1} \right|^2 . \tag{2.12}$$

Since, $|\delta| \leq \frac{2\pi}{2^{m+1}}$, it follows $|\delta|2^m \leq \pi/2$, and thus $|e^{i2^m\delta} - 1| \geq \delta 2^m/(\pi/2)$, and $|e^{i\delta} - 1| \leq \delta$. Therefore, the probability of obtaining the best estimate $\tilde{\theta}$ is

$$\Pr(\tilde{\theta}) \geq \frac{1}{4^m} \left(\frac{\delta 2^m/(\pi/2)}{\delta} \right)^2 = \frac{4}{\pi^2} \approx 0.405 . \tag{2.13}$$

This quantum algorithm returns either of the two closest m-bit estimates of θ with probability lower bound $8/\pi^2$ [94].

The performance of the quantum algorithm is related to the cost of state preparations. For precision $\epsilon = \mathcal{O}(1/M)$, the quantum algorithm requires $M = 2^m$ implementations of U. This gives a quadratic cost improvement over standard (classical) methods [95]. We can also increase the confidence level c of the estimation by repeating the PEA for L independent times and letting $\hat{\theta}_1, \ldots, \hat{\theta}_L$ be L estimates of θ obtained in each of these applications. We can bound the probability that $\hat{\theta}_i \notin [\theta_l, \theta_r]$, where θ_l and θ_r as the two closest m-bit approximations of θ, by $p_f = 1 - 8/\pi^2$ from above [93]. We then choose the median of these L estimates as the estimate $\hat{\theta}$, so that the probability that $\hat{\theta} \notin [\theta_l, \theta_r]$ can be bounded by [93, 96]

$$\frac{1}{2} \left(2\sqrt{p_f(1 - p_f)} \right)^L \leq \frac{1}{2}(0.8)^L . \tag{2.14}$$

Thus, $L = O(|\log(1-c)|)$ repetitions of PEA are required to achieve a confidence level c. Then in total, the number of implementations the unitary U is

$$N_r = L \times M . \tag{2.15}$$

With some modifications to the single-qubit PEA, we can also estimate the eigenphase of a unitary operator U acting on n-qubit states. First, we need to prepare the eigenstate of U with the eigenphase $e^{i\theta}$. Let $|\Psi\rangle$ satisfy $U|\Psi\rangle = e^{i\theta}|\Psi\rangle$, and let us assume that we can efficiently prepare it by implementing V, $|\Psi\rangle = V|00\ldots0\rangle$. Similar to the singe-qubit PEA, we can define the controlled unitary gate ${}^{\mathrm{c}}U$ acting on the $n+1$ qubits, which implements U on the state if and only if the ancilla qubit being in the state $|1\rangle_{\mathrm{a}}$. The PEA for eigenphase estimation is:

Input: n-qubit unitaries U and V, and a precision parameter $\epsilon > 0$.

1. Obtain the smallest integer m such that $M \geq 2\pi/\epsilon$, with $M = 2^m$.
2.
    2.1 Prepare $|\Psi\rangle$ and the single-qubit ancilla state $|+\rangle_{\mathrm{a}}$, and apply ${}^{\mathrm{c}}U$, $M/2$ times.
    2.2 Apply a Hadamard transformation and measure the ancilla qubit in the computational basis.
        Let $b'_m \in \{0,1\}$ be the measurement outcome.

3. Do the following for each $k = (m-1), \ldots, 1$:
    3.1 Prepare the single-qubit ancilla state $|+\rangle_{\mathrm{a}}$ and apply ${}^{\mathrm{c}}U$, 2^{k-1} times.
    3.2 Compensate the phase of $|1\rangle_{\mathrm{a}}$ by $e^{-i\pi[.b'_{k+1}\ldots b'_m]}$.
    3.3 Apply a Hadamard transformation and measure the ancilla qubit in the computational basis.
        Let $b'_k \in \{0,1\}$ be the measurement outcome.

Output: An estimate of θ as $\hat{\theta} = 2\pi[.b'_1\ldots b'_m]$.

The outcome of this algorithm is the same as that of the single-qubit PEA and the probability of the outputs $\hat{\theta}$ is given by Eq. (2.11). Because of this similarity, we can estimate the eigenphase θ of a unitary operator U with probability of, at least, $8/\pi^2$ in a single run. We can also repeat this algorithm L times to reach a desired confidence level c, with $L = O(|\log(1-c)|)$. The number of uses of the unitary gate ${}^{\mathrm{c}}U$, N_r, and L uses of the state preparation gate V will dominate the cost and therefore complexity of this algorithm.

2.1.4.1 Expectation values estimation

Besides the eigenphase estimation the PEA can also be used as a subroutine for estimating the expectation value of operators [93, 97]. Considering estimating the
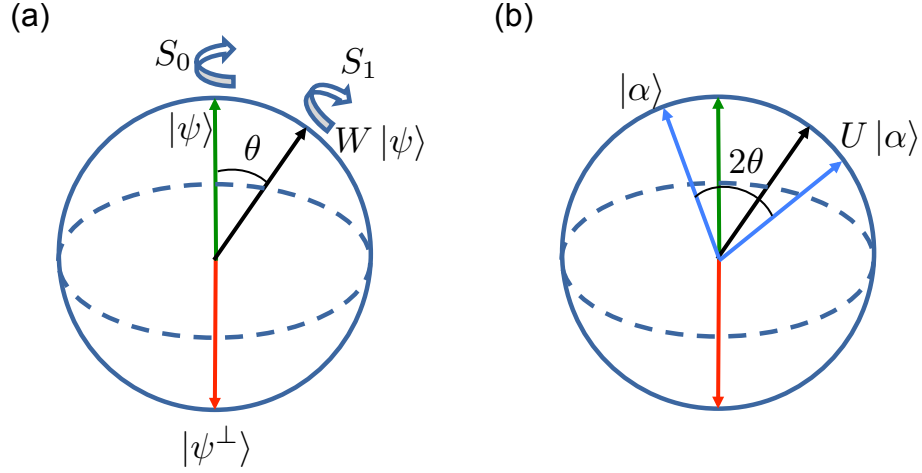
FIGURE 2.3: Bloch sphere representation of the two-dimensional vector space spanned by $|\Psi\rangle$ and $W|\Psi\rangle = \cos(\theta/2)|\Psi\rangle + e^{i\phi}\sin(\theta/2)|\Psi^\perp\rangle$. We obtain the overlap between $|\Psi\rangle$ and $W|\Psi\rangle$, $w = \cos(\theta/2)$. (a) Representation of the two reflections S_0 and $S_1 = WS_0W^\dagger$, with S_0 defined in Eq. (2.16). (b) Representation of the effective rotation $U = S_0S_1$ for an angle of 2θ for an arbitrary vector $|\alpha\rangle$ (blue). The eigenvalues of U are $e^{\pm i\theta}$ and its eigenphases are $\pm\theta$.

expectation value w of a unitary operator W, the value of w is associated with the pure n-qubit state $|\Psi\rangle = V|00\ldots0\rangle$ and $w = \langle\Psi|W|\Psi\rangle$. For simplicity, we assume that $w \in [0, 1]$. We refer to [93] for the general case estimating a complex expectation value. We can represent $W|\Psi\rangle = \cos(\theta/2)|\Psi\rangle + e^{i\varphi}\sin(\theta/2)|\Psi^\perp\rangle$, where $|\Psi^\perp\rangle$ is a state orthogonal to $|\Psi\rangle$. Then the quantum states $|\Psi\rangle$ and $W|\Psi\rangle$ can span a two-dimensional Hilbert space, as in Fig. 2.3. The overlap between $|\Psi\rangle$ and $W|\Psi\rangle$ is then the expectation value $w = \cos(\theta/2)$. The next step is to construct a unitary operation U with eigenphase θ, so that we can apply the PEA.

First, we can design a unitary operation which implements a "reflection" operation. We introduce a unitary operation S_0 implementing by applying $V^\dagger$, reflection over $|00\ldots0\rangle$, and then applying V, $(S_0 = V(\mathbb{1}_{2^n} - 2|00\ldots0\rangle\langle00\ldots0|)V^\dagger)$.

$$S_0|\Psi\rangle = -|\Psi\rangle \qquad S_0|\Psi^\dagger\rangle = |\Psi^\dagger\rangle \qquad\qquad (2.16)$$

Second, we can design a unitary operation which implements a reflection over the state $W|\Psi\rangle$, $S_1 = WS_0W^\dagger$. The gate cost of S_1 is twice the gate cost of W. With these two reflection operations, we can construct a rotation, $U = S_0S_1$, by an angle of 2θ. By applying the PEA to estimate the eigenphase of U, we can

then obtain the expectation value w of unitary operator W. For the input state $|\Psi\rangle$, it can be shown that

$$|\Psi\rangle = \frac{1}{\sqrt{2}} \left(|\Psi_+\rangle + |\Psi_-\rangle \right) , \tag{2.17}$$

where $|\Psi_\pm\rangle$ are two eigenstates of U, $U|\Psi_\pm\rangle = e^{\pm i\theta}|\Psi_\pm\rangle$. We will obtain an estimate of θ or $-\theta$ with equal probability and any of these estimations suffices to determine $w = \cos(\theta/2)$. With all the steps, the quantum algorithm to estimate an expectation value w is:

Input: n-qubit unitaries W and V, and a precision parameter $\epsilon > 0$.

1. Obtain the smallest integer m such that $M \geq 2\pi/\epsilon$, with $M = 2^m$.
2.
    2.1 Prepare $|\Psi\rangle$ and the single-qubit ancilla state $|+\rangle_{\mathrm{a}}$, and apply $^{\mathrm{c}}U$, $M/2$ times. Here, $U = S_0 S_1$.
    2.2 Apply a Hadamard transformation and measure the ancilla qubit in the computational basis.
        Let $b'_m \in \{0, 1\}$ be the measurement outcome.

3. Do the following for each $k = (m-1), \ldots, 1$:
    3.1 Prepare the single-qubit ancilla state $|+\rangle_{\mathrm{a}}$ and apply $^{\mathrm{c}}U$, 2^{k-1} times.
    3.2 Compensate the phase of $|1\rangle_{\mathrm{a}}$ by $e^{-i\pi[.b'_{k+1}\ldots b'_m]}$.
    3.3 Apply a Hadamard transformation and measure the ancilla qubit in the computational basis.
        Let $b'_k \in \{0, 1\}$ be the measurement outcome.

Output: $\hat{w}$, an estimate of $w = \langle\Psi| W |\Psi\rangle$ as $\cos(\hat{\theta}/2)$, with $\hat{\theta} = 2\pi[.b'_1 \ldots b'_m]$.

Since the uncertainty of $\hat{\theta}$ is ϵ, then the precision ϵ' in the estimation of w at first order in ϵ is $O((\epsilon/2)\sin(\hat{\theta}/2))$. Thus, when w is near 1 (i.e, θ and the estimating output $\hat{\theta}$ are near zero), this algorithm provides more precise estimates. The error in estimate the expectation value w can be bounded as,

$$|\hat{w} - w| = |\cos(\hat{\theta}/2) - \cos(\theta/2)| \leq \epsilon' = |\cos((\hat{\theta} + \epsilon)/2) - \cos(\hat{\theta}/2)| , \tag{2.18}$$

which is valid when $0 \leq \hat{\theta} \leq \pi$ and $0 < \epsilon \leq 1$. A similar bound can be obtained for $-\pi \leq \hat{\theta} \leq 0$.

The results of probability to generate the one of the best two estimates still holds,

$$\Pr(|\hat{w} - w| \leq \epsilon') \geq 8/\pi^2 \ . \tag{2.19}$$

So, we can reach the confidence level c by obtaining $L = O(|\log(1-c)|)$ independent estimates and computing the median as the best estimate (Eq. (2.14)).

This algorithm can also provide an estimation of expectation value of an observable (not necessary unitary operator) for various problems [98, 99]. With certain conditions of the observable, it is possible to construct a unitary operator in larger dimension which has the same expectation value, so we can apply the PEA to obtain estimates with high precision. We refer to [93, 97–99] for more details and a more general case.

2.2 Adiabatic quantum computing

In the previous section, we talked about quantum algorithms in the circuit model and how the PEA can obtain the information simulating classical probabilistic problems. Quantum algorithms are described by means of quantum circuits. However, the circuit model may not always be suitable to describe all quantum information processing systems. Adiabatic quantum computing has been proposed as an alternative. The idea of the adiabatic quantum computation was first proposed in 2000 [100], where it was shown that we can encode the solution of a problem in the ground state of a known Hamiltonian. Now, this technology was used in a wide range of topics like the quantum search [74, 101], quantum annealing [72, 102, 103] and period finding [104].

In majority of situations, when the ground state of target Hamiltonian is hard to realise, we can still try to start with a system that easy to prepare and evolve the whole system under a time-dependent Hamiltonian, which is a linear interpolation of the initial Hamiltonian (H_0) and the final (target) Hamiltonian H_f, $H(t) = (1 - s(t))H_0 + s(t)H_f$. The adiabatic theorem [88] of quantum mechanics ensures that if we start with the ground state of the initial Hamiltonian and evolve the system "slowly", it will remains in the ground state of instantaneous Hamiltonian provided that there is always a gap between the ground state and the first excited state. After an infinitely long time (since we change the Hamiltonian infinite slowly), the system would end up in the target ground state. In the case of finite speed, we obtain the state in target ground state with a fidelity that depends on the speed of the ramp, and the details of the Hamiltonian.

During the adiabatic state transformation, the ground state changes from one simple initial ground state of H_0 to the ground state of H_f, which encodes the

solution of the problem. The probability that system is found in an excited state depends on the gap between those states and changing speed of the Hamiltonian. Thus, we should be more careful when the gap is very small, for instance, at critical point for systems where there is a phase transition, and reduce the speed of adiabatic ramping. If we don't have access to the instantaneous ground state, the condition of speed of changing Hamiltonian (adiabatic condition) around minimum gap should remain global. In this case of linear interpolation, the adiabatic condition express the relation between total evolution time and minimal energy gap.

2.2.1   Adiabatic theorem of quantum mechanics

The adiabatic approximation is a popular method of quantum mechanics used to derive solutions of the Schrödinger equation under a slowly changing Hamiltonian. According to the Schrödinger equation, the state vector $|\psi(t)\rangle$ evolves as

$$i\frac{d}{dt}|\psi(t)\rangle = H(t)|\psi(t)\rangle \ , \tag{2.20}$$

where $|\psi(0)\rangle$ is the ground state of the Hamiltonian $H(0)$, and we consider $\hbar = 1$. The eigenstates of the instantaneous Hamiltonian $|n(t)\rangle$ are:

$$H(t)|n(t)\rangle = E_n(t)|n(t)\rangle \ , \tag{2.21}$$

where $E_n(t)$ are the corresponding eigenvalues (energy) of Hamiltonian. To solve the equation, we expand the state vector in the basis of eigenstates $|n(t)\rangle$

$$|\psi(t)\rangle = \sum_n a_n(t) \exp\left(-i\int_0^t E_n(t')dt'\right)|n(t)\rangle \ . \tag{2.22}$$

Then the time derivative of the state is

$$\begin{aligned}
\frac{d}{dt}|\psi(t)\rangle = &\sum_n \dot{a}_n(t) \exp\left(-i\int_0^t E_n(t')dt'\right)|n(t)\rangle \\
&+ \sum_n \dot{a}_n(t) \exp\left(-i\int_0^t E_n(t')dt'\right)|\dot{n}(t)\rangle \\
&+ \sum_n a_n(t) \exp\left(-i\int_0^t E_n(t')dt'\right)(-iE_n(t))|n(t)\rangle \ .
\end{aligned} \tag{2.23}$$

The Hamiltonian $H(t)$ in the eigenbasis takes the form $H(t) = \sum_n E_n(t) |n(t)\rangle \langle n(t)|$, and the right hand side of Eq. (2.20) becomes

$$H(t) |\psi(t)\rangle = \sum_n E_n(t) |n(t)\rangle \langle n(t)|\psi(t)\rangle . \tag{2.24}$$

Multiply both side of the Eq. (2.20) by $\langle m|$ and we have

$$-iE_m a_m \exp\left(-i \int_0^t E_m(t')dt'\right) = \dot{a}_m(t) \exp\left(-i \int_0^t E_m(t')dt'\right)$$
$$- iE_m a_m \exp\left(-i \int_0^t E_m(t')dt'\right)$$
$$+ \sum_n a_n(t) \exp\left(-i \int_0^t E_n(t')dt'\right) \langle m|\dot{n}\rangle \tag{2.25}$$

Then we get the derivative of projection parameter:

$$\dot{a}_m = -\sum_{n \neq m} a_n \langle m|\dot{n}\rangle \exp\left(-i \int_0^t \Delta E_{nm}(t')dt'\right) . \tag{2.26}$$

with the energy gap $\Delta E_{nm} = E_n - E_m$. From the time derivative of Eq. (2.21), we have

$$\dot{H} |n\rangle + H |\dot{n}\rangle = \dot{E}_n |n\rangle + E_n |\dot{n}\rangle , \tag{2.27}$$

and multiplied both side by $\langle m|$, we get

$$\langle m|\dot{n}\rangle = \frac{\langle m| \dot{H} |n\rangle}{\Delta E_{nm}(t)} . \tag{2.28}$$

Therefore, the equation (2.26) can be rewritten in the form:

$$\dot{a}_m = -a_m \langle m|\dot{m}\rangle - \sum_{n \neq m} a_n \frac{\langle m| \dot{H} |n\rangle}{\Delta E_{nm}(t)} \exp\left(-i \int_0^t \Delta E_{nm}(t')dt'\right) . \tag{2.29}$$

In an adiabatic evolution, the state vector may remain in the same eigenstate as in the beginning, while also obtain a phase factor. The phase that is introduced by the adiabatic evolution has a contribution from the evolution of the state, and another from the evolution of eigenstates with the time-dependent Hamiltonian. The first term refers to the Berry phase. Calculating the Berry phase $\theta(t)$ [105]:

$$\theta_n(t) = i \int_0^t dt' \langle n(t')|\dot{n}(t')\rangle , \tag{2.30}$$

and the time derivative of $a_m e^{-i\theta_m}$ is

$$\frac{\partial}{\partial t}(a_m e^{-i\theta_m}) = \dot{a}_m e^{-i\theta_m} + a_m e^{-i\theta_m} \langle m|\dot{m}\rangle . \qquad (2.31)$$

Substituted Eq. (2.29) to Eq. (2.31), we have

$$\frac{\partial}{\partial t}(a_m e^{-i\theta_m}) = -\sum_{n\neq m} a_n \frac{\langle m|\dot{H}|n\rangle}{\Delta E_{nm}(t)} e^{-i\theta_m} \exp\left(-i\int_0^t \Delta E_{nm}(t')\mathrm{d}t'\right) . \qquad (2.32)$$

Change the variable to $s(t) = t/T$, where T is the total evolution time, and integrating with respect to $s(t)$, we get

$$a_m(s)e^{-i\theta_m(s)} = a_m(0) - \sum_{n\neq m}\int_0^s \mathrm{d}s'\Delta E_{nm}(s')A_{mn}(s')\exp\left(-iT\int_0^{s'}\Delta E_{nm}(s'')\mathrm{d}s''\right) ,$$

$$\qquad (2.33)$$

with $s(t) \in [0,1]$. The elements A_{mn} are defined as:

$$A_{mn}(s) = a_n(s)\frac{\langle m(s)|\dot{H}|n(s)\rangle}{\Delta E_{nm}^2(t)}e^{-i\theta_m(s)} . \qquad (2.34)$$

The exponential terms on the right hand side of Eq. 2.33 can then be simplified as

$$\exp\left(-iT\int_0^{s'}\Delta E_{nm}(s'')\mathrm{d}s''\right) = \frac{i}{T\Delta E_{nm}}\frac{d}{ds'}\exp\left(-iT\int_0^{s'}\Delta E_{nm}(s'')\mathrm{d}s''\right) . \qquad (2.35)$$

The we can integrate Eq.2.33 by parts:

$$a_m(s)e^{-i\theta_m}(s) = a_m(0) + \frac{i}{T}\sum_{n\neq m}A_{mn}(0) - \frac{i}{T}\sum_{n\neq m}A_{mn}(s)\exp\left(-iT\int_0^s\Delta E_{nm}(s')\mathrm{d}s'\right)$$

$$+ \frac{i}{T}\sum_{n\neq m}\int_0^s\mathrm{d}s'\left(\frac{d}{ds'}A_{mn}(s')\right)\exp\left(-iT\int_0^{s'}\Delta E_{nm}(s'')\mathrm{d}s''\right) . \qquad (2.36)$$

The adiabatic condition can be obtained by assuming that the last integral vanishes when $T \to \infty$, while the energy difference ΔE_{nm} remains finite. According

to the Riemann-Lebesgue lemma, the condition is

$$\frac{A_{mn}(s)}{T} \to 0 \tag{2.37}$$

throughout the adiabatic state transformation and all the coupling state $|m\rangle$ and $|n\rangle$. Then the adiabatic condition is:

$$T \gg \frac{\mathcal{E}}{(\Delta E)^2} , \tag{2.38}$$

with

$$\mathcal{E} = \max_{s\in[0,1]} \left\| \langle m(s)| \frac{dH(s)}{ds} |n(s)\rangle \right\| , \tag{2.39}$$

and

$$\Delta E = \min_{s\in[0,1]} \Delta E_{nm}(s) . \tag{2.40}$$

When the adiabatic condition is satisfied throughout the time evolution, the system will stay close to the ground state in the instantaneous Hamiltonian. At the end of the evolution, the fidelity of the system in the ground state of target Hamiltonian is close to 1.

2.2.2 Adiabatic quantum algorithms

The adiabatic quantum computing is used to achieve the answer to certain classical problems encoded in a quantum state. Then a potentially complicated Hamiltonian may be found, whose ground state is the quantum state that describes the answer. Even if the ground state of this complicated Hamiltonian is hard to achieve directly, we can still implement an adiabatic quantum algorithm to obtain that ground state. We label the complicated Hamiltonian H_f as our target Hamiltonian. We label a simple Hamiltonian where we have full access to the ground state, H_0, and use it as the initial Hamiltonian, which is linked to the target Hamiltonian. The structure of adiabatic quantum algorithms with linear interpolation of Hamiltonians can be formed as following:

- prepare the system as the ground state $|\psi_0\rangle$ of a designed Hamiltonian H_0, which is easy to access and smoothly linked to the target Hamiltonian H_f.

- evolve the system under linear interpolation of initial Hamiltonian and final Hamiltonian $H(s) = (1-s)H_0 + sH_f$ with the time dependent parameter s

in the condition of $s(0) = 0$, $s(T) = 1$. The speed of evolution is determined by the adiabatic condition (2.38).

- after a total time of T, the system ends up in a quantum state $|\phi_T\rangle$ which is very close to the ground state $|\psi_f\rangle$ of H_f.

Having the adiabatic condition (Eq. (2.38)), we can come to the conclusion that if we can spend total time $T \to \infty$, the fidelity ($|\langle\phi_T|\psi_f\rangle|^2$) would approach to 1. However, an explicit expression for the final fidelity of state preparation as a function of evolution time is difficult to obtain. With finite evolution time, it is therefore hard to compare adiabatic quantum algorithms to classical algorithms theoretically.

2.2.3   Eigenpath of adiabatic transformation

The time cost of adiabatic quantum algorithms is highly related to the speed of the changing interaction parameter and the spectrum of the time-dependent Hamiltonian. In this section, we introduce the concept of the eigenpath of the adiabatic state transformation that captures the essence of the adiabatic process. The bound on the length of the eigenpath could be used as an input of a quantum algorithm where minimum knowledge of Hamiltonian is assumed, and thus provides a bound on the time costs in some algorithms [69, 106–109].

Here, we consider the derivative of the Hamiltonian and the eigenstate with respect to the changing parameter $s(t)$. The eigenstates of instantaneous Hamiltonian, $|n(s)\rangle$, are nondegenerate, and ΔE is the minimum spectral gap throughout the process. Here we choose one of the eigenstates $|\phi(s)\rangle$ as the initial state. We assume that the state is differentiable, and the phases of the $|\phi(s)\rangle$ are chosen geometrically, so that $\langle\partial_s\phi(s)|\,\phi(s)\rangle = 0$. The path of $|\phi(s)\rangle$ in continuous adiabatic evolution is called the eigenpath, and the eigenpath length [107] is,

$$L = \int_0^1 \||\partial_s\phi(s)\rangle\|\,ds\,. \tag{2.41}$$

In many cases, the eigenpath length is a constant, $L = \mathcal{O}(1)$, such as flipping a qubit from $|0\rangle$ to $|1\rangle$. A common bound of the eigenpath length is, $L \le \left\|\dot{H}\right\|/\Delta E$. Here the norm $\left\|\dot{H}\right\|$ denotes the spectral norm. In the previous eigenpath traversal (EPT) methods, the time cost T has depends on the minimal gap of Hamiltonian and also the eigenpath length [107]. However, the time cost of the EPT methods has not shown advantages over that of the AQC (Eq. (2.38)). Later in Sec. 5.2, an improved bound for the eigenpath length L^* is developed. From the improved

bound of eigenpath length, the time cost of the quantum algorithm is improved (Sec. 5.3.3). With detailed error analysis in Sec. 5.3.2, the improved EPT methods demonstrate the advantage of the time cost over the AQC methods in terms of the overall gap dependence.

2.3 Conclusions

In the first half of the chapter, we provided an overview of quantum computation and a brief introduction to the phase estimation algorithm. We will develop a new quantum algorithm based on the phase estimation algorithm, and apply our algorithm to a fluid dynamics problem, specially the turbulence mixing problem and the reacting flow problem, in Chap. 8. In the second half of this chapter, we introduced adiabatic quantum computing and calculated the adiabatic condition of the evolution time in linear interpolation cases. Then we introduced the concept of the eigenpath, which is used in the eigenpath traversal methods to bound the time cost. In the Chap. 5, we present our research on improving adiabatic quantum computing with finite evolution time by performing randomised time evolution.

Chapter 3

Background techniques with cold atoms in optical lattices

In this chapter, we introduce the physical system that we will study in this thesis, cold atoms in optical lattices. Recent experimental developments provide tools to manipulate such system with fine control of the parameters and good isolation from its environment. This makes this system a promising platform for quantum simulation. Understanding the principles of atom-atom and atom-light interactions is very important to realise interesting quantum many-body systems and study their properties and dynamics.

We first introduce the background of cold atoms in optical lattices and the corresponding theoretical model. Secondly, we introduce amplitude noise in optical lattices in Sec. 3.3. This noise is introduced by fluctuations of the optical potential which is caused by fluctuations of the intensity of the laser producing the optical lattice. Then we introduce a recently proposed technique to engineer such noise in Sec. 3.4, which later will be used to introduce useful noise in Chap. 6.

3.1 Background

Optical lattices are formed by coherent laser beams creating a periodic potential that can be used to confine neutral atoms via AC Stark shift. Due to atom-light (dipole-field) interactions in a semiclassical model, the ground state energy of an atom has an energy shift. According to perturbation theory, the energy shift is proportional to the intensity of the laser field. A detailed explanation can be found in [12, 110]. As a result, neutral atoms prepared in the ground state are not excited by off-resonant laser light but feel an optical potential, which is
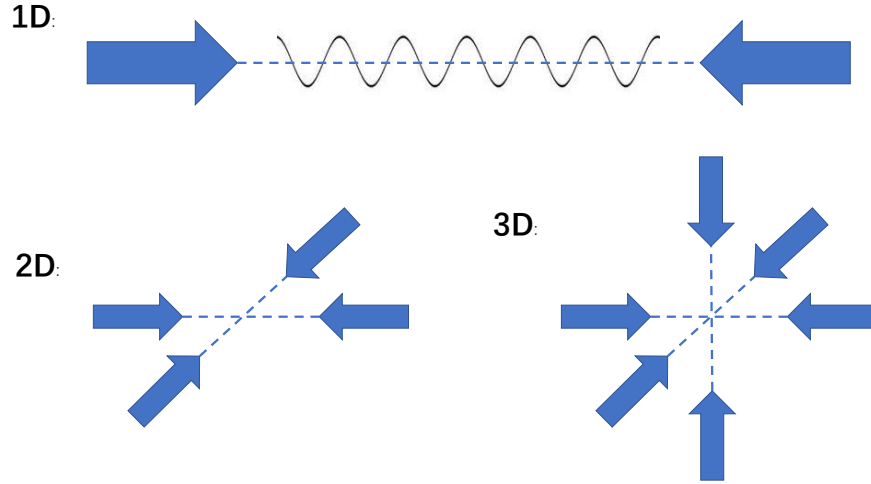
FIGURE 3.1: Optical lattices formed by interfering counter propagating laser beams. The arrows demonstrate the directions of the laser beams and the standing waves represent the periodic potential of laser beams.

proportional to the intensity of the laser. Taking a one-dimensional optical lattice as an example, a standing wave can be formed by a pair of counter-propagating laser beams with the same frequency and polarisation, as shown in Fig. 3.1. By adding more pairs of laser beams, the optical lattice can be extended to higher dimensions. In the experiments, motion of atoms along one dimension in a lattice can be formed by a 3-D optical lattice where two directions are highly confined. By tuning the lattice depth V, the optical lattices can provide fine control of the many-body dynamics of atoms, including the on-site interactions and the tunnelling rate [19, 23]. In a 3-D optical lattice,

$$V(x, y, z) = V_0[\sin^2(kx) + \sin^2(ky) + \sin^2(kz)] , \qquad (3.1)$$

where $k = 2\pi/\lambda$ is the wave number of the laser, λ is the laser wavelength, and V_0 is the depth of optical lattices. The phase transition according to Bose-Hubbard model from the superfluid (SF) phase to the Mott insulator (MI) phase at low temperatures as the ratio of the on-site interaction U to the tunnelling parameter J increases is realised later in experiments [23, 111, 112]. Simulating a quantum system may be very difficult, especially when dealing with large systems. Using some controllable quantum systems to study another system that is less controllable or accessible is the key idea of quantum simulation. Quantum simulators are designed to implement certain quantum simulations [6, 113, 114]. Cold atoms in optical lattices are a promising candidate for quantum simulations since they

can be well isolated from their environment and the system parameters can be controlled very precisely [8].

3.2   Bose-Hubbard Hamiltonian

A second quantised Bose-Hubbard Hamiltonian can be written as

$$H_{BH} = -J \sum_{\langle i,j \rangle} \hat{b}_i^\dagger \hat{b}_j + \frac{U}{2} \sum_i \hat{n}_i(\hat{n}_i - 1) - \mu \sum_i \hat{n}_i \, , \qquad (3.2)$$

where $\hat{b}_i^\dagger$, $\hat{b}_i$ are bosonic creation and annihilation operators with commutation relations $[\hat{b}_i, \hat{b}_j^\dagger] = \delta_{ij}$, $\hat{n}_i = \hat{b}_i^\dagger \hat{b}_i$ are the number operators and μ is the chemical potential.

Considering the lowest band Bose-Hubbard model, the on-site interaction U and nearest neighbour tunnelling rate J can be represented in the Wannier function basis as:

$$U = \frac{4\pi\hbar a_s}{m} \int d^3x |w(\vec{x})|^4 \, , \qquad (3.3)$$

$$J = \int d^3x w^*(\vec{x}) \Big(-\frac{\hbar^2}{2m}\nabla^2 + V(\vec{x}) \Big) w(\vec{x} - \vec{a}) \, , \qquad (3.4)$$

where a_s is the scattering length, $w(\vec{x})$ are the lowest-band Wannier functions, and $\vec{a}$ is the lattice spacing. The Wannier functions describe wave functions of a single particle, and they are localised around each lattice site. The lowest-band Wannier functions are defined by the Bloch equations,

$$w(\vec{x} - \vec{x}_i) = \frac{1}{\sqrt{M}} \int e^{-i\vec{q}\cdot\vec{x}_i} \Phi_{\vec{q}}(\vec{x}) d\vec{q} \, , \qquad (3.5)$$

where $\vec{x}_i$ are the positions of minima of the lattice energy potential, M is the normalisation parameter, $\vec{q}$ is the quasimomentum, and $\Phi_{\vec{q}}(\vec{x}) = e^{i\vec{q}\cdot\vec{x}} u_{\vec{q}}(\vec{x})$ are the Bloch functions [115]. The functions $u_{\vec{q}}(\vec{x})$ have the same periodicity as the lattice potential $V(\vec{x})$ and are the solution of the Schrödinger equation $[\frac{(\hat{p}+\vec{q})^2}{2m} + V(\vec{x})]u_{\vec{q}}(\vec{x}) = E_{\vec{q}}u_{\vec{q}}(\vec{x})$. The definition of the Wannier function is not unique, because of the choice of the global phase of $\Phi_{\vec{q}}$ and $u_{\vec{q}}$. However, it is shown [116] that there exists one and only one completely real Wannier function for each band that is exponentially localised. These functions cab be symmetric or anti-symmetric with respect to the maxima or minima of the potential. And they decay exponentially from the centre of the site where they are localised. This

form of Wannier function is considered maximally localised, and it is used to construct the Hubbard model.

The main conditions for the validity of the single-band Bose-Hubbard model are:

- The atom-atom interactions are only two-body interactions. This requires the gas to be sufficiently dilute, $\rho a^3 \ll 1$, where $\rho = N/V$ is the average density of N atoms trapped in a large volume V, and a is the range of atom-atom interactions. This means that 3 or more atoms interactions at the same time are less likely to happen, thus that can be neglected.

- The temperature is low enough so that the two-body interactions of the atoms can be described by low-energy s-wave scattering. In this situation, the de Broglie wavelength $\lambda_{dB} = 2\pi\hbar/p$, where p is the momentum of particles, is much larger than the atom-atom interaction range $\lambda_{dB} \gg a$. Then the scattering amplitude and angle are independent of the energy of colliding particles.

- When the lattice depth increases, the tunnelling amplitude to further site will decay faster than the amplitude of neighbouring site. Also, the on-site interaction will increase along with the lattice depth, but the inter-site interaction will decrease exponentially. So when the lattice depth is deep enough, long-range tunnelling and inter-site interactions can be neglected.

- The temperature T is smaller than the band separation ω in the optical lattice which depends on the lattice depth to justify the lowest band treatment, $\hbar\omega \gg J, U, k_B T$.

The system described by the Bose-Hubbard model can be in two different regimes. When the interaction dominates the Hamiltonian, given the particles number is commensurate with the number of sites, the system is in the Mott insulator phase. When the kinetic energy dominates the Hamiltonian, the system is in the superfluid phase. The transition between the Mott insulator and superfluid phase is due to the competition between the kinetic energy and the interaction energy.

The zero-temperature phase diagram of the Bose-Hubbard Model in the homogeneous case was first investigated by Fisher *et al.* [117], sketched in Fig. 3.2. The phase transition described by the Bose-Hubbard model in optical lattices was first observed in cold atoms by Greiner et al. [23], driving the system from a superfluid (SF) phase to a Mott insulator (MI) phase.

The ground state of a Bose-Hubbard model with $U/J \to 0$ describes the superfluid phase, where the system minimises kinetic energy. The particles intend to

delocalise over the whole lattice. For a system with M lattice sites and N Bosons, the ideal ground state can be written as

$$|\psi_{SF}\rangle = \left(\frac{1}{\sqrt{M}} \sum_{i=1}^{M} \hat{b}_i^\dagger \right)^N |0\rangle \ , \tag{3.6}$$

where $|0\rangle$ is the vacuum state. The probability for k atoms to be found at the i-th lattice site in the ground state is [118]

$$p(k; N, 1/M) = \binom{N}{k} \left(\frac{1}{M} \right)^k \left(1 - \frac{1}{M} \right)^{N-k} \tag{3.7}$$

This is a binomial distribution for a probability $1/M$ and N trials. The average number of particle per site $\bar{n}$ is given by $\bar{n} = N/M$ and the number fluctuation is $\sqrt{N/M(1 - 1/M)} \approx \sqrt{\bar{n}}$. In the limit that $N, M \to \infty$ with N/M a fixed number, the binomial distribution becomes the Poisson distribution and the ground state becomes indistinguishable in practice from a coherent state [22]

$$|\psi_{SF}\rangle = \prod_i \exp\left(\sqrt{\frac{N}{M}} \hat{b}_i^\dagger \right) |0\rangle \ , \tag{3.8}$$

with Poisson number statistics on each site. This state implies that the particles are localised in momentum space.

As the ratio U/J increases, the on-site interactions make tunnelling of particles to neighbouring sites less probable. For a large U/J, if the number of particles is commensurate with the number of lattice sites, the system is in the Mott insulator phase, and the particles are localised on particular sites. In the limit of $U/J \to \infty$ with the average filling factor $n = N/M$ an integer, the ground state of the Bose-Hubbard Hamiltonian can be written as

$$|\psi_{MI}\rangle \propto \prod_{i=1}^{M} \left(\hat{b}_i^\dagger \right)^n |0\rangle \propto \prod_i^{M} |n\rangle_i \ . \tag{3.9}$$

where $|n\rangle_i$ is the eigenstate of $\hat{n}_i = \hat{b}_i^\dagger \hat{b}_i$ with the corresponding eigenvalue n. In this case, the state corresponds to a fixed number of particles on each site.

We have discussed two extreme regime of the parameter $U/J \to 0$ and $U/J \to \infty$. The state in each limit has very different energy spectrum and phase coherence. For example, in the Mott insulator phase when $U/J \gg 1$, the energy spectrum has a finite gap $\Delta = U$. On the other hand, the energy spectrum of superfluid is gapless ($\Delta = 0$). When a system is initially prepared to be in the superfluid phase ($U/J \ll 1$), and the interaction energy parameter U is slowly increasing,

the energy gap is expected to become non-zero at the critical point $(U/J)_c$ and grows with U. The sharp transition of the phase can be qualitatively explained as the following. In general, consider the Hamiltonian which varies as a function of a dimensionless coupling g, $H(g) = H_1 + gH_2$. The ground state energy will generically be a smooth, analytic function of g for the case of a finite lattice. The possibility of an exception is the case when g couples to a conserved quantity, i.e. $[H_1, H_2] = 0$. Then there can be a level-crossing when an excited state becomes the ground state at $g = g_c$. At this point, the ground state energy is a nonanalytic function of g [24]. For Bose-Hubbard model, the competition between the kinetic energy and the potential energy leads to an avoided level-crossing between the ground and an excited state in a finite lattice, and it could become progressively sharper as the lattice size increases.

For finite U and J with infinite lattice, the ground state of this many-body system cannot be exactly obtained analytically. This makes it difficult to calculate the critical value of the phase transition point $(U/J)_c$ in general. However, for an integer average filling factor $\bar{n}$, we can obtain analytical solutions of phase transition point cases via mean-field theory [119]. For example, in a 2D or 3D lattices with $\bar{n} = 1$, the critical point is $(U/J)_c = 5.8z$, where $z = 2d$ is the number of nearest neighbours in d-dimsional optical lattices ($z = 4$ in 2D lattices). For 1D Bose-Hubbard model with $\bar{n} = 1$, the best known phase transition point is $(U/J)_c \approx 3.3$ from numerical calculations using the density matrix renormlisation group (DMRG) method [120].

3.3   Amplitude noise in optical lattices

Naturally, the fluctuation of the laser intensity will affect the depth of lattice, and thus introduce noise to the system. Different heating processes depend on the spectrum of the intensity noise spectrum. When noise is at frequencies of the order of band separation, the system undertakes an inter-band transition and particles are transferred to higher Bloch bands. Noise at lower frequencies of the order of the tunnelling parameter J and on-site interaction strength U will introduce intra-band heating for atoms within the lowest band. When the noise is weak for inter-band processes, the evolution of atoms in the optical lattice is in the lowest Bloch band. Considering on 1D model, in the deep lattice regime where the lattice potential is much larger than the recoil energy, $V \gg E_R = \hbar^2 k^2/2m$, where m is the mass of atoms and k is the wave number of the laser light, the
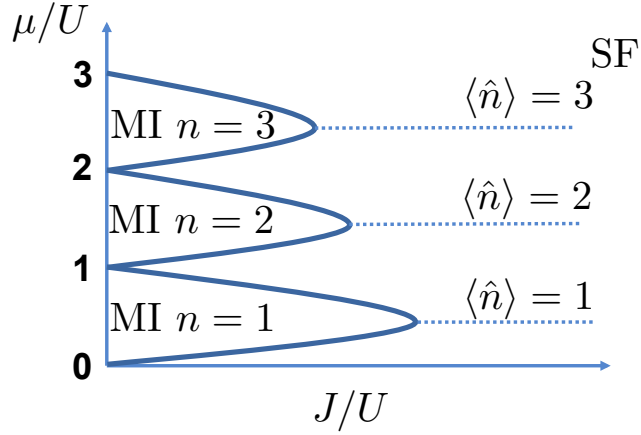
FIGURE 3.2: Sketch of the zero temperature phase diagram of the Bose-Hubbard model. The lobes show the Mott insulator phase with fixed average filling factor $\bar{n} = 1, 2, 3$. The phase transition happens at the intersection of the lobes and the dashed lines with fixed average particle number. In those cases, the value of $(J/U)_c$ decreases as the density of particles increases.

dependencies of coefficients to the lattice depth are:

$$\frac{U}{E_R} = 4\sqrt{2\pi}\frac{a_s}{\lambda}\left(\frac{V}{E_R}\right)^{1/4} \ , \tag{3.10}$$

$$\frac{J}{E_R} = \frac{4}{\sqrt{\pi}}\left(\frac{V}{E_R}\right)^{3/4} e^{\left(-2\sqrt{V/E_R}\right)} \ , \tag{3.11}$$

where a_s is the scattering length, λ is the wavelength of optical lattices. The fluctuation of the lattice depth V will affect the coefficients. We can calculate the derivative of U and J with respect to the lattice depth V

$$\frac{dU}{dV} = \frac{E_R}{4V}\frac{U}{E_R} \ , \tag{3.12}$$

$$\frac{dJ}{dV} = \left[\frac{3E_R}{4V} - \left(\frac{V}{E_R}\right)^{-1/2}\right]\frac{J}{E_R} \ , \tag{3.13}$$

and the first order expansion of the Hamiltonian with respect to the fluctuation δV is then

$$H_{sys} = H_{BH}(J, U) + H_{BH}\left(\frac{dJ}{dV}, \frac{dU}{dV}\right)\delta V \ , \tag{3.14}$$

$$H_{BH}(J, U) = -J\sum_{\langle i,j\rangle} b_i^\dagger b_j + \frac{U}{2}\sum_i n_i(n_i - 1) \ . \tag{3.15}$$

Because the spectrum of the noise is slowly varying on the scale of U and J, the fluctuation of depth can be approximated as white noise $\delta V = \sqrt{2\Gamma}\xi(t)$, with the correlation function $\langle \delta V(t)\delta V(t')\rangle = 2\Gamma\delta(t - t')$. This 1D Bose-Hubbard model is the one we use in later chapter 6 and 7. In general, this white noise will introduce heating effects to the system. In the adiabatic state preparation process, the heating effect will decrease the final fidelity to the target ground state. The total energy of the system will increase as the noise strength increases and the ramping time becomes longer. Simulations and discussions of this process will be addressed in later sections.

3.4 Noise engineering in optical lattices: dressed lattice scheme

As mentioned in the previous section, amplitude noise can introduce fluctuation of parameters in the Hamiltonian. Heating effects will occur in the system and jeopardise state preparation and unitary processes. A recently proposed dressed lattice scheme[121, 122] provides an alternative method to engineering amplitude noise so that the relative fluctuation of parameters in the Hamiltonian can be adjusted.

This scheme requires detuned optical lattices produced from the same laser source so that the noise is uniform in the system. Two atomic levels $(|g\rangle, |e\rangle)$ are trapped by a blue-detuned lattice and for the other two ancillary energy levels $(|h\rangle, |f\rangle)$ the same laser is red-detuned, as shown in Fig. 3.3. Then the lower energy states $|g\rangle, |h\rangle$ of each system are coupled to form a dressed state. This coupling Ω_{gh} will introduce an additional tunnelling so that the atom in $|g\rangle$ can move from site to site via the virtual auxiliary state $|h\rangle$. The energy shift of the red-detuned lattice is proportional to $-(V_0 + \delta V)$, and the energy shift is proportional to $\sqrt{V_0 + \delta V}$ in the blue-detuned lattice. For an appropriate choice of the detuning, a small increase of the lattice depth will decrease the energy difference of two energy level $|h\rangle$ and $|g\rangle$ and the red detuning Δ from the coupling Ω_{gh} is weakened. Thus, the increase of the lattice depth can enhance the tunnelling process via the state $|h\rangle$
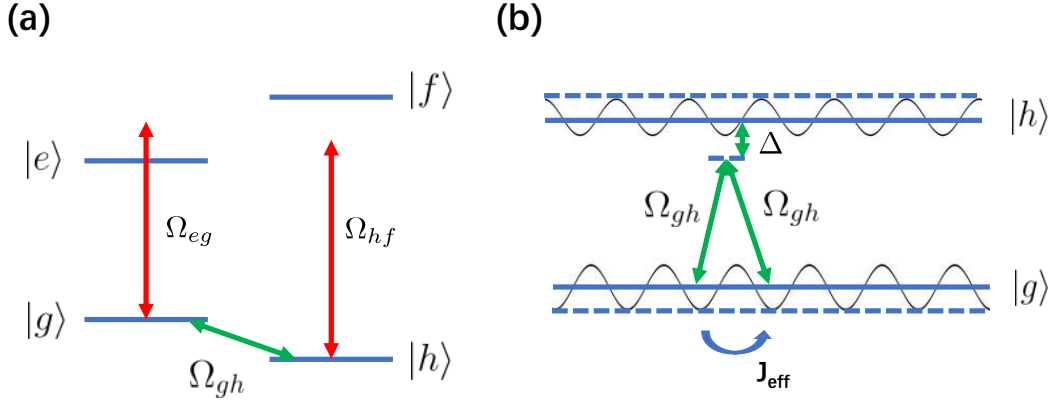
FIGURE 3.3: Dressed lattice scheme. In (a), the detuned lattice scheme is shown. The original atomic levels ($|g\rangle$, $|e\rangle$) are in a blue-detuned lattice and the other two ancillary energy levels ($|h\rangle$, $|f\rangle$) are red detuned. The two lower energy states $|g\rangle$ and $|h\rangle$ are coupled Ω_{gh} to introduce additional tunnelling. In (b), we show how the additional tunnelling is introduced. The energy shift of red-detuned lattice ($|h\rangle$, $|f\rangle$) is proportional to $-(V_0 + \delta V)$, and the energy shift of the blue-detuned lattice ($|g\rangle$, $|e\rangle$) is proportional to $\sqrt{V_0 + \delta V}$. In this case, when $\delta V > 0$, the coupling between $|g\rangle$ and $|h\rangle$ is enhanced and the tunnelling effect also increases via these ancillary states. With fine tuning of the optical lattices, $dJ_{\text{eff}}/dV > 0$.

to be surpass the loss of the tunnelling from site to site directly in the opticall lattice. In this situation, the effective tunnelling with both the direct tunnelling effect and the additional tunnelling effect will increase, so that $dJ_{\text{eff}}/dV > 0$. We refer to [121] for more details.

Using this dressed lattice scheme, the heating rate of the time-independent Hamiltonian (Eq. (3.14)) with amplitude noise can be calculated as [121]

$$\langle \dot{H}_{sys} \rangle = \Gamma \left(\frac{1}{J_0} \frac{dJ}{dV} - \frac{1}{U_0} \frac{dU}{dV} \right)^2 \langle [[H_J, H_U], H_J] \rangle , \qquad (3.16)$$

in the white noise limit, $\langle \delta V(t) \delta V'(t) \rangle = 2\Gamma \delta(t - t')$, and first order expansion of parameters $J = J_0 + \frac{dJ}{dV} \delta V$, $U = U_0 + \frac{dU}{dV} \delta V$. For the simplicity of this equation, H_J and H_U denote different terms in the Hamiltonian, $H_{BH} = H_J + H_U$,

$H_J = -J \sum \hat{b}_i^\dagger \hat{b}_j$, and $H_U = U/2 \sum \hat{n}_i(\hat{n}_i - 1)$. The fluctuation of parameters can also be parametrised introducing θ, λ to simplify calculations as

$$\sqrt{2\Gamma} \frac{dU/dV}{U} = \lambda \sin^2 \theta \ , \tag{3.17}$$

$$\sqrt{2\Gamma} \frac{dJ/dV}{J} = \lambda \cos^2 \theta \qquad \theta \in [0, \pi/2) \ . \tag{3.18}$$

Thus the heating rates due to the noise can be represented in the parameter space of θ when θ is close to $\pi/4$ as,

$$\langle \dot{H}_{sys} \rangle \propto \left(\theta - \frac{\pi}{4} \right)^2 \ , \tag{3.19}$$

which defines a sweet spot in parameter space of $\theta_{sw} = \pi/4$, where introducing noise will cause no heating to first order for atoms in the optical lattice. Imperfect implementation of noise engineering can be then parametrised as an offset of $\theta \neq \theta_{sw}$, $\Delta\theta = \theta - \theta_{sw}$. The effect of imperfect implementation can introduce an interesting behaviour in adiabatic state preparation. We will present our detailed research in Sec. 6.3.2 and Sec. 7.3.

3.5 Conclusions

In this chapter, we presented the background theory of cold atoms in optical lattices, which is the physical system that we will study in our research. We provided the background of the optical lattices that confine the ultracold atoms in periodic optical potentials. We also introduced amplitude noise in optical lattices, and explained how to describe a noisy system characterised approximately by white noise. In the end, we introduced a recently proposed scheme to engineer the amplitude noise to reduce the heating effect. The dressed lattice scheme provides the theoretical background to realise the noise regimes of our research on adiabatic state preparation in optical lattices with the presence of the amplitude noise in Chap. 6. By applying numerical simulations driving the ground state of the Mott insulator to the superfluid phase, we are able to identify the regimes where having the classical noise can improve the final fidelity of the state preparation. In Chap. 7, we discuss thermalisation of energy introduced by amplitude noises in optical lattices, and show different behaviours in the superfluid phase and the Mott insulator phase.

Chapter 4

Computational methods

In the fundamental research of theoretical study, numerical simulations play an important role, especially when analytical solutions are hard to obtain. However, as the system of interest grows larger and larger, the computational resources required to simulate the behaviour of the system exactly can be enomorous. To study the dynamics of a system in a pure state $|\psi\rangle$, the dimension of the corresponding Hilbert space is $\dim(|\phi\rangle) = \mathcal{O}(N)$. For example, to describe a one dimensional Ising spin chain with M spins using exact diagonalization, the dimension of Hilbert space is 2^M. Moreover, to study an even more complex system like an open quantum system, the system is no longer a pure state, but a mixed state, and the equation of motion is described with the density operator $\rho = \sum_{ij} C_{ij} |\phi_i\rangle \langle\phi_j|$, which requires extra resource since the Hilbert space is of dimension of $\dim(\rho) = \mathcal{O}(N^2)$, with $\dim(|\phi\rangle) = \mathcal{O}(N)$ if the density operator is not sparse. Confronted these problems, many mathematical techniques have been developed to describe such systems.

In this chapter, first we will introduce computational methods that we used to conduct our numerical simulations within a reasonable level of error: the Time-Evolving Block Decimation (TEBD) algorithm [123, 124] in Sec. 4.1. The TEBD technique provides us with access to the dynamics of 1D lattice systems with large Hilbert spaces. Matrix Product State (MPS) is introduced so that we can manage the quantum state presentation with limited resources. In Sec. 4.2, we will introduce the background of open systems, classical stochastic process and a computational method, the master equation approach. The master equation approach is to tackle the time evolution of an open many-body system, via the evolution under the stochastic Schrödinger equation.

4.1 Time-evolving block decimation algorithm

In this section, we will provide a brief overview of the computational methods used in this thesis to deal with large system calculations. Density Matrix Renormalization Group (DMRG) techniques were first introduced [78, 79] by S. White, to calculate the ground states of large one dimensional system with high precision. Later, the Time-Evolving Block Decimation (TEBD) algorithm [125, 126] was developed to study the time-evolution of a 1D system using DMRG methods. There are certain systems for which those computational methods can be performed efficiently, for example, a one-dimensional system described by a gapped Hamiltonian. Usually, the quantum state of the objective system has different amplitudes determined by the basis of the Hilbert space, for instance, the computational basis or eigenbasis. The idea of the TEBD is to change the basis adaptively and keep most relevant basis states without a significant change of the physics features. This will result in a truncation of the full Hilbert space and consider only a subspace of the Hilbert space (shown in Fig. 4.1). When the interactions in the system are local and between few bodies, the amount of entanglement is limited, and the TEBD is highly efficient.

In the following subsections, we will introduce the MPS representation for quantum states in 1D systems and how to calculate local expectation values and implement two-site gates in MPS formalism. Then we will introduce how to describe time evolutions with MPS. The time evolution operator can be decomposed into the form of sweeps of two-site gates via Suzuki-Trotter expansion. Finally, we will introduce the imaginary time evolution to search for the ground state of the system.

4.1.1 Matrix product state (MPS) representation

As discussed in the previous section, the exact representation of a quantum state of a large physical system requires storage of enormous number of coefficients. An approximate state representation is required for such a calculation. It can be useful to discuss this in terms of entanglement, which has a direct relation to the Schmidt rank [4], the number of coefficients in a bipartite Schmidt decomposition. We use these relations between those quantities to describe how well we represent the system. Considering a quantum state of a one dimensional system with M sites, on each site, a local dimension d represents the number of possible configurations. For example, a one-dimensional Ising chain has the local dimension $d = 2$, and for Bosons in an optical lattice in one dimension, the local dimension is one more than the maximum number of particles that can sit on one site. The Hilbert space on each site is spanned by the set of vectors $\{i\}$, and the
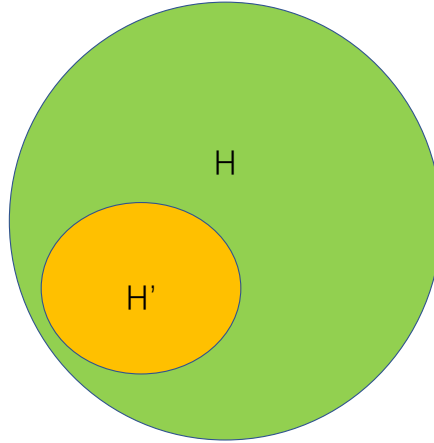
FIGURE 4.1: A sketch of the subspace (H') of a full Hilbert space (H) for a 1D system with a Hamiltonian with local interaction within few bodies. The domain of the dynamics we are interested does not span the whole Hilbert space (H) because of the nature of the Hamiltonian, and TEBD method can benefit from a truncated representation of the quantum state that only includes H'. Within certain error, the computational resource required to catch the physics is less than that using of full Hilbert space.

whole Hilbert space is of dimension d^M. Then, to describe the quantum state we would require d^M coefficients,

$$|\phi\rangle = \sum_{i_1,...i_M}^{d} C_{i_1,...,i_M} |i_1,...,i_M\rangle \ . \tag{4.1}$$

In the TEBD algorithm or general cases, the coefficients will be within as a product of local tensors, so that we can apply truncation with the help of the Schmidt decomposition.

4.1.1.1 Schmidt decomposition

Consider a bipartite quantum state of a system with two subsystem A and B, and the Hilbert space $\mathcal{H} = \mathcal{H}_A \otimes \mathcal{H}_B$, with dimensions d_A and d_B. The quantum

Examples of tensors:

| Scalar | Vector | Matrix | Rank-3 Tensor |

Examples of tensors contractions:

$$\sum_j A_{ij} B_{jk} = C_{ik}$$
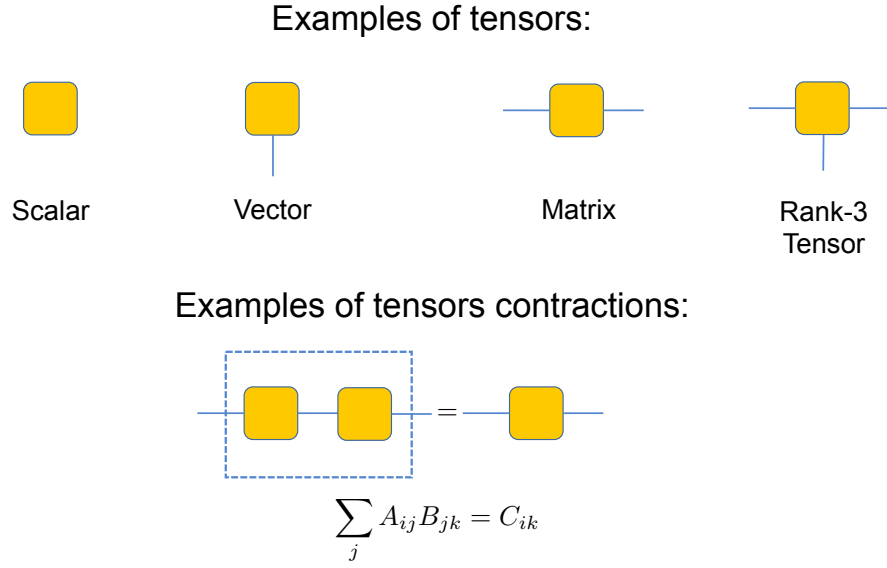
FIGURE 4.2: Graphical notation we use in this chapter to represent tensor networks. Each tensor (shown as a box) has a number of indices (shown as legs attached to the box). The tensor with different value of indices represent different type of mathematical objects, shown in this figure. When two boxes are connected, a contraction is representd as the dashed box with the corresponding index.

state can be written as,

$$|\psi_{AB}\rangle = \sum_{i=1}^{d_A} \sum_{j=1}^{d_B} C_{i,j} |i\rangle_A \otimes |j\rangle_B \ , \tag{4.2}$$

where $\{|i\rangle_A\}$ and $\{|j\rangle_B\}$ are orthonormal bases of the subsystems. Using singular value decomposition (SVD) [127], the matrix $C_{i,j}$ can be decomposed into,

$$C = USV^\dagger \tag{4.3}$$

or in terms of the elements,

$$C_{i,j} = \sum_k^{\chi_{AB}} U_{i,k} S_{k,k} V_{k,j} \ , \tag{4.4}$$

with $\chi_{AB} = \min(d_A, d_B)$. U and V are unitary matrices with dimension d_A^2 and d_B^2, and S is a diagonal $d_A \times d_B$ matrix, with the non-negative singular values of

C. The Schmidt coefficients defined as $\lambda_k \equiv S_{k,k}$, satisfy,

$$\sum_k \lambda_k^2 = 1 \ . \tag{4.5}$$

The number of non-zero λ_k is the Schmidt rank. Rearranging the coefficients of $C_{i,j}$ and absorbing the coefficients corresponding to each subsystem, the quantum state can be represented as a linear combination of product states,

$$|\psi_{AB}\rangle = \sum_k^{\chi_{AB}} \lambda_k |\Phi_k^A\rangle \otimes |\Phi_k^B\rangle \ , \tag{4.6}$$

where the orthonormal basis of two subsystems A and B are defined as,

$$|\Phi_k^A\rangle \equiv \sum_i U_{i,k} |i\rangle_A \ , \quad \text{and} \quad |\Phi_k^B\rangle \equiv \sum_j V_{k,j} |j\rangle_B \ . \tag{4.7}$$

The Schmidt coefficients provide the amplitude of the system in the bipartite basis and the values of the Schmidt coefficients are related to the entanglement. For example if there is one Schmidt coefficient much larger than the others, that means the system is mostly a product state with perturbations. If all of the coefficients have the same value, the system is in a maximally entangled state. One way to quantify the entanglement between the subsystems is via the von Neumann entropy,

$$S_{VN}(\rho_A) = -\text{tr}\{\rho_A \log_2 \rho_A\} = -\text{tr}\{\rho_B \log_2 \rho_B\} = S_{VN}(\rho_B) \ , \tag{4.8}$$

where $\rho_A \equiv \text{tr}_B\{|\Psi_{AB}\rangle \langle\Psi_{AB}|\}$ and $\rho_A \equiv \text{tr}_B\{|\Psi_{AB}\rangle \langle\Psi_{AB}|\}$ are the reduced density matrices and $\text{tr}_{A,B}$ are partial trace over A or B subsystems. Substituting Eq. 4.6 to Eq. (4.8), the von Neumann entropy is then

$$S_{VN} = -\sum_k^{\chi_{AB}} \{\lambda_k^2 \log_2 \lambda_k^2\} \ . \tag{4.9}$$

The range of von Neumann entropy is $0 \leq S_{VN} \leq \log_2(\chi_{AB})$. For a product state, the von Neumann entropy is $S = 0$, and the von Neumann entropy of a maximally entangled state is given by $S = \log_2(\chi_{AB})$. A simple example to consider is a two-qubit system. The von Neumann entropy of a non-entangled state $|0\rangle_A \otimes |0\rangle_B$ where $\lambda_k = 1$ as in Eq. (4.6), is zero. For one of the Bell states [4], which is a maximally entangled state,

$$|\Psi^+\rangle = \frac{1}{\sqrt{2}}(|0\rangle_A \otimes |0\rangle_B + |1\rangle_A \otimes |1\rangle_B) \ . \tag{4.10}$$

The Schmidt coefficients are $\lambda_1 = \lambda_2 = \frac{1}{\sqrt{2}}$, and the Schmidt rank is $\chi_{AB} = 2$. The von Neumann entropy then is

$$S_{VN} = -2[(\frac{1}{\sqrt{2}})^2 \log_2(\frac{1}{\sqrt{2}})^2] = 1$$
$$= \log_2(\chi_{AB}) \ . \tag{4.11}$$

4.1.1.2   Truncated MPS

Similar to two-qubit systems, an arbitrary one-dimensional state with M sites can also be represented in such a way. This representation can be achieved by repeatedly applying Schmidt decomposition site by site from the left end or the right end of the chain, as in the case of the two-qubit system, defines new bipartite subsystem, as shown in Fig. 4.3. In the end, the coefficients of a state with M sites in Eq. 4.1 can be written as a contraction of tensor products,

$$C_{i_1,\ldots i_M} = \sum_{\alpha_1}^{\chi_1} \sum_{\alpha_2}^{\chi_2} \cdots \sum_{\alpha_{M-1}}^{\chi_{M-1}} \Gamma_{\alpha_1}^{[1]i_1} \lambda_{a_1}^{[1]} \Gamma_{\alpha_1 \alpha_2}^{[2]i_2} \lambda_{a_2}^{[2]} \ldots \lambda_{a_{M-1}}^{[M-1]} \Gamma_{a_M}^{[M]i_M} \ , \tag{4.12}$$

where $\Gamma_{\alpha_{m-1}\alpha_m}^{[m]i_m}$ is a tensor associated with site number m, α_m represents the ordinal number of Schmidt coefficients, i denotes the physical index of the system, and $\lambda_{\alpha_m}^{[i]}$ are tensors of Schmidt coefficients. This format of the coefficients $C_{i_1,\ldots i_M}$ has the error associated with bond dimensions χ_i, and easy to truncate by changing the number of χ_i

We can describe this in mathematical details by applying Schmidt decompositions in the corresponding bond on the first site, we obtain a structure that resembles the one in Eq. 4.6

$$|\psi\rangle = \sum_{\alpha_1}^{\chi_1} \lambda_{\alpha_1}^{[1]} |\Psi_{\alpha_1}^{[1]}\rangle \otimes |\Psi_{\alpha_1}^{[2,\ldots,M]}\rangle \ . \tag{4.13}$$

Then each of the Schmidt vectors $\{|\Psi_{\alpha_1}^{[1]}\rangle\}$ and $\{|\Psi_{\alpha_1}^{[2,\ldots,M]}\rangle\}$ can be rewritten into the computational basis of local sites as follows,

$$|\Psi_{\alpha_1}^{[1]}\rangle = \sum_{i_1}^{d} \Gamma_{\alpha_1}^{[1]i_1} |i_1\rangle \ , \tag{4.14}$$

$$|\Psi_{\alpha_1}^{[2,\ldots,M]}\rangle = \sum_{i_2}^{d} \Gamma_{\alpha_1 \alpha_2}^{[2]i_2} |i_2\rangle \otimes |j_{\alpha_2,i_2}^{[3,\ldots,M]}\rangle \ , \tag{4.15}$$
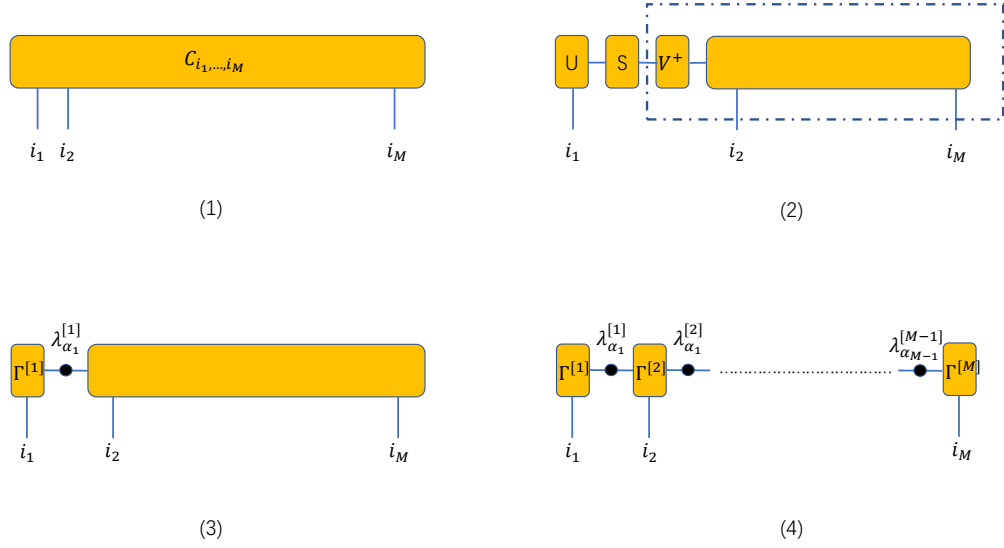
FIGURE 4.3: In this figure, we show the process of construction of MPS from one end of the chain. (1) the coefficients describing a quantum state of M sites. (2) application of SVD on the first site, and regroup the S, and $V^\dagger$ with the rest of the chain (3) redefining the tensor as each local dimension d_i, and forming the diagonal matrix $\lambda^{[1]}_{\alpha_1}$ with Schmidt coefficients. (4) repeating this process to the other end of the chain.

where the non-normalised states $|j^{[3,...,M]}_{\alpha_2,i_2}\rangle$ represent the basis for the rest of the chain and can be normalised as we repeat the same process for the rest of the chain. After applying the process above to all the local sites, we can achieve the representation in Eq. 4.12. This is an exact representation where we replace all d^M coefficient as the matrix products with $(d\chi^2_{\max} + \chi_{\max})M$ coefficients. $\chi_{\max} = \max(\chi_i)$, the maximum Schmidt rank among all the local sites. The maximal value of the Schmidt rank can grow exponentially as the system size increases. Under certain conditions, a truncated MPS form can be achieved within the desired error. To achieve a truncated MPS, we have the Schmidt coefficients ordered and keep the largest ones. This will result in a truncation in summing over α_i and the rest of terms which has the indices larger than certain value $\chi \leq \max(\chi_i)$ will be discarded. The value of χ can be fixed or flexible according to the need of the calculation precision or the site number . In the numerical simulations in this thesis, the value of χ, noted as the bond dimension D is fixed during the calculation and uniform on the sites. Such truncation reduces the Hilbert space with less weighted basis and the reduced Hilbert space which remains tractable. The truncation error introduced in each truncation step can

easily be calculated as,

$$\epsilon_i = \sum_{\alpha_i=D+1}^{\chi_i} (\lambda_{\alpha_i}^{[i]})^2 \ . \tag{4.16}$$

This approximation cannot represent heavily entangled states, as the maximal bipartite entanglement, quantified by the von Neumann entropy given by,

$$S_{VN} = -\sum_{\alpha_i}^{D} \lambda_{\alpha_i}^2 \log_2(\lambda_{\alpha_i}^2) \ , \tag{4.17}$$

where the two subsystems are bonded at the $i-$th site. In our research, the convergence of bond dimension is always critical when applying large scale simulation.

4.1.2 Local expectation values and two-site gates

As we discussed in the previous section, a state in the MPS form can be efficiently stored within a truncated Hilbert space if the entanglement is less than that given by certain criteria. Having the MPS form of a quantum state, the quantum operations acting on the state are adapted to similar matrix product form.

4.1.2.1 One-site operators and expectation values

One operator acting on a single site ($i-$th site) can be represented in the computational basis in the following form $\hat{O}^{[i]} \equiv \sum_{j,k} O_j^{[i]k} |j_i\rangle \langle k_i|$. With the MPS representation in Eq. 4.12, we can explicitly separate the basis in such a way that the operator can act on site i,

$$|\Psi\rangle = \sum_l \sum_{\alpha_{i-1},\alpha_i} \lambda_{\alpha_{i-1}}^{[i-1]} \Gamma_{\alpha_{i-1}\alpha_i}^{[i]l} \lambda_{\alpha_i}^{[i]} |\Psi_{\alpha_{i-1}}^{[1,...,i-1]}\rangle \otimes |l_i\rangle \otimes |\Psi_{\alpha_{i-1}}^{[i+1,...,M]}\rangle \ , \tag{4.18}$$

with the local basis on $i-$th state represented as $\{|l_i\rangle\}$. To calculate an updated quantum state when we apply an operator $O^{[i]}$, only the tensors $\Gamma_{\alpha_{i-1}\alpha_i}^{[i]l}$ need to be updated,

$$\tilde{\Gamma}_{\alpha_{i-1}\alpha_i}^{[i]j} = \sum_k O_j^{[i]k} \Gamma_{\alpha_{i-1}\alpha_i}^{[i]l} \delta_{k,l} \ . \tag{4.19}$$

Then the local expectation value can be calculated as

$$\langle\Psi|\hat{O}^{[i]}|\Psi\rangle = \sum_{j,l}\sum_{\alpha_{i-1},\alpha_i}(\lambda_{\alpha_{i-1}}^{[i-1]})^2(\lambda_{\alpha_i}^{[i]})^2\tilde{\Gamma}_{\alpha_{i-1}\alpha_i}^{[i]j}\Gamma_{\alpha_{i-1}\alpha_i}^{*[i]l}\delta_{jl}\ , \qquad (4.20)$$

and the complexity of this calculation is in the order of D^2d^2 as $j,l \leq d$ and $\alpha_{i-1},\alpha_i \leq D$.
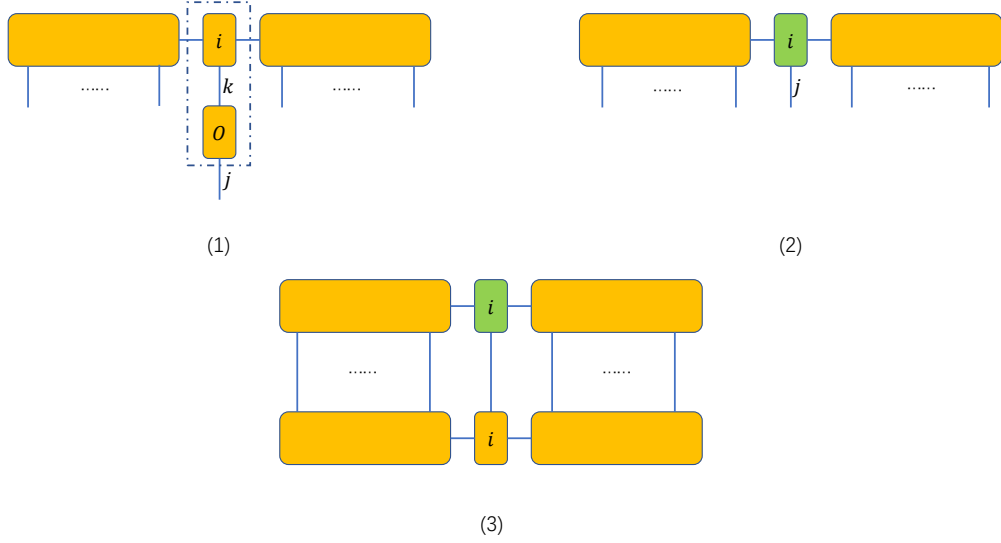
FIGURE 4.4: Demonstration of the process of updating local sites and calculating expectation values. (1) tensor of the local state needed to be updated. (2) update of the state by summing over corresponding indices, $\mathcal{O}(D^2d)$ operatios are required (3) contract the coefficients to calculate the expectation value.

4.1.2.2 Two-site gates

Similarly to case of one-site gates, we can rewrite the two-site gate in the local basis, $U^{[i,i+1]} \equiv U_{j_i,j_{i+1}}^{k_i,k_{i+1}}|j_i,j_{i+1}\rangle\langle k_i,k_{i+1}|$. Then the quantum state can be updated locally as,

$$|\tilde{\Psi}\rangle = \sum_{j_i,j_{i+1}}\sum_{\alpha_{i-1},\alpha_i,\alpha_{i+1}}\tilde{U}_{\alpha_{i-1}\alpha_{i+1}}^{j_i,j_{i+1}}|\Psi_{\alpha_{i-1}}^{[1,\dots,i-1]}\rangle\otimes|j_i,j_{i+1}\rangle\otimes|\Psi_{\alpha_{i+2}}^{[i+2,\dots,M]}\rangle\ , \qquad (4.21)$$

with,

$$\tilde{U}_{\alpha_{i-1}\alpha_{i+1}}^{j_i,j_{i+1}} \equiv U_{\alpha_{i-1}\alpha_{i+1}}^{j_i,j_{i+1}}\sum_{\alpha_i}\lambda_{\alpha_{i-1}}^{[i-1]}\lambda_{\alpha_i}^{[i]}\lambda_{\alpha_{i+1}}^{[i+1]}\Gamma_{\alpha_{i-1}\alpha_i}^{[i]j_i}\Gamma_{\alpha_i\alpha_{i+1}}^{[i]j_{i+1}}\ . \qquad (4.22)$$

To apply this update, we contract in two steps with operations in the order of $D^3 d^2$ and $D^2 d^4$. As the quantum state is updated as in Eq. 4.21, additional operations are required to restore its MPS form. This is shown in Fig. 4.5.
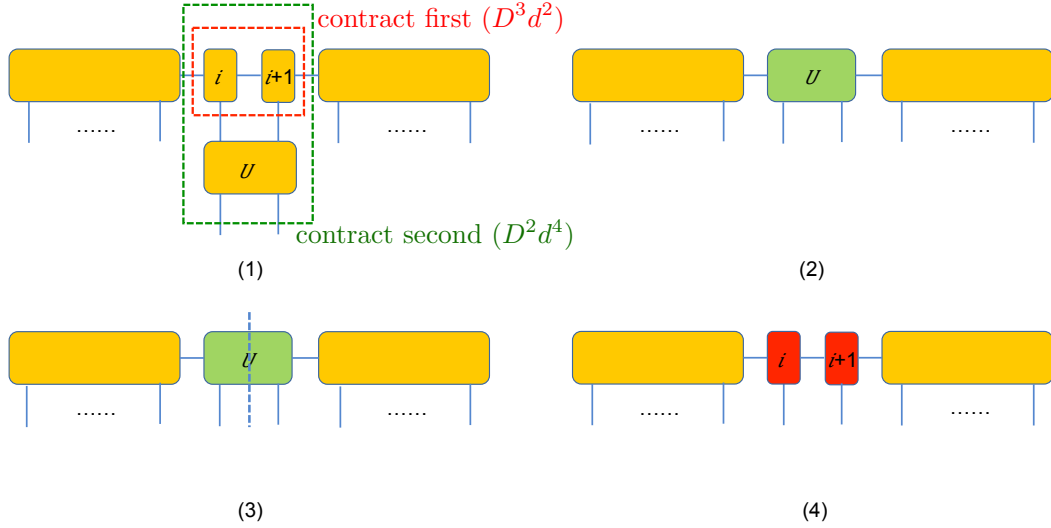
FIGURE 4.5: Demonstration of the process of updating local sites. (1) tensors of local state $(i, i+1)$ needed to be updated. (2) rewrite the updated state as in three part product form, the first contract needs $\mathcal{O}(D^3 d^2)$, and the second contract needs $\mathcal{O}(D^2 d^4)$ operations (3) applying Schmidt decompositon on the bond between $i-$th and $(i+1)-$th site, and keep only first D largest Schmidt coefficient to implement truncation (4) restore the updated quantum state back to MPS form. $\mathcal{O}(D^3 d^3)$ operations are required

With the help of one-site gates, two-site gates and the capability of evaluating expectation values, we are able to implement real- (imaginary-) time evolution, which is the key feature of TEBD algorithm as we will describe in the following section.

4.1.3 Suzuki-Trotter expansion and time evolution

Simulating the time evolution operator applied to the MPS describing our quantum state can be achieved by applying two-site gates to the MPS in a small time interval. It is most straight-forward if the Hamiltonian of the system only contains next-neighbour interactions. If this condition is satisfied it can be written as the sum over two-site Hamiltonians, $\hat{H}_{sys} = \sum_i^{M-1} \hat{H}_{i,i+1}$. The unitary time evolution operator in each time step within the interval Δt then can be represented

as

$$\hat{U}_{sys} \equiv e^{-i\hat{H}_{sys}\Delta t} = e^{-i\hat{\sum}_i^{M-1}\hat{H}_{i,i+1}\Delta t} . \tag{4.23}$$

Here we have chosen the unit system where $\hbar \equiv 1$. Via Suzuki-Trotter expansion [128], we are able to rewrite the time-evolution operator in Eq. 4.23 as a sum of operators that are only related to next-neighbour interaction, so that we can implement those operators as two-site gates.

$$\hat{U}_{sys} = \prod_i \hat{U}_{i,i+1}$$

$$\hat{U}_{i,i+1} \equiv e^{-i\hat{H}_{i,i+1}\Delta t'} . \tag{4.24}$$

One thing to be noted is that the time interval $\Delta t'$ of each two-site gate $\hat{U}_{j,j+1}$ are not necessarily equivalent to the original time step Δt. In general, the two-site gates do not commute with each other, thus, the error of this expansion will be a function of this chosen time interval $\Delta t'$. The value of $\Delta t'$ that depends on the order of the Suzuki-Trotter expansion, is directly related to the error in simulating the original time evolution operator $\hat{U}_{sys}$. For example, the intuitive expansion with two non-commuting operators $[\hat{A}, \hat{B}] \neq 0$ is,

$$e^{(\hat{A}+\hat{B})\Delta t} = e^{\hat{A}\Delta t}e^{\hat{B}\Delta t} + \mathcal{O}(\Delta t^2) . \tag{4.25}$$

This is the first order expansion that can be applied to our next-neighbour operators generating the $\hat{U}_{j,j+1}$ by defining $e^{\hat{A}\Delta t} = \prod_{\text{odd}} e^{-i\hat{H}_{i,i+1}\Delta t}$ and $e^{\hat{B}\Delta t} = \prod_{\text{even}} e^{-i\hat{H}_{i,i+1}\Delta t}$. Applying those two-site gates will have an error of $\mathcal{O}(\Delta t^2)$.

In practice, higher order expansions are implemented to increase accuracy and decrease computational time. Here we introduce the second-order expansion which is used in our numerical simulations,

$$e^{(\hat{A}+\hat{B})\Delta t} = e^{\hat{A}\Delta t/2}e^{\hat{B}\Delta t}e^{\hat{A}\Delta t/2} + \mathcal{O}(\Delta t^3) , \tag{4.26}$$

as shown in Fig. 4.6.

Higher order expansions, like 4-th order Trotter expansion, can also be implemented. We refer [129] for details of high-order expansions. We do not use high-order expansions because the stochastic equations we will propagate in this thesis require small timesteps to more accurately represent dynamics with white noise.
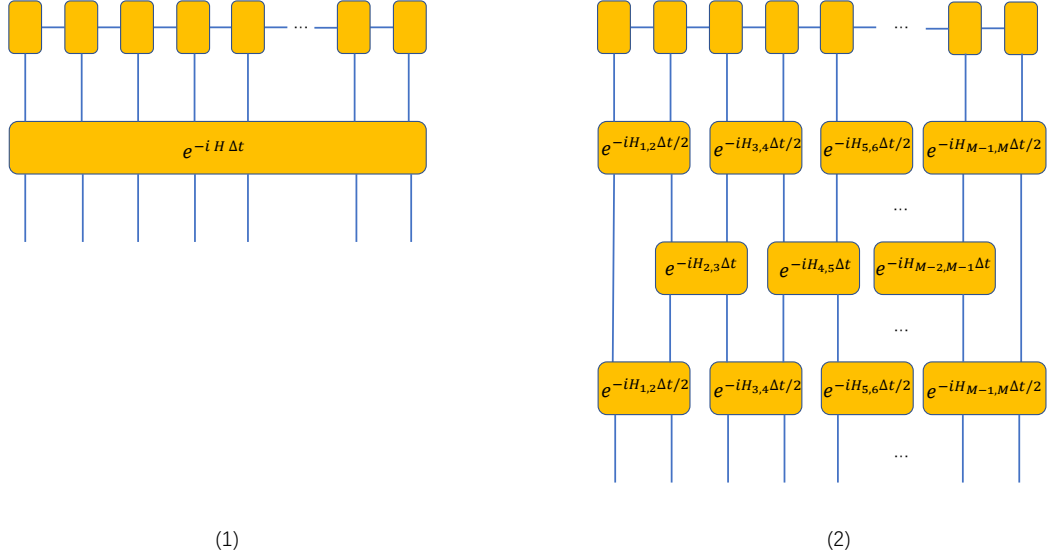
FIGURE 4.6: Implementation of time evolution of a MPS with even number of sites by second order Suzuki-Trotter expansion of the time evolution operator (1) the original unitary operator $e^{-iH\Delta t}$ apply on a MPS (2) the implementation of two-site gates, first applying the odd site evolution operators with $\Delta t/2$, then applying even site evolution operators with Δt, and finaly applying the odd site evolution operators with $\Delta t/2$, as shown in Eq. 4.26.

4.1.4 Imaginary time evolution

The capability to implement time evolution operators not only provides the advantages for TEBD to simulate the dynamics of complex systems, but also supports the calculation of ground states via time evolution of imaginary time $t = -i\tau$ under the Hamiltonian of the system, $\hat{H}_{sys}$. The ground state of the Hamiltonian $\hat{H}_{sys}$ can be computed as

$$|\Psi_{GS}\rangle = \lim_{\tau \to \infty} \frac{e^{-\hat{H}_{sys}\tau} |\Psi_0\rangle}{\left\| e^{-\hat{H}_{sys}\tau} |\Psi_0\rangle \right\|} , \qquad (4.27)$$

with the initial state $|\Psi_0\rangle$. Theoretically, the initial state needs to be chosen with a non-zero overlap with the ground state, i.e. $\langle\Psi_0|\Psi_{GS}\rangle \neq 0$, and the system has a non-degenerate ground state and the minimum value of the energy differences between eigenstates larger than zero, $\Delta_{\min} > 0$. By expanding the initial state in

the eigenbasis of $\hat{H}_{sys}$, $\{|E_n\rangle\}$, with the eigenenergies $E_0 < E_1 < ...$,

$$|\Psi_0\rangle = \sum_{n=0} c_n |E_n\rangle \ . \tag{4.28}$$

When we substitute this into Eq. 4.27, the evolved state is seen to be proportional to the ground state at infinite time, assuming the energy of ground state $E_0 = 0$ and $E_n > 0$ for $n > 0$,

$$\begin{aligned}
|\Psi_{GS}\rangle &\propto \lim_{\tau\to\infty} \sum_{n=0} e^{-E_n\tau} c_n |E_n\rangle \\
&\propto \lim_{\tau\to\infty} (c_0 |E_0\rangle + \sum_{n=1} e^{-E_n\tau} c_n |E_n\rangle) \\
&\propto |E_0\rangle \ . \tag{4.29}
\end{aligned}$$

The TEBD method can realise the calculation of ground states, by applying imaginary time evolution $\Delta t = -i\Delta\tau$ via the Suzuki-Trotter expansion. One way to test whether the evolved state is the ground state is to implement real-time evolution under the system Hamiltonian $\hat{H}_{sys}$, then to check whether long-range quantities or the state itself change in time, thus testing that the evolved state is at least an eigenstate.

In practice, the condition of $\langle\Psi_0|\Psi_{GS}\rangle \neq 0$ is not necessarily required. Numerical errors will typically leads to non-zero population in the ground state regardless of the choice of initial state.

4.2 Open systems, classical stochastic processes and the master equation approach

In the study of open quantum systems, the Lindblad equation [130] is the most useful tool to describe non-unitary Markovian processes such as dissipation and decoherence. In quantum optics, the simplest example of this is the spontaneous emission process in two-level systems that can be described by a Lindblad equation [4]. Here in this section, we start from introducing basic concepts of stochastic processes and Ito calculus to derive a special form of Lindblad equation, which captures the nature of Markovian processes involving classical noise in the white noise limit.

4.2.1 Stochastic processes

In situations where the system of interest either involves random processes or the Hilbert space of such systems is hard to manage, a statistical method is often required to access the dynamics of the system. The understanding of stochastic processes can be very useful in describing corresponding physical systems.

There are two main streams of studying stochastic processes, which focus on different aspects of dynamics. The one that studies the evolution of probability distributions for values of a given quantity of interest which can be described by particular equations, is to solve the Fokker-Planck Equation (FPE) [131]. The general form of the FPE for a single stochastic variable, x, is

$$\frac{\partial p(x,t)}{\partial t} = -\frac{\partial}{\partial x}a_1(x)p(x,t) + \frac{1}{2}\frac{\partial^2}{\partial x^2}a_2(x)p(x,t) \ , \qquad (4.30)$$

where a_1 is called the drift coefficient, a_2 is often referred as the diffusion coefficient, and $p(x,t)$ is the probability density of the stochastic variable x at time t.

The other stream that follows the evolution of the stochastic variable along each individual trajectory with random elements as noise, is to solve the Stochastic Differential Equation (SDE). Both of these two methods have the same origin in the study of Brownian motion problems. In most of the cases, the Fokker-Planck equation can be solved directly or be treated as a set of stochastic differential equation of random variables. In this chapter, we mainly focus on the SDE, and later the derivation of a special form of Lindblad equation.

4.2.1.1 Wiener process

The Wiener process is a continuous-time stochastic process, sometimes referred as the Standard Brownian motion process or Brownian motion. The study of the Wiener process developed mathematical tools which can be used to describe more complex random processes. The Wiener process is the solution of a simple FPE in which the drift coefficient is zero and the diffusion coefficient is one in Eq. 4.30. The FPE of the Wiener process is,

$$\frac{\partial}{\partial t}p(w,t|w_0,t_0) = \frac{1}{2}\frac{\partial^2}{\partial w^2}p(w,t|w_0,t_0) \ , \qquad (4.31)$$

where $p(w, t|w_0, t_0)$ is the conditional probability of w at time t given the event that $w = w_0$ at time t_0. The initial condition is

$$p(w, t_0|w_0, t_0) = \delta(w - w_0) \ . \tag{4.32}$$

To solve this equation, we can use the characteristic function, which is the Fourier transform of $p(w, t|w_0, t_0)$.

$$\phi(s, t) = \int_{-\infty}^{\infty} \mathrm{d}w\, p(w, t|w_0, t_0) e^{isw} \ . \tag{4.33}$$

Taking both sides of Eq. 4.31 and integrating by parts, together with the assumption of $\{p, \partial p / \partial w\} \to 0$ as $w \to \pm\infty$, the equation of characteristic function is as follows,

$$\frac{\partial}{\partial t}\phi(s, t) = -\frac{1}{2}s^2\phi \ , \tag{4.34}$$

with the corresponding initial condition is $\phi(s, t_0) = e^{isw_0}$. The solution of Eq. 4.34 is simple, and will lead us to the solution of the conditional probability distribution.

$$\phi(s, t) = \phi(s, t_0) \exp[-s^2(t - t_0)/2] \ , \tag{4.35}$$

$$p(w, t|w_0, t_0) = \frac{1}{2\pi} \int_{-\infty}^{\infty} \mathrm{d}s\, \phi(s, t) e^{-isw}$$

$$= \frac{1}{\sqrt{2\pi(t - t_0)}} \exp[-\frac{(w - w_0)^2}{2(t - t_0)}] \ . \tag{4.36}$$

Then the sample paths $W(t)$ have the following statistics,

$$\langle W(t) \rangle = w_0 \quad \langle [W(t) - w_0]^2 \rangle = t - t_0 \ . \tag{4.37}$$

4.2.2 Stochastic differential equation

The concept of stochastic differential equations become widely used in the study of stochastic processes [131]. A general form of Langevin's equation is

$$\frac{dx}{dt} = a(x, t) + b(x, t)\xi(t) \ , \tag{4.38}$$

where x is the stochastic variable of interest, and $a(x, t)$ and $b(x, t)$ are functions describing the motion of the variable. $\xi(t)$ is considered a rapid fluctuation term

and related to white noise. For every different time, the values of $\xi(t)$ and $\xi(t')$ are independent of each other. Conventionally, we assume the mean value of $\xi(t)$ is zero. These two assumptions provide the conditions on $\xi(t)$.

$$\langle \xi(t) \rangle = 0 \ , \quad \text{and} \quad \langle \xi(t)\xi(t') \rangle = \delta(t - t') \ . \tag{4.39}$$

In physical reality, the white noise limit is an idealisation, and no realistic fluctuation would have an infinite variance. Generalisations of this include the case of the Ornstein-Uhlenbeck process for which, the fluctuating signal has a finite correlation time,

$$\langle X(t)X(t') \rangle = \frac{D}{2k} e^{-k|t-t'|} \ , \tag{4.40}$$

and in the limit of certain conditions, $D = k^2$ and $k \to \infty$, this correlation time becomes,

$$\lim_{k \to \infty} \langle X(t)X(t') \rangle = \delta(t - t') \ . \tag{4.41}$$

This delta function implies that the future behaviour at time t does not depends on the history at time t', but only on its present state. This simplification is known as the Markov approximation. Since the delta function can simplify calculations, the Markov approximation is often chosen as the first assumption, which is valid in the situation with an infinitesimal correlation time.

4.2.2.1   Integral of $\xi(t)$

The new random fluctuating term $\xi(t)$ in Eq. (4.38) plays an important role in a wider range of stochastic problems and can be directly related to Wiener process. Consider the integral of $\xi(t)$ here, $u(t)$,

$$u(t) = \int_0^t \mathrm{d}s\xi(s) \ . \tag{4.42}$$

To discuss the relation between $u(t)$ and $u(t')$, we assume that $t' > t$, and derive the calculation of $u(t')$ as below,

$$
\begin{aligned}
u(t') &= \int_0^t \mathrm{d}s\xi(s) + \int_t^{t'} \mathrm{d}s'\xi(s') \\
&= \lim_{\epsilon \to 0} \int_0^{t-\epsilon} \mathrm{d}s\xi(s) + \int_t^{t'} \mathrm{d}s'\xi(s') \ .
\end{aligned}
\tag{4.43}
$$

The increments $\xi(s)$ and $\xi(s')$ are totally independent of each other, thus $u(t')$ can be determined only from $u(t)$, which leads to the conclusion that $u(t)$ is a Markovian process. On calculating the mean value and variance of the increment $u(t+dt) - u(t)$, the relation between $u(t)$ and $W(t)$ becomes clearer.

$$\langle u(t+dt) - u(t) \rangle = \langle \int_t^{t+dt} ds\xi(s) \rangle = 0 , \tag{4.44}$$

$$\langle [u(t+dt) - u(t)]^2 \rangle = \langle \int_t^{t+dt} ds \int_t^{t+dt} ds'\xi(s)\xi(s') \rangle$$

$$= \int_t^{t+dt} ds \int_t^{t+dt} ds'\delta(s-s') = dt . \tag{4.45}$$

From Eq. 4.37, the mean value and variance of $\Delta W(t) = W(t+\Delta t) - W(t)$ can be evaluated as,

$$\langle \Delta W(t) \rangle = 0 , \quad \text{and} \quad \langle \Delta W(t)^2 \rangle = \Delta t . \tag{4.46}$$

That is, $u(t)$ is indeed the Wiener process, and $\xi(t)dt = dW(t)$. This relation will be used to derive the Lindblad equation in the next section. Another way to prove that $u(t)$ is the Wiener process is via calculating drift and diffusion coefficients in the FPE (Eq. 4.30).

$$a_1(t) = \lim_{dt \to 0} \langle u(t+dt) - u(t) \rangle = 0 , \tag{4.47}$$

$$a_2(t) = \lim_{dt \to 0} \langle [u(t+dt) - u(t)]^2 \rangle / dt = 1 . \tag{4.48}$$

and result in the same FPE of $u(t)$ as of Eq. 4.31.

4.2.2.2 Stochastic Integration and Ito rules

The nature of $W(t)$ as a non-differentiable process will lead to interesting results in different calculus. Consider an arbitrary function $G(t)$ as a function of t and $W(t)$, the stochastic integral $\int_{t_0}^t G(t')dW(t')$ can be evaluated as the sum of area below the function,

$$S_n = \sum_{i=1}^n G(\tau_i)[W(t_i) - W(t_{i-1})] , \tag{4.49}$$

as we divide $[t_0, t]$ into n intervals $\{t_0, t_1, ..., t_{n-1}, t\}$, and $\tau_i \in [t_{i-1}, t_i]$. There are two different types of definition of stochastic integral depending on the choice of

τ. One is call Ito stochastic integral, defined as,

$$\int_{t_0}^{t} G(t')dW(t') = \text{ms-}\lim_{n\to\infty} \left\{ \sum_i G(t_{i-1})[W(t_i) - W(t_{i-1})] \right\} \quad (I). \qquad (4.50)$$

ms-lim denotes mean-square limit that if

$$\lim_{n\to\infty} \langle (S - S_n)^2 \rangle = 0 \quad \text{then} \quad S = \text{ms-}\lim_{n\to\infty} S_n. \qquad (4.51)$$

The other one, Stratonovich stochastic integral, is slightly different

$$\int_{t_0}^{t} G(t')dW(t') = \text{ms-}\lim_{n\to\infty} \left\{ \sum_i \frac{1}{2}(G(t_{i-1} + G(t_i))[W(t_i) - W(t_{i-1})] \right\} \quad (S).$$
$$(4.52)$$

These two different integral will be noted with (S) and (I) in the following sections. To demonstrate the difference of these two types of stochastic integrals, we calculate the integral with $G(t) = W(t)$ as an example,

$$\int_{t_0}^{t} W(t')dW(t') = \text{ms-}\lim_{n\to\infty} \frac{1}{2} \sum_i^n [W(t_i) + W(t_{i-1})][W(t_i) - W(t_{i-1})] \quad (S)$$

$$= \text{ms-}\lim_{n\to\infty} \frac{1}{2} \sum_i^n [W(t_i)^2 - W(t_{i-1})^2]$$

$$= \frac{1}{2}W(t)^2 - \frac{1}{2}W(t_0)^2 \quad (S) \qquad (4.53)$$

$$\int_{t_0}^{t} W(t')dW(t') = \text{ms-}\lim_{n\to\infty} \sum_i^n W(t_{i-1})[W(t_i) - W(t_{i-1})] \quad (S)$$

$$= \text{ms-}\lim_{n\to\infty} \frac{1}{2} \sum_i^n \{[W(t_i) + \Delta W(t_i)]^2 - W(t_{i-1})^2 - \Delta W(t_i)^2\}$$

$$= \frac{1}{2}W(t)^2 - \frac{1}{2}W(t_0)^2 - \frac{1}{2}\text{ms-}\lim_{n\to\infty} \sum_{i=1}^n \Delta W(t_i)^2$$
$$(4.54)$$

The Stratonovich integral have closer relationship to ordinary calculus. On the other hand, the Ito integral has its own advantages calculating stochastic average value of certain type of function $G(t)$, when they are statistically independent

(non-anticipating) of $dW(t)$. In this case,

$$\left\langle \int_{t_0}^t G(t')dW(t') \right\rangle = \int_{t_0}^t \langle G(t') \rangle \langle dW(t') \rangle = 0 , \qquad (4.55)$$

while calculation of the Stratonovich integral might be much more difficult to apply. In general, the stochastic average values of the same integral from both definition will be the same.

In the integral of an arbitrary non-anticipating function $G(t)$, the high order of increment $\Delta W(t)^{2+N}$ ($N \geq 0$) might appear due to consideration of higher order approximation or product of first order calculation. It is easy to shown the features of $dW(t)$ with higher order satisfy the formula,

$$[dW(t)]^2 \equiv dt, \quad [dW(t)]^{2+N} \equiv 0 \quad \text{for } N > 0 \qquad (4.56)$$

this is the Ito rules. The Ito rules are valid only for the Ito integral, as the derivation used that $\Delta W(t_i)$ is independent of $G(t_{i-1})$.

4.2.2.3 Ito stochastic differential equation and Ito correction

In this section, we would like to introduce the Ito stochastic differential equation (SDE), and then establish the relation between the Stratonovich SDE and the Ito correction. Consider a random variable satisfying the Ito SDE,

$$dx(t) = a(x,t)dt + b(x,t)dW(t) \quad \text{(I)} , \qquad (4.57)$$

the sign "(I)" shown at the end of the equation denotes the Ito SDE, and "(S)" denotes the Stratonovich SDE. For a function of $x(t)$, $f(x)$, the increments representing the stochastic process are,

$$df(x) = \{f'(x)a(x,t) + \frac{1}{2}f''(x)b(x,t)^2\}dt + f'(x)b(x,t)dW(t) \quad \text{(I)} , \qquad (4.58)$$

using the expansion $df = f'dx + 1/2f''(dx)^2 + ...$. Eq. 4.58 is referred as the Ito formula. The terms of higher order than dW^2 and dt are discarded. The second term on the right hand side of the formula with $f''(x)$ is called the Ito correction. However, the Stratonovich calculus for $f(x)$ is

$$df(x) = \{f'(x)a(x,t)\}dt + f'(x)b(x,t)dW(t) \quad \text{(I)} , \qquad (4.59)$$

without the Ito correction term. In the physical situation where white noise approximation stands, the Stratonovich represents the system better. The transformation from the Stratonovich SDE to the Ito SDE can be implemented with

correction terms. Assume the random variable $x(t)$ is a solution of the Ito SDE, thus Eq. 4.57 holds. The Stratonovich SDE is then,

$$\mathrm{d}x(t) = a(x,t)\mathrm{d}t + b\left(\frac{x(t)+x(t+\mathrm{d}t)}{2},t\right)\mathrm{d}W(t) \quad (S) \,,$$

$$= a(x,t)\mathrm{d}t + b(x+\frac{1}{2}\mathrm{d}x,t)\mathrm{d}W(t) \,,$$

$$\approx a(x,t)\mathrm{d}t + b(x,t)\mathrm{d}W(t) + \frac{\partial b}{\partial x}\frac{\mathrm{d}x}{2}\mathrm{d}W(t) \,.$$

by substituting Eq. 4.57, we derive,

$$\mathrm{d}x(t) = a(x,t)t + b(x,t)\mathrm{d}W(t) + \frac{\partial b(x,t)}{\partial x}\frac{a(x,t)\mathrm{d}t + b(x,t)\mathrm{d}W(t)}{2}\mathrm{d}W(t) \,,$$

$$= \left(a(x,t) + \frac{1}{2}b(x,t)\frac{\partial b(x,t)}{\partial x}\right)\mathrm{d}t + b(x,t)\mathrm{d}W(t) \quad (S) \,. \tag{4.60}$$

One of the advantage of the Ito form is that when the interested function is non-anticipating, the calculation is much easier than the Stratonovich calculus to reach the same results. In this thesis, we mainly discuss the type of noise in optical lattice that can be characterised as white noise, which the interested function is non-anticipating. We convert the physical description of the system, which is Stratonovich calculus, to Ito calculus to simplify the calculation to obtain stochastic average effects.

4.2.2.4 Multiplicative stochastic differential equation

The multiplicative stochastic differential equation (MSDE), a subset of SDE which are less complicated to solve. The general form is,

$$\frac{d}{dt}u(t) = \left(A[x(t),t] + B[x(t),t]\xi(t)\right)u(t) \,, \tag{4.61}$$

where $A[x(t),t]$ is the statistical component and $B[x(t),t]$ is the stochastic component. The relation between Stratonovich MSDE and Ito MSDE can be easily formed, if the coefficients before dt and $dW(t)$ are independent of $u(t)$

$$du^S(t) = (Adt + BdW(t))u^S(t) \qquad (S) \tag{4.62}$$

$$du^I(t) = (A + \frac{1}{2}B^2)u^I(t)dt + Bu^I(t)dW(t) \qquad (I) \tag{4.63}$$

These formulae play a key role in the derivation of Lindblad equation in the following section.

4.2.3 Stochastic Schrödinger equation and Lindblad equation

In this section, we will start from the Schrödinger equation with a "noisy" Hamiltonian to derive a special form of Lindblad equation:

$$\frac{\mathrm{d}\rho}{\mathrm{d}t} = -i[H_0, \rho] + \Gamma\{2A\rho A - A^2\rho - \rho A^2\} \,, \tag{4.64}$$

where the operators ρ, H_0, A are time-dependent, and Γ is a constant. The density operator ρ is the stochastic average of quantum states $|\phi(t)\rangle$, $\rho(t) = \langle|\phi(t)\rangle\langle\phi(t)|\rangle$. By introducing a noise term in the system Hamiltonian, the ordinary Schrödinger equation becomes a Stochastic Schrödinger equation, and also a Stratonovich MSDE. Consider a general form of noisy Hamiltonian such as,

$$H(t) = H_0(t) + \sqrt{2\Gamma}\eta(t)A(t) \,. \tag{4.65}$$

The function $\eta(t)$ is used to characterize the noise, with relation to a random variable,

$$u(t) = \int_0^t \eta(t)\mathrm{d}t \,, \tag{4.66}$$

where $H_0(t)$ is the original Hamiltonian, and $A(t)$ is the noise operator. Here we assume an initial condition without losing generality, $u(0) = 0$.

In the time evolution of the physical system, we consider that the noise fluctuates much faster than the evolution. So in a short time interval $t' \in (t, t+dt)$, the noise operator $A(t)$ and the Hamiltonian $H_0(t)$ are unchanged. In this assumption, the only time dependent term is noise, i.e. $\tau_c \ll \Delta t$, and Δt is a length of one time step, which is a constant. Then the Hamiltonian in the time interval $(t, t + dt)$ should be,

$$H(t') = H_0(t) + \sqrt{2\Gamma}\eta(t')A(t) \tag{4.67}$$

for any time $t' \in [t, t + \Delta t)$.

4.2.3.1 White noise limit

To simplify the calculation, we can assume that the noise term is in the white noise limit, i.e $\eta(t) = \xi(t)$, with the correlation $\langle\xi(t)\xi(t')\rangle = \delta(t-t')$. In the white noise limit, the noisy Hamiltonian in a short time interval remains unchanged.

Here we take an example of a time-independent system with fast fluctuation white noise to derive the Lindblad equation

$$H = H_0 + (\sqrt{2\Gamma})\xi(t)A \ , \tag{4.68}$$

with noise $dW(t) = \xi(t)dt$ as in the previous sections and the stochastic behaviour remains, $\langle dW(t)^2 \rangle = dt$. The operator A is then the noise operator.

In this case, the Stochastic Schrödinger equation is,

$$i\frac{d\,|\psi(t)\rangle}{dt} = (H_0 + (\sqrt{2\Gamma})\xi(t)A)\,|\psi(t)\rangle \qquad (S) \tag{4.69}$$

$$|d\psi\rangle \equiv \{-iH_0 dt - i(\sqrt{2\Gamma})A dW(t)\}\,|\psi(t)\rangle \qquad (S) \tag{4.70}$$

It is clear that this is a multiplicative stochastic differential equation. To calculate the stochastic average behaviour of the quantum state $|\psi(t)\rangle$, we can convert it to an Ito (M)SDE, using Eq. 4.62,

$$|d\psi\rangle = \{(-iH_0 - \Gamma A^2)dt - i(\sqrt{2\Gamma})A dW(t)\}\,|\psi\rangle \qquad (I) \tag{4.71}$$

$$\langle d\psi| = \langle\psi|\,\{(+iH_0 - \Gamma A^2)dt + i(\sqrt{2\Gamma})A dW(t)\} \qquad (I) \tag{4.72}$$

where we use $|d\psi\rangle$ and $\langle d\psi|$ to denote the increments.

Then the MSDE of $d\rho$, with Ito rules applied, is,

$$\begin{aligned} d\rho &\equiv \langle |d\psi\rangle\,\langle\psi| + |\psi\rangle\,\langle d\psi|) + |d\psi\rangle\,\langle d\psi|\rangle \\ &= \langle\{(-iH_0 - \Gamma A^2)dt - i(\sqrt{2\Gamma})A dW(t)\}\rangle\rho \\ &\quad + \rho\langle\{(+iH_0 - \Gamma A^2)dt + i(\sqrt{2\Gamma})A dW(t)\}\rangle \\ &\quad + 2\Gamma A\rho A dt \\ d\rho &= \langle\{-i[H_0,\rho] + \Gamma(2A\rho A - A^2\rho - \rho A^2)\}dt - i\sqrt{2\Gamma}[A,\rho]dW(t)\rangle \qquad (I) \end{aligned} \tag{4.73}$$
$$\tag{4.74}$$

where $\langle\dots\rangle$ notes the stochastic average. With the features of white noise applied, the equation of motion of density operator can be derived as,

$$\begin{aligned} \dot\rho &= -i[H_0,\rho] + \Gamma(2A\rho A - A^2\rho - \rho A^2) \\ &= -i[H_0,\rho] + \Gamma[A,[\rho,A]] \ , \end{aligned} \tag{4.75}$$

where $\Gamma > 0$. That's exactly what we used in Lindblad equation (4.64) and implies the physics is Markovian, which means the dynamics of the system depends only on the current state. In this derivation, we applied the Ito rules

because of the white noise approximation that our interested function (ρ) is non-anticipating. The Ito rules results in the error going with the first order of dt. This will support the choice of second order of Suzuki-Trotter decomposition of time evolutions used when we simulate the dynamics of noisy systems in later sections, as the simulation result convergent with the lowest order of error. For cases with coloured noise, a higher order of expansion and corrections will be needed in the master equation.

4.3   Conclusion

In this chapter, we introduce the main computational methods that we used in this thesis. In the first half of this chapter, we presented an overview of the TEBD method and the MPS presentation that provide access to study large-size systems with manageable computational resources, by considering only the relevant subspace of the Hilbert space. The master equation approach that describes the stochastic average effect of the time evolution of the stochastic Schrödinger equation provides insight into the averaged dynamics without stochastic errors.

In the following chapters, we obtain many numerical results applying the methods we introduced in this chapter. For example, the ground states and time evolution of large size Bose-Hubbard model in Chap. 6 and 7 are calculated by applying t-DMRG methods, and the study of two-level systems in the presence of classical noise are conducted exactly via the master equation method.

Chapter 5

Improving the randomisation method in adiabatic quantum computing

In this chapter[1], we revisit a recently proposed algorithm of quantum computing, the randomisation method, which is designed to achieve better performance over standard adiabatic quantum computing. The principle of the randomisation method is to simulate projective measurements into the instantaneous eigenbasis of Hamiltonian and to induce a version of the quantum Zeno effect in adiabatic state preparation. However, the results from previous research did not demonstrate better bounds of the time cost over standard adiabatic quantum computing. We continue our study to improve the randomisation method. In Sec. 5.2, we obtain an improved upper bound on the eigenpath length considering the second derivative of the Hamiltonian. In Sec. 5.3, we analyse errors from parametrization and imperfect measurements with a lower bound of the final fidelity of state preparation. We then obtain better bounds for the time cost of the algorithm in terms of the dependence relation of the minimal spectral gap during the state transformation. In Sec. 5.4, we provide two applications of our improved method, and observe speedups over previous research.

---

[1]This work is taken in part from the publication *Improved bounds for eigenpath traversal*, H.-T. Chiang, G. Xu, and R. D. Somma, Phys. Rev. A **89**, 012314, 2014.

The author of this thesis performed the analysis of final fidelities in this work.

5.1 Introduction

The eigenstates of a Hamiltonian can often grant access to the solution of many problems in quantum information, physics and optimization [24, 65, 102, 109, 132–137]. To prepare such eigenstates, we can begin in a state that can be reliably and reproducibly prepared and then change the interaction parameters of the controlled Hamiltonians under which the system evolves, which is the key feature of adiabatic quantum computation (AQC). The adiabatic theorem [138, 139] requires that the system is in an eigenstate as an initial state. By changing the Hamiltonian parameters slowly enough, the evolved state will be sufficiently close to an eigenstate of the system, and continuously connected to the final eigenstate.

Several examples of quantum speedups via AQC have been demonstrated (c.f., [101, 103, 104, 109]). In particular, the mapping between quantum circuits and AQC Hamiltonians is established [140–148]. In AQC, we assume the knowledge of instantaneous Hamiltonians $H(s)$, along the adiabatic path $0 \leq s \leq 1$, that have non-degenerate and continuously related eigenstates $|\psi(s)\rangle$. The goal is to prepare $|\psi(1)\rangle$ from $|\psi(0)\rangle$, within a small error ε, by increasing s with certain interpolation. The evolution time T required to achieve an error below ε determines the cost of the algorithm in AQC, which depends on properties of the instantaneous Hamiltonians in the evolution, like the rate of change or minimal spectral gaps. An upper bound to the cost based on the commonly used quantum adiabatic approximation, is given by [149, 150]

$$T_{\mathrm{AQC}} = \kappa \max_{s} \left[\frac{\|\ddot{H}\|}{\varepsilon \Delta^2}, \frac{\|\dot{H}\|^2}{\varepsilon \Delta^3} \right] . \tag{5.1}$$

This means, to prepare the final eigenstate within error ε, we can increase the parameter s accordingly. For linear ramping, $s(t) = t/T_{\mathrm{AQC}}$, the time cost will be $T = T_{\mathrm{AQC}}$. κ is a constant and Δ is the minimal spectral gap of H, defined as the smallest absolute difference between the eigenvalue of $|\psi(s)\rangle$ and other eigenvalues. $s(t)$ will need to vary slowly when Δ is small. All derivatives are with respect to s unless stated otherwise, e.g., $\dot{X} = \partial X / \partial s$ and $\ddot{X} = \partial^2 X / \partial s^2$. $\|X\|$ denotes the spectral norm of an operator or matrix and $\| |\phi\rangle \|$ denotes the Euclidean norm. For some example, (e.g., Rabi oscillations, c.f. [151, 152]), the bound in Eq. (5.1) is tight and a lower bound exits, in the order of $\|\dot{H}\|^2/\Delta^3 > \|\ddot{H}\|/\Delta^2$.

From Eq. (5.1), the dependence of T_{AQC} on the gap is rather poor, specially in the cases that $\Delta \ll 1$. In some cases, though, this bound can cause significant overestimation of the actual cost needed. Recent research [106–108] proposed

new methods to improve dependence on the gap. One of those methods, based on randomisation of time steps in the evolution, can realise a quantum Zeno effect by simulating projective measurements in the instantaneous eigenbasis [107]. The only difference between this "randomisation method" (RM) and AQC is that the schedule $s(t)$ is randomly chosen according to a probability distribution. The variance of the probability distribution is related to the approximation error, and also depends on the spectral gap of the Hamiltonians.

The time cost T of the randomisation method for eigenpath traversal (EPT) also depends on the eigenstate path length, $L = \int_0^1 ds \|\|\dot{\psi}\rangle\|$ in Sec. 2.2.3. The cost is upper bounded, with approximation error $\varepsilon < 1$, by [106–109]

$$T_{\text{EPT}} = \kappa' \frac{L^c \log(L/\varepsilon)}{\varepsilon \min_s \Delta} , \qquad (5.2)$$

where κ' is a constant, and $c = 1, 2$ depends on the details of the method. For the case that L can be bounded independently of the gap, having an explicit dependence in the L or its bound is very important. For example, the time cost can achieve better bound [109] and can provide a quantum speedup of simulated annealing method used for optimization [153] (Sec. 5.4.2). For some of optimisation problems, the spectral gap Δ decreases exponentially in the problem size, but on the other hand, L increases only polynomially, and $T_{\text{EPT}} \ll T_{\text{AQC}}$ in Refs. [106–108] can prepare the final eigenstate with much lower cost than standard AQC.

To have an analytical form of L is very hard in most general cases. Here, we consider an upper bound $L^* \geq L$, which can be calculated based on the knowledge of the Hamiltonians, and then reach a new bound T_{EPT} obtained in Refs. [107, 108]. A commonly used path length bound is

$$L^* = \max_s \frac{\|\dot{H}\|}{\Delta} , \qquad (5.3)$$

known $\|\dot{H}\|$ and Δ and $\|\|\dot{\psi}\rangle\| \leq \|\dot{H}\|/\Delta$. Having Eq. (5.3), a new upper bound for the cost of the eigenpath traversal method is then [106–109]

$$T_{\text{EPT}} = \kappa' \max_s \frac{\|\dot{H}\|^c}{\varepsilon \Delta^{c+1}} \log(\|\dot{H}\|/(\varepsilon \Delta)) . \qquad (5.4)$$

However, for the RM, $c = 2$, and T_{EPT} can be larger than T_{AQC} if the parametrization is different from the uniform one. Since T_{AQC} and T_{EPT} depend on $1/\Delta^3$, it is not clear the RM has any advantages over standard AQC.

In this chapter, we obtain better bounds for the cost of the methods mentioned in Refs. [106–108], in terms of the spectral gap, the error, $\|\dot{H}\|$ and $\|\ddot{H}\|$. We would

like to discuss more about the randomisation method described in Ref. [107], because of the simple connection between RM and standard AQC. Some of our results can also be used to improve the cost of those other methods as well. In Sec. 5.2, we focus on an improved bound on the path length L^*, which is of order $1/\sqrt{\Delta}$ if $|\psi(s)\rangle$ is the ground state of $H(s)$. This bound can be used in general Hamiltonian paths, and we also focus on those Hamiltonians that are *frustration free*. These allow a more practical form of the bounds to be written and are important roles in other fields (e.g. condensed matter theory [136, 154], optimization [155], and quantum information [156–158]). In Sec. 5.3, having the improved bound, we obtain a new average cost for the RM of order $1/\Delta^2$. In the situation that $\Delta \ll 1$, the RM can provide a quantum speed up over standard AQC - or at least better probable bound. In Sec. 5.3.2 an analysis of Ref. [107] about the cost scaling factor is conducted, and results in elimination of the logarithmic factor present in Eqs. (5.2) and (5.4). In Sec. 5.4 we apply our improved bounds to the preparation of projected entangled pair states [159] (PEPS) and the quantum simulation of classical annealing processes [109, 153]. By using the results for frustration-free Hamiltonians, we can show that the RM has an average cost of order $1/\Delta^{3/2}$ for the preparation of PEPS, and for the method based on fixed-point search the cost is of order $1/\Delta$ (up to a logarithmic correction).

5.2 Improved bound on the path length

As mentioned in Sec. 2.2.3, the path length of a continuous and differentiable state $\{|\psi(s)\rangle\}$, is

$$L = \int_0^1 ds \|\,|\dot{\psi}\rangle\,\| \,,$$

where $s \in [0, 1]$. Also, $\langle \psi|\dot{\psi}\rangle = 0$ can be ensured. We assume that $|\psi\rangle$ is a non-degenerate eigenstate of H of eigenvalue 0, so that $|\dot{\psi}\rangle = -H^{-1}\dot{H}\,|\psi\rangle$. The inverse of Hamiltonian, H^{-1}, is in the subspace orthogonal to $|\psi\rangle$. In this case, an upper bound of $\max_s(\|\dot{H}\|/\Delta)$ on L can be obtained by substituting the expression into the definition of L, which is commonly used in adiabatic approximations.

In the case that $|\psi\rangle$ is the ground state of H and the state path is two times differentiable, we can derive a tighter bound on L in terms of the spectral gap. According to the Cauchy-Schwarz inequality,

$$L^2 \leq \int_0^1 ds \,\|\,|\dot{\psi}\rangle\,\|^2 \,. \tag{5.5}$$

A detailed derivation is provided below. As $|\psi\rangle$ is the ground state, and $H|\psi\rangle = 0$, we have

$$|\dot{\psi}\rangle = -H^{-1}\dot{H}|\psi\rangle \ ,$$

so H^{-1} (inverse to H) is in the subspace orthogonal to $|\psi\rangle$. Having the assumption that $\dot{H}$ exists and $\|\dot{H}\| < \infty$ and $H \geq 0$, we have

$$
\begin{aligned}
\||\dot{\psi}\rangle\|^2 &= \langle\psi|\dot{H}H^{-2}\dot{H}|\psi\rangle \\
&\leq \|H^{-1/2}\|^2\|H^{-1/2}\dot{H}|\psi\rangle\|^2 \\
&\leq \frac{1}{\Delta}\langle\psi|\dot{H}H^{-1}\dot{H}|\psi\rangle \\
&= \frac{-1}{\Delta}\langle\psi|\dot{H}|\dot{\psi}\rangle
\end{aligned}
\tag{5.6}
$$

using Cauchy-Schwarz inequality. In addition, from the second derivative of $H|\psi\rangle = 0$, we have the relation that,

$$\dot{H}|\dot{\psi}\rangle = -\frac{1}{2}[\ddot{H}|\psi\rangle + H|\ddot{\psi}\rangle] \ ,$$

and using Eq. (5.6) we obtain the desired bound as

$$\||\dot{\psi}\rangle\|^2 \leq \frac{1}{2\Delta}\langle\psi|\ddot{H}|\psi\rangle \ . \tag{5.7}$$

This assumes the existence of $\ddot{H}$ with $\|\ddot{H}\| < \infty$. Together with equations (5.5) and (5.7), we have

$$L^2 \leq \int_0^1 ds\, \frac{1}{2\Delta}\langle\psi|\ddot{H}|\psi\rangle \ .$$

In the case that the ground state energy $E \neq 0$, we then obtain,

$$L \leq L^* = \left(\int_0^1 ds\, \frac{1}{2\Delta}\langle\psi|\ddot{H} - \ddot{E}|\psi\rangle\right)^{1/2} \ . \tag{5.8}$$

5.2.1   General interpolations

In general, because $\langle\psi|\,\ddot{H}-\ddot{E}\,|\psi\rangle \geq 0$, the right hand side of Eq. (5.8) can be bounded so that

$$L^* \leq \max_s \sqrt{\frac{\|\ddot{H}\| - (\dot{E}(1) - \dot{E}(0))}{2\Delta}}$$

$$\leq \max_s \sqrt{\frac{\|\ddot{H}\| + 2\|\dot{H}\|}{2\Delta}} \; ,$$

where $\dot{E}(0)$ and $\dot{E}(1)$ are the first derivative of the ground state energy at $s = 0$ and $s = 1$. The spectral gap Δ usually decreases exponentially with the system size.

5.2.2   Linear interpolations

In a case that the time-dependent Hamiltonian is constructed as a linear interpolation of two Hamiltonians, $H(s) = (1 - s)H_0 + sH_f$, where, H_0 and H_f are the initial and final Hamiltonians, we can eliminate the term $\left\|\ddot{H}\right\|$, and the bound is

$$L^* \leq \max_s \sqrt{\frac{\dot{E}(1) - \dot{E}(0)}{2\Delta}}$$

$$\leq \max_s \sqrt{\frac{\|\dot{H}\|}{\Delta}} \; .$$

5.2.3   Frustration-free Hamiltonians

A frustration-free Hamiltonian $H = \sum_k \Pi_k$ is the sum of a set of Hamiltonians $\{\Pi_k\}$ that shares all the same ground states. Usually, Π_k corresponds to local operators and our assumptions hold, for a ground state $|\psi\rangle$ with eigenvalue 0, $H\,|\psi\rangle = \Pi_k\,|\psi\rangle = 0$ for all k, and $\Pi_k \geq 0$. In this case, the *local* bound on the rate of change of the state in Eq. (5.7) applies directly,

$$L^* \leq \max_s \sqrt{\frac{\|\ddot{H}\|}{2\Delta}} \; . \tag{5.9}$$

5.3 Improved bounds of time cost

In Ref. [107], the "randomization method" (RM) was proposed using phase randomization to traverse the eigenpath. The essence of the RM is: For a discrete Hamiltonian path $\{H(s)\}$, the discretisation $0 < s_1 < s_2 < \ldots < s_q = 1$ is determined by the final-state preparation error. At the j-th step of the RM, we evolve with the constant Hamiltonian $H(s_j)$ for a random time t_j. The distribution of this random time depends on $\Delta(s_j)$, the minimal gap of this step, and the error. For an example, the PDF of t_j could be a normal distribution of zero mean and standard deviation of order $1/\Delta(s_j)$. This randomisation introduced by the evolution will induce dephasing and a reduction of the *coherences* between $|\psi(s_j)\rangle$ and any other eigenstate (see Secs. 5.3.1 and 5.3.2). In other words, evolution randomisation simulates a projective measurement onto $|\psi(s_j)\rangle$. Then, the sequence of measurements of $|\psi(s_1)\rangle, |\psi(s_2)\rangle, \ldots$ induces a version of the quantum Zeno effect, resulted in the preparation of $|\psi(s_q)\rangle$. With a proper choice of $s_1, s_2 \ldots, s_q$, the state preparation can be achieved with arbitrarily high probability. The basic steps of the RM are demonstrated in Fig. 5.1; more details are in Secs. 5.3.1 and 5.3.2.

In general, the average cost of the RM is the number of steps q times the average (absolute) evolution time per randomization step; the latter is often proportional to the inverse spectral gap Δ [107]. For a uniform parametrization under which $\int_0^1 ds \||\dot{\psi}\rangle\| = L$ for all s, and with the error ε, we can calculate that $q \propto L^2/\varepsilon$, and thus obtain an optimal average cost of order $L^2/(\varepsilon\Delta)$. If the evolving times of each step are nonnegative (or nonpositive), an additional logarithmic factor (Eq. (5.4)) was needed for the cost analysis [107].

In the case that the given parametrization is not uniform, the RM requires $q = (L^*)^2$ to succeed, where L^* is an upper bound on L. A standard choice for L^* is the one in Eq. (5.3), which gives an overall cost of order $1/\Delta^3$ because the number of points in the discretization is on the order of $\max_s(1/\Delta^2)$. In this section, we are going to show that the upper bound obtained in Sec. 5.2 can be used to obtain a better discretization for the RM than that of Ref. [107]. With this new result, we can achieve an improved average cost of order $\max_s(1/\Delta^2)$. We also implement new error analysis to avoid the logarithmic correction in the cost when the random times are nonnegative (or nonpositive).

5.3.1 Parametrization errors

In this section we analyse the errors due to the choice of discretization. We assume perfect measurements of the $|\psi(s)\rangle$ in the RM, and discuss about errors in the
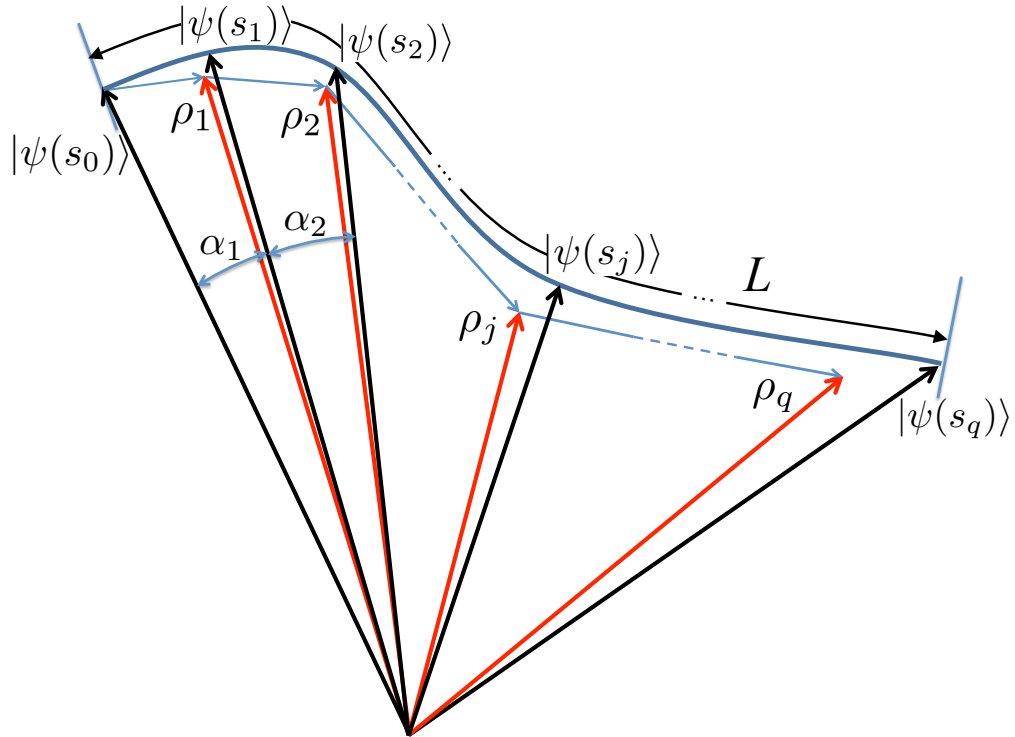
FIGURE 5.1: Basic steps of the RM and state representation. At the jth step, the RM prepares the mixed state ρ_j (represented by a red arrow) that has large probability of being in $|\psi(s_j)\rangle$ (represented by a black arrow) after measurement. The preparation of ρ_j is done by evolving ρ_{j-1} with the Hamiltonian $H(s_j)$ for random time t_j. The number of steps q is obtained so that the final error probability is bounded by some given $\varepsilon > 0$. The length of continuous eigenpath L can be bounded (Secs. 5.2), and the angles α between the eigen vectors are related to discretization and the final-state preparation error.

case of imperfect measurements due to evolution randomization in Sec. 5.3.2. We let $0 < s_1 < s_2 < \ldots < s_q = 1$. Note any discretization of $[0, 1]$, where q, the total number of intervals, will be obtained below. A upper bound of the error of preparation or quantum *infidelity* $(1 - F)$ in the preparation of $|\psi(s_q)\rangle$ can be

obtained as

$$1 - F = 1 - \prod_{j=1}^{q} \cos^2(\alpha_j)$$

$$\leq \sum_{j=1}^{q} \sin^2(\alpha_j) \, ,$$

where the 'angles' α_j are determined from $\cos\alpha_j = \langle\psi(s_{j-1})|\psi(s_j)\rangle \in \mathbb{R}$ as shown in Fig. 5.1. Without loss of generality, we can assume $\alpha_j \in [0, \pi/2]$. Then it follows that

$$\sin\alpha_j = \| \, |\psi(s_{j-1})\rangle - \cos\alpha_j \, |\psi(s_j)\rangle \, \|$$

$$\leq \| \, |\psi(s_{j-1})\rangle - e^{i\phi} \, |\psi(s_j)\rangle \, \| \, . \tag{5.10}$$

The phase $\phi \in \mathbb{R}$ can be arbitrary. Next, we split the interval $[s_{j-1}, s_j]$ into r segments of size $(s_j - s_{j-1})/r$ and thus define $r+1$ points in this interval $s_j^n = s_{j-1} + (s_j - s_{j-1})n/r$, with $n = 0, 1, \ldots, r$. The corresponding eigenstates along the eigenpath at each point are now $|\psi(s_j^n)\rangle$ and, we also define $\cos\beta_n = \langle\psi(s_j^{n-1})|\psi(s_j^n)\rangle \in \mathbb{R}$. In particular, when $n = 0$, $|\psi(s_j^0)\rangle = |\psi(s_{j-1})\rangle$ and $n = r$, a global phase is added $|\psi(s_j^n)\rangle = e^{i\phi}|\psi(s_j)\rangle$.

From Eq. (5.10) we obtain

$$\sin\alpha_j \leq \| \sum_{n=0}^{r-1} \left(|\psi(s_j^n)\rangle - |\psi(s_j^{n+1})\rangle \right) \|$$

$$\leq \sum_{n=0}^{r-1} \left\| |\psi(s_j^n)\rangle - |\psi(s_j^{n+1})\rangle \right\| \, ,$$

where we used the triangle inequality. Also,

$$\sin\alpha_j \leq \lim_{r\to\infty} \sum_{n=0}^{r-1} \frac{\left\| |\psi(s_j^n)\rangle - |\psi(s_j^{n+1})\rangle \right\|}{s_j^{n+1} - s_j^n} \frac{n}{r}(s_j - s_{j-1})$$

$$\leq \int_{s_{j-1}}^{s_j} ds \, \| |\dot\psi\rangle \| \, , \tag{5.11}$$

since the phase of $|\psi\rangle$ can be chosen arbitrarily, we can assume that $\langle\dot\psi|\psi\rangle \in \mathbb{R}$, and thus $\langle\dot\psi|\psi\rangle = 0$ from the normalization condition. The derivatives of $|\psi\rangle$ are required so the inequality in Eq. (5.11) holds, which means the eigenpath is

differentiable. Since

$$\int_{s_{j-1}}^{s_j} ds \int_{s_{j-1}}^{s_j} ds \; \| \, |\partial_s \psi(s)\rangle \, \|^2 - \left(\int_{s_{j-1}}^{s_j} ds \; \| \, |\partial_s \psi(s)\rangle \, \| \right)^2 \geq 0$$

from the Cauchy-Schwarz inequality, we obtain the desired bound as

$$\sin \alpha_j \leq \left(\int_{s_{j-1}}^{s_j} ds \int_{s_{j-1}}^{s_j} ds \; \| \, |\dot\psi\rangle \, \|^2 \right)^{1/2} .$$

Then we have,

$$\sin^2(\alpha_j) \leq (s_j - s_{j-1}) \int_{s_{j-1}}^{s_j} ds \; \| \, |\dot\psi\rangle \, \|^2 \; , \tag{5.12}$$

for a differentiable path. By choosing a discretization $s_j = j \, \delta s$, where $\delta s \leq \varepsilon / \int_0^1 ds \| \partial_s \, |\psi(s)\rangle \, \|^2$, the infidelity can be bounded by ε:

$$\sum_{j=1}^{q} \sin^2(\alpha_j) \leq \varepsilon \; . \tag{5.13}$$

Using the main result of Sec. 5.2 the bounding of L and the expression of final infidelity (Eq. (5.12)), we can obtain a sufficient condition for the discretisation Eq. (5.13):

$$\delta s = \frac{\varepsilon}{(L^*)^2} \; .$$

Here we assume that $|\psi\rangle$ is the ground state of H. The total number of steps in the state preparation is then

$$q = \frac{1}{\delta s} = \frac{\int_0^1 ds \, \langle \psi | \, \ddot H - \ddot E \, | \psi \rangle}{(2\Delta)\varepsilon} \; , \tag{5.14}$$

which is proportional to $\max_s(1/\Delta)$. Overall, the average cost of the RM is of order $\max_s(1/\Delta^2)$ showing a better gap dependence than that in Ref. [107]. In the next section, we will show how the evolution randomisation can mimic projective measurements onto eigenstates and provide detailed error analysis.

5.3.2 Imperfect measurements

In the previous section, we discussed new results of error and discretisation with the assumption of perfect projective measurements of $|\psi\rangle$, which eliminates all coherences between $|\psi\rangle$ and its orthogonal complement. In the density matrix form of system ρ after the perfect measurement, $\langle\psi|\rho|\psi^\perp\rangle = 0$ for all other eigenstates $|\psi^\perp\rangle$. Ref. [107] shows how we can simulate projective measurements with the random evolution time t in a distribution where $t \in (-\infty, \infty)$. However, if t can only be nonnegative (or nonpositive), the coherences are only reduced by a multiplicative factor $0 < \varepsilon' < 1$ which means the simulated measurement isn't perfect or *weak*. In Ref. [107], the choice $\varepsilon' = \varepsilon/q$ achieves overall error ε in the preparation, which can be implemented by a sequence of unity-like quantum operations. The imperfect simulations of projective measurements introduce an additional factor in the cost of RM, which is of order $\log(q/\varepsilon)$ [Eq. (5.2)]. When $q \gg 1$, and $\Delta \ll 1$, the corresponding cost can be large. Nevertheless, here we present an improved error analysis of the RM and show that the final error of preparation can still be of order ε, when ε' from the imperfect measurements is a constant independent of ε. Then we obtain an improved cost for the RM where the $\log(q/\varepsilon)$ factor isn't necessary. In the following derivations to demonstrate the improved scaling, we define ρ_j as the density matrix at the j th step of the RM ($j = 0, 1, \ldots, q$) after the randomized evolution with $H(s_j)$. The density operator can be decomposed to four parts,

$$\rho_j = \Pr(j) |\psi(s_j)\rangle\langle\psi(s_j)| + (1 - \Pr(j))\rho_j^\perp + $$
$$ + |\xi_j\rangle\langle\psi(s_j)| + |\psi(s_j)\rangle\langle\xi_j| \ ,$$

where $\Pr(j) = \langle\psi(s_j)|\rho_j|\psi(s_j)\rangle$ is the probability (fidelity) of ρ_j in $|\psi(s_j)\rangle$. $\rho_j^\perp$ is a density matrix in the subspace of $\{|\psi(s_j)^\perp\rangle\langle\psi(s_j)^\perp|\}$, which means $\rho_j^\perp|\psi(s_j)\rangle = 0$. The (unnormalized) state $|\xi_j\rangle$ is in the subspace of $\{|\psi(s_j)^\perp\rangle\}$ and denotes the *coherences* between $|\psi(s_j)\rangle$ and its orthogonal space. The norm of $|\xi_j\rangle$ denotes a coherence factor:

$$c_j = \| |\xi_j\rangle \| \ .$$

In the case of projective measurements, $c_j = 0$ in each step. The main principle of the RM to achieve high fidelity is to simulate projective measurements by keeping c_j sufficiently small via randomised evolution.

At the $j + 1$ th step, we evolve with $H(s_{j+1})$ for a random time t from some distribution $f(t)$. Here we discuss the situation that distribution $f(t)$ is independent

of the time step. Then,

$$\rho_{j+1} = \int dt \ e^{-iH(s_{j+1})t}\rho_j e^{iH(s_{j+1})t} \ . \tag{5.15}$$

The evolution under $H(s_{j+1})$ leaves the eigenstate $|\psi(s_{j+1})\rangle$ invariant (up to a global phase). Then, we can derive the fidelity changes to

$$\begin{aligned} \Pr(j+1) &= \langle\psi(s_{j+1})|\,\rho_{j+1}\,|\psi(s_{j+1})\rangle \\ &= \langle\psi(s_{j+1})|\,\rho_j\,|\psi(s_{j+1})\rangle \ , \end{aligned}$$

with $|\psi(s_{j+1})\rangle = \cos\alpha_{j+1}|\psi(s_j)\rangle + \sin\alpha_{j+1}|\psi^\perp(s_j)\rangle$, as in Fig. 5.1. Then,

$$\Pr(j+1) \geq \cos^2\alpha_{j+1}\Pr(j) - 2\sin\alpha_{j+1}c_j \ . \tag{5.16}$$

Here, we assumed the worst case scenario for which $\langle\xi_j|\psi(s_{j+1})\rangle = -c_j\sin\alpha_{j+1}$ and $\alpha_{j+1} \in [0, \pi/2]$. The coherence factor at the $j+1$ th step can also calculated as

$$\begin{aligned} c_{j+1} &= \|\,|\xi_{j+1}\rangle\,\| \\ &= \|P_{j+1}^\perp \rho_{j+1}\,|\psi(s_{j+1})\rangle\,\| \\ &= \left\|P_{j+1}^\perp \int dt\ f(t) e^{-iH(s_{j+1})t}\rho_j e^{iH(s_{j+1})t}\,|\psi(s_{j+1})\rangle\right\| \ , \end{aligned}$$

where $f(t)$ is the PDF for the randomised evolution time at that step. Since $e^{iH(s_{j+1})t}$ leaves $|\psi(s_{j+1})\rangle$ invariant (up to a global phase) and

$$\int dt\ f(t) e^{-iH(s_{j+1})t}|\bar\psi^\perp(s_{j+1})\rangle\,\langle\psi^\perp(s_{j+1})|\,e^{iH(s_{j+1})t} \leq \varepsilon'|\bar\psi^\perp(s_{j+1})\rangle\,\langle\psi^\perp(s_{j+1})|$$

$$\int dt\ f(t) e^{-iH(s_{j+1})t}|\psi^\perp(s_{j+1})\rangle\,\langle\bar\psi^\perp(s_{j+1})|\,e^{iH(s_{j+1})t} \leq \varepsilon'|\psi^\perp(s_{j+1})\rangle\,\langle\bar\psi^\perp(s_{j+1})|$$

$$\tag{5.17}$$

for any unit state $|\bar\psi^\perp(s_{j+1})\rangle$ in the subspace of $\{|\psi^\perp(s_{j+1})\rangle\}$, we arrive at

$$c_{j+1} \leq \varepsilon'\|P_{j+1}^\perp\rho_j\,|\psi(s_{j+1})\rangle\,\| \ . \tag{5.18}$$

Here we introduce a factor $\varepsilon' < 1$ that denotes the magnitude of reduction in coherence after each time step, due to randomised time evolution. Taking one term in coherences as an example, the stochastic average of random time evolution under $H(s_{j+1})$ applied to ρ_j transforms the coherences $|\psi(s_{j+1})\rangle\langle\bar\psi(s_{j+1}^\perp)|$ to an

integral,

$$\int dt\, f(t) e^{-iH(s_{j+1})t} \, |\psi(s_{j+1})\rangle \, \langle \bar{\psi}(s_{j+1}^{\perp})| \, e^{iH(s_{j+1})t} \; ,$$

where $|\bar{\psi}(s_{j+1})^{\perp}\rangle$ is a normalized state orthogonal to $|\psi(s_{j+1})\rangle$. Then, we can define an upper bound of such multiplicative factor,

$$\varepsilon' = \left\| \int dt\, f(t) e^{i\Delta t} \right\| \; . \tag{5.19}$$

where $\Delta \leq \Delta(s_{j+1})$ and it is straight-forward to show that $\varepsilon' < 1$ that gives the results in Eq.(5.17).

The next target is to bound the right hand side of Eq. (5.18). Using the definition of the 'angles' α_{j+1}, and substitute $|\psi(s_{j+1})\rangle = \cos\alpha_{j+1}\,|\psi(s_j)\rangle + \sin\alpha_{j+1}\,|\psi^{\perp}(s_j)\rangle$, then obtain

$$c_{j+1} \leq \varepsilon' \left[\cos\alpha_{j+1} \| P_{j+1}^{\perp} \left(\Pr(j)\,|\psi(s_j)\rangle + |\xi_j\rangle \right) \| + \right. $$
$$\left. + \sin\alpha_{j+1} \| P_{j+1}^{\perp} \rho_j\, |\psi^{\perp}(s_j)\rangle \| \right] \; ,$$

here we used the triangle inequality and $\rho_j\,|\psi(s_j)\rangle = \Pr(j)\,|\psi(s_j)\rangle + |\xi_j\rangle$. Also, $\| P_{j+1}^{\perp}\,|\psi(s_j)\rangle \| = \| \, |\psi(s_j)\rangle - \cos\alpha_{j+1}\,|\psi(s_{j+1})\rangle \| = \sin\alpha_{j+1}$, and

$$\rho_j\,|\psi^{\perp}(s_j)\rangle = $$
$$= (1 - \Pr(j))\rho_j^{\perp}\,|\psi^{\perp}(s_j)\rangle + |\psi(s_j)\rangle\langle\xi_j|\,\psi^{\perp}(s_j)\rangle \; .$$

By using the Cauchy-Schwarz inequality, we obtain

$$c_{j+1} \leq \varepsilon' \left[\cos\alpha_{j+1}\Pr(j)\sin\alpha_{j+1} + \cos\alpha_{j+1}c_j + \right. $$
$$\left. + \sin\alpha_{j+1}(1 - \Pr(j)) + \sin^2(\alpha_{j+1})c_j \right] \; ,$$

and reach the recursion formula for coherences

$$c_{j+1} \leq \varepsilon' \left[\sin\alpha_{j+1} + (1 + \sin^2(\alpha_{j+1}))c_j \right] \; . \tag{5.20}$$

In the beginning of the time evolution, the initial state is exactly $\rho_0 = |\psi(s_0)\rangle\,\langle\psi(s_0)|$, thus $c_0 = 0$ and, by iteration of Eq. (5.20), we have

$$c_{j+1} \leq \varepsilon' \sin\alpha_{j+1} + (\varepsilon')^2(1 + \sin^2(\alpha_{j+1}))\sin\alpha_j + \dots$$
$$\dots + (\varepsilon')^{j+1}(1 + \sin^2(\alpha_{j+1}))\dots(1 + \sin^2(\alpha_2))\sin\alpha_1 \; .$$

To establish the relation between ε' and the error ε coming from discretisation in case of perfect measurements, we recall the condition

$$\sum_{j=1}^{q} \sin^2(\alpha_j) \leq \varepsilon$$

of Eq. (5.13). Then,

$$\prod_{j>1}^{q}(1 + \sin^2(\alpha_j)) \leq \prod_{j=1}^{q}(1 + \sin^2(\alpha_j))$$

$$\leq 1 + \sum_{j=1}^{q} \sin^2(\alpha_j) + \left(\sum_{j=1}^{q} \sin^2(\alpha_j)\right)^2 + \dots$$

$$\leq \sum_{j\geq0}^{q} \varepsilon^j \leq 1/(1-\varepsilon) \,.$$

By bounding the prefactor in each term in previous formula, we can obtain the desired bound of coherences,

$$c_j \leq \frac{1}{1-\varepsilon}(\varepsilon' \sin \alpha_j + \varepsilon'^2 \sin \alpha_{j-1} + \dots + \varepsilon'^j \sin \alpha_1) \,. \tag{5.21}$$

As mentioned before, the whole process of the RM starts with $|\psi(s_0)\rangle$, so initially the fidelity $\Pr(0) = 1$ and coherence $c_0 = 0$. By iteration of Eq. (5.16) we obtain a bound of final fidelity

$$\Pr(q) \geq \prod_{j=1}^{q} \cos^2(\alpha_j) - 2\sum_{j=1}^{q} \sin \alpha_j c_{j-1} \,. \tag{5.22}$$

The first term on the right-hand-side of Eq. (5.22) represents the error in the case where all projective measurements are implemented perfectly, i.e., when $c_j = 0$ for all j. This term can be bounded from below by $1 - \sum_{j=1}^{q} \sin^2(\alpha_j) \geq 1 - \varepsilon$, as described in Sec. 5.3.1. The second term represents the imperfect implementation of projective measurements, which can be also bounded by using Eq. (5.21),

$$\frac{2}{1-\varepsilon}\sum_{j=1}^{q} \sin \alpha_j \left(\varepsilon' \sin \alpha_{j-1} + \varepsilon'^2 \sin \alpha_{j-2} + \dots\right), \tag{5.23}$$

and using the definitions of $\alpha_k \in [0, \pi/2]$ and $(\sin \alpha_j - \sin \alpha_{j-k})^2 \geq 0$,

$$\sum_{j=1}^{q} \sin \alpha_j \sin \alpha_{j-k} \leq \sum_{j=1}^{q} \sin^2(\alpha_j) \leq \varepsilon .$$

we can bound the fidelity of the RM in the state preparation after total q steps,

$$\Pr(q) \geq 1 - \varepsilon - \frac{2\varepsilon\varepsilon'}{(1-\varepsilon)(1-\varepsilon')} . \tag{5.24}$$

The factor ε' demonstrate how well the randomisation evolution simulates the projective measurements, and the case when $\varepsilon' = 0$ agrees with the perfect measurement scenario.

5.3.3 Total cost

Based on the bound of the final fidelity in Eq. (5.24), we can choose a constant ε' to achieve the desired error or infidelity which is of the order of ε. For example, the PDF of randomised time steps can be a normal distribution $f(t)$ with standard deviation of order $1/\Delta$. Then, the Fourier transform of $f(t)$, which is a normal distribution with standard deviation of order Δ, implies a constant upper bound ε' (Eq. (5.19)). In this case, the average cost per step of the RM is of order $1/\Delta$. Multiplying the average cost per step by the total number of steps in Eq. (5.14), an upper bound of the total average cost of the RM can be reached,

$$\frac{(L^*)^2}{\varepsilon\Delta} \leq \kappa' \max_s \frac{\|\ddot{H}\| + 2\|\dot{H}\|}{\varepsilon 2\Delta^2(s)} , \tag{5.25}$$

for general interpolations (Sec. 5.2.1). The prefactor $\kappa' \approx \sqrt{2/\pi}$ is also constant [107]. For specific Hamiltonians or interpolations, such an upper bound can be further improved as in Secs. 5.2.2 and 5.2.3. Previous research provides an upper bound of the cost, which is on the order of $\max_s[\log(1/\Delta)/\Delta^3]$ in Ref. [107]. In terms of the gap dependence, our result in Eq. (5.25) is significantly improved.

5.4 Applications

Our method can apply to many problems in physics, optimization, and quantum information, and new improved bounds for eigenpath traversal will help to

demonstrate quantum speedups in many cases. In this section, we take two important examples to demonstrate polynomial quantum speedups by applying our method.

5.4.1 Preparation of projected entangled pair states

Projected entangled pair states (PEPS), a computational variational state that generalise matrix product states to higher spatial dimensions, can be interpreted as pairs of maximally entangled states which are supported in subspaces of projected auxiliary systems [80, 82, 159, 160]. The extensions from one-dimensional MPS to PEPS lead to many applications, like variational methods for finding the ground state of spin systems. This feature of PEPS can be applied to solving combinatorial optimization and quantum information problems, and ground state preparation is essential for such problems. With the interest in PEPS, recent techniques have been proposed for the preparation of exact PEPS on a quantum computer [137, 158]. In terms of the preparation of PEPS, the key property is that they can be realised as the ground states of a certain configurations of frustration-free Hamiltonians. Having the improved bound of the RM obtained previously, we can analyse the cost of PEPS preparation. Here we assume a frustration-free Hamiltonian path as $H(s) = \sum_{k=1}^{L} \Pi_k(s)$ and the ground state $|\psi\rangle$ with corresponding eigenvalue 0. Applying the results of Sec. 5.2.3 we obtain a cost for the RM upper bounded by

$$T_{RM} \leq \max_s \frac{L\|\ddot{H}\|}{2\varepsilon\Delta} \ .$$

This cost of the RM can be improved further by the spectral gap amplification technique [158] constructing the related Hamiltonian

$$H' = \sqrt{\|\Pi\|} \sum_{k=1}^{L} \sqrt{\Pi_k} \otimes [|k\rangle \langle 0| + |0\rangle \langle k|] \ ,$$

where we introduce an ancillary system and $|k\rangle$, $k = 0, 1, \ldots L$ specifies an orthonormal basis of this ancillary system. H' then has $|\psi\rangle \otimes |0\rangle$ as the ground state, the spectral gap Δ' has a lower bound on the order of the square root of that of, $\Delta' \geq \sqrt{\Delta\|\Pi\|}$, where $\|\Pi\| = \max_k \|\Pi_k\|$. We refer to Ref. [158] for detailed analysis of the full spectrum and properties of H'. Then when we have the access to $\sqrt{\Pi_k}$, we can apply the randomised time evolution of the RM using H' instead. In each step, the average time cost is of order $1/\Delta' \propto 1/\sqrt{\Delta\|\Pi\|}$,

which results in an overall time cost upper bounded by,

$$\kappa' \max_s \frac{\|\dddot{H}\|}{2\varepsilon\|\Pi\|^{1/2}} \times \frac{1}{\Delta^{3/2}} . \tag{5.26}$$

By applying the same technique, an improved bound on the cost in comparison with other eigenpath traversal methods [108] can be achieved

$$\kappa' \max_s \frac{\sqrt{\|\ddot{H}\|/2} \times \log(\sqrt{\|\ddot{H}/(2\Delta)}/\varepsilon)}{\varepsilon\|\Pi\|^{1/2}} \times \frac{1}{\Delta} . \tag{5.27}$$

This bound (5.27) is derived from Eq. (5.2) in the case of $c = 1$, replacing Δ by Δ' and L by L^* as in Eq. (5.9). This bound of the cost is proportional to the inverse of the gap $T \propto 1/\Delta$, which is known as the quantum metrology limit. On the other hand, the requirement of the access to $\sqrt{\Pi_k}$ can be satisfied for many frustration-free Hamiltonians, for example, when the terms Π_k are projectors and $\sqrt{\Pi_k} = \Pi_k$.

5.4.2   Quantum simulated annealing

Combinatorial optimisation problems is a topic consisting of finding an optimal configuration from a finite set. Simulated annealing (SA), a probabilistic method for approximating the global optimum with a given objective function, is usually applied to solve such problems. In practice, SA is implemented via Markov-Chain Monte Carlo techniques. For example, to find the global minimum of a given objective function E, SA generates a stochastic sequence of configurations σ at each step. During the annealing process, the probability of a system being in the configuration σ with the given function E, at inverse temperature β_i satisfies the Boltzmann distribution.

$$P_\sigma = \frac{1}{\mathcal{Z}} e^{-\beta_i E[\sigma]} \tag{5.28}$$

Then apply random perturbation to the configuration and generate σ'. If $E[\sigma'] < E[\sigma]$, then the configuration is updated to σ', otherwise, accept the new configuration with probability $P = \exp(-\beta_i(E[\sigma'] - E[\sigma]))$. After the number of updates satisfies a criterion, the inverse temperature increases to β_{i+1}. As the end of the evolution, the configurations converge to the Gibbs distribution determined by the inverse temperature β_q, where q is the total number of time steps, and the objective function is E. In the limit of $\beta_q \gg 1$, the final sequences are sampled from the Gibbs distribution that is dominated by the configuration σ that minimises the function E [161]. The annealing process is specified by the annealing

schedule of inverse temperature $\beta_0 = 0 < \beta_1 < \ldots < \beta_q$, where q is a finite constant determining the cost of the method. An upper bound of this number is $\mathcal{O}(\max_\beta 1/\Delta(\beta))$, where $\Delta(\beta)$ is the spectral gap of the stochastic matrix. A recent proposed quantum algorithm [109] provides an approach to sample from the same Gibbs distribution, using the RM to traverse a path of states $|\psi(\beta)\rangle$. The quantum state $|\psi(\beta)\rangle$ contains the information of the corresponding Gibbs state that encodes the amplitudes with the probabilities. It is defined as

$$|\psi(\beta)\rangle = \frac{1}{\sqrt{\mathcal{Z}}} \sum_{\{\sigma\}} e^{-\beta E[\sigma]/2} |\sigma\rangle \ , \tag{5.29}$$

where $\mathcal{Z} = \sum_{\{\sigma\}} \exp(-\beta E[\sigma])$ is the partition function, the $|\sigma\rangle$ is the quantum state represents the configuration σ and forms an orthonormal basis $\{|\sigma\rangle\}$.

In previous research [109], the time cost of the quantum algorithm was of the order of

$$\max_\beta q \log q / \sqrt{\Delta(\beta)} \tag{5.30}$$

with $q = \beta_q^2 E_M^2/(4\varepsilon)$ and E_M is the maximum of absolute value of $E[\sigma]$. ε represents the overall error (in the probability that the configuration does not minimize E) and q is the number of points in the discretization of annealing schedule. Previously, a bound of the value of q was related to the eigenpath length L, defined $L = \int_0^{\beta_q} d\beta \| |\partial_\beta \psi(\beta)\rangle \|$, $q \geq L^2/\varepsilon$. Comparing the results from Ref. [109], the bound of the cost (5.30) has a square root improvement over the classical method ($\mathcal{O}(\max_\beta 1/\Delta(\beta))$) in terms of the spectral gap $\Delta(\beta)$. In the cases where $\Delta(\beta)$ is small, the advantages of the improved bound will be considerable.

Furthermore, we can apply our new results for the discretisation schedule and eigenpath length in Sec. 5.3 to reach a better bound on the cost of the RM for this problem. From the Eq. (5.14), we could write the formula of the number of steps of the RM, q^*, by changing variables $ds = d\beta/\beta_q$. That is,

$$q^* = \frac{\beta_q}{\varepsilon} \int_0^{\beta_q} d\beta \| |\partial_\beta \psi(\beta)\rangle \|^2 \ . \tag{5.31}$$

For a constant probability error ε, β_q is proportional to the value of $\log(1/\varepsilon)/\gamma$, where γ is the minimal gap of the range of E.

The eigenpath in QSA is determined by the definition of the quantum state $|\psi(\beta)\rangle$ (5.29). The differential of the quantum state with respect of β is

$$|\partial_\beta \psi(\beta)\rangle = \frac{1}{2}\left[\langle E\rangle |\psi(\beta)\rangle - \frac{1}{\sqrt{\mathcal{Z}}}\sum_\sigma E[\sigma]e^{-\beta E[\sigma]/2}|\sigma\rangle\right] , \qquad (5.32)$$

where

$$\langle E\rangle = \frac{1}{\mathcal{Z}}\sum_\sigma E[\sigma]e^{-\beta E[\sigma]}$$

is the ensemble average for the energy E at inverse temperature β. Because $\{|\sigma\rangle\}$ is an orthonormal basis, Eq. (5.32) can be written as

$$\| |\partial_\beta \psi(\beta)\rangle \|^2 = \frac{1}{4}\sum_\sigma(\langle E\rangle - E[\sigma])^2 \times \frac{e^{-\beta E[\sigma]}}{\mathcal{Z}}$$

$$= \frac{1}{4}\left(\langle E^2\rangle - \langle E\rangle^2\right) ,$$

This equation connects the rate of change of the state with the thermodynamic fluctuations of E. On the other hand, the differential of the ensemble average of the energy function is also related to the fluctuations,

$$\partial_\beta\langle E\rangle = \partial_\beta\frac{1}{\mathcal{Z}}\sum_\sigma E[\sigma]e^{-\beta E[\sigma]}$$

$$= \frac{-\partial_\beta\mathcal{Z}}{\mathcal{Z}^2}\sum_\sigma E[\sigma]e^{-\beta E[\sigma]} - \frac{1}{\mathcal{Z}}\sum_\sigma E^2[\sigma]e^{-\beta E[\sigma]}$$

$$= \langle E\rangle^2 - \langle E^2\rangle ,$$

and therefore, the changing rate of the quantum state is

$$\| |\partial_\beta \psi(\beta)\rangle \|^2 = -\frac{\partial_\beta\langle E\rangle}{4} . \qquad (5.33)$$

This result of Eq. (5.33) provides the new bound of the number of steps needed in the RM. Substitute Eq. (5.33) into the integral of Eq. (5.31), we obtain

$$q^* = \frac{\beta_q(\langle E\rangle_0 - \langle E\rangle_{\beta_q})}{4\varepsilon} .$$

In addition, we shift the value of E to satisfy $\langle E\rangle_0 = 0$. In many cases, for instance, where E describes a Ising mode this condition is already satisfied. In the limit of $\beta_q \gg 1$, the ensemble average value of the given function converges

to the minimal value, $\langle E \rangle_{\beta_q} \approx -E_M$ and the total number of steps becomes

$$q^* \leq \frac{\beta_q E_M}{4\varepsilon} \ .$$

To sum up, our improved average cost of the RM for the QSA problem is

$$T_{\text{QSA}} = \kappa' \max_\beta \frac{\beta_q E_M}{4\varepsilon \sqrt{\Delta(\beta)}} \tag{5.34}$$

where κ' is a small constant. The new results for the cost of our algorithm (5.34) demonstrate a better performance compared with the previous cost given by Eq. (5.30), which is of order

$$\max_\beta \frac{\beta_q^2 E_M^2 \log(\beta_q^2 E_M^2 / \varepsilon)}{\varepsilon \sqrt{\Delta(\beta)}}$$

in the large E_M and β_q limit.

In this section, we demonstrated two applications of the randomisation method with the improved bound on the cost and the discretisation, and compared our new results to previous research.

5.5 Conclusions

In this chapter, we presented an improved upper bound for the length L of the eigenpath traversed by the changing eigenstates of time-dependent Hamiltonians. The new bound is of the order of the square root of that in previous research. It results in an overall improvement of the average cost of adiabatic state transformations with randomised time evolutions. The average cost of the randomisation method is of the order of $1/\Delta^2$, which shows a significant speed up or improved bound compared with conventional AQC, which has the cost upper bounded by a value of the order of $1/\Delta^3$. In the cases of frustration-free systems, the average cost of the randomisation method can be further improved to the order of $1/\Delta^{3/2}$, by applying the spectral gap amplification technique. The minimal spectral gap Δ throughout the adiabatic state transformation can be very small, thus the randomisation method provides an alternative to improve the transformation with proven lower cost.

We also conducted a detailed error analysis of the randomisation method on the two cases of perfect simulated measurements and imperfect measurements. The result of a lower bound of the final fidelity has a correction term when imperfect

measurements are performed, and this correction term is proved to be of the same order as the error with perfect measurements with a reasonable prefactor. So we proved that the randomised evolution can perform weak measurements with a constant multiplicative factor, and result in a reasonable final fidelity of state preparation with bounded error. This is improved from the requirement that the reduction on coherences shall depend on the eigenpath length in previous research, and eliminates the logarithm term in the average cost.

Although we compare upper bounds of the randomisation method and the adiabatic quantum computing method in terms of the gap dependence, it still remains open to show how generic the advantages are. For example, in the case that the AQC as a cost in the order of $1/\Delta^3$, then the randomisation method has a clear advantage. Compared to the cost of quantum adiabatic approximations, we provide a eigenpath traversal method that performs at a lower cost in terms of the gap, which is hard to improve in previous methods [149, 150, 162, 163], .

Another contribution we made, is that the improved bound on the eigenpath length can be applied to other eigenpath traversal methods such as that in Ref. [108], and obtain a lower cost. We demonstrated an example that our bound on the eigenpath length provides a cost in the order of $1/\Delta^{3/2}$ in general and if the system can be described by frustration-free Hamiltonians, the cost is in the order of $1/\Delta$.

Chapter 6

Adiabatic state preparation in the presence of classical noise

An important challenge for experiments with ultra-cold atoms is the preparation of low-temperature many-body states which are sensitive to the temperature and the environment. One possible route is via the technique of adiabatic state preparation. However, the influence of classical noise in these adiabatic dynamics remains unclear. At the same time, the adiabatic condition as shown in Eq. (2.38) implies that adiabatic state preparation requires long timescales to satisfy the adiabatic approximation. It is therefore very important to find the optimal regimes for adiabatic state preparation.

In this chapter, we adapt the idea of the recently proposed eigenpath traversal method, the randomisation method [69] to the context of adiabatic state preparation in the presence of classical noise. The randomised time evolution mentioned in Ref. [69] can be described as an adiabatic state transformation under a time-dependent noisy Hamiltonian where the noise term is proportional to the original Hamiltonian. Recent research [121] proposed a dressed lattice scheme that can engineer the amplitude noise of optical lattices to realise such noise. We demonstrate that by introducing proper noise we can improve the final fidelity of the state preparation, especially when the evolution time is limited, taking the examples of the one-dimensional Bose-Hubbard model with ramps from the Mott insulator phase to the superfluid phase and also comparing this to an analytical study of a two-level system. We also consider the cases when the noise is not perfectly implemented and show the robustness of state preparation to imperfect noise, and characterising the resulting heating and dephasing for many-body states. We compute the corresponding dynamics using the stochastic many-body Schrödinger equation and master equation approaches as introduced in Chap. 4.

6.1   Introduction

The essence of the randomisation method from Chapter 5 is to simulate projective measurements in each time step onto an instantaneous eigenbasis through dephasing. During the time evolution, the time step is $\delta t(1+x)$ where x is a random variable of a certain probability distribution function (PDF) $f(x)$ with finite variance, such as a Gaussian distribution. At the time t_i, the equation of motion can be written as

$$|\psi(t_i)\rangle = \exp[-iH(t_i)\delta t(1+x)]\,|\psi(t_i - \delta t)\rangle \ . \tag{6.1}$$

If the system cannot evolve back in time, then $1 + x > 0$ should be considered when choosing $f(x)$. Then we can calculate the average effect on the system as reductions in off-diagonal elements of the density matrix in the basis of Hamiltonian eigenstates, applying a multiplicative factor less than 1 to these elements. Representing the evolving quantum state in the eigenbasis $\{\phi_j(t_i)\}$ of the instantaneous Hamiltonian $H(t_i)$, $\psi(t_i - \delta t) = \sum_j c_j \phi_j(t_i)$, the average state of the system after the randomised time evolution is

$$\rho(t_i) = \sum_{jk} \eta_{jk} c_j c_k^* \,|\phi_j(t_i)\rangle\,\langle\phi_k(t_i)|\, e^{i\Delta_{jk}\delta t} \ , \tag{6.2}$$

where $\Delta_{jk}(t_i)$ is the energy difference between the kth and jth eigenstates, and $\Delta_{jk}(t_i) = E_k(t_i) - E_j(t_i)$. The multiplicative factor η_{jk} is defined as $\eta_{jk} = \int dx\, f(x)\exp(i\Delta_{jk}x\delta t)$ which is the Fourier transform of probability distribution function $f(x)$. For instance, when the PDF of $x(t)$ is Gaussian with a standard deviation σ, $f(x) = (2\sigma^2\pi)^{-1/2}\exp(-x^2/\sigma^2)$, the multiplicative factor applied on the off-diagonal terms is $\eta_{jk} = \exp(-\Delta_{jk}^2\delta t^2\sigma^2/4) < 1$ and for the diagonal terms, $\eta_{jj} = 1$. By calibrating the probability distribution function carefully, the multiplicative factor of off-diagonal elements in instantaneous eigenbasis can be close to zero, and the diagonal terms remain invariant. These average effects can be interpreted as simulating projective measurements onto the instantaneous eigenbasis. By applying repeated projective measurements, the coherent process of exciting the system to higher energy states is inhibited.

Although the results in Chapter 5 for the upper bounds of time cost show a speed-up over conventional adiabatic state transformations in terms of the gap dependence, the advantages of having randomised time evolution in adiabatic state preparation have not yet been clearly demonstrated for specific example problems.

This inspires us to develop an interpretation of an adiabatic process with classical noise in the system to realise the idea of the randomisation method. With classical

noise involved in the system of interest, the total Hamiltonian consists of two components, $H_{sys} = H_0 + A\xi(t)$, where H_0 is the originally designed Hamiltonian and A is a hermitian operator. Here we characterise the classical noise as a white noise, and $\xi(t)$ is the Wiener increment, with the correlation function $\langle \xi(t)\xi(t') \rangle = \delta(t - t')$. The relation between the randomisation method and the adiabatic state preparation in the presence of classical noise can be established when the classical noise is proportional to the original Hamiltonian up to a constant α, $A = \alpha H_0$. Thus, the noisy Hamiltonian is $H_{sys} = H_0 + \alpha H_0 \xi(t) = H_0(1 + \alpha\xi(t))$. The equation of motion of the adiabatic process then becomes a stochastic Schrödinger equation, $d\,|\psi(t)\rangle\,/dt = -iH_0(1 + \alpha\xi(t))\,|\psi(t)\rangle$, and it is analogous to the randomisation method replacing $x \to \alpha\xi(t)$. This transformation provides an alternative way to realise the randomisation method, and suggests the possibility to enhance adiabatic state preparation by adding noise.

In the next sections, we present numerical simulation results for a Bose-Hubbard model with amplitude noise, showing that the tailored noise can improve the final fidelity in adiabatic state preparation. We also conduct simulations with imperfect implementation of the noise, and observe robust behaviours of the final fidelity. To understand the behaviour of the fidelity for noise not proportional to the Hamiltonian, we conduct analytical calculations in general and for the Bose-Hubbard model. From the study of similar behaviours of fidelities of the adiabatic process in two-level systems, we are able to understate how classical noise affects the adiabatic process in more detail.

6.2   Bose-Hubbard model with noise proportional to the Hamiltonian

In this section, we take the Bose-Hubbard model with the noise proportional to the original Hamiltonian as an example and present numerical results that show improvement of the final fidelity in preparing the ground state in the superfluid phase. The simulations are conducted for both small systems with varying evolution time and noise strength, and for large systems with limited evolution time. The simulations are based on the stochastic Schrödinger equation evolution and density matrix renormalisation group methods.

In the experimental set-up of optical lattices, the fluctuation of laser intensity is inevitable, and such fluctuations can result in a global amplitude noise in lattice depth. The corresponding optical lattice potential $V(x) = V_0(x) + \delta V(x, t)$ then fluctuates around the designed value $V_0(x)$. Depending on the individual experimental set-up, the spectrum of the noise will lead to different heating processes.

Dealing with noise with frequencies of the order of the Bloch band separation will cause inter-band transitions. For the cases that noise with frequencies of the order of the hopping amplitude J and the interaction coefficient U, intra-band heating will dominate the dynamics. For small fluctuations, we are able to approximate the Hamiltonian of the first order expansion with respect to the fluctuation and derive the formulae for the coefficients, for instance, the hopping coefficient $J(V(t)) \approx J_0(V_0) + \frac{dJ}{dV}\delta V(t)$. The Hamiltonian with amplitude noise in the system can be expressed as the following:

$$H_{BH}(J, U) = -J\sum_{\langle i,j \rangle} b_i^\dagger b_j + \frac{U}{2}\sum_i n_i(n_i - 1) \,, \tag{6.3}$$

$$H_{sys} = H_{BH}(J_0 + \frac{dJ}{dV}\delta V, U_0 + \frac{dU}{dV}\delta V) \,, \tag{6.4}$$

$$= H_0 + H_1 \delta V(t) \,. \tag{6.5}$$

where $H_0 = H_{BH}(J_0, U_0)$ denotes the designed Hamiltonian and $H_1 = H_{BH}(\frac{dJ}{dV}, \frac{dU}{dV})$ denotes the noise operator. During the adiabatic state transformation, we assume that the fast fluctuation approximation holds in the white noise limit. The correlation function of the white noise is then $\langle \delta V(t)\delta V(t')\rangle = 2\Gamma\delta(t - t')$, where 2Γ is the spectral power of amplitude noise. In the situation that the noise is proportional to the original Hamiltonian, the time-dependent system Hamiltonian can be expressed as,

$$H_{sys}(t) = H_0(t) + H_0(t)\sqrt{2\Gamma}\xi(t) \,, \tag{6.6}$$

where Γ can be considered as the strength of the white noise. In the presence of noise proportional to the original Hamiltonian, the Schrödinger equation becomes a multiplicative stochastic differential equation (MSDE) and the stochastic average of the dynamics is a mixed state. From the analytical calculation of Sec. 4.2, the equation of motion for the averaged density operator, $\rho(t)$ takes the Lindblad form of the master equation:

$$\frac{d|\psi(t)\rangle}{dt} = -iH_0(t)(1 + \sqrt{2\Gamma}\xi(t))|\psi(t)\rangle \,, \tag{6.7}$$

$$\dot{\rho}(t) = -i[H_0(t), \rho(t)] - \Gamma[H_0(t), [H_0(t), \rho(t)]] \,. \tag{6.8}$$

Taking the noisy Bose-Hubbard model as an example, we simulate the adiabatic state preparation of the ground state of the superfluid (SF) phase ($U_0/J_0 = 2$), from the Mott insulator (MI) phase ($U_0/J_0 = 10$). The ramping of the interactive parameter is linear $g(t) \equiv U_0(t)/J_0 = 10 - 8t/T$ where T is the total evolution time. The particle number is conserved throughout the adiabatic process and has the same value as the number of sites. In the beginning, the system is in the

ground state of the MI phase $|\phi_{MI}\rangle$ such that particles tend to be localised on each site, then we drive the system under the stochastic Schrödinger equation via sampling the random number from a normal distribution where the variance is the size of time step dt to represent $\xi(t)dt$. After one sequence of time evolution, we calculate the fidelity F between the system and the ground state of the superfluid phase $|\phi_{SF}\rangle$, $F = |\langle\psi(T)|\phi_{SF}\rangle|^2$. We repeat this calculation to obtain the average of final fidelities and stochastic errors.

First we simulate the dynamics of a small system with 8 particles and 8 sites, when the ground states in the MI phase and the SF phase can be calculated via exact diagonalisation. The numerical simulations include variations of the evolution time and the noise strength, and the behaviour of the fidelities is shown in Fig.6.1. The results of the adiabatic state preparation without the noise is plotted on the left edge with different TJ_0 for comparison. From there, we note that achieving a better fidelity requires longer ramping time for the adiabatic condition to be satisfied. When the ramping time is limited, non-adiabaticity dominates the process and the final fidelity of state preparation is reduced. The near edge of the plot shows the fidelity behaviour when the evolution time is limited $(TJ_0 = 1)$. It can be clearly observed that when adding noise proportional to the original Hamiltonian, the noisy processes outperform the conventional adiabatic state preparation. As we increase the strength of the noise, the corresponding fidelity grows as well. From the direct relation to the randomisation method, the strength of the noise proportional to the Hamiltonian is related to the variance of the PDF of the random variable. Therefore, increasing the noise strength enhances simulated projective measurements onto the instantaneous eigenbasis, and results in the quantum Zeno effect that suppress coherent processes due to non-adiabaticity.

As the system size grows, the minimum gap of the Hamiltonian (at least near the critical point) usually decreases algebraically. To achieve a high fidelity of state preparation, it consumes considerable time to satisfy the adiabatic theorem. In practice, the enormous time cost is problematic to experiments due to the limited coherence time of a complex system. We continue our numerical simulation with a larger system of the Bose-Hubbard model of 16 particles and 16 sites, to prepare the ground state of the superfluid phase $(U_0/J_0 = 2)$, from the ground state of the Mott insulator $(U_0/J_0 = 10)$. The ramping of the interactive parameter g is linear in time and has the same form of the small scale simulation. We obtain the ground states of the superfluid phase and the Mott insulator phase via imaginary time evolution using TEBD methods. The time evolutions of the quantum state, which is in the form of a matrix product state, are repeated 100 times to obtain average fidelities and stochastic errors. Fig. 6.2 shows our results for limited time evolution $TJ_0 = 1$. Again, introducing certain noise helps to prepare the target state. As the ramping time is limited, the noise-free case achieves a poor fidelity
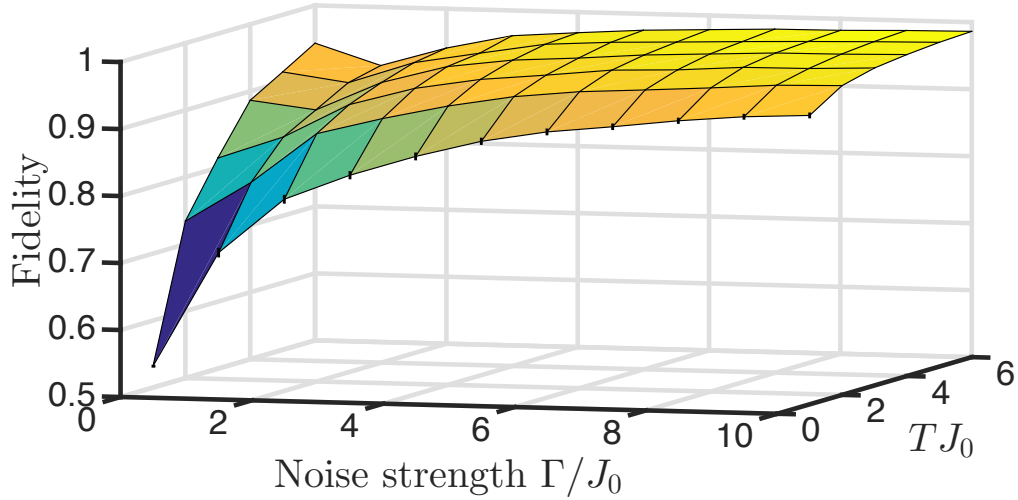
FIGURE 6.1: Final fidelites of adiabatic state preparations, obtained from exact diagonalisation calculations of the Bose-Hubbard model of 8 particles and 8 sites. Data points are averaged values over 100 runs, $dt = 10^{-3}$, and statistical error bars are shown only on the near edge. This plot shows the fidelities of adiabatic state preparation under different ramp times (TJ_0) and noise strengths (Γ/J_0). The initial state is the ground state of the Mott insulator phase $(U_0/J_0 = 10)$, and evolves under the noisy Hamiltonian with the time-dependent parameter $g(t) \equiv U_0(t)/J_0 = 10 - 8t/T$. The fidelity F is between the evolved state $|\psi(T)\rangle$ after time T and the ground state of superfluid phase $(U_0/J_0 = 2)$ $|\phi_{SF}\rangle$, $F = |\langle\psi(T)|\phi_{SF}\rangle|^2$. The left edge of this plot where $\Gamma = 0$ shows the noise-free cases, and it demonstrates how the fidelites change along with increasing evolution time. In the limited ramp time regime, for example $TJ_0 = 1$, the adiabatic condition is not fulfilled throughout the adiabatic process and that results in a poor final fidelity at the end of the ramping. The near edge of this plot shows that in the limited time regime, introducing noise proportional to the original Hamiltnonian induces the quantum Zeno effect which enhances adiabaticity. This results in an improvement of final fidelities that normally requires longer ramping time in noise-free situations. In the situation that ramping time is long (shown at the back of the plot), the behaviour of the fidelity requires more discussions.

$F \approx 0.19$. However, with the help of noise proportional to the Hamiltonian, the final fidelity increases as the noise gets stronger.

Our numerical simulation results for the noisy adiabatic state preparation of the small system and the large system of the Bose-Hubbard model show that introducing certain noise will improve the fidelities in certain regimes, especially when the ramping time is limited. The classical noise proportional to the original
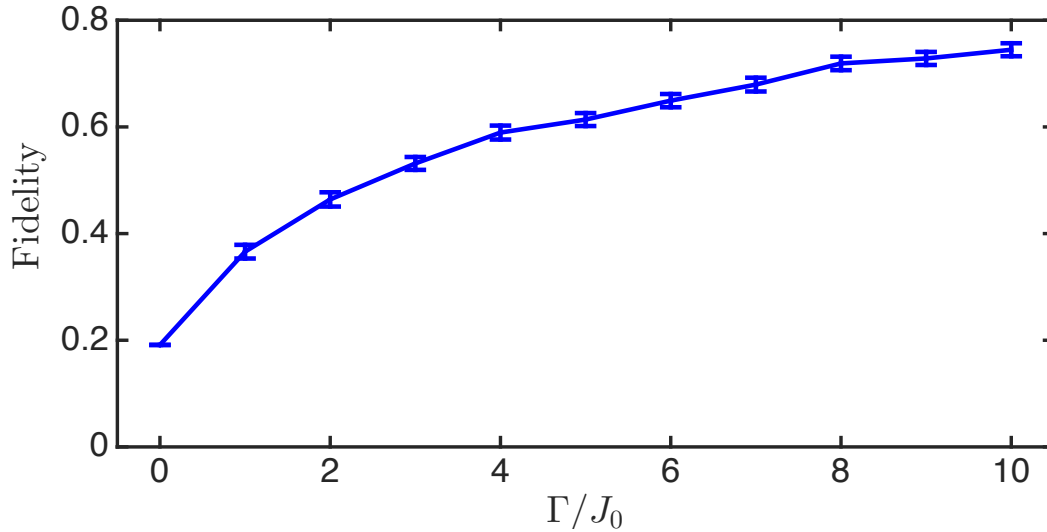
FIGURE 6.2: Final fidelities of adiabatic state preparation, obtained from DMRG calculations of the Bose Hubbard model of 16 particles and 16 sites. This plot shows the fidelities of adiabatic state preparations under the same ramping time $TJ_0 = 1$ with different noise strengths. The initial state is the ground state of Mott insulator ($U_0/J_0 = 10$), and the final fidelity is compared with the ground state of superfluid phase ($U_0/J_0 = 2$). The data point is averaged over 100 repetitions, and the convergency of the time step $dt = 10^{-5}$ and the bond dimension $D = 128$ have been checked. When the ramping time is limited ($TJ_0 = 1$), the fidelity of the noise-free case ($\Gamma = 0$) is less than 0.20, and the non-adiabaticity is predominant in the process. By introducing the noise proportional to the original Hamiltonian, we can observe an improvement of fidelities shown as the points with error bars. As the noise strength grows, the quantum channel effectively performs better simulation of projective measurements onto instantaneous eigenbasis throughout the adiabatic ramping, thus performing the quantum Zeno effect to enhance adiabaticity.

Hamiltonian introduced to the system can perform average effects simulating projective measurements onto the instantaneous eigenbasis. This behaviour induces a quantum Zeno effect and suppresses non-adiabaticity caused by the limited ramping time. Taking an example of the adiabatic state preparation in the Bose-Hubbard model with amplitude noise, we demonstrated how final fidelities can be enhanced especially in the limited ramping time regime. Although certain constraints on the noise should be satisfied to achieve such improvements, we will show how to engineer the noise proportional to the Hamiltonian in optical lattices in the next section, and demonstrate the robustness of fidelities against imperfect implementations of the scheme.

6.3   Experimental implementation of noise proportional to the Hamiltonian and robustness against imperfect implementation

In this section, we discuss the condition required to introduce noise proportional to the Hamiltonian in the context of the Bose-Hubbard model with amplitude noise in optical lattices. Then, we will present numerical simulations in the limited ramping time regime where the noise proportional to the Hamiltonian shows the advantages for preparing the target state but with imperfect implementations. We will demonstrate the robustness of the method and present the interesting effect that the maximum fidelity does not always occur when the noise is exactly proportional to the Hamiltonian.

6.3.1   Engineering the amplitude noise

In the previous Sec. 6.2, we discussed the effect of classical noise during the adiabatic process. From numerical simulation results, introducing classical noise which is proportional to the original Hamiltonian will provide improvements of state preparations, especially in the case of limited ramping time. The condition of such results relies on the dependencies of the hopping rate J and the on-site interaction coefficient U on the fluctuation of depth of optical lattices V. However, fine control of noise cannot be realised easily in most of experiments. In this section, with help of a recent proposal of a dressed lattice scheme, we indicate how to engineer the noise proportional to the Hamiltonian in optical lattices and later demonstrate the robustness of noisy adiabatic processes under imperfect implementation of this control.

Starting with the condition of the noise proportional to the Hamiltonian, i.e. $H_1 \propto H_0$, we acquire the requirement of the dependency of coefficients on the amplitude fluctuation

$$\frac{1}{J_0}\frac{dJ}{dV} = \frac{1}{U_0}\frac{dU}{dV} \ . \tag{6.9}$$

In general, the amplitude noise in conventional experiments would induce heating effects to the system. A computed heating rate [121] in the presence of the amplitude noise in a static designed Hamiltonian shows the relation between the noise strength and the heating rate in the white noise limit. We denote the tunnelling components as $H_J = -J \sum \hat{b}_i^\dagger \hat{b}_j$, and the interaction components as

$H_U = \frac{U}{2}\sum \hat{n}_i(\hat{n}_i - 1)$. The heating rate can be expressed as

$$\langle\dot{H}_{sys}\rangle = \Gamma \left(\frac{1}{J_0}\frac{dJ}{dV} - \frac{1}{U_0}\frac{dU}{dV}\right)^2 \langle[[H_J, H_U], H_J]\rangle . \tag{6.10}$$

In the experiments, as the depth of optical lattice increases, the on-site interaction is enhanced, $dU/dV > 0$; on the other hand, tunnelling becomes unlikely to happen, $dJ/dV < 0$. That is the reason why in general, the heating rate is positive and introducing noise will heat up the system, which reduces the final fidelity of adiabatic state preparation.

From the heating rate (6.10) and the condition that noise is proportional to the Hamiltonian (6.9), we understand that the noise proportional to the Hamiltonian will introduce no heating to the system. With the help of the proposed dressed lattice scheme [121, 122], we can engineer an effective Hamiltonian with additional optical lattices, and coupling between ancillary energy levels and original atom levels. Thus the noise proportional to the Hamiltonian (Eq. 6.9) can be realised, as we discussed in Sec. 3.4.

In this section, we introduced the condition of noise proportional to the Hamiltonian (6.9), the difficulties of realising such noise. Using the dressed lattice scheme introduced in Sec. 3.4, we can realise such noise in optical lattices. In the next section, we will demonstrate simulations that use this noise engineering technique to improve fidelities of adiabatic state preparations and the robustness of systems against imperfect implementations of the dressed lattice scheme.

6.3.2   Robustness against imperfect implementation

As mentioned in Sec. 3.4, with the help of the dressed state scheme to tailor amplitude noise, we are able to improve the fidelity of adiabatic state preparations in the Bose-Hubbard model. Taking an example of one situation that might occur in experiments, we will demonstrate behaviours of systems under imperfect implementation to show the robustness and explain the phenomena in later sections.

We can parameterise the correlations between the noise on J and U by θ, λ to simplify calculations, where $\sqrt{2\Gamma}\frac{dU/dV}{U} = \lambda\sin^2\theta$, $\sqrt{2\Gamma}\frac{dJ/dV}{J} = \lambda\cos^2\theta$ when $\theta \in [0, \pi/2)$. The heating rate in this representation can be expressed in parameter space of θ as

$$\langle\dot{H}_{sys}\rangle \propto \left(\theta - \frac{\pi}{4}\right)^2 \tag{6.11}$$

This defines a sweet spot in the parameter space of θ, $\theta_{sw} = \pi/4$, where introducing noise will cause no heating and the white noise term $H_1 \propto H_0$. Consider the situation that the system sits close to the sweet spot, but with a small offset $\Delta\theta$, that is $\theta = \pi/4 + \Delta\theta$. Then the heating rate is proportional to second order of $\Delta\theta$, $\langle \dot{H}_{sys} \rangle \propto \Delta\theta^2$. In these cases, the heat introduced to the system will jeopardise the adiabatic state preparation by exciting the system to excited states. Competition between heating and the dephasing effect that suppresses the non-adiabaticity, might result in unknown behaviours of the final fidelities which interest us most. We conduct numerical simulations in these cases for both a small system and the large system visited in the previous section 6.2 to understand the reactions of the system with the classical noise with both heating effects and dephasing effects.

First, we simulate similar adiabatic state preparations of a small system of 4 particles in 4 sites in the Bose-Hubbard model with different values of the noise offset. In the representation of θ space, we rewrite the Hamiltonian as

$$H_{sys}(t) = H_0(t) + (2\cos^2\theta H_J + 2\sin^2\theta H_U(t))\sqrt{2\Gamma}\xi(t) . \tag{6.12}$$

where $H_0(t) = H_{BH}(t)$, and H_J and H_U are as in Eq. (6.10). The simulations are done via the master equation approach with exact diagonalisation. Fig. 6.3 shows the final fidelities of the adiabatic state preparation for a ramping time $TJ_0 = 0.1$ (Fig. 6.3(a)) and $TJ_0 = 1$ (Fig. 6.3(b)). In Fig. 6.3(a), the noisy system (blue line) still has better fidelities than the noise-free case (black line), within the range of the offset $\Delta/\Delta_{sw} \in [-0.1, 0.1]$ and the noise strength $\Gamma = J_0$. When the offset is negative $\Delta\theta < 0$, the fidelity increases as the noise is further away from the sweet spot and reaches the maximum value around $\Delta/\Delta_{sw} = -0.09$. This behaviour is not symmetric around the sweet spot. When the offset is positive, the further away from the sweet spot, the worse the fidelity it achieves in the end. For the case of a longer ramping time shown in Fig.6.3(b) $TJ_0 = 1$, similar behaviour happens for positive offsets, but for negative offsets, there is an optimal choice of noise set-up θ_{opt} that gives the maximum fidelity under this circumstance. In the range of offsets $\Delta\theta/\theta_{sw} \in [-0.05, 0.04]$, the adiabatic state preparations show better performances over the noise-free case, thus the robustness against imperfect implementations is observed. As ramping time grows longer, the θ_{opt} shifts to the sweet spot.

The fact that adiabatic state preparation with noise not proportional to the Hamiltonian outperform the noise-free evolution can be explained by understanding that the quantum Zeno effect can still suppress heating effect in that regime. However, the phenomenon that an optimal set-up occurs at negative offset regimes and the shift of such optimal offset still remains unclear.
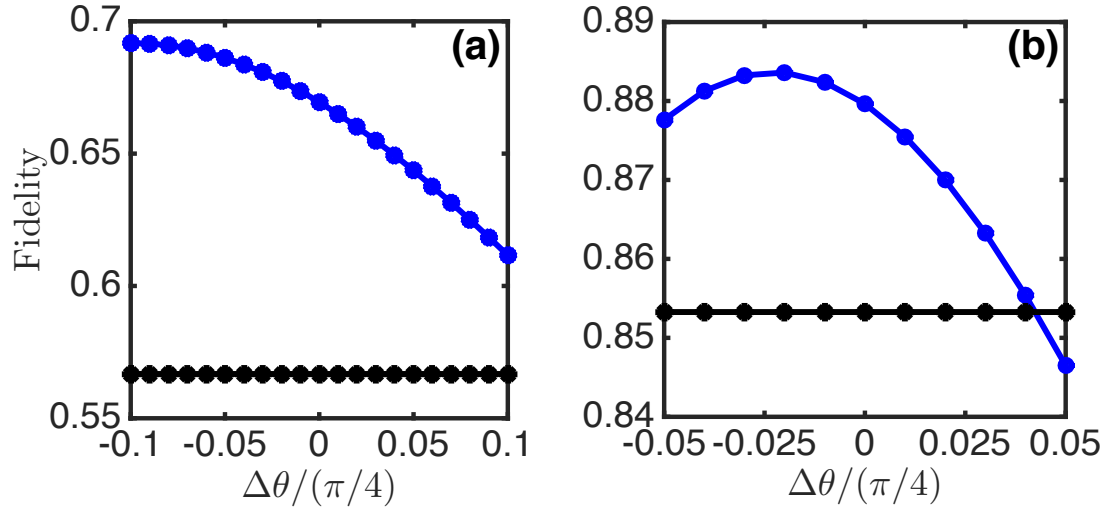
FIGURE 6.3: Final fidelities of adiabatic state preparation, obtained from exact diagonalisation simulations of the Bose-Hubbard model of 4 sites and 4 particles. The system starts with the ground state of the Mott insulator phase $(U_0(0)/J_0 = 10)$, and evolves under the noisy Hamiltonian that ramps linearly $g(t) \equiv U_0(t)/J_0 = 10 - 8t/T$ to the superfluid phase. The fidelities are between the system and the ground state of the superfluid phase $(U_0(T)/J_0 = 2)$. Plots correspond to situations with different ramping times $TJ_0 = 0.1$ (a) and $TJ_0 = 1$ (b), while the noise strength is $\Gamma = J_0$ for both cases. Imperfect engineering of the noise proportional to the Hamiltonian will lead to noise being outside the sweet spot $(\Delta\theta = \theta - \pi/4)$. The noisy Hamiltonian is expressed as $H_{sys}(t) = H_0(t) + (2\cos^2\theta H_J + 2\sin^2\theta H_U(t))\sqrt{2\Gamma}\xi(t)$, where H_J and H_U are the kinetic and interactive components of the Bose-Hubbard model. Black lines show the fidelities of noise-free cases in each case. Blue lines represent the fidelities of noisy adiabatic state preparations with different values of the offset. Even if the implementation is imperfect, the noise can still improve the fidelity in some regimes. In the short ramping case (a), the fidelites reach the maximum value at $\Delta/\Delta_{sw} = -0.09$, and decrease as the offset varies from zero to a positive value. Overall, the fidelities of noisy cases are still higher than the noise-fress case, which shows the robustness against the imperfect implementation of the noise proportional to the Hamiltonian. For the long ramping time, the noise-free cases perform a reasonable state preparation $F \approx 0.85$ and introducing noise can not provide much help even at the sweet spot. When the noise is tilted to negative offset, $\Delta\theta < 0$, the system performs with better fidelity than at the sweet spot. For both cases, the θ_{opt} that gives the maximum fidelity is less than θ_{sw}, and as the ramping time T increases, $\Delta\theta_{opt} = \theta_{opt} - \theta_{sw}$ shifts to 0.

To check that this phenomenon is not caused by the limited size of system, we

conduct simulations for a larger system with 16 particles and 16 sites. The simulations are in the parameter regime of noise strength $\Gamma = 2.25 J_0$, and we investigate two cases with different values of evolving time $(T J_0 = 0.1, 1)$, shown in Fig. 6.4. Similar to the results of the small system calculations, the optimal choice of offset is negative, and as the ramping time grows, the optimal offset shifts back to the sweet spot.
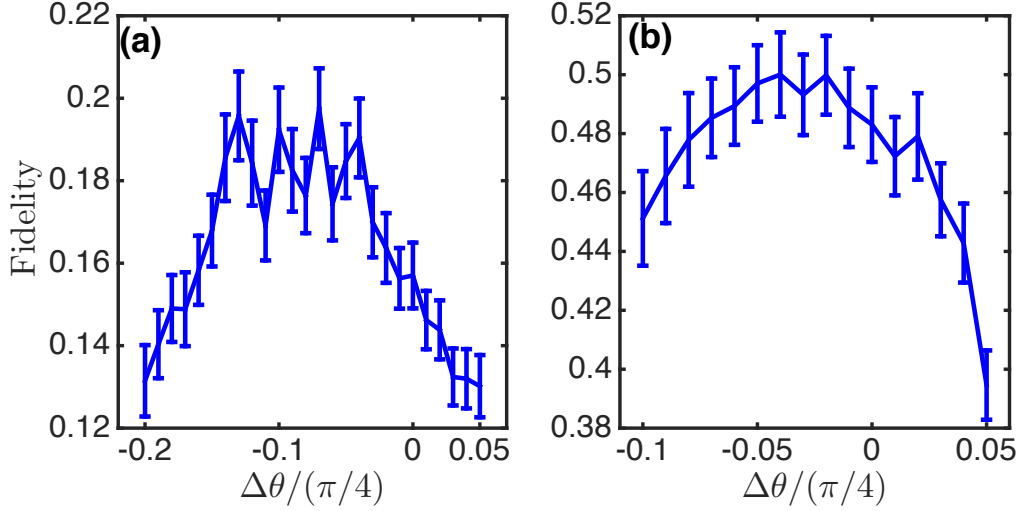

FIGURE 6.4: Final fidelities of adiabatic state preparation, obtained from DMRG calculations of the Bose Hubbard model of 16 particles and 16 sites. In the plot, it shows fidelities of adiabatic state preparations with the noise strength $\Gamma = 2.25 J_0$ but different ramping times $T J_0 = 0.1$ (a) and $T J_0 = 1$ (b). We investigate the cases mainly with negative noise offsets $\Delta\theta = \theta - \pi/4 < 0$ from the sweet spot. The noisy Hamiltonian is $H_{sys}(t) = H_0(t) + (2\cos^2\theta H_J + 2\sin^2\theta H_U(t))\sqrt{2\Gamma}\xi(t)$, where H_J, and H_U are the kinetic and interactive components of the Bose-Hubbard model. The system evolves under $H_{sys}(t)$ from the ground state of the Mott insulator phase $(U_0(0)/J_0 = 10)$, to superfluid regimes $(U_0(T)/J_0 = 2)$. The changing of the parameter $g(t)$ is linear in time $g(t) \equiv U_0(t)/J_0 = 10 - 8t/T$. The fidelities are between the final state with the ground state of the superfluid phase. Convergencies of the time step $dt = 10^{-5}$ and the bond dimension $D = 128$ have been checked. The noise is not proportional to the Hamiltonian, which results in a small offset away from the sweet spot. The heating rate is proportional to the square of the offset, and such heat might reduce the final fidelity. When the noise is tilted to negative offset, $\Delta\theta < 0$, the noisy time evolutions give better overal fidelities than that of the sweet spot in a certain range. The θ_{opt} that gives maximum fidelity is alway less than θ_{sw}, and as the ramping time T increases, $\Delta\theta_{opt}$ shifts to 0.

The different values of offset for maximum fidelity requires deeper understanding of the dynamics during the adiabatic state transformation. We will further study

the Bose-Hubbard model and also a simple two-level system to give an analytical explanation for this behaviour in next section.

6.4   Adiabatic dynamics with tilted noise

To study how general classical noise affects the final fidelity of adiabatic state preparation is important yet hard to achieve. Due to the limit of computational power, it is hard to access the instantaneous eigenbasis using exact diagonalisation for a large system, as the Hilbert space increases in system size exponentially. In this section, we assume that the classical noise is close to the designed Hamiltonian. As the heating rate is in the second order of offset, we keep up to the second order of offset to study dynamics during adiabatic state transformation. For the Bose-Hubbard model, we present calculations in each timestep, and for a two-level system that behaves similarly to the Bose-Hubbard model in terms of fidelities, we present analytical calculations of the final fidelity as a function of the noise offset, and compare it with numerical results of optimal offsets for different ramping times. From theoretical understanding of the heating and the dephasing close to the critical point where the minimum gap is and outside of the critical area, we are able to explain the parabolic-like behaviour of the fidelities of the adiabatic state preparation with imperfectly implemented noise and provide insights of the Bose-Hubbard cases analogous to the two-level system.

6.4.1   Study of the Bose-Hubbard model

To obtain a deeper understanding of the noisy process, we calculate the fidelity of the evolving state to the instantaneous ground state. Therefore, we are able to keep track of how different components of the noisy Hamiltonian affect the fidelity, and observe the dephasing effect to off-diagonal terms of density matrix in the instantaneous eigenbasis. We expand the noise term H_1 close to the sweet spot with respect to $\Delta\theta$. The zero-th order component is equal to the original Hamiltonian and the first order H_N can be expressed as a linear combination of H_J and H_U, i.e.

$$H_{sys}(t) = H_0(t) + H_1(t)\sqrt{2\Gamma}\xi(t) \,, \tag{6.13}$$

$$H_1(t) = H_0(t) + 2\Delta\theta H_N(t) \,, \tag{6.14}$$

$$H_N(t) = -H_J + H_U(t) \,. \tag{6.15}$$

The equation of motion is the stochastic Schrödinger equation in Stratonovich calculus as discussed in Sec. 4.2.2.3,

$$\frac{d}{dt}\left|\psi(t)\right\rangle = -iH_{sys}(t)\left|\psi(t)\right\rangle \quad \text{(S)}$$

Expanding the evolving state $\left|\psi(t)\right\rangle$ to the eigenbasis of the instantaneous original Hamiltonian $H_0(t)$, we have $\left|\psi(t)\right\rangle = \sum_n C_n(t)\left|\phi_n(t)\right\rangle$. $\{\left|\phi_n(t)\right\rangle\}$ denote the eigenvectors and $\{C_n\}$ are the complex components. The stochastic Schrödinger equation can be used to derive to the equation of motion for different components,

$$\dot{C}_k(t) = \sum_n C_n(t)\left\langle\phi_k(t)\right| - iH_{sys}(t)\left|\phi_n(t)\right\rangle$$

$$- \sum_n C_n(t)\left\langle\phi_k(t)\right|\frac{d}{dt}\left|\phi_n(t)\right\rangle \quad \text{(S)} . \tag{6.16}$$

The fidelity is defined as $F(t) = C_g(t)C_g^*(t)$, where C_g denotes the complex components of the ground state $\left|\phi_g(t)\right\rangle$. Keeping up to the first order of dt, the change of the fidelity is $\Delta F(t) = F(t+dt) - F(t) = [\dot{C}_g(t)C_g^*(t) + C_g(t)\dot{C}_g^*(t)]dt$. By applying Ito calculus, the stochastic average of the fidelity in the instantaneous eigenbasis, up to the second order in $\Delta\theta$, is

$$\overline{\frac{dF(t)}{dt}} \approx -\overline{F(t)}4\Gamma\Delta\theta^2\sum_{n\neq g}|H_N^{gn}|^2$$

$$- \sum_{n\neq g}\rho_{gn}\{\frac{\left\langle\phi_g(t)\right|\frac{d}{dt}H_0(t)\left|\phi_n(t)\right\rangle^\dagger}{\Delta_{ng}(t)} + \Gamma\Delta\theta H_N^{gn}$$

$$+ 2\Gamma\Delta\theta^2 H_N^{gn}\Delta_N^{gn}(t)] + c.c\} , \tag{6.17}$$

where $H_N^{gn} = \left\langle\phi_g(t)\right|H_N(t)\left|\phi_n(t)\right\rangle$, the noise offset term H_N is represented in the eigenbasis, $\rho_{nm}(t) = \overline{c_n(t)c_m^*(t)}$, $\Delta_{ng}(t) = E_n(t) - E_g(t)$ and $\Delta_N^{gn}(t) = H_N^{nn}(t) - H_N^{gg}(t)$. This formula also neglects the influences of coherent processes between excited states in the near-adiabatic assumption, thus $\rho_{nm} \to 0$, where $n, m \neq g$ are excited states. The first term shows how heating reduces the fidelity, which is of the order of $-4\Gamma\Delta\theta^2$. The multiplier of off-diagonal terms ρ_{nm} which represents the coherent processes between the ground state and excited states is affected by the non-adiabaticity caused by the changing rate of the Hamiltonian, and additional noise influences. The dephasing for off-diagonal terms can be calculated

as

$$
\frac{d\rho_{gn}(t)}{dt} \approx \rho_{gn}(t)\{i\Delta_{ng} - \frac{\Gamma}{4}\Delta_{ng}^2 + \Gamma\Delta\theta\Delta_{ng}\Delta_N^{ng} + \Gamma\Delta\theta^2(\Delta_N^{ng})^2\}
$$
$$
- \overline{F(t)}\{\frac{\langle\phi_g(t)|\frac{d}{dt}H_0(t)|\phi_n(t)\rangle}{\Delta_{ng}(t)} + \Gamma\Delta\theta\Delta_{ng}H_N^{gn} + \Gamma\Delta\theta^2 H_N^{gn}\Delta_N^{ng}\} , \quad (6.18)
$$

where we neglect the influence of off-diagonal terms in the density matrix ρ_{nm}, where $n, m \neq g$. In this expression of off-diagonal terms, it is clear that dephasing effects reduce non-adiabticity in each time step. The ρ_{gn} terms on the right-hand-side generate the dephasing and the $\overline{F(t)}$ terms represent the occupation leakage due to the non-adiabaticity and the heating in the state transformation. In the expression for the multiplier to the ρ_{gn} term, the term in the first order of $\Delta\theta$ represents how offset influences the dephasing effects and the second order term which represents the heating effect destroys dephasing effects. The offset noise can enhance or reduce the dephasing, depending on the sign of $\Delta\theta\Delta_N^{ng}$. The last two terms show how the noise offset affects non-adiabaticity.

To summarise the role of tilted noise in the adiabatic state preparation of the Bose-Hubbard model, the heating effect reduces the final fidelity and reduces the effects of dephasing. Also, the tilted noise can enhance the dephasing in certain regimes of the adiabatic process, compensating for the heating effect overall. According to numerical results shown in Fig. 6.4, there are still some questions which need to be investigated. To explain the parabolic-like shape of fidelities, the shift of optimal offset to the sweet spot as the time grows, and the advantages of certain regimes of negative offset, requires a deeper understanding of how the tilted noise affects the system during the adiabatic state transformation and what the overall effect on the final fidelity is. Although we have the expression for the fidelity and of the off-diagonal terms of the density matrix, obtaining the explicit overall effect of heating and dephasing effects is hard to achieve. Under the near-adiabatic approximation, we can approximate that the coherent coupling only happens between the ground state and excited states, and the coupling between excited states is suppressed by adiabaticity. In the next section, we will reproduce the fidelity behaviour caused by the tilted noise and conduct our study of the overall effect of classical noise from there.

6.4.2   Study of a two-level system

We now consider an exactly solvable system to discuss the role of tilted noise in the adiabatic state transformation. First of all, we construct a two-level system in the presence of classical noise to reproduce the parabolic-like behaviour of fidelities corresponding to tilted noise. The designed adiabatic process is to flip

the spin of a qubit from negative direction $|0\rangle$ to positive direction $|1\rangle$ of σ_z. The noisy system can be characterised as,

$$H_0(t) = J(\sigma_x + g(t)\sigma_z) \tag{6.19}$$

$$g(t) = -10 + 20\frac{t}{T} \tag{6.20}$$

$$H_1(t) = 2J(\cos^2(\theta)\sigma_x + g(t)\sin^2(\theta)\sigma_z) \tag{6.21}$$

$$H_{sys}(t) = H_0(t) + \sqrt{2\Gamma}\xi(t)H_1(t) \tag{6.22}$$

$$\dot{\rho}(t) = -[H_0(t), \rho(t)] - \Gamma[H_1(t), [H_1(t), \rho(t)]] \tag{6.23}$$

where σ_i are Pauli matrices. Similar to the setup of the Bose-Hubbard model, the parameter θ prefers a sweet spot $\theta_{sw} = \pi/4$ to provide the noise proportional to the Hamiltonian. By simulating the adiabatic state preparations via a master equation and exact diagonalisation calculations, we are able to reproduce the same parabolic-like behaviour as that in the Bose-Hubbard model, shown in Fig. 6.5.

Because the Hilbert space of this two-level system is small, we performed numerical simulations of the adiabatic state preparation using the time evolution of the master equation $\dot{\rho}(t) = -i[H_0(t), \rho(t)] - \Gamma[H_1(t), [H_1(t), \rho(t)]]$ to obtain exact stochastic average results. The numerical simulation results are presented in Fig. 6.5. The same parabolic-like shape of the final fidelities and the shift of optimal offsets are reproduced. In the rest of this section, we analyse the dynamics of the system. From analytical results of final fidelities, we are able to explain the shift of the optimal offset. Based on calculations of the dephasing effect and the heating effect in the eigenbasis of the instantaneous Hamiltonian, we are able to explain why the optimal offset is always negative.

We expand the noise Hamiltonian close to the sweet spot ($\theta \approx \pi/4$), $H_1 = H_0 + 2\Delta\theta H_N$, with $H_N = -\sigma_x + g(t)\sigma_z$, and represent the evolving state $|\psi(t)\rangle = c_0(t)|\phi_0(t)\rangle + c_1(t)|\phi_1(t)\rangle$ in the instantaneous eigenspace $\{|\phi_0(t)\rangle, |\phi_1(t)\rangle\}$ of the original Hamiltonian $H_0(t)$. To reduce the complexity of the formula expressions, we define $\alpha(t) = c_0(t)c_0^*(t) - c_1(t)c_1^*(t)$ and $\beta(t) = c_1(t)c_0^*(t)$, $\eta(t) = c_1^*(t)c_0(t)$. Under the near-adiabatic condition and strong noise, we assume $\dot{\beta} = \dot{\eta} = 0$, and derive the equation of motion for parameter $\alpha(t)$

$$\dot{\alpha}(t) = \frac{\alpha(t)}{16\Gamma}\left(-4\dot{g}^2\frac{1}{(1+g(t)^2)^3} + \Delta\theta\dot{g}^2 32\frac{g(t)^2 - 1}{(g(t)^2 + 1)^4}\right.$$
$$\left. + \Delta\theta^2[-256\frac{g(t)^2}{(1+g(t)^2)^2} + 128\dot{g}^2\frac{(g(t)^2 - 1)^2}{(g(t)^2 + 1)^5} - 64\dot{g}^2\frac{g(t)^4 + 1}{(g(t)^2 + 1)^5}]\right), \tag{6.24}$$

where $\dot{g}$ is the linear ramping speed with an absolute value which depends on the total evolution time T, $|\dot{g}| = 20/T$. Integrated throughout the time evolution
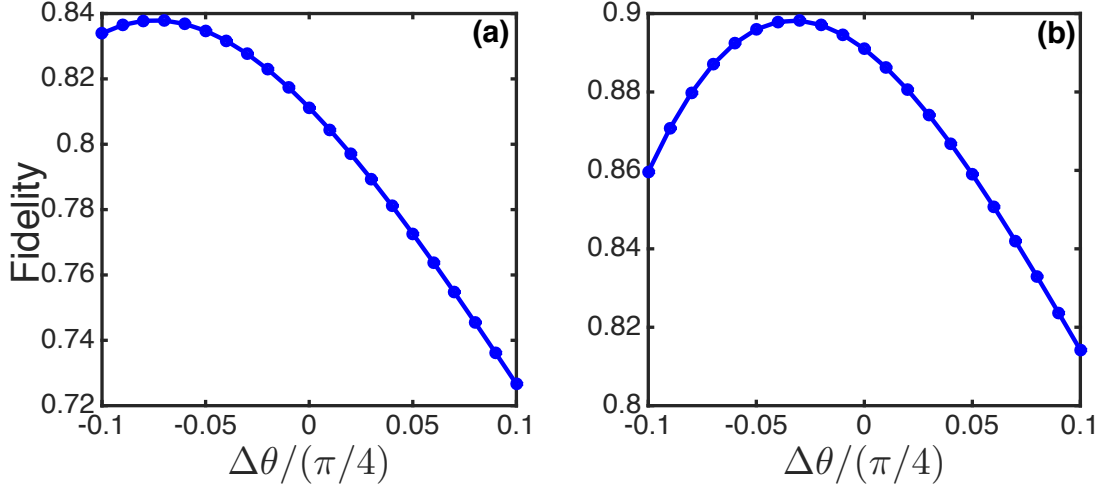
FIGURE 6.5: Final fidelities of adiabatic state preparations, obtained from exact diagonalisation calculations of two-level system. Plots are of different evolution times $TJ = 10$ (a), 20 (b). The noise strength is $\Gamma = J$, and $dt = 10^{-4}$. The ramping is linear $g(t) = -10 + 20t/T$. The master equation of time evolution is Eq. (6.23). The system evolves from the ground state $|\phi_0(0)\rangle$ of $H_0(0)$, i.e. $\rho(0) = |\phi_0(0)\rangle \langle \phi_0(0)|$. The fidelities are calculated between the final state and the ground state of $H_0(T)$. These plots show how noise that close to the sweet spot ($\Delta\theta = \theta - \pi/4$) can affect final fidelities. The heating effect introduced by noise is proportional to the second order of the noise offset $\Delta\theta$, and the further the noise is away from sweet spot, the more heating it introduces into the system. When the noise is tilted to negative offsets, $\Delta\theta < 0$, the system gives better fidelity at the end of the ramp than at the sweet spot cases in a certain range. The θ_{opt} that gives maximum fidelity is alway less than θ_{sw}. As the ramping time T grows, $\Delta\theta_{opt} = \theta_{opt} - \theta_{sw}$ shifts to 0.

with the initial condition $\alpha(0) = 1$, we obtain

$$\ln(\alpha(T)) = \frac{1}{16\Gamma|\dot{g}|}[-\dot{g}^2\frac{3\pi}{2} + \Delta\theta\dot{g}^2(-8\pi) + \Delta\theta^2(-128\pi + 11\pi\dot{g}^2)] \ . \qquad (6.25)$$

At the sweet spot, which means $\Delta\theta = 0$, the expression becomes $\ln(\alpha(T)) = -3\pi|\dot{g}|/32\Gamma$. Since $e^x \approx 1+x$, as $x \to 0$, and since by definition $F = (\alpha(T)-1)/2$, the final fidelity F_{sw} and tunnelling rate R_{sw} to the exited state on sweet spot are

$$F_{sw} \approx 1 - \frac{3\pi|\dot{g}|}{64\Gamma} \ , \qquad (6.26)$$

$$R_{sw} = \frac{3\pi|\dot{g}|}{64\Gamma} \ . \qquad (6.27)$$

Comparing our result to previous results from relevant research [164] on Landau-Zener tunnelling, we see that the adapted tunnelling rate in our notation is,

$$R_{tunnel} = \frac{\pi|\dot{g}|}{16\Gamma} > R_{sw} \;. \tag{6.28}$$

The improvement is mainly caused by the different set-ups of the noise term. In our case, the effective noise strength is greater than or equal to that of the processes of ref. [164], and the noise proportional to the Hamiltonian suppresses the coherent tunnelling and reduces the overall tunnelling rate.

Using Eq. (6.25), we obtain the equation of the final fidelity with respect to $\Delta\theta$ up to second order, the optimal value of noise offset and the corresponding fidelity,

$$F = 1 + \frac{1}{32\Gamma|\dot{g}|}[-\dot{g}^2\frac{3\pi}{2} + \Delta\theta\dot{g}^2(-8\pi) + \Delta\theta^2(-128\pi + 11\pi\dot{g}^2)] \;, \tag{6.29}$$

$$\Delta\theta_{opt} = \frac{\dot{g}^2}{-128 + 11\dot{g}^2} \;, \tag{6.30}$$

$$F_{opt} = 1 - \frac{1}{32\Gamma|\dot{g}|}\left(\frac{3\pi}{2}\dot{g}^2 - \frac{16\pi}{128 - 11\dot{g}^2}\dot{g}^4\right) \;. \tag{6.31}$$

In the expression for the final fidelity [Eq. (6.29)], the heating is in the second order of offset $\Delta\theta$, while the dephasing effect of the tilted noise is in the order of $\Delta\theta$ and $\Delta\theta^2$. Thus the final fidelity is a parabolic polynomial of the noise offset $\Delta\theta$. From the expression of the optimal offset $\Delta\theta$ [Eq. (6.30)], the optimal value of offset is always negative in the adiabatic regime $|\dot{g}| \ll 1$, and as ramping speed $|\dot{g}|$ decreases, the optimal offset noise $\Delta\theta_{opt} \approx -\dot{g}^2/32$ shifts to zero.

To compare analytical calculations with numerical simulations, we run simulations of different values of the total time T and the noise offset θ, shown in Fig. 6.6. The optimal offset $\Delta\theta_{opt}$ at certain T is determined by fitting the data with second order polynomial of fidelities $(F(\theta, \theta^2))$, and calculating the condition of maximum fidelity $\Delta\theta_{opt}(\dot{g})$. The error shown in Fig. 6.6 is the fitting error. Simulations are performed by evolving the master equation using exact diagonalisation methods. It shows the behaviour of optimal offset $\Delta\theta$ changing according to ramping speed $\dot{g}$.

The numerical simulation results agree with analytical calculations. The optimal offset is always negative $\Delta\theta_{opt} < 0$. As the speed of the adiabatic ramping $|\dot{g}| \ll 1$ decreases, the value of $\Delta\theta_{opt}$ of maximum fidelity shifts to 0 linearly. This shift is due to competition between the dephasing and the heating. The heating introduced into the system accumulates along with the growth of the ramping time, and the reduction to fidelity by heating effect increases accordingly.
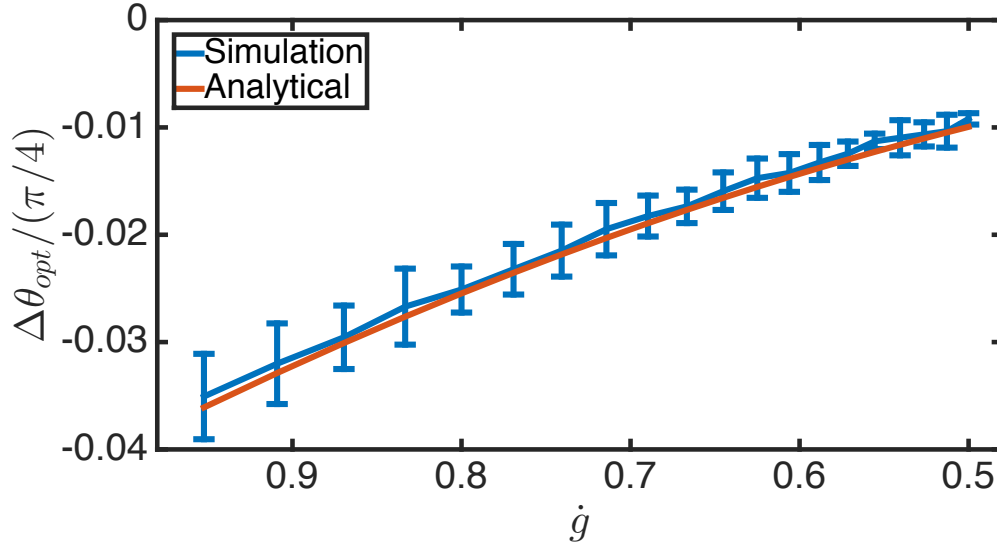
FIGURE 6.6: Plots for optimal noise offset Δ_{opt}, obtained from master equation and exact diagonalisation calculations of two level system (single qubit). Plot of optimal $\Delta\theta$ which provide maximum final fidelity in two level system calculation, and analytical result (Eq.6.30). The simulation is under master equation (6.23). The changing parameter is $g(t) = -10 + 20t/T$ and the noise strength $\Gamma = J$, $dt = 10^{-4}$. This figure shows the value of $\Delta\theta_{opt}$ that gives maximum fidelity in the same ramping time, and the behaviour of $\Delta\theta_{opt}$ corresponding to different evolution speeds $|\dot{g}|$. As the evolution time increases, the value of θ_{opt} comes closer to the sweet spot $\theta_{sw} = \pi/4$ in both cases. The more adiabatic the ramping is, the more reduction of final fidelity is done by introducing heating to the system, which agrees with the shift of θ_{opt} to the sweet spot in the previous numerical result. At the sweet spot, the noise proportional to the Hamiltonian introduces no heating. From the analytic calculation, the noise with time-independent offset has a stronger dephasing effect in the area $|g| \ll 1$, and then provides more help to suppress the non-adiabaticity result in compensation of heating throughout the process.

In these cases, the quantum Zeno effect by dephasing can no longer compensates the reduction of fidelity done by heating effects overall, so the optimal offset shifts to the sweet spot where no heating is introduced to the system.

To understand the preference for the optimal noise offset being negative, we focus on the transformation matrix of the instantaneous state along the adiabatic process. From analytical calculations, we are able to gain insight into the dephasing effect acting on off-diagonal elements of density matrix. The equation of motion

for the evolution of the system can be expressed as

$$
\begin{pmatrix} \dot{\alpha}(t) \\ \dot{\beta}(t) \\ \dot{\eta}(t) \end{pmatrix} = U(t) \begin{pmatrix} \alpha(t) \\ \beta(t) \\ \eta(t) \end{pmatrix} , \tag{6.32}
$$

where $U(t)$ is the transformation matrix. We can understand how the noise affects dephasing effects in adiabatic dynamics, from the dephasing factor U_{22} on the coherent term $\beta(t)$ that dominates the transformation,

$$
U_{22}(t) = -\Gamma \left[4(1 + g(t)^2) - 16\Delta\theta(1 - g(t)^2) + 16\Delta\theta^2 \frac{1 + g(t)^4}{1 + g(t)^2} \right] + 2i\sqrt{1 + g^2} . \tag{6.33}
$$

From this equation, it is clear that when the system passes the critical region $g(t) \to 0$, having a negative offset of noise $\Delta\theta < 0$ will enhance the dephasing, because the first order term $-16\Delta\theta(1-g(t)^2)$ has the same sign as the zero-th term $4(1+g(t)^2)$ which is the dominant dephasing term. In this area close to the critical point $g = 0$, the fidelity drops significantly but the dephasing effect can reduce the drop caused by heating and non-adiabaticity. Taking two set-ups of the tilted noise with the same heating effects but opposite sign to distinguish dephasing effects, we track the instantaneous fidelities throughout the state preparation, shown in Fig. 6.7.

The fidelity initially equals one since the initial state is the ground state of $H_0(0)$, and the drop of fidelity happens close to the critical point. From different offsets $\Delta\theta_1 < 0$ and $\Delta\theta_2 > 0$ with the same heating rate $|\Delta\theta_1| = |\Delta\theta_2|$, we can observe the different dropping amplitudes of the fidelity close to the critical point. The drop of the fidelity is mainly caused by fast ramping speeds, i.e. in the regime where non-adiabaticity dominates the evolution. With the negative offset $\Delta\theta_1$, the dephasing is enhanced, so that the amplitude of the dropping in critical area is smaller than that of the case $\Delta\theta_2$. When the system passes the critical area, the adiabatic condition is satisfied again, so the fidelity remains almost invariant in the rest of the process.

In this section, we constructed a two-level system scenario to reproduce the fidelity behaviour of the Bose-Hubbard model reacting to the different values of noise offset. Then we presented analytical calculations of the adiabatic dynamics of this two-level system via a master equation method, and tested these by simulation results from an exact diagonalisation approach. From the parabolic expression of the final fidelity with respect to the noise "tilt", we are able to recover the Landau-Zener tunnelling rate when the classical noise is on the sweet spot, and explain the behaviour of the optimal noise offset shifting to the sweet spot ($\Delta_{opt} \to 0^-$) as the ramping time grows longer. Comparing the behaviour of instantaneous fidelities
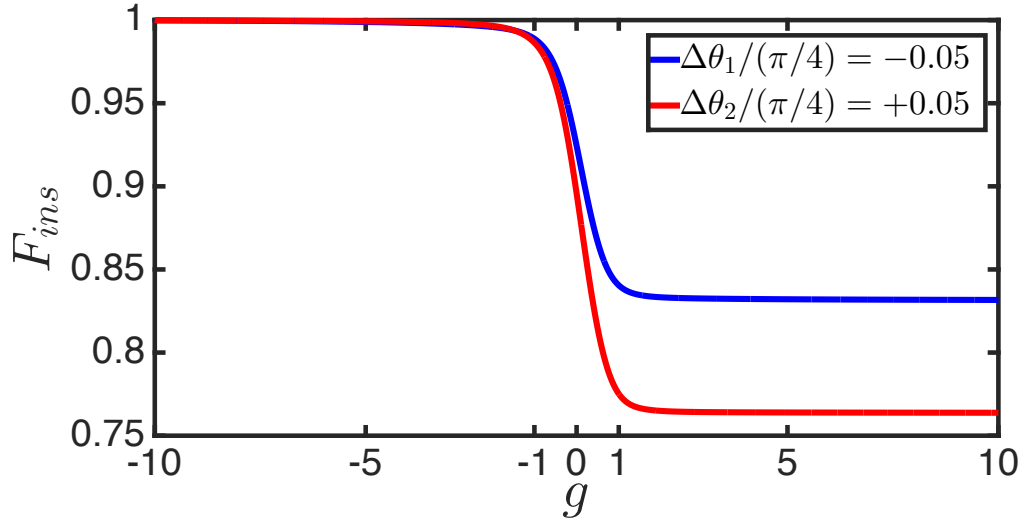
FIGURE 6.7: Instantaneous fidelities during adiabatic state preparations, obtained from exact diagonalisation calculations via master equation method of a two-level system (single qubit). Plots of fidelities to instantaneous ground states are of adiabatic rampings with different noise offsets. The ramping time is $TJ = 10$, and the noise strength is $\Gamma = J$ for both cases. The time step is $dt = 10^{-4}$. The system evolves under master equation (6.23), from the ground state $|\phi_0(0)\rangle$ of $H_0(0)$, $\rho(0) = |\phi_0(0)\rangle \langle\phi_0(0)|$. The fidelities shown are calculated between the evolving density matrix $\rho(t)$ and instantaneous ground states $|\phi_0(t)\rangle$, $F_{ins}(t) = \langle\phi_0(t)| \rho(t) |\phi_0(t)\rangle$. The changing parameter is $g(t) = -10 + 20t/T$. The blue line represents the noise with negative offset case $\Delta\theta_1 = -0.05\theta_{sw}$, and the red line represents the positive offset case $\Delta\theta_2 = 0.05\theta_{sw}$. Initially, $F_{ins}(0) = 1$ in both cases, and remains slightly decreasing until $g(t) \approx -1$, because the adiabatic condition is satisfied in this regime. When the parameter is close to critical point, the gap of the system is small and the fidelity drops due to the non-adiabaticity. The fidelity of the system with negative offset drops less amplitude than that of system with positive offset, shown in the area of $|g| \leq 1$. This behaviour can be interpreted as negative offset has stronger dephasing effect to suppress the non-adibaticity in Eq. 6.33. After passing the critical area, the adiabatic condition is satisfied again, so the fidelities are steady in the rest of adiabatic processes in both cases.

during the adiabatic state transformation with two values of the noise offset of same amplitude but different sign, we observed how dephasing effect suppress the non-adiabaticity in the critical region. The negative offset gives stronger dephasing effects close to the critical point, so the overall fidelity is better than positive offset with the same heating rate. When the offset is further away from the sweet spot, the dephasing effect can no longer compensate the reduction of

fidelity introduced by the heating. In the strong noise case and near-adiabatic limit, the Bose-Hubbard model dynamics will adapt analogous behaviour to what we have seen from the two-level system.

6.5   Conclusions

In this chapter, we adapted a recent proposed quantum algorithm [69], which claimed the potential of outperforming adiabatic quantum computing, to the adiabatic state preparation with the noise proportional to the Hamiltonian. Taking the Bose-Hubbard model as an example, we conducted numerical simulations for both a small system and a large system. With the numerical results, we were able to identify a regime where introducing a noise proportional to the original Hamiltonian improves the state preparation, especially when the evolution time is limited. With a recently developed dressed lattice scheme engineering of the amplitude noise of optical lattices, we are able to demonstrate a physical system that could have the noise proportional to the Hamiltonian in an effective Hamiltonian. We also conducted numerical simulations to demonstrate the robustness of our method against imperfect implementations of such noise. The behaviour of the preparation fidelities with different values of the noise offset away from sweet spot implies an intriguing mechanism of the classical noise which affects the adiabatic state preparation. By studying the Bose-Hubbard model, we acquire insight into how the heating jeopardises the state preparation and reduces the dephasing effect. We also studied the competition between the heating effect and the dephasing effect to explain such behaviour. The analysis of a two-level system reproduces the same parabolic-like behaviour of the final fidelities in the Bose-Hubbard model. Because of the access of the instantaneous eigenbasis, we are able to apply the master equation approach to study the averaged dynamics. We studied the competition between the heating and dephasing effects through analytical calculations of the instantaneous fidelity. We identified the regime that the dephasing enhanced by the tilted noise can compensate the fidelity reduction caused by the heating results in an overall higher final state fidelity.

Chapter 7

Thermalisation of energy introduced by amplitude noise in optical lattices

In the previous chapter, we adapted the idea of adiabatic quantum computing with randomised time steps to adiabatic state preparation with engineered amplitude noise in optical lattices (see Sec. 6.2). Under the condition that the noise operator is proportional to the designed Hamiltonian, there is no heat introduced to the system. When the noise is tilted from the noise proportional to the Hamiltonian, the heating rate is in the second order of the offset. In this chapter, we continue to investigate amplitude noise in optical lattices and discuss thermalisation behaviour of the system. In Sec. 7.2, we discuss the total energy after the adiabatic state preparation under the influence of the amplitude noise naturally caused by lattice depth fluctuations. In Sec. 7.3, we investigate the thermalisation after an application of engineered amplitude noise. We compute the dynamics in the Mott Insulator and the superfluid phases, and identify for different regimes whether observables relax to thermal values after short times.

7.1   Introduction

Usually, the fluctuation of the depth of an optical lattice is one of the sources of heating. The heating induces out-of-equilibrium dynamics and thermalisation processes are expected to be very important. Typically, it is assumed that the energy introduced into the system will be thermalised and cause an effective temperature increase. But the question about conditions for and regimes of thermalisation is still unanswered. Recently, experiments with strongly interacting

cold gases realised the confinement of movement in one dimension [25]. These experiments have demonstrated a regime in which systems do not thermalise in the traditional sense [165]. However, sometimes these systems can relax to a distribution of steady states in a generalised Gibbs ensemble [166, 167].

The study of thermalisation has an impact on the application of cold atoms as a platform of quantum simulation and quantum computation. For now, the experiments can realise many interesting many-body Hamiltonians and study corresponding quantum states. One of the key challenges for current experiments is to realise states with small energy gaps which usually require a very low temperature [168]. Adiabatic state preparation is one of the approaches to realise such states. In Chap. 6, we presented our study of adiabatic state preparation of the ground state of a superfluid phase under the influence of amplitude noise. There we identified a regime where introducing a certain type of noise can improve final fidelities of state preparations. A recent proposal for engineering amplitude noise [121] provides us with the method to realise the noise proportional to the Hamiltonian. We would now like to understand, when this is imperfect and noise induces heating, whether the final state is really a thermal state. We also want to better understand how to optimise adiabatic ramps in the presence of unwanted noise.

In this chapter, we present our research on adiabatic state preparation with naturally occurring amplitude noise which is not engineered to be proportional to the Hamiltonian. We discuss the corresponding behaviour of the total energy at the end of the adiabatic evolution with different ramping times and a constant noise strength in Sec. 7.2. Furthermore, we investigate the thermalisation process of the system after an application of an amplitude noise pulse in Sec. 7.3.

7.2 Adiabatic state preparations with naturally occurring amplitude noises

Naturally, the fluctuations of laser amplitude will affect the depth of the lattice $V = V_0 + \delta V(t)$, and thus introduce noise to the system. The noise with frequencies of order of the tunnelling parameter J and the on-site interaction strength U will induce intra-band heating for atoms within the lowest band. While under the influence of the noise at frequencies of the band separation, the particles are transferred to a higher band which is called an inter-band process. In the situation where the noise is weak for inter-band processes, the Hamiltonian of the

system is

$$H_{sys} = H_0(J_0, U_0) + H_1(\frac{dJ}{dV}, \frac{dU}{dV})\delta V \ , \tag{7.1}$$

$$H_1(\frac{dJ}{dV}, \frac{dU}{dV}) = -\frac{dJ}{dV}\sum_{\langle i,j \rangle} b_i^\dagger b_j + \frac{1}{2}\frac{dU}{dV}\sum_i n_i(n_i - 1) \ , \tag{7.2}$$

where H_0 and H_1 are Bose-Hubbard Hamiltonians, U_0 and J_0 are designed parameters of the Bose-Hubbard model. As described in Sec. 3.3, the fluctuations of the tunnelling parameter J and the on-site interaction strength U can be characterised as

$$\frac{dU}{dV} = \frac{E_R}{4V}\frac{U}{E_R} \ , \tag{7.3}$$

$$\frac{dJ}{dV} = [\frac{3E_R}{4V} - (\frac{V}{E_R})^{-1/2}]\frac{J}{E_R} \ , \tag{7.4}$$

and the dynamics of the adiabatic state preparations can be described as

$$\dot\rho = -i[H_0, \rho] - \Gamma[H_1, [H_1, \rho]] \ . \tag{7.5}$$

With this setting of the amplitude noise, the heating introduced to the system will cause a decrease of fidelities in adiabatic state preparation. Here we take adiabatic state preparations of the ground state of the superfluid phase ($U_0/J_0 = 2$) from the ground state of the Mott Insulator phase ($U_0/J_0 = 10$) as an example, to demonstrate the final fidelities in corresponding evolution times with a constant noise strength. Our results are shown in Fig. 7.1. From our numerical simulations, it is clearly demonstrated the reduction in fidelity due to adiabatic state preparation compared with noise-free cases. Without the amplitude noise, the fidelity increases as the evolution time grows as shown by the red line. However, under amplitude noise with strength $\Gamma = 0.6J_0$, the final fidelity (blue line) reaches a maximal value around 0.94 with a longer evolution time around $T \approx 10/J_0$. This figure also demonstrates the competition between the adiabaticity and heating effects. After the maximum value of fidelities, the extra adiabaticity can no longer compensate for the heating effect which results in a drop of the fidelity.

To demonstrate the amount of energy introduced to the system, we present our calculation of total energy after the adiabatic state preparation in Fig. 7.2.

The energy inputs are mainly from non-adiabaticity of the time evolution and the heating effects, introduced by the amplitude noise. Here we present an analysis of these two sources in terms of the evolution time.
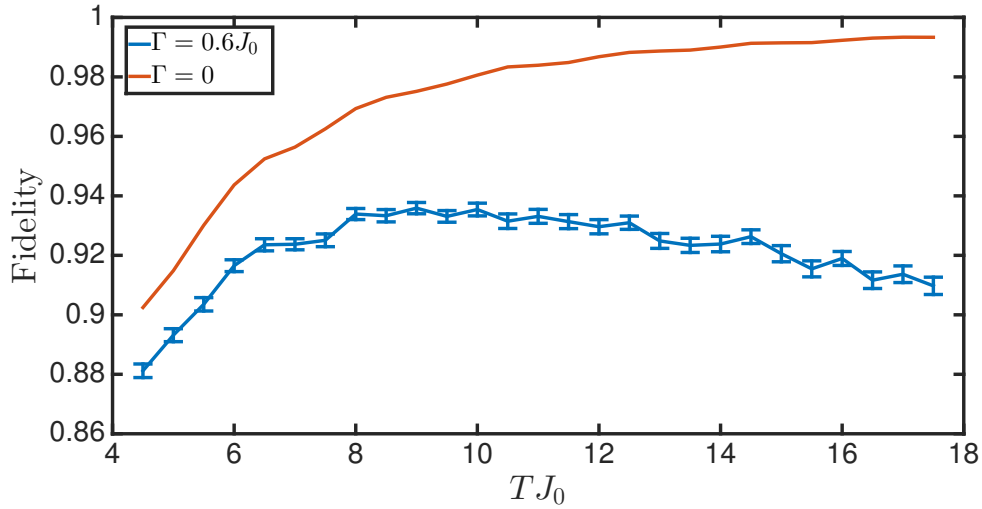
FIGURE 7.1: Final fidelities of adiabatic state preparations as a function of the evolution time, obtained from exact diagonalisation calculations of the Bose-Hubbard model with 8 sites and 8 particles. The inital state is the ground state of the Mott insulator phase ($U_0/J_0 = 10$) and the target state is the ground state of superfluid phase ($U_0/J_0 = 2$). The noise strength $\Gamma = 0.6J_0$ which introduces intra-band heating to the system. Data points of noisy processes are averaged values over 100 runs, dt=1e-3, and error bars represent statistical errors. The red line represents fidelities of noise-free cases and the blue line represents fidelities of noisy state preparations. Without the amplitude noise, the final fidelity increases as the evolution time grows. However, for fidelities of noisy state preparation, the maximum value is below 0.94, but the evolution time is $T \approx 10/J_0$. This clearly demonstrates the damage to adiabatic state preparaions from heating effects.

From the calculated heating rate of the noise presented in Ref. [121], we can obtain the energy input from the amplitude noise. We find

$$\langle \dot{H}_{sys} \rangle \propto \Gamma(\frac{1}{J}\frac{dJ}{dV} - \frac{1}{U}\frac{dU}{dV})^2 \, , \tag{7.6}$$

$$\Delta E_{amp} = \int_0^T dt \langle \dot{H}_{sys}(t) \rangle = \frac{T}{8}\int_2^{10} dg \langle \dot{H}_{sys}(g) \rangle \propto \Gamma T \, , \tag{7.7}$$

where the interactive parameter g is linear in time, $g(t) = U_0(t)/J_0 = 10 - 8t/T$, and T is the evolution time. The energy input from amplitude noise, noted as ΔE_{amp} accumulates linearly in time.

The energy input from non-adiabaticity is hard to calculate analytically. Here we assume the time evolution is in the near-adiabatic regime with a weak noise. In this case, the fidelity is close to 1 and the occupation amplitude of the ground state
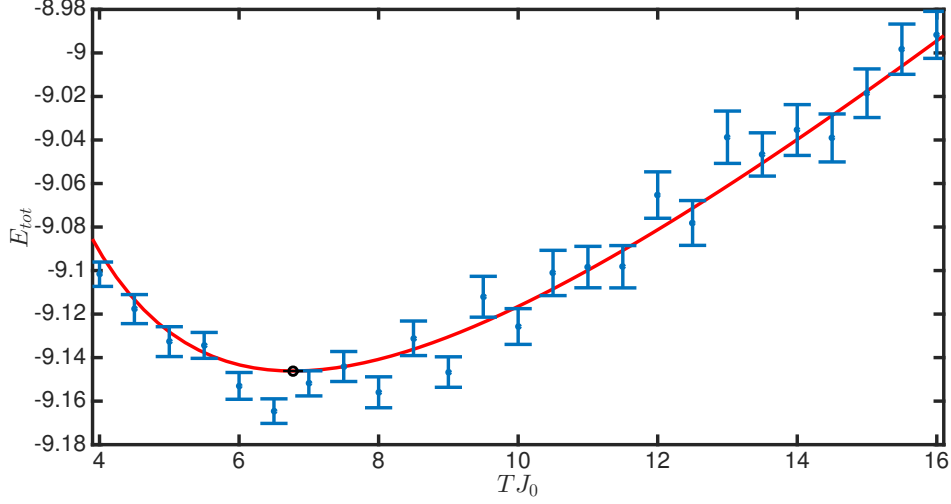
FIGURE 7.2: Total energies after after adiabatic state preparation as a function of the evolution time, obtained from exact diagonalisation propagation of the Bose-Hubbard model with 8 sites and 8 particles. The simulation parameters in the calculation are the same as shown in Fig. 7.1. The energy values are shown in blue, and a fitting function in the form of $E = aT + b/T + c$ is plotted in red, where $a \approx 0.0285$, $b \approx 1.3089$ and $c \approx -9.5327$. From fitting parameters, the minimum of total energy is shown as black dot with the error bar associated with 95% confidence of fitting parameters. The behaviour of final fidelities shows the competition of the adiabaticity and the heating. The adiabaticity comes is of the order of $1/T$ from the Landau-Zener formula in near-adiabatic condition as in Eq. (7.7), and the heating effect is of order of T as in Eq. (7.8).

is dominant. We consider an effective two-level system consisting of the ground state and an excited state with second dominant occupation amplitude in the spectrum. From the Landau-Zener transformation, the probability of tunnelling P_t is usually proportional to the speed of changing parameter $|\dot{g}|$ and the inverse of the noise strength Γ, $P_t \propto |\dot{g}|/\Gamma = 1/(\Gamma T)$. The final state $|\psi_T\rangle$ can be expressed (up to a relative phase) in the effective two-level system as, $|\psi_T\rangle = \sqrt{1 - P_t} |\phi_{SF}\rangle + \sqrt{P_t} |\phi_i\rangle$, where $|\phi_{SF}\rangle$ is the ground state of the superfluid phase with a corresponding energy E_g^{SF}, and $|\phi_i\rangle$ is the second dominant eigenstate associated with an eigenenergy E_{ex}. Then the energy difference between the final state and the ground state is

$$\Delta E_{na} = \langle E \rangle_{LZ} - E_g^{SF} = \langle \psi_T | H_{BH} | \psi_T \rangle - E_g^{SF} = \Delta \cdot P_t \propto 1/(\Gamma T) , \qquad (7.8)$$

where Δ is the energy gap between the ground state and the excited state, $\Delta = E_{ex} - E_g^{SF}$.

The different dependences (shown in Eq. (7.7) and Eq. (7.8)) of the energy inputs with respect to the evolution time result in a competition. As the evolution time increases, the non-adiabaticity introduces less energy as the adiabatic condition is better satisfied, while the heating accumulates energy over time. This competition relation can be presented as a function $E = aT + b/T + c$, where $a \propto \Gamma$ and $b \propto 1/\Gamma$. We use this relation as a fitting function to study the behaviour of the total energy.

We apply the fitting function of the total energy as a function of the adiabatic ramping time T for different values of the noise strength. Our results are shown in Fig. 7.3. We found that values of the evolution time that give minimal energy T_{min} (black line) vary. The value of T_{min} is,

$$T_{min} = \sqrt{\frac{b}{a}} \propto 1/\Gamma \ , \tag{7.9}$$

where the error bar of T_{min} is obtained from $\Delta T_{min} = \frac{T_{min}}{2}(\frac{-\Delta a}{a} + \frac{\Delta b}{b})$, where Δa and Δb are from 95% confidence bound from fitting parameter.
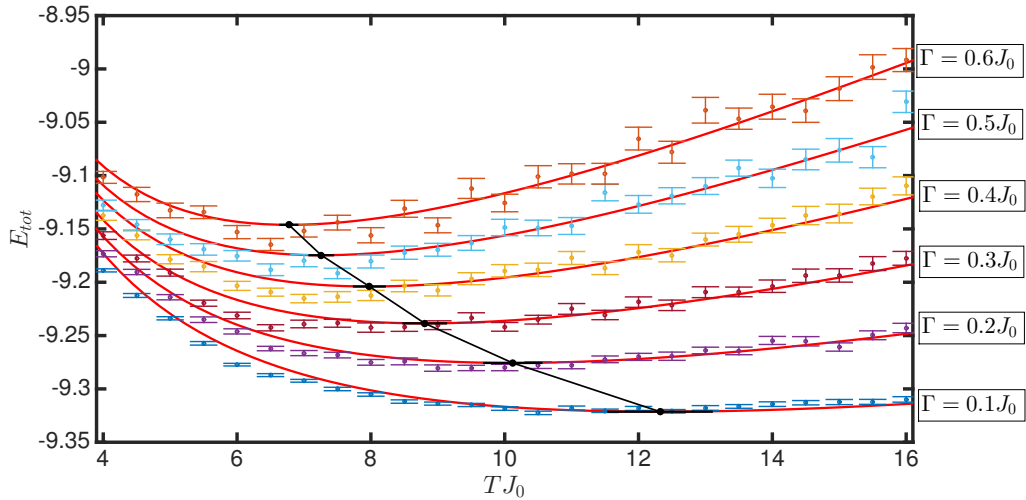
FIGURE 7.3: Total energy after adiabatic state preparation as a function of the evolution time, obtained from exact diagonalisation calculation of the Bose-Hubbard model with 8 sites and 8 particles. The data shown here is for noise strength $\Gamma/J_0 = 0.1, ..., 0.6$. The averaged total energy is calculated over 100 runs, and the error bars represent the statistical errors. The fitting function is $E = aT + b/T + c$ (red line). The calculated value of T_{min} (Eq. 7.9) that giving minimum total energy according to the noise strength (black) with the error bar associated with 95% confidence of fitting parameters, shifts to zero as the noise becomes stronger.

A clear relation between T_{min} and noise strength Γ/J shown in Fig. 7.4 shows agreement with the analysis in Eq. (7.9).
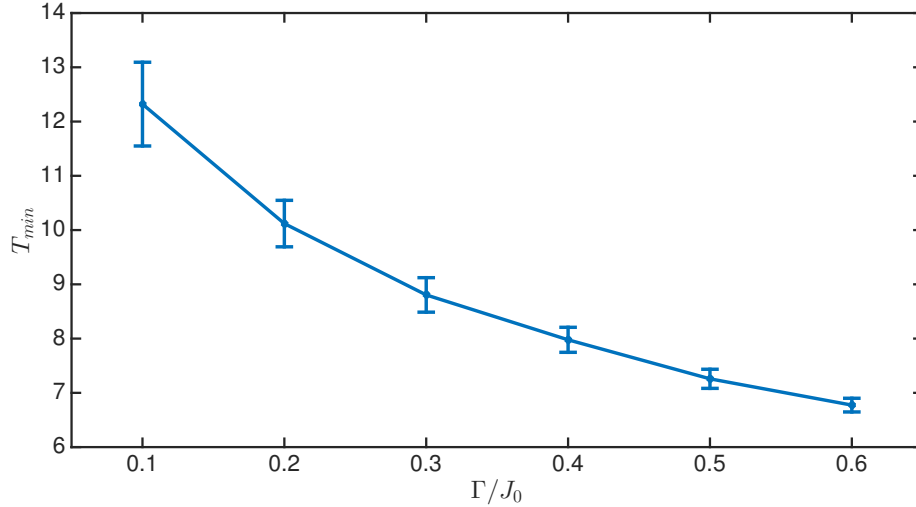
FIGURE 7.4: Values of T_{min} of adiabatic state preparations as a function of the noise strength, obtained from exact diagonalisation calcualtions of the Bose-Hubbard model with 8 sites and 8 particles. As the noise strength increases, the value of T_{min} deceases as in Eq. (7.9).

In this section, we analysed the dependence of the energy input with respect to the evolution time both for the non-adiabaticity and the heating effect. From the numerical results and quantity analysis, we are able to explain the behaviour of the total energy in different settings, and obtain deeper understanding of the amplitude noise in adiabatic state preparations.

7.3   Thermalisation of amplitude noise

Often, the energy introduced by the heating is assumed to be thermalised and increase the temperature. However, different types of classical noise introduce different heating dynamics to atoms in optical lattices. For example, the effects of amplitude noise in optical lattices are significant for both Mott Insulator and superfluid phases (Sec. 3.4), but spontaneous emissions have a very weak heating influence on the atoms in the lowest band in the Mott Insulator phase [169]. The heating effect and thermalisation of spontaneous emissions have been previously investigated [37, 170]. Unlike the local quench from the spontaneous emission, the amplitude noise is global and the thermalisation behaviour can be different.

In this section, we discuss the behaviour of the system after an amplitude noise pulse. Initially, the system is in the ground state of the Bose-Hubbard Hamiltonian in different phases. Then, an amplitude noise pulse is applied to the system for a total time $T_{pulse}J_0 = 1$. After the noise is turned off, the system evolves under the same Hamiltonian for an amount of time. The Hamiltonian of the system with amplitude noise is in the form

$$H_{sys} = H_0(J_0, U_0) + H_1(\frac{dJ}{dV}, \frac{dU}{dV})\delta V \tag{7.10}$$

$$H_1(\frac{dJ}{dV}, \frac{dU}{dV})\delta V = \sqrt{2\Gamma}\xi(t)\left(-2\cos^2(\theta)J\sum_{\langle i,j\rangle} b_i^\dagger b_j + 2\sin^2(\theta)\frac{U}{2}\sum_i n_i(n_i - 1)\right) \tag{7.11}$$

where H_0 is the Bose-Hubbard Hamiltonian. In the noise pulse period, the dynamics of the system can be calculated via the master equation

$$\dot{\rho}(t) = -i[H_0, \rho] - \Gamma[H_1, [H_1, \rho(t)]] . \tag{7.12}$$

To study the dynamics described by the master equation, we simulate the trajectories of stochastic Schrödinger equations of a quantum state, and calculate averaged values of the quantity of interest. In the following research, we focus on the behaviour of the kinetic energy of the system, $E_{\rm kin} = \langle H_{\rm kin}\rangle$ where $H_{\rm kin} = -J_0\sum_{\langle i,j\rangle} b_i^\dagger b_j$. As mentioned in Sec. 4.2, the time evolution in the presence of the noise is implemented by evolving the quantum state with small time step dt to make sure the Ito rules (Eq. 4.56) applies, so that the system is considered under the influence of white noise. Because of the noise operator H_1 is global, the advantages of this approach compared to quantum trajectories method [85] is that the effective Hamiltonian in the evolution costs less computational resources than the latter. In the method, the effective Hamiltonian $H_{sys} = H_0 + H_1\delta V$, where δV can be sampled from a normal distribution. Applying quantum trajectories method requires evolution with the effective Hamiltonian is $H_{\rm eff} = H_0 - i\Gamma H_1^2$. The calculation of H_1^2 in quantum trajectories method cost more computational resources than the approach of evolution under stochastic Schrödinger equation which requires only the evolution with the first order of H_1, especially when the system size is large.

The process can be addressed as

- Set the initial state as the ground state $|E_0(g)\rangle$ of the Bose-Hubbard Hamiltonian with a given value $g = U_0/J_0$

- Evolve under noisy Hamiltonian H_{sys} with different random sampling for a total time $T_{pulse}J_0 = 1$, and reach the quantum state after the noise pulse, $|\psi(0)\rangle$.

- Turn off the noise and evolve the system with the Bose-Hubbard Hamiltonian of the same value of g for a total relaxation time $TJ_0 = 10$. The instantaneous quantum state is $|\psi(t)\rangle = e^{-iH_0 t}|\psi(0)\rangle$.

- Track on the average value of the kinetic energy $E_{\mathrm{kin}}(t)$ as a function of relaxation time

Whether a system will be thermalised under unitary time evolutions can be discussed in the context of the "eigenstate thermalisation hypothesis" [171–173]. This theory describes a steady state that the system might relax to. Since we apply amplitude noise to the ground state of the Bose-Hubbard Hamiltonian, the quantum state after the pulse $|\psi(0)\rangle$ is not an eigenstate $|E_n\rangle$. When a system has a well-defined total energy E, quantum statistical mechanics assumes that the average value of some observable $(\hat{O})$ quantity $\langle\psi|\hat{O}|\psi\rangle$ over time $(\langle\ldots\rangle_t)$ is equal to an ensemble average of all states around the energy E [171]:

$$\langle\langle\psi|\hat{O}|\psi\rangle\rangle_t = \sum_j \Delta(E, E_j)\langle E_j|\hat{O}|E_j\rangle \equiv \langle\hat{O}\rangle_{micro}\,, \qquad (7.13)$$

where $\Delta(E, E_j)$ is a normalised function of E_j that is sharply peaked at $\langle E_j| H|E_j\rangle = E$. We expand the quantum state $|\psi(0)\rangle$ in the eigenbasis $\{|E_n\rangle\}$ with associated eigenenergy E_n, as $|\psi(0)\rangle = \sum_n C_n|E_n\rangle$. The kinetic energy can be obtained as

$$\begin{aligned} E_{\mathrm{kin}}(t) &= \langle\psi(t)|H_{\mathrm{kin}}|\psi(t)\rangle \\ &= \sum_n |C_n|^2\langle E_n|H_{\mathrm{kin}}|E_n\rangle + \sum_{n\neq n'} C_n^* C_{n'}\langle E_n|H_{\mathrm{kin}}|E_{n'}\rangle e^{-i(E_n - E_{n'})t}\,. \end{aligned}$$

$$(7.14)$$

The second term will vanish in the long-time average,

$$\lim_{T\to\infty}\frac{1}{T}\int_0^T \sum_{n\neq n'} C_n^* C_{n'}\langle E_n|H_{\mathrm{kin}}|E_{n'}\rangle e^{-i(E_n - E_{n'})t} = 0\,, \qquad (7.15)$$

and we can obtain the kinetic energy of the steady state

$$E_{\mathrm{kin}}^\infty = \sum_n |C_n|^2\langle E_n|H_{\mathrm{kin}}|E_n\rangle\,. \qquad (7.16)$$

The expression of the steady kinetic energy depends on two main factors: the coefficients C_n in the expansion, and the kinetic energy of the eigenstate $\langle E_n|H_{\mathrm{kin}}|E_n\rangle$.If

the kinetic energies in the eigenstates vary smoothly with E in a windows determined by C_n and off-diagonal terms are small ($\langle E_n | H_{\text{kin}} | E_{n'} \rangle \to 0$), the system will relax to a state that the observable can be described with a micro-canonical ensemble where the probability of the system being in eigenstates is peaked in one particular eigenstate. We refer [171, 172] for more detailed discussions.

The setting of our amplitude noise is weak, the noise strength is $\Gamma = 0.1 J_0$, and the offset is $\Delta\theta = 0.01\pi/4$. The energy input from this amplitude noise is small, and the thermalisation process is mainly determined by a low energy eigenspace. Here we use exact diagonalisation to calculate low energy eigenstates of the Bose-Hubbard model with 10 particles and 10 sites. From the low energy spectrum of 1000 lowest eigenstates, we calculate the equilibrium value of kinetic energy $E_{\text{kin}}^{\text{eq}}$ from exponential fitting of the inverse temperature β that gives the same mean-energy. Also the E_{kin}^{∞} are obtained in the low energy spectrum. Our numerical results are shown in Fig. 7.5. The dynamics shown on the left is the kinetic energy in the relaxation time where the system is evolving under the corresponding Bose-Hubbard Hamiltonian. In the superfluid phase, like for $g = 1, 2$, the kinetic energy E_{kin} relaxes to the $E_{\text{kin}}^{\text{eq}}$ from Boltzmann distribution within statistical error, which indicates thermalisation of the kinect energy. However, in the Mott Insulator phase for $g = 4, 5$, the kinetic E_{kin} relaxes to the E_{kin}^{∞}, which does not correspond to Boltzmann distribution with the appropriate mean total energy. To understand the change of the behaviour, we exploit the fact that the setting of this amplitude noise is weak, and gives rise to populations of low energy states. The dominant amplitude is of the ground state, shown on the right side of Fig. 7.5. In the superfluid phase, the E_{kin} grows linearly as a function of E_n [37]. This growth implies a very weak interaction energy, and in the limiting cases of $U = 0$, the total energy is exactly the kinetic energy. At the phase transition point between $U_0/J_0 \approx 3$ and $U_0/J_0 \approx 4$, the distribution of kinetic energy in eigenstates has a non-linear relation with the eigenenergy, and a thermal kinetic energy is not expected. This is directly analogous to the results of Ref. [37, 170], and the corresponding discussion of the relation between the kinetic energy and the eigenenergy of a eigenstate in the Bose-Hubbard model. We expect similar behaviour for larger systems within the weak noise regime.

In this section, we studied the dynamics of the system after an amplitude noise pulse, and observed a change in the thermalisation behaviour at the phase transition point between the superfluid and Mott Insulator phases. The kinetic energy relaxes to a steady value which corresponds to a thermal distribution in the superfluid phase. However, in the Mott Insulator phase, the kinetic energy relaxes to a steady value which is clearly non-thermal. Because the analysis of our results depends on low energy spectrum, the understanding of thermalisation may extend to much larger system with a weak amplitude noise.

7.4 Conclusions

In this chapter, we extended our research to discuss energy input in adiabatic processes with amplitude noise. First, we discussed the competition of the non-adiabaticity and the amplitude noise in final fidelities. The maximal fidelity is found at the point that the adiabaticity can no longer compensate the heating effects. We also observe the difference of evolution times providing maximal fidelity and minimal total energy. Thereby, we studied the total energy after adiabatic state preparation to obtain a full understanding of the amplitude noise. Through quantitative analysis of the energy inputs from non-adiabaticity and heating effects, we are able to explain the behaviour of the evolution time associated with minimal total energy with constant noise strength.

We also studied the thermalisation behaviour of the system after an application of amplitude noise pulse. We take the kinetic energy as the quantity of interest, as any non-local observables will never thermalised [173]. In both the superfluid phase and the Mott Insulator phase, the kinetic energy relaxes to a steady value, which corresponds to a thermal distribution only in the superfluid phase. The understanding of thermalisation behaviour may provide insights of protecting fragile quantum states that are sensitive to temperature.
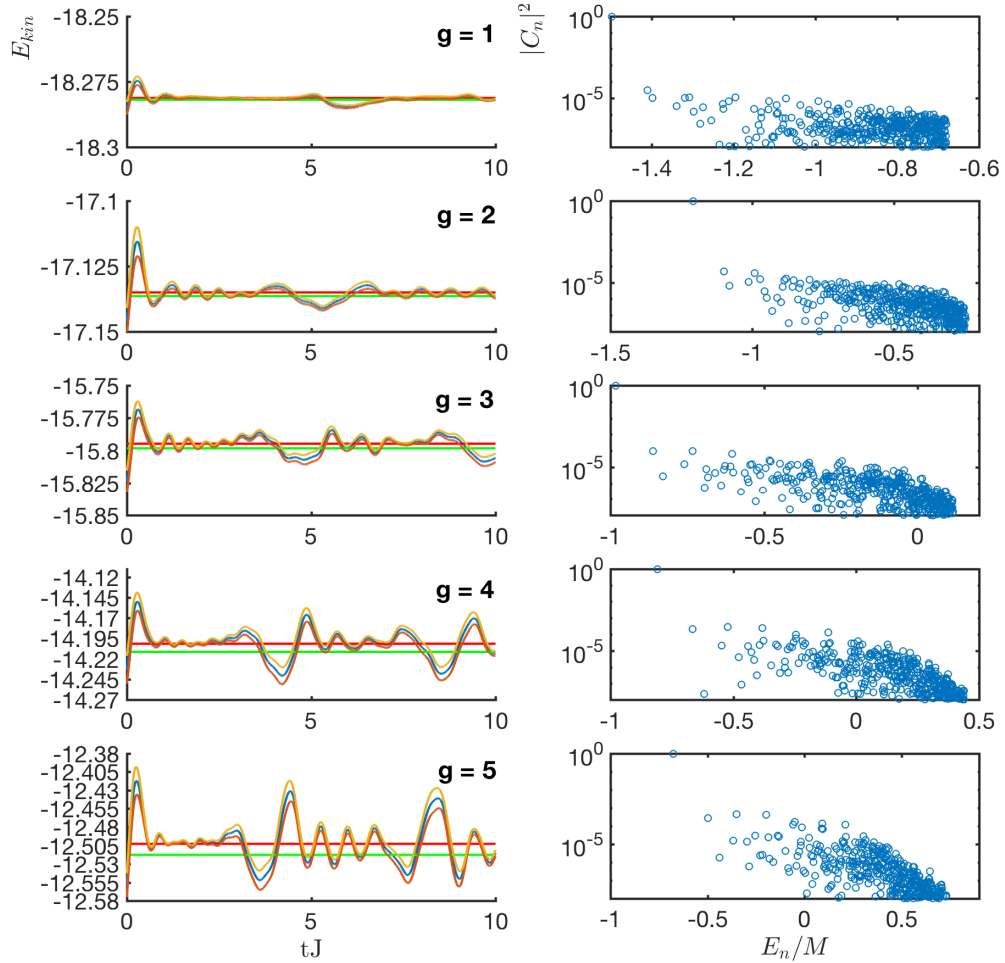
FIGURE 7.5: Kinetic energies as a function of time (left panels) and corresponding occupation numbers in the lowest 1000 eigenstates after the application of the noise pulse (right panels), obtained from exact diagonalisation calculations for Bose-Hubbard model with 10 particles and 10 sites. The amplitude noise is turned for $T_{pulse} = 1/J_0$ with the noise strength is $\Gamma = 0.1J_0$ and $\theta = 0.99\pi/4$, as in Eq. 7.10. At $t = 0$, the noise is turned off and the system evolves under the Bose-Hubbard model Hamilatonian. The kinectic energy (blue line) E_{kin} are demonstrated in figures on the left (with yellow and orange lines show the statistical error). The red lines are the weighted kinetic energy in diagonal ensemble E_{kin}^{∞}, calculated as in Eq. 7.16. The green lines represent the equilibrium kinetic energy from exponential fitting $E_{\text{kin}}^{\text{eq}}$ of corresponding eigenenergies. In the superfluid regime ($g = 1, 2$), the kinetic energy relax to $E_{\text{kin}}^{\text{eq}}$, which indicates a thermalisation of the system. In the Mott Insulator phase, especially for $g = 5$, the kinetic energy relax to E_{kin}^{∞}, which is far from $E_{\text{kin}}^{\text{eq}}$. The fluctuations afterwards are due to limited size effects. The figures on the right show the distributions of occupation probablities ($|C_n|^2$) in the lowest 1000 eigenstates after the application of the noise pulse.

Chapter 8

A quantum algorithm for turbulent mixing of fluids

In this chapter[1], we discuss applying quantum algorithms to fluid dynamics problems. With the rapid developments of quantum algorithms and quantum hardware, it is an opportune time to identify potential applications of quantum algorithms and quantum computers. This conversation will not only raise attention from both the engineering community regarding these technologies and the physics community, but also provide a framework to identify requirements of future practical quantum computers. The intellectual exchanges established will surely benefit both fields.

8.1   Introduction

The use of large quantum computers providing answers to problems intractable by classical computers has been discussed in a lot of contexts over the last 30 years [174]. In the last few years, there has been a increasing interest in quantum algorithms providing quantum speed up over classical Monte Carlo (MC) techniques [53, 92, 93, 97, 109, 175–178]. As MC techniques are implemented widely in science, the realisation of large-scale quantum computers has the potential to boost computation in a wide range of subjects. Rapid developments of platforms for quantum computing has been reported [179–186], and questions

---

[1]This work is taken in part from the publication *Turbulent Mixing Simulation via a Quantum Algorithm* G. Xu, A. J. Daley, P. Givi, R. D. Somma, AIAA journal pp. 1-13, 2017/12/13 2017

The author of this thesis performed all of the numerical calculations, analytical calculations of the error of quantum algorithm, wrote the sections on numerical calculations, and produced all the plots.

about the impact of new developments and the potential applications are very important. Here, we would like to establish connections between fluid engineering and quantum computing, providing a quantum speed up for a class of turbulent flow problems on a quantum computer, and to initiate further discussions linking these two fields.

In fluid mechanics, there is one category of the dynamic of the system can be characterised by partial differential equations like FokkerPlanck equations and Navier-Stokes equations. One approach to answer these problems is to solve the equations directly. For now it is difficult to solve a complex system analytically via a classical algorithm. However, for a simple system that has linear equations to describe the dynamics, the quantum computer can solve the problems [58, 60, 187]. Another approach is to simulate the dynamics under the equations via classical MC methods, especially a class of turbulent scalar mixing problems [188–196]. applying probability density function (PDF) methods, for instance, Reynolds averaged Navier-Stokes (RANS) [197, 198] and large eddy simulation (LES) [199, 200]. The efficiency of the PDF simulations is very important to reach high accuracy especially for large scale system. It is a open question that whether quantum computation can improve the accuracy of these problem.

To utilise classical MC methods for PDF transport simulations, the PDF is represented as computational elements or particles moving in the fluid and the random events of each element are determined according to a chosen physics model [201–203]. The statistics of the ensemble are described by the average data of the function(s) of interest. We then repeat the MC process many times to obtain an estimated value of the function of interest with desired accuracy. The parameters of the calculation that determine the complexity of the MC calculation include the desired final precision $\epsilon \ll 1$ and c, which is the confidence level of the estimation. In the situation that the interested quantity has bounded moments, for instance in turbulent mixing, we can estimate the repetition number N_r to achieve such conditions. From the central limit theorem, the statistical error of the estimation is proportional to the inverse of the square root of the repetition number, $\varepsilon \propto 1/\sqrt{N_r}$. Thus, the complexity dependence of MC is proportional to $1/\varepsilon^2$. In conventional techniques, this dependence is inevitable and better algorithms are highly desirable.

Recent research in quantum enhanced measurements (quantum metrology) [91–93] extend the abilities of quantum computers for better estimations of certain quantities in terms of a quadratically improved precision scaling in the error. In other words, the quantum computer requires quadratically less resources to reach the same precision as classical MC calculations. These methods apply to more general problems estimating expected values of interesting quantities with minimal assumptions and arbitrary confidence levels [93]. However, the

adaption of such methods to improve the classical MC method had been done only recently [97].

Here, we develop a quantum algorithm adapted from [93] to solve fluid dynamics MC problems. We tailor our quantum algorithm for turbulent mixing problems and compare specific examples for reacting flow described by coalescence/dispersion (C/D) closure [204–206], but in general, what we do here applies to large classes of mixing problems. Estimating the properties of the PDF of a simple binary scalar mixing process, we demonstrate comparisons of the errors between MC methods and our quantum algorithm and present a quadratic speedup over MC methods in terms of number of repetitions N_r. In the setting of binary mixing, an analytical solution for the moments can be acquired and allows us to analyse the statistical errors. The MC simulations are implemented to calculate the 4-th central moment of the PDF during the dynamics as an example, to understand the behaviour of MC methods. Then we simulate our quantum algorithm by sampling the probability distribution of the measurement outcomes. Naturally our quantum algorithm requires significantly many more qubits than a classical computer could handle. Nevertheless, due to the simplicity of this problem, the probability distribution of the outputs can be obtained analytically, which is not possible in general cases. We then compare the errors of estimations between quantum algorithm and MC methods with same value of N_r, and the error scaling presents a quadratic speed up. Similar results will hold for estimating other properties of the PDF.

In this chapter, we briefly introduce the turbulent scalar mixing problems and the C/D closure in Sec. 8.2, followed by reacting flow problems in Sec 8.3. We then describe the implementation of the classical MC method and demonstrate numerical calculations estimating the 4-th moment of the PDF solving a binary mixing problem as an example, as well as the mean fraction conversion of mass fraction of fuel in reacting flow as another example. In Sec. 8.5, we present our quantum algorithm tailored to simulate the C/D model and provide the simulation of the binary mixing problem. By comparison of the error scaling of both methods, we are able to identify the advantages of the quantum algorithm. We conclude and discuss the outlook of the topics related to our research in Sec. 8.6.

8.2   Turbulent scalar mixing

In this section, we introduce the background of turbulent scalar mixing problems that can be solved by the single-point PDF transport equation. Specifically, we consider a coalescence/dispersion (C/D) mixing model where we can obtain analytical solutions of central moments for the purpose of demonstrating different

methods. We consider the mixing of Fickian scalars[2] $\phi = \phi(\vec{x}, t)$, where $\vec{x}$ is the position in space, starting from a binary state in the range $\phi_\ell \leq \phi \leq \phi_u$. We denote the PDF of the scalar as $P(\psi, t)$, with ψ representing the composition domain of ϕ. With the homogeneous turbulent flow assumption, the statistics are independent of spatial degrees of freedom. The equations of motion for the PDF $P(\psi, t)$ are [195]

$$\frac{\partial P(\psi, t)}{\partial t} + \frac{\partial^2 (\mathcal{E} P(\psi, t))}{\partial \psi^2} = 0 \, , \tag{8.1}$$

$$\frac{\partial P(\psi, t)}{\partial t} + \frac{\partial (\mathcal{D} P(\psi, t))}{\partial \psi} = 0 \, . \tag{8.2}$$

Here, $\mathcal{E}$ is the conditional expected value of the scalar dissipation of $\phi(\vec{x}, t)$ and $\mathcal{D}$ denotes the conditional expected value of the scalar diffusion. $\mathcal{E}$ and $\mathcal{D}$ are defined as

$$\mathcal{E}(\psi, t) = E[\Gamma \nabla \phi \cdot \nabla \phi | \phi(\vec{x}, t) = \psi], \quad \mathcal{D}(\psi, t) = E[\Gamma \nabla^2 \phi | \phi(\vec{x}, t) = \psi], \tag{8.3}$$

where Γ is the binary Fickian diffusion coefficient. We use the standard statistical notation where $E[y]$ denotes the expected value of a random variable y and $E[y|z]$ denote the conditional expected value of y, conditioned on an event z. The single-point PDF description $P(\psi, t)$ has been used to solve many turbulence closure problems [204–216]. The available models take the form of a Langevin equation with the corresponding Fokker-Planck equation describing the PDF, or the form of a phenomenological transport equation for the PDF evolution [217].

To demonstrate the performance of MC methods in a simple example, we consider the coalescence/dispersion (C/D) mixing models, described by the equation of motion [205, 206].

$$\frac{\partial P(\psi, t)}{\partial t} = -2\beta\omega P(\psi, t)$$
$$+ 2\beta\omega \int d\psi' \int d\psi'' P(\psi', t) P(\psi'', t) \int_0^1 d\alpha A(\alpha)$$
$$\times \delta[\psi - (1 - \alpha)\psi' - \frac{1}{2}\alpha(\psi' + \psi'')] \, , \tag{8.4}$$

where $\delta(x)$ denotes the Dirac delta function, and $A(\alpha)$ is the PDF of the random variable α with the range of $\alpha \in [0, 1]$. The conditions of mixing are detemined by the value of α. For example, in the so-called Curl's model [218], we have $A(\alpha) = \delta(\alpha - 1)$ and $A(\alpha) = 1$ in the closure of Janicka *et al.* [204]. The parameter ω denotes the mixing frequency and determines the decay of the variance. The

---

[2]stochastically distributed scalar variables in Fickian diffusion process

parameter β is related to the PDF of α, as follows:

$$\beta = \frac{1}{a_1 - \frac{1}{2}a_2} \ , \ a_m = \int_0^1 d\alpha \ \alpha^m A(\alpha) \ , \tag{8.5}$$

where a_m denotes the m-th moments of the random variable α. Characterised by Eq. (8.4), all C/D models have the same rate of variance decay as ω.
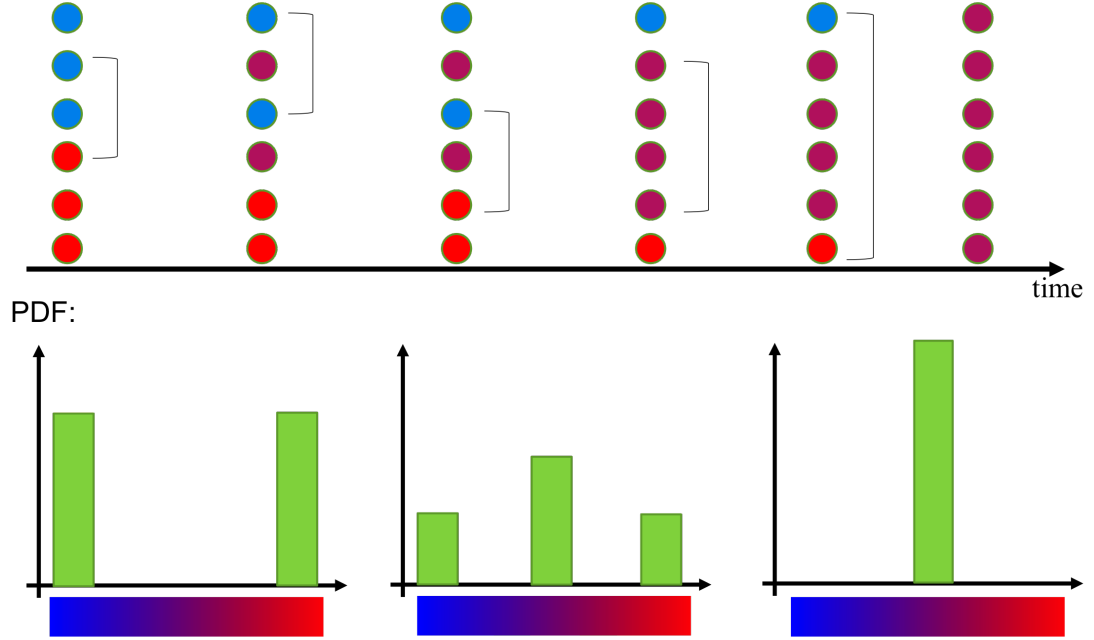

FIGURE 8.1: Sketch of binary mixing scheme of a homogeneous system. The colours associate with the circles represent different values of scalar associated with the simulation element. The figure above shows the mixing process with initial condition of PDF $P(\psi, 0) = \frac{1}{2}\delta(\psi - \phi_l) + \frac{1}{2}\delta(\psi - \phi_u)$, where ψ represents the Fickian scalar and ϕ_l, ϕ_u represent the lower and upper limit of the scalar range. As time grows, the elements exchange and rearrange the scalar values randomly and the probability distribution function of the scalar changes accordingly. The simulation via classical Monte Carlo is to obtain an estimation of the PDF as a function of time.

The central moments μ_l $(l = 1, 2, \ldots)$ can be used to describe the properties of the PDF, defined as

$$\mu_l(t) = E[(\psi - E[\psi])^l] \ . \tag{8.6}$$

In many cases, we can obtain analytical expressions of such moments, which are useful to demonstrate the accuracy of algorithms. In binary mixing problems (see Fig. 8.1), we choose the initial condition $P(\psi, t = 0) = \frac{1}{2}[\delta(\psi - \phi_\ell) + \delta(\psi - \phi_u)]$,

where the bounds are $\phi_\ell = -1$, $\phi_u = 1$ in Curl's model. We provide the first four central moments expressed as:

$$\mu_1(t) = \mu_1(0) = 0 \ , \tag{8.7}$$

$$\mu_2(t) \equiv \sigma^2(t) = e^{-2\omega t} \ , \tag{8.8}$$

$$\mu_3(t) = \mu_3(0) = 0, \tag{8.9}$$

$$\mu_4(t) = \left(4e^{\gamma \omega t} - 3\right) e^{-4\omega t} \ , \tag{8.10}$$

where

$$\gamma = \frac{a_2 + \frac{1}{4}a_4 - a_3}{a_1 - \frac{1}{2}a_2} \ . \tag{8.11}$$

8.3 Reacting flows

The research on turbulence reacting flow by Li and Toor [219], and Dutta and Tarbell [220] provide us means to predict the mean rate of reactant conversion in a chemical reaction of the type $A + B \to P$ in homogeneous turbulent flows, where A and B are two reacting chemicals and P denotes their products. Using the probability density function (PDF) method of coalescence/dispersion (C/D) model developed by Frankel, Madnia and Givi [221], we can obtain very accurate classical Monte Carlo (MC) simulation results with high precision. The MC method requires N_r repetitions to achieve a desired accuracy with the dependence $\epsilon = \mathcal{O}(\frac{1}{N_r})$. In a system with homogeneous turbulent flow, described by the C/D model, the PDF of the Fickian scalars ϕ of the field can also provide insight to track different chemical components, represented as a scalar function of ϕ.

With the assumption of an infinitely fast chemistry compared to other timescales of the dynamics, i.e. $F + O \to P$, the dynamics of two components fuel ($F(t)$) and oxidizer ($O(t)$) are scalar functions are related to the evolution of field scalars $\psi(t)$. The general form of the evolution equations of this model was described in Eq. (8.4). Here, we take the mean fractional mass conversion $\mathcal{F}$ of the fuel F as an example to compare the performance of classical MC simulation and our quantum algorithm. The scalar function of fuel in an infinitely fast reacting flow is,

$$F(\psi) = H(\psi) \cdot \psi \ , \tag{8.12}$$

where ψ is the field scalar, and H is the Heaviside step function $H(x) = 0.5(1 + sgn(x))$. In this setting, the positive scalars $\psi > 0$ represent the fuel. The

corresponding oxidizer scalar function then is,

$$O(\psi) = (H(\psi) - 1) \cdot \psi \, , \tag{8.13}$$

where all the negative scalars represent the oxidizer.

Here, we focus on applying MC simulation and our quantum algorithm to estimate the mean fractional mass conversion of the fuel:

$$\mathcal{F}(t) = 1 - \frac{\langle F \rangle_t}{\langle F \rangle_0} \, , \tag{8.14}$$

where $\langle F \rangle$ represents the stochastic average value of function F. The range of $\mathcal{F}(t)$ is $[0, 1]$ in this setting. Initially $\mathcal{F}(0) = 0$ by definition. In the setting of the initial condition $P(\psi, 0) = \frac{1}{2}[\delta(\psi - 1) + \delta(\psi + 1)]$ with Curl's model, $P(\psi, \infty) = \delta(\psi)$ and $F(\infty) = 0$, then the value of $\mathcal{F}(\infty) = 1$. This feature of $\mathcal{F}$ can be simulated directly by our quantum PEA without normalisation.

8.4 Monte Carlo methods for the C/D model

To simulate a system describe by the C/D model [Eq. (8.4)] using a classical MC method, we choose a number of computational elements or "particles" N_p. Each particle is associated with a scalar $\psi^k(i, t_j)$ in the simulation of random processes, where $i = 1, \ldots, N_p$ is particle number, $j = 0, \ldots, N_t$ is the time step, and $k = 1, \ldots, N_r$ is the number of realisations. These particles are related to different populations of different values of ψ, so the number of particles N_p also contributes to determining the accuracy of simulations. The variable t_j denotes the time at the j-th step, and is defined as $t_j = j\Delta t$. To reach desired precision and confidence level, the algorithm should be repeated N_r times. The total evolution time $t > 0$, β and the mixing frequency ω are defined by the physical process of the C/D model (Sec. 8.2). The accuracy and the complexity of the simulation are related to the numerical parameters like Δt, N_p, and N_r. The explicit processing of classical MC algorithm is:

Input: $P(\psi, 0)$, t, β, ω, Δt, N_p, N_r

1. Calculate $N_t = \lceil t/\Delta t \rceil$, $N_s = \lceil \beta\omega\Delta t N_p \rceil$. Set $k = 1$, $j = 1$, $n_s = 1$, and $t_0 = 0$.
2. Repeat until $k > N_r$:
    2.1. For $i = 1, \ldots, N_p$, initialize $\psi^k(i, 0)$ according to a discrete initial probability distribution $Q(\psi^k(1, 0), \ldots, \psi^k(N_p, 0))$ realising $P(\psi, 0)$.
    2.2. Repeat until $j > N_t$:
        2.2.1. Set $t_j = j\Delta t$ and initiate $\psi^k(i, t_j) := \psi^k(i, t_{j-1})$ for all $i \in \{1, \ldots, N_p\}$.
        2.2.2. Repeat until $n_s > N_s$:
            2.2.2.1. Obtain random integers $i_1, i_2 \in \{1, \ldots, N_p\}$.
            2.2.2.2. Sample a value of $\alpha \in [0, 1]$ according to the probability distribution $A(\alpha)$.
            2.2.2.3. Perform the mixing transformation:

$$\psi^k(i_1, t_j) \leftarrow (1-\alpha)\psi^k(i_1, t_j) + \alpha(\psi^k(i_1, t_j) + \psi^k(i_2, t_j))/2,$$
$$\psi^k(i_2, t_j) \leftarrow (1-\alpha)\psi^k(i_2, t_j) + \alpha(\psi^k(i_1, t_j) + \psi^k(i_2, t_j))/2.$$

            2.2.2.4. $n_s \leftarrow n_s + 1$.
        2.2.3. $j \leftarrow j + 1$.
    2.3. $k \leftarrow k + 1$:

3. **Output**: $\psi^k(i, t_j)$ for all k, i, t_j.

The initial discrete distribution $Q(\psi^k(1, 0), \ldots, \psi^k(N_p, 0))$ simulates $P(\psi, 0)$ in Eq. (8.4) and is independent of the number of realisations. At time t_j, the the MC method provides a distribution $Q(\psi^k(1, t_j), \ldots, \psi^k(N_p, t_j))$ to estimate $P(\psi, t_j)$ or central moments of ψ. To estimate the PDF, we build a histogram with the values of $\psi^k(i, t_j)$ within a corresponding (machine) precision $\Delta\psi$ after proper normalisation. Different central moments of the distribution $P(\psi, t)$ estimated by the MC method can be calculated as

$$\hat{\mu}_l(t_j) := \frac{1}{N_r} \sum_{k=1}^{N_r} \hat{\mu}_l^k(t_j) \, , \tag{8.15}$$

with the estimation from each MC run calculated with outputs of a random vector $(\psi^k(1, t), \ldots, \psi^k(N_p, t))$ as

$$\hat{\mu}_l^k(t_j) := \frac{1}{N_p} \sum_{i=1}^{N_p} \left(\psi^k(i, t_j) - \hat{E}[\psi^k(t_j)] \right)^l \, . \tag{8.16}$$

The notation $\hat{X}$ denotes an estimator of X. The estimator of the expected value of $\psi^k(i, t_j)$, $\hat{E}[\psi^k(t_j)]$ after the k-th realisation is

$$\hat{E}[\psi^k(t_j)] := \frac{1}{N_p} \sum_{i=1}^{N_p} \psi^k(i, t_j) \ . \tag{8.17}$$

As described above, the MC algorithm takes the repetition number N_r as input and outputs $\psi^k(i, t_j)$ mimic the process according to the PDF transport function. The usual modification to achieve certain accuracy is to replace N_r by a function of the desired ϵ. To estimate specific properties of the PDF like the central moments, modifications of outputting the estimator rather than all values of $\psi^k(i, t_j)$ after each realisation can result in improvements in efficiency due to reduction of memory usage.

8.4.1 Complexity

Now we will discuss the complexity of implementing the MC method. For simplicity, we omit certain logarithmic factors in the expression of order notations. Disregarding the complexity of the initial state preparation $\psi^k(1, 0), \ldots, \psi^k(N_p, 0)$ and the complexity of the random number sampling, the dominant term in the expression of the complexity of the MC method is the number of updates of the state vector $\psi^k(i, t_j)$. To reach designated accuracy which depends on both N_r and N_p, the complexity to estimate relevant quantities is $O(N_r \ N_t \ N_s) = O(N_r t \beta \omega N_p)$. The overall precision ϵ, in the case of fixed N_p and constant confidence level c, has a direct relation with the number of repetitions N_r. That is, $\epsilon = O(1/\sqrt{N_r})$ from Chebyshev's inequality. Having the ϵ as an input parameter, the complexity of the MC method is of $\mathcal{O}(t \beta \omega N_p / \epsilon^2)$.

8.4.2 Example: classical Monte Carlo simulations of binary mixing

To demonstrate the performance and the complexity of the MC method, as well as to provide a basis for comparison with our quantum algorithm, we implement the MC simulation of a simple binary mixing problem that can be analytically solved. This will help to benchmark our algorithm to meet the expected performance of simulating a complex problem where the solution is unknown. In Curl's model, the PDF of the random variable α is $A(\alpha) = \delta(\alpha - 1)$, and the coefficients in analytical solution have been calculated as in Eq. (8.5) and Eq. (8.11), $\beta = 2$,

$\gamma = 0.5$. The mixing frequency is set to $\omega = 1$. The simulation is of the evolution time up to $t = 1$, and other numerical parameters are set to $\Delta t = 0.1$ and $N_p = 10^3$. The initial state is set according to the PDF $P(\psi, 0) = \frac{1}{2}\delta(\psi - 1) + \frac{1}{2}\delta(\psi + 1)$ taking the form of $\psi^k(i, 0) = -1$ for all $1 \le i \le N_p/2$, and $\psi^k(i, 0) = +1$ otherwise. We apply the MC method to estimate the 4-th central moment as a function of time, an as exactly solved for comparison in our restricted model in Eq. (8.10). However, the analytical solution is in the limit of infinite computational particles $N_p = \infty$. The statistical error with $N_p = 1000$ will be much smaller than the difference between the estimation and the analytical value. Therefore, we conduct a a very accurate simulation for finite number of particles $N_p = 10^3$ by repeating the MC method $N_r = 2^{20} \times 60$ times. The factorisation of this expression in this form is related to that of our quantum algorithm and discussed in 2.15. We denotes the result of such accurate estimate as $\tilde{\mu}_4(t)$, and the estimations from other simulations are then denoted as $\hat{\mu}_4(t)$ in Eq. (8.15).

The simulation results of MC methods are shown in Fig. 8.2. In Fig. 8.2 (a) we show the behaviour of $\hat{\mu}_4(t)$ exponentially decaying as a function of time for $N_r = 2^{10} \times 24$, and a comparison to the analytical solution. In Fig. 8.2 (b) we compare $\hat{\mu}_4(t)$ with different value of N_r normalised by a very accurate estimation $\tilde{\mu}_4(t)$. Note that $\hat{E}[\psi^k(t_j)] = 0$ in this case [see Eq. (8.17)]. To obtain the error bars of Fig. 8.2 (b), we first computed the moment $\hat{\mu}_4^k(t_j)$ for all the realisations $k = 1, \dots, N_r$, according to Eq. (8.16) in each run. Then, the estimated standard deviation associated with the average value $\hat{\mu}_4(t)$ (Eq. (8.15)) is

$$\hat{\sigma}_{\mu_4}(t_j) = \left[\frac{\sum_{k=1}^{N_r}(\hat{\mu}_4^k(t_j) - \hat{\mu}_4(t_j))^2}{(N_r - 1)} \right]^{1/2}. \tag{8.18}$$

To reach a 99.75% confidence level of estimating $\mu_4(t)$, the statistical error should be

$$\epsilon_C(t_j) := 3\hat{\sigma}_{\mu_4}(t_j) \tag{8.19}$$

which is defined as the error of the MC simulation in this setting. The error bars of Fig. 8.2 (b) denote the regions

$$\left[\frac{\hat{\mu}_4(t_j) - \epsilon_C(t_j)}{\tilde{\mu}_4(t_j)}, \frac{\hat{\mu}_4(t_j) + \epsilon_C(t_j)}{\tilde{\mu}_4(t_j)} \right]. \tag{8.20}$$

From the simulation results (Fig. 8.2) and the analysis above (Eq. 8.19), we observe that the dependence of the estimation errors with respect to the number of repetitions is of order $1/\sqrt{N_r}$. In the next sections (Sec. 8.5), we will present our quantum algorithm that can improve this dependence quadratically.

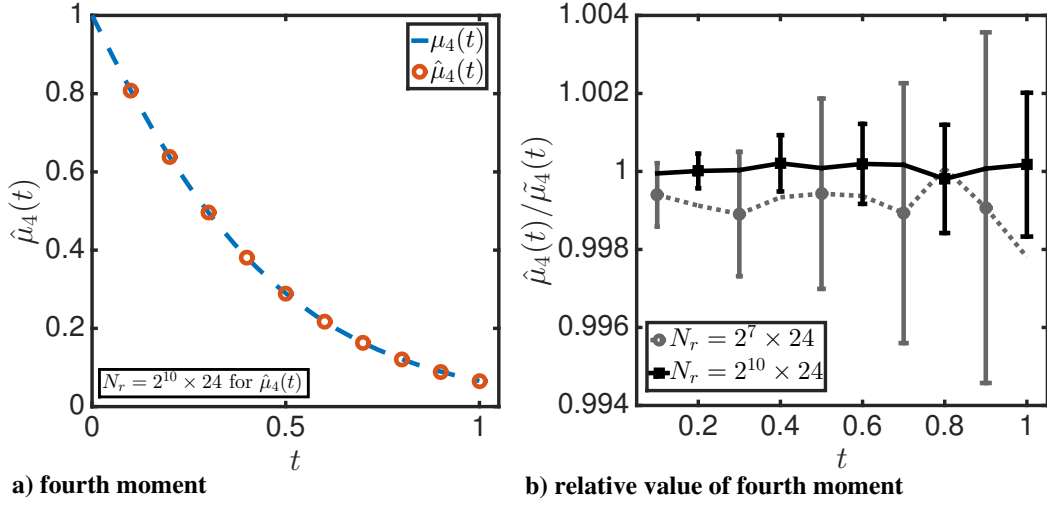a) fourth moment   b) relative value of fourth moment

FIGURE 8.2: Estimates of the 4-th central moment of the PDF for computational elements, obtained from MC simulations of a simple binary mixing problems using Curl's model. (a) Exponential decay of the estimated 4-th central moment $\hat{\mu}_4(t)$ [Eq. (8.15)] as a function of time for a number of repetitions $N_r = 2^{10} \times 24$. The estimated moments are very close to the exact solution $\mu_4(t)$ (dashed line), given by Eq. (8.10). (b) The estimated 4-th central moment relative to a very accurate estimate $\tilde{\mu}_4(t)$ for $N_p = 10^3$. To reach a confidence level of 99.75%, the error bars include up to three estimated standard deviations of the central moment [Eq. (8.19)]. The standard deviation is estimated by running the MC method N_r times, for $N_r = 2^7 \times 24$ (dotted line, odd positions) and $N_r = 2^{10} \times 24$ (solid line, even positions). The relative error increases with t as both $\hat{\mu}_4(t)$ and $\tilde{\mu}_4(t)$ decay exponentially with t. The estimation error of $\hat{\mu}_4(t)$ is of order $1/\sqrt{N_r}$. Both of the figures obtained from simulations with initial PDF $P(\psi, 0) = \frac{1}{2}\delta(\psi - 1) + \frac{1}{2}\delta(\psi + 1)$. The simulation parameters are $\beta = 2$, $\omega = 1$, $\gamma = 0.5$, $t = 1$, $\Delta t = 0.1$, and $N_p = 10^3$. The initial values are set so that $\psi^k(i, 0) = -1$ for all $i \leq N_p/2$ and $\psi^k(i, 0) = +1$, otherwise. This figure was reproduced from [222]

8.4.3 Example: classical Monte Carlo simulations of reacting flow

To estimate the mean fractional mass conversion of the fuel, we can simulate the PDF transport equation via a similar routine introduced by Sec. 8.4 and calculate the fuel function Eq. (8.12) and the mean fractional mass conversion Eq. (8.14). With the same settings of the system as we described in Sec. 8.4.2, the estimation

of the fuel function is

$$\hat{\mathcal{F}}^k(t_j) = 1 - \frac{2}{N_p} \sum_{i=1}^{N_p} H(\psi_i^k(t_j)) \cdot \psi_i^k(t_j) \ , \tag{8.21}$$

and, the estimator of the mean fractional mass conversion is

$$\hat{\mathcal{F}}(t_j) = \frac{1}{N_r} \sum_{k=1}^{N_r} \hat{\mathcal{F}}^k(t_j) \ . \tag{8.22}$$

The simulation results of MC method are shown in Fig. 8.3. As in Fig. 8.3 (a), we demonstrate the behaviour of $\hat{\mathcal{F}}(t)$ growing as a function of time for $N_r = 2^{17} \times 24$, and comparing to a very accurate results obtained for $N_r = 2^{17} \times 60$. In Fig. 8.3 (b), we demonstrate the simulation results of different values of repetitions and the deceasing of the error bars as the repetition number grows. The error bars are obtained in Fig. 8.3 (b) as following. We calculate the $\hat{\mathcal{F}}^k(t_j)$ (Eq. (8.21)) during the time evolution of each realisation. After all the N_r repetitions, we calculate the average value to generate $\hat{\mathcal{F}}(t_j)$ as in Eq. (8.22). Then the estimated standard deviation associated with the average value $\hat{\mathcal{F}}(t)$ is,

$$\hat{\sigma}_{\mathcal{F}}(t_j) = \left[\frac{\sum_{k=1}^{N_r}(\hat{\mathcal{F}}^k(t_j) - \hat{\mathcal{F}}(t_j))^2}{(N_r - 1)} \right]^{1/2} \ . \tag{8.23}$$

To reach a 99.75% confidence level of estimating $\mathcal{F}(t)$, the statistical error should be

$$\epsilon_C(t_j) := 3\hat{\sigma}_{\mathcal{F}}(t_j) \ , \tag{8.24}$$

which is defined as the error of the MC simulation in this setting. The error bars of Fig. 8.2 (b) denote the regions

$$\left[\frac{\hat{\mathcal{F}}(t_j) - \epsilon_C(t_j)}{\tilde{\mathcal{F}}(t_j)}, \frac{\hat{\mathcal{F}}(t_j) + \epsilon_C(t_j)}{\tilde{\mathcal{F}}(t_j)} \right] \ . \tag{8.25}$$

From the numerical simulation (Fig.8.3) and analysis of the statistical error (Eq. (8.24)), we observe that the classical error scales as square root of the repetition number $\epsilon_C \propto \mathcal{O}(1/\sqrt{N_r})$. These results provide a nice base for comparisons between the classical MC method and our quantum algorithm.
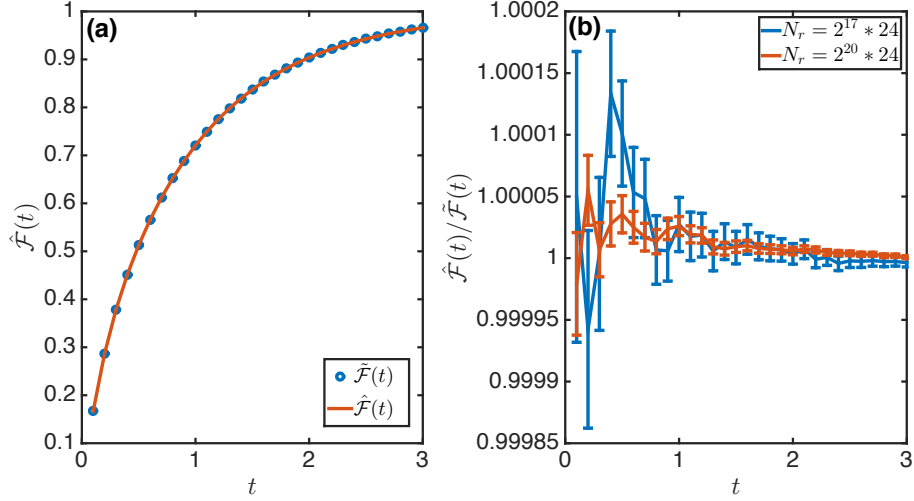
FIGURE 8.3: Estimates of the mean fractional mass conversion of fuels, obtained from MC simulations of a reacting flow process using Curl's model. (a) Growth of the estimated mean fractional mass conversion of fuels $\hat{\mathcal{F}}(t)$ [Eq. (8.14)] as a function of time for a number of repetitions $N_r = 2^{17} \times 24$. The estimated moments are very close to the exact solution $\mathcal{F}(t)$ (dashed line), given by Eq. (8.14). (b) The estimated mass fraction of fuels normalised with a very accurate estimate $\tilde{\mathcal{F}}(t)$ for $N_p = 10^3$. To reach a confidence level of 99.75%, the error bars include up to three estimated standard deviations of the central moment [Eq. (8.19)]. The standard deviation is estimated by running the MC method N_r times, for $N_r = 2^{17} \times 24$ (blue line) and $N_r = 2^{20} \times 24$ (red line). The relative error decreases with t as both $\hat{\mathcal{F}}(t)$ and $\tilde{\mathcal{F}}(t)$ increase with t to 3. The estimation error of $\hat{\mathcal{F}}(t)$ is of order $1/\sqrt{N_r}$. Both of the figures obtained from simulations with initial PDF $P(\psi, 0) = \frac{1}{2}\delta(\psi - 1) + \frac{1}{2}\delta(\psi + 1)$. The simulation parameters are $\beta = 2$, $\omega = 1$, $\Delta t = 0.1$, and $N_p = 10^3$. The initial values are set so that $\psi^k(i, 0) = -1$ for all $i \leq N_p/2$ and $\psi^k(i, 0) = +1$, otherwise.

8.5   A quantum algorithm for the C/D model

We present our quantum algorithm to simulate the same problem that can be solved by classical MC methods as in Sec. 8.4. We will illustrate that our algorithm provides a quadratic speedup over the MC method for high precision estimation of the properties of ψ. In this section, we first introduce the algorithm in Sec. 8.5.1, followed by the numerical simulations of the corresponding PEA of the quantum algorithm tailored for binary mixing problems in Sec. 8.5.3. The

comparison between the errors of classical MC methods and our quantum algorithm will be made, and the scaling of the error with respect to the repetition number will demonstrate the quantum speedup.

8.5.1   General statement of the algorithm

To build our quantum algorithm, the preparation of the initial quantum state $|\Psi\rangle$ is very important. The design of such initial state should encode all the information of the PDF in the discrete presentation like that of the MC algorithm in Sec. 8.4. The preparation is a sequence of elementary gates that mimic the random processes as in the MC method with reversible operations described in Sec. 2.1.3. The expression of the initial quantum state after the state preparation is,

$$
\begin{aligned}
|\Psi\rangle &= V\,|00\ldots0\rangle \\
&= \sum_{\psi_1,\ldots,\psi_{N_p}} \sqrt{Q(\psi_1,\ldots,\psi_{N_p})}\,|\psi_1,\ldots,\psi_{N_p}\rangle\,|\xi_{\psi_1,\ldots,\psi_{N_p}}\rangle\,. \quad (8.26)
\end{aligned}
$$

The amplitudes are related to the probabilities $Q(\psi_1,\ldots,\psi_{N_p},t_j)$ when $\psi^k(i,t_j) = \psi_i$, which are the same as that of the MC algorithm.

$$
Q(\psi_1,\ldots,\psi_{N_p}) = Q(\psi^k(1,t_j) = \psi_1,\ldots,\psi^k(N_p,t_j) = \psi_{N_p}) \quad (8.27)
$$

The state vector $|\psi_1,\ldots,\psi_{N_p}\rangle$ is a state where ψ_i is a binary representation of the computational basis. The ancillary state $|\xi_{\psi_1,\ldots,\psi_{N_p}}\rangle$ contains information for the implementation of state preparation and will be discarded. The algorithm for initial state preparation is:

Input: t, β, ω, Δt, N_p, N_r

1. Obtain $N_t = \lceil t/\Delta t \rceil$, $N_s = \lceil \beta\omega\Delta t N_p \rceil$.
2. Obtain the expression of all simple classical gates $v_1,\ldots,v_T$ required in the MC algorithm of Sec. 8.4.
3. Obtain the one and two-qubit gates $\tilde{v}_1,\ldots,\tilde{v}_T$ that are reversible versions of the v_i (Sec. 2.1.3) like a controlled gate with ancillary qubits.
4. Construct a unitary gate $V = \tilde{v}_T\ldots\tilde{v}_1$ and implement V on the state $|00\ldots0\rangle$.

Output: The quantum state $|\Psi\rangle = V\,|00\ldots0\rangle$.

A measurement on $|\Psi\rangle$ of the registers with $|\psi_1, \ldots, \psi_{N_p}\rangle$ encoded will output the configuration $\psi_1, \ldots, \psi_{N_p}$ with probability $Q(\psi_1, \ldots, \psi_{N_p})$. Instead of implementing such measurements directly, we employ the quantum metrology techniques introduced in Sec. 2.1.4 for better performance. The number of qubits to represent $|\Psi\rangle$ scales with the number of bits in the implementation of the classical MC method. The complexity of preparation of $|\Psi\rangle$ is similar to that of a single run of the MC algorithm because of the mapping from operations in the classical MC algorithm to an equivalent reversible unitary operation. Our algorithm is designed to reduce the required resource in terms of repetition number N_r.

Our algorithm provides estimates of certain properties of the distribution $Q(\psi_1, \ldots, \psi_{N_p})$. We take the estimation of the *l*-th central moment in Eq. (8.6) as an example. With a large value of N_r, the MC method provides the estimates of PDF, $Q(\psi_1, \ldots, \psi_{N_p})$, and then the *j*-th moment using Eq. (8.15) becomes

$$\frac{1}{N_p} \sum_{\psi_i, \ldots, \psi_{N_p}} Q(\psi_1, \ldots, \psi_{N_p}) \left[(\psi_1 - \tilde{E}[\psi^k(t_j)])^l + \ldots + (\psi_{N_p} - \tilde{E}[\psi^k(t_j)])^l \right] \ . \tag{8.28}$$

Here,

$$\tilde{E}[\psi^k(t_j)] := \frac{1}{N_p} \sum_{\psi_1, \ldots, \psi_{N_p}} Q(\psi_1, \ldots, \psi_{N_p})(\psi_1 + \ldots + \psi_{N_p}) \ . \tag{8.29}$$

In the binary mixing problem with the initial condition $P(\psi, t = 0) = \frac{1}{2}[\delta(\psi - \phi_\ell) + \delta(\psi - \phi_u)]$, the first moment $\tilde{E}[\psi^k(t_j)] = 0$. Then it is simple to construct a (diagonal) observable A satisfying the condition

$$\langle\Psi| A |\Psi\rangle = \frac{1}{N_p} \sum_{\psi_1, \ldots, \psi_{N_p}} Q(\psi_1, \ldots, \psi_{N_p})((\psi_1)^l + \ldots + (\psi_{N_p})^l) \ , \tag{8.30}$$

with the property

$$A|\psi_1, \ldots, \psi_{N_p}\rangle = \frac{1}{N_p}((\psi_1)^l + \ldots + (\psi_{N_p})^l)|\psi_1, \ldots, \psi_{N_p}\rangle \ . \tag{8.31}$$

In the case of binary mixing, the range of the scalar is $|\psi_i| \leq 1$. Then we construct a unitary W that implements

$$W |\psi_1, \ldots, \psi_{N_p}\rangle |0\rangle_{\mathrm{a}} = A |\psi_1, \ldots, \psi_{N_p}\rangle |0\rangle_{\mathrm{a}} + |\phi^\perp\rangle |1\rangle_{\mathrm{a}} \ , \tag{8.32}$$

where $|\phi^\perp\rangle$ is a quantum state in the same space of the observable A. For example, in block-matrix form,

$$W = \begin{pmatrix} A & \sqrt{1-A^2} \\ \sqrt{1-A^2} & -A \end{pmatrix} , \qquad (8.33)$$

where the first column of blocks corresponds to the subspace associated with $|0\rangle_\mathrm{a}$. The gate complexity of W has a polynomial dependence with respect to N_p. For equation (8.32) the expectation value of W associated with the prepared state is

$$
\begin{aligned}
w &= \langle\Psi|\,\langle 0|_\mathrm{a}\, W\,|\Psi\rangle\,|0\rangle_\mathrm{a} \\
&= \frac{1}{N_p} \sum_{\psi_1,\dots,\psi_{N_p}} Q(\psi_1,\dots,\psi_{N_p})((\psi_1)^l + \dots + (\psi_{N_p})^l) .
\end{aligned} \qquad (8.34)
$$

The task of estimating the l-th central moment [Eq. (8.28)] is reduced to estimating the expectation value of a unitary W [Eq. (8.34)].

On the other hand, the expression of the observable A can be varied from problem to problem. For example, for a reacting flow problem in Sec. 8.3, we can tailor our quantum algorithm to estimate the mean fractional mass conversion by simply redefining the observable A to have the form,

$$A|\psi_1,\dots,\psi_{N_p}\rangle = 1 - \frac{2}{N_p}(\psi_1 H(\psi_1) + \dots + \psi_{N_p}H(\psi_{N_p}))|\psi_1,\dots,\psi_{N_p}\rangle . \qquad (8.35)$$

where $H(x)$ is the Heaviside step function. Then by applying the same techniques as above in building the unitary W, we will have an expectation value w associated with the prepared state,

$$
\begin{aligned}
w &= \langle\Psi|\,\langle 0|_\mathrm{a}\, W\,|\Psi\rangle\,|0\rangle_\mathrm{a} \\
&= 1 - \frac{2}{N_p} \sum_{\psi_1,\dots,\psi_{N_p}} Q(\psi_1,\dots,\psi_{N_p})(\psi_1 H(\psi_1) + \dots + \psi_{N_p}H(\psi_{N_p})) .
\end{aligned} \qquad (8.36)
$$

From the analysis of the error shown in Eq. (2.18) in Sec. 2.1.4, the precision of the estimation is better when the expected value of a unitary W is close to 1. However, for most mixing problems including binary mixing, the l-th central moment decays as a function of t. The estimation of a small value of $\mu_l(t)$ can be improved by calculating a shifted expectation value of W defined as,

$$W|\psi_1,\dots,\psi_{N_p}\rangle\,|0\rangle_\mathrm{a} = (1-A)|\psi_1,\dots,\psi_{N_p}\rangle\,|0\rangle_\mathrm{a} + |\eta^\perp\rangle\,|1\rangle_\mathrm{a} , \qquad (8.37)$$

where $|\eta^\perp\rangle$ is also a quantum state. With this shift when $\mu_l(t)$ is small, the estimation of w within precision ϵ' (Eq. (2.18)) results in the same order of precision. In the simulation of the reacting flows, we did not apply this shift.

With this state preparation and translation from the quantity of interest to the expectation value of a unitary to estimate, we use the techniques of quantum metrology to estimate the l-th central moment of the PDF. In summary, our algorithm is then:

Input: l, t, β, ω, Δt, N_p, ϵ

1. Obtain $N_t = \lceil t/\Delta t \rceil$, $N_s = \lceil \beta\omega\Delta t N_p \rceil$ and the smallest integer m such that $M \geq 2\pi/\epsilon$, with $M = 2^m$.
2. Construct the state preparation unitary V for $|\Psi\rangle$ as in Eq. (8.26).
3. Construct the unitary W as in Eq. (8.32) or Eq. (8.37).
4. Construct the unitary $U = S_0 S_1 = S_0 W S_0 W^\dagger$, where $S_0 = \mathbb{1}_{2^n} - 2|\Psi\rangle\langle\Psi|$ performs reflection operation.
5.
    5.1 Prepare $|\Psi\rangle = V|0\ldots0\rangle$ and a single-qubit ancilla state in $|+\rangle_a$ as the control qubit, and apply ^cU, $M/2$ times.
    5.2 Apply a Hadamard transformation and measure the ancilla qubit in the computational basis.
        Let $b'_m \in \{0,1\}$ denote the measurement outcome.

6. Repeat the following for each k in the order $k = (m-1),\ldots,1$:
    6.1 Prepare a single-qubit ancilla state in $|+\rangle_a$ and apply ^cU, 2^{k-1} times.
    6.2 Compensate the phase of $|1\rangle_a$ by $e^{-i\pi[.b'_{k+1}\ldots b'_m]}$.
    6.3 Apply a Hadamard transformation and measure the ancilla qubit in the computational basis.
        Let $b'_k \in \{0,1\}$ denote the measurement outcome.

Output: An estimate of the l-th central moment as $\cos(\hat{\theta}/2)$, with $\hat{\theta} = 2\pi[.b'_1\ldots b'_m]$.

The confidence level for the estimation in a single execution of the algorithm is bounded from below by $8/\pi^2$ and to reach arbitrarily confidence, we can repeat estimation for L times, as described in Sec. 2.1.4 [Eq. (2.14)].

8.5.2 Complexity

In this section we analyse the complexity of the our algorithm and compare that to the MC method. For simplicity, we disregard logarithmic factors in the order notation. The complexity to the state preparation $|\Psi\rangle$ is determined by the total number of elementary gates to apply V. As V is constructed using reversible equivalents of the operations implementing the MC method, we assume the complexity of V is of order $O(N_t N_s) = O(t\beta\omega N_p)$, the number of simple operations in one MC realisation. The complexity of W, related to the corresponding function of ψ_i to estimate interested properties, is $O((N_p)^q)$ for some positive constant q. The constructed unitary U to estimate eigenphases uses two instances of V and two instances of $V^\dagger$, which results in a complexity of $O(t\beta\omega N_p)$. The complexity of U and V can be dominant in the total complexity. Combined with the total number of calling U for $M = \mathcal{O}(\varepsilon)$ times, the overall complexity of our algorithm is then $O(t\beta\omega N_p/\epsilon)$. Compare this result with that in Sec. 8.4.1, the dependence on ϵ is quadratically better. To reach an arbitrary confidence level c, an additional prefactor in order $O(|\log(1-c)|)$ should apply to the complexity.

8.5.3 Example: quantum algorithm for binary mixing

We apply our main quantum algorithm for simulations of the binary mixing problem and compare the performance with that of the MC simulations of Sec. 8.4. Our quantum algorithm requires a large number of qubits which is beyond the reach of classical computers or current quantum devices. Here, we simulate our quantum algorithm via sampling from the distribution of the measurement outputs due to the simplicity of the problem, which we can base on classical MC simulations with high precision.

We consider the same parameters as the binary mixing problem of Sec. 8.4.2. We implement the quantum algorithm L times to reach the same confidence level $c = 99.75\%$ as has been demonstrated with MC. We then obtain L values of the estimator and compute the median value to provide the estimate. From Eq. (2.14), the number of repetitions to reach confidence level $c = 99.75\%$ shall satisfy this condition,

$$L \geq \frac{\log(2 \times (1 - 0.9975))}{\log(0.8)} \,, \tag{8.38}$$

and we can choose $L = 24$. This is the reason why we present the N_r in this section using the convenient factorization, $N_r = 2^m \times 24$.

Our classical simulations of the quantum algorithm are implemented as follows. With the knowledge of the analytical solution of 4-th central moments, we assume that $0 \leq \theta/2 < \pi/2$, and then $0 \leq 2\theta < 2\pi$. By estimating 2θ, we gain a factor of $1/2$ in the error analysis. The probability distribution of estimating 2θ is given by Eq. (2.11), simply replacing $\theta \to 2\theta$ and $\hat{\theta} \to 2\hat{\theta}$. In the quantum algorithm, this could be realised by replacing $U \to U^2$ without changing the order of magnitude of the complexity. According to this probability distribution of measurement outputs as we run our quantum algorithm in Sec. 8.5, we obtain $L = 24$ estimates of a phase $2\hat{\theta}_i$. In our case, our task is to obtain an estimate of the 4-th central moment, notated as $\hat{\mu}_4(t)$. We define the unitary W accordingly via Eq. (8.32) and Eq. (8.37) to reduce the error as explained in Sec. 2.1.4, Eqs. (2.18) and (2.19).

We first apply the MC techniques of Sec. 8.4.2 for $N_r = 2^{20} \times 60$ times to obtain a very accurate estimate of $\mu_4(t)$, $\tilde{\mu}_4(t)$. This would not be possible in more general mixing problems, and that is the justification for designing a quantum algorithm. Then we can obtain the expression of an actual θ, which will be estimated by the PEA.

$$\theta/2 = \begin{cases} \arccos(1 - \tilde{\mu}_4(t)) & \text{if } \tilde{\mu}_4(t) \leq 1/2 \\ \arccos(\tilde{\mu}_4(t)) & \text{if } \tilde{\mu}_4(t) > 1/2 \,. \end{cases}$$

After simple calculations of the distribution function Eq. (2.11) in the case of estimating 2θ, it can be shown that

$$\Pr(b'_m = 0) = \frac{1}{2}\left(1 + \cos(M\theta)\right) \,, \ \Pr(b'_m = 1) = 1 - \Pr(b'_m = 0), \qquad (8.39)$$

where $M = 2^m \geq 2\pi/\epsilon$ and b'_m is the last digit of the binary representation of $2\hat{\theta} = 2\pi[.b'_1 \ldots b'_m]$. Recursively we calculate the remaining digits for $k = m-1, \ldots, 1$,

$$\Pr(b'_k = 0) = \frac{1}{2}\left(1 + \cos(2^k\theta - \pi[.b'_{k+1} \ldots b'_m])\right) \,, \ \Pr(b'_k = 1) = 1 - \Pr(b'_k = 0) \,. \tag{8.40}$$

This calculation provides a way to simulate our quantum algorithm on a classical computer by sampling each digit according to a distribution that depends on previous outcomes.

In Fig. 8.4 (a), we provide simulation results for the estimate of the 4-th central moment, $\hat{\mu}_4(t)$, obtained by using our quantum algorithm. We used $m = 10$ bits of precision and repeated the simulation $L = 24$ times; the corresponding repetition number is, $N_r = 2^{10} \times 24$. As in Sec. 8.4.2, we observe that the 4-th central moment decays exponentially in time. In Fig. 8.4 (b), we show the estimates $\hat{\mu}_4(t)$ normalised with $\tilde{\mu}_4(t)$ for different values of m. When $t \geq 0.3$,

the quantum algorithm estimates the value $1 - \mu_4(t)$, rather than $\mu_4(t)$, to reduce estimation errors. we obtain the error bars as,

$$\epsilon_Q := \left| \cos((\hat{\theta} + \epsilon/2)/2) - \cos(\hat{\theta}/2) \right| \tag{8.41}$$

from Eq. (2.18) replaced ϵ by $\epsilon/2 \geq 2\pi/2^{m+1}$, since we are estimating 2θ within precision ϵ. The results shown in Fig. 8.4 should be compared with those in Fig. 8.2.

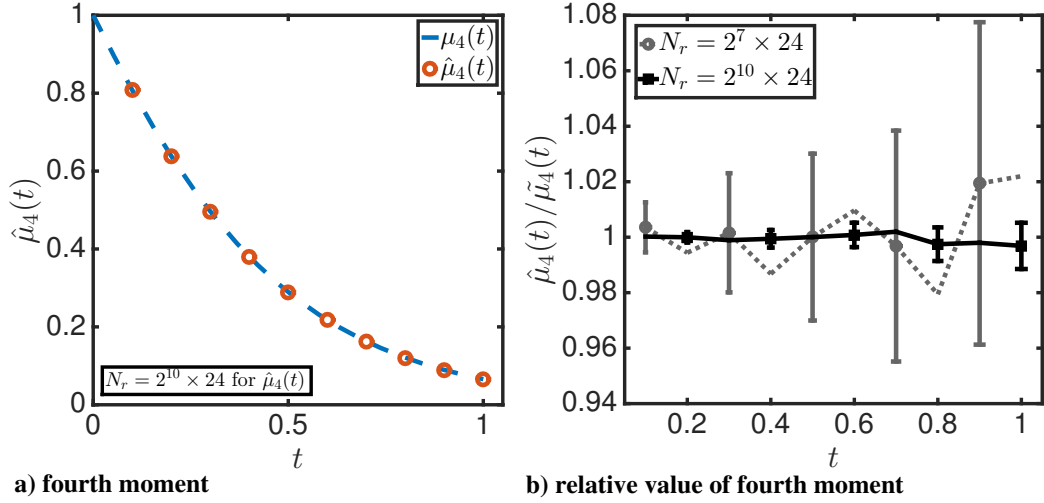**a) fourth moment**   **b) relative value of fourth moment**

FIGURE 8.4: Estimates of the 4-th central moment of the PDF for computational elements, obtained from Quantum-algorithm simulation of a simple binary mixing process using Curl's model with the same simulation parameters in Fig. 8.2. (a) Exponential decay of the estimated 4-th central moment $\hat{\mu}_4(t)$, as a function of time for a number of state preparations $N_r = 2^{10} \times 24$ [Eq. (2.15)]. This was obtained as $\hat{\mu}_4(t) = \cos(\hat{\theta}/2)$ ($t < 0.3$) or $\hat{\mu}_4(t) = 1 - \cos(\hat{\theta}/2)$ ($t \geq 0.3$), where $\hat{\theta}$ is the phase estimate obtained by the quantum PEA. The estimated moments are very close to the exact solution $\mu_4(t)$ (dashed line), given by Eq. (8.10). (b) The estimated 4-th central moment relative to a very accurate estimate $\tilde{\mu}_4(t)$ for $N_p = 10^3$. The data shown here are for $N_r = 2^7 \times 24$ (dotted line, odd positions) and $N_r = 2^{10} \times 24$ (solid line, even positions). To reach a confidence level of 99.75 %, the error bars were obtained from Eq.(8.41). The relative error increases with t as both $\hat{\mu}_4(t)$ and $\tilde{\mu}_4(t)$ decay exponentially with t. The estimation error of $\hat{\mu}_4(t)$ is of the order of $1/N_r$. Note that in (b) we use a different scale to that shown in Fig.8.2(b), and that it is not meaningful to compare the quantum and classical algorithms based on these figures alone, as the algorithms would run on different hardware. The advantage of the quantum algorithm is in the scaling with N_r, which we plot in Fig. 8.5, and discuss in detail in the text. This figure was reproduced from [222].

In Fig. 8.5, we compare the errors output by the classical MC method (ϵ_C) and our quantum algorithm (ϵ_Q). The results are for estimating the 4-th central moment of the binary mixing model at different time t and different repetition number. The errors were obtained from Eqs. (8.18) and (8.41). The different scalings of these algorithms clearly show the advantages of the quantum algorithm as N_r becomes larger.
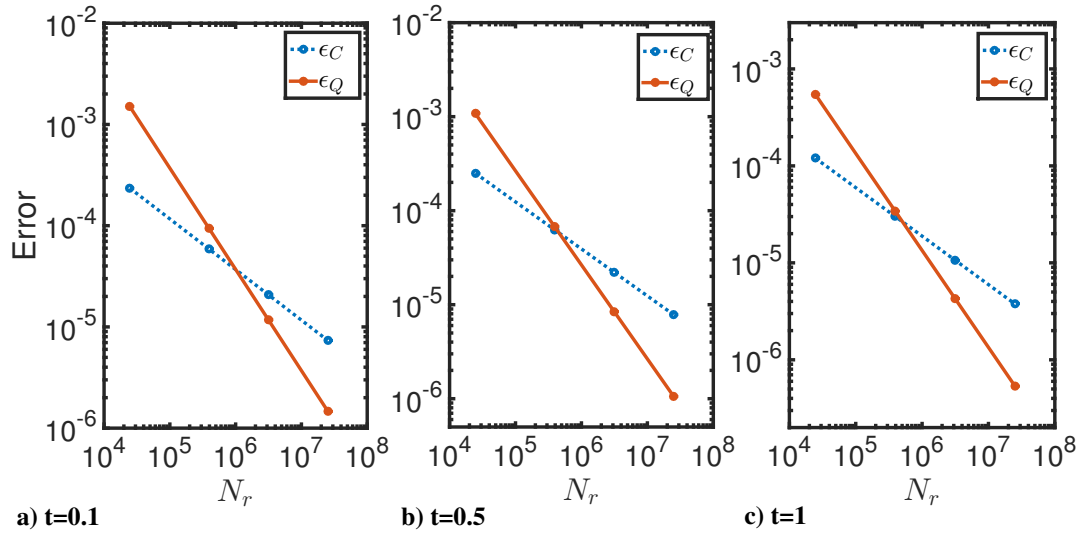

FIGURE 8.5: Comparison of the errors output by the classical MC method (ϵ_C) and our quantum PEA (ϵ_Q). The results are for the 4-th central moment of the binary mixing model studied in Secs. 8.4.2 and 8.5.3, for different values of t and N_r. The latter refers to the number of repetitions of the classical MC method or the number of state preparations needed by our quantum PEA. The data points are for $N_r = 2^m \times L$, where $m = 10, 14, 17, 20$ and $L = 24$. The confidence level of the estimation is 99.75%. The logarithmic scale allows us to observe clearly a better precision dependence, in terms of N_r, for our quantum PEA than for MC simulations. This figure was reproduced from [222].

This comparison of two algorithms demonstrates the power of quantum computing in the error scaling in terms of the number of repetitions. This quantum speed-up of error scaling proves the potential of quantum computers performing high-precision parameter estimation in the future.

8.5.4   Example: quantum algorithm for reacting flow

Because of the similar nature of the two problems: turbulent mixing problem and reacting flows, both of them are described in the C/D model, therefore we are able

to tailor our quantum algorithm with the same routine but a different observable to calculate different functions of interest, as discussed in Sec. 8.5.1. Without going through of the whole process again, we simply look at the differences between the implementations of solving the two problems.

The function we are would like to calculate here is the mean fractional mass conversion as in Eq. (8.14). By designing a observable which has an expectation value as in Eq. (8.36), we will have the unitary operator with the eigenphase

$$\theta/2 = \arccos(\tilde{\mathcal{F}}(t)) \ ,$$

where $\tilde{\mathcal{F}}(t)$ is a very accurate simulation result obtained via classical MC using $N_r = 2^{20} \times 60$ repetitions. To use results from the MC method as an input for the simulation is not possible in general cases. The rest of the simulation is the same as that of Sec. 8.5.3

Here we show our classical simulation of our quantum algorithm in estimating $\mathcal{F}(t)$ in Fig. 8.6. Simulations are for different values of time up to 3 ($t \leq 3$). In Fig. 8.6 (a), we demonstrate the simulation with $m = 17$ digits in our quantum algorithm and show the growth of $\mathcal{F}(t)$ as a function of time. In Fig. 8.6 (b), the simulation results are very close the very accurate simulation result $\tilde{\mathcal{F}}(t)$ via the MC method using $N_r = 2^{20} \times 60$, since the analytical solution of $\mathcal{F}$ varies from different models. Then we demonstrate the simulation results for two different parameters, $m = 17$ and $m = 20$ normalised with $\tilde{\mathcal{F}}(t)$. The relative errors are decreasing in time because the value of $\mathcal{F}(t)$ is increased to 1. The performance of the quantum algorithm shown in Fig. 8.6 should be compared with those in Fig. 8.3.

We then demonstrate the comparison of the errors from the classical MC method (ϵ_C) and our quantum algorithm (ϵ_Q) in Fig. 8.7. A similar conclusion can be reached as in the comparison made for turbulent mixing problem, that the error scaling in terms of the repetition number show the same quadratic quantum speed-up.

8.6 Conclusions and outlook

In this chapter, we first gave an overview of using MC methods to simulate the PDF transport equations which can be utilised in the simulations of different subjects in fluid dynamics. Then we provided the background of two fluid dynamics problems: turbulent mixing problems and reacting flows problem as examples, followed by numerical simulations estimating quantities of interest in different
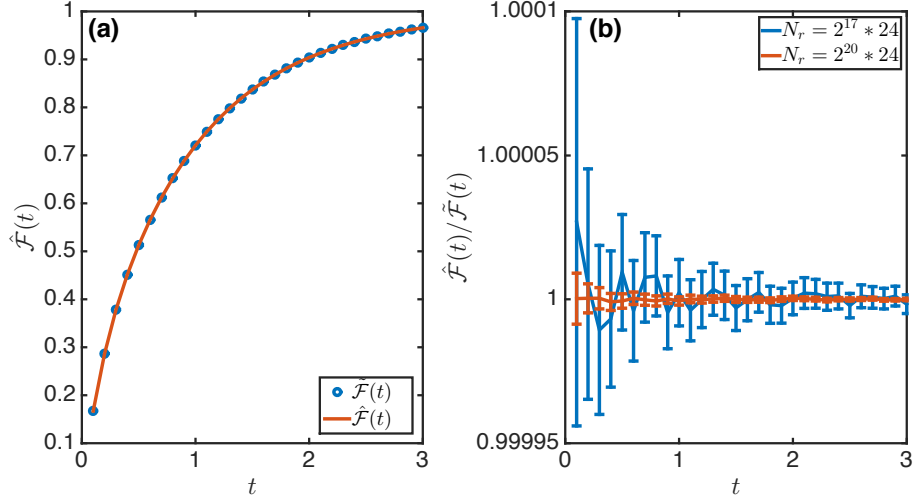
FIGURE 8.6: Estimation of the mean fractional mass conversion of fuels, obtained from quantum-algorithm simulations of a reacting flow problem described by Curl's model with the same simulation parameters in Fig. 8.3. (a) Growth of the estimated mass fraction of fuels $\hat{\mathcal{F}}(t)$, as a function of time for a number of state preparations $N_r = 2^{17} \times 24$ [Eq. (2.15)]. This was obtained as $\hat{\mathcal{F}}(t) = \cos(\hat{\theta}/2)$, where $\hat{\theta}$ is the phase estimate obtained by the quantum PEA. The estimated moments are very close to a very accurate simulation $\tilde{\mathcal{F}}(t)$ (dashed line), given by the MC calculations using $N_r = 2^{20} \times 60$. (b) The estimated mass fraction of fuels relative to a very accurate estimate $\tilde{\mathcal{F}}(t)$ for $N_p = 10^3$. The dataset shown here is for $N_r = 2^{17} \times 24$ (blue line) and $N_r = 2^{20} \times 24$ (red line). To reach a confidence level of 99.75 %, the error bars were obtained from Eq.(8.41). The relative error decreases with t as both $\hat{\mathcal{F}}(t)$ and $\tilde{\mathcal{F}}(t)$ increase with t to 3. The estimation error of $\hat{\mathcal{F}}(t)$ is of the order of $1/N_r$. Note that in (b) we use a different scale to that shown in Fig.8.3(b) because of the different range of errors. By using $m = 17, 20$ bits, we already observe better performance of the quantum PEA over the MC. Furthermore, the advantage of the quantum algorithm is in the scaling with N_r, which we plot in Fig. 8.7, and discuss in detail in the text.

example topics. Then we presented a quantum algorithm for solving MC mixing problems from fluid dynamics. Our quantum algorithm provides a quadratic speed-up over classical MC methods in terms of the number of repetitions that are required to achieve a desired precision. We then apply our tailored quantum algorithm to specific example problems via changing the observables, estimating the precision obtained as a function of the repetition number in classical MC methods. By illustrating the error scaling from numerical simulations of our quantum PEA, we observe the expected quantum speed-up over classical algorithms
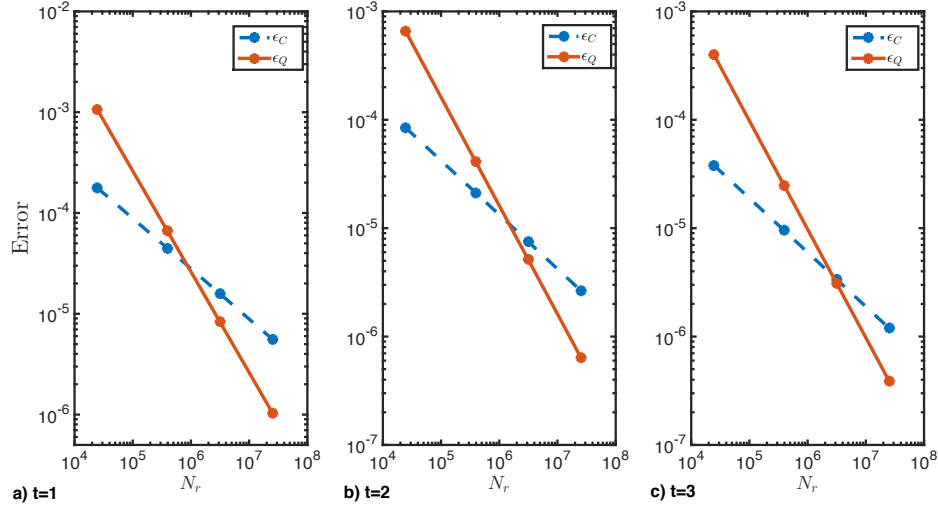
FIGURE 8.7: Comparison of the errors output by the classical MC method (ϵ_C) and our quantum PEA (ϵ_Q). The results are for the mass fraction of fuels of the reacting flow problem studied in Secs. 8.4.3 and 8.5.3, for different values of t and N_r. The latter refers to the number of repetitions of the classical MC method or the number of state preparations needed by our quantum PEA. The data points are for $N_r = 2^m \times L$, where $m = 10, 14, 17, 20$ and $L = 24$. The confidence level of the estimation is 99.75%. The logarithmic scale allows us to observe clearly a better precision dependence, in terms of N_r, for our quantum PEA than for MC simulations.

compared to the MC calculation.

This quantum algorithm can be applied to a range of fluid dynamics problems, and in this chapter we showed two of them. The potential power of quantum computing in this area is demonstrated. More broadly, this study provides us a basis to discuss the potential applications of future quantum computers in fluid dynamics. Recent developments in quantum hardware are very encouraging [179–186] and we expect some time in the future to implement our quantum algorithm on a large quantum computer. The investigation of the detailed application of this technology to solve fluid dynamics problems motivates algorithm development in quantum computing, and help us to understand the potential impact of quantum computers. Our specific examples highlight also how studying potential applications could give feedback and requirements about the implementation of quantum algorithms.

Chapter 9

Conclusions and outlook

The research presented in this thesis involves topics of adiabatic quantum computing, adiabatic state preparations and designing quantum algorithms to provide a quantum speed-up for turbulent mixing problems. Our results demonstrate advantages of a eigenpath transversal algorithm over conventional adiabatic quantum computing, the assistance of classical noise in adiabatic state preparation, thermalisation of cold atoms in optical lattices after heating due to classical noise and a quantum speed-up of tailored algorithms over classical Monte Carlo methods in turbulent fluid mixing. Our research contributes to different aspects of quantum simulation, quantum algorithms and quantum computation, and in a big picture, quantum simulators and quantum computers.

In Chap. 5, we presented an eigenpath transversal algorithm, the randomisation method, with improved bounds on the eigenpath length and on the time cost of the algorithm. The advantage of the randomisation method over conventional adiabatic quantum computing is demonstrated in terms of the dependence of the time cost on the gap. Because of the connection to adiabatic quantum computing, the randomisation method can be future applied to a wide range of problems which can be solved by adiabatic quantum computing. The improved bound on the eigenpath length can also apply to other eigenpath transversal methods. This project can open several directions in the future. First, because the upper bound of the time cost is loose, it will be very intriguing to search for particular problems where the randomisation method outperforms conventional adiabatic quantum computing. Secondly, many quantum algorithms have been proven to have a quantum speed up over classical algorithms. How to modify the randomisation method to solve classical problems and how the performance is compared with classical algorithm will be interesting to investigate.

In Chap. 6, we adapted the random time evolution approach from the randomisation method to the situation of adiabatic state preparation of many-body system with classical noise. As an example, we considered noise during adiabatic state preparation in the Bose-Hubbard model. We also discuss the realisation of such noise by engineering amplitude fluctuations in optical lattices and its robustness against imperfect implementations. The study of the fidelities with tilted noise provides deeper understanding of the competition between the heating and dephasing effects. The potential directions of future research could be as follows. First, it will be interesting to see implementations our method in experiments with cold Bosons in optical lattices with amplitude noise. Secondly, this study can be extended to other systems like Fermions in optical lattices or trapped ions. To realise classical noise proportional to the Hamiltonian could be challenging with different experimental settings. Last, how other noise effects, for example, spontaneous emissions, can influence state preparations also opens a wide range of future directions.

In Chap. 7, we continued our study of amplitude noise in optical lattices and discuss the influence on the total energy after the adiabatic state preparation and the thermalisation after application of noise. We identify the regime of minimal total energy resulting from the competition between non-adiabaticity and noise accumulations as we increase the evolution time with a fixed noise strength. Also, after application of an amplitude noise pulse, we study thermalisation behaviour in the superfluid phase, and show that in the Mott insulator phase, thermalisation is not observed. In the future, it will be interesting to study the behaviour of the state preparation fidelity as a function of evolution time with a fixed noise strength to identify an optimal evolution time that gives the maximum fidelity and compare those two optimal values of time. The second direction of this project is to see experimental implementation of the amplitude noise pulses and observe the system and compare the experimental results to our numerical simulations. This research overall will form a basis for better understanding and diagnosing typical heating processes for cold atoms in optical lattices.

In Chap. 8, we developed a quantum algorithm based on the phase estimation algorithm to solve specific problems in fluid dynamics. We take two examples, turbulent scalar mixing and reacting flows, to demonstrate the quantum speedup achieved by a quantum algorithm over classical Monte Carlo calculations showing the error scaling in terms of number of repetitions. This is intended to start a conversation with the fluid dynamics engineering community. The quantum hardware undergoes a rapid developing period. Our research can estimate potential impacts of quantum computers. The study of complexity and the depth of quantum algorithms can also provide information on requirements of quantum devices for practical implementations. The first direction of future research would be to optimise our quantum algorithm to realise parallelisation. The second one,

is to simulate the probability distribution function transport equation directly, instead of mimicking the classical method. The potential outcome may lead to the elimination of the simulation error from the limited number of computational elements. Lastly we can investigate the potential to design quantum algorithms to solve partial differential equations, like the Fokker-Planck equation and Navier-Stokes equation that are widely used in engineering. One possible path is via tensor network theory for solving partial differential equations (PDEs) [223, 224]. Tensor networks methods are widely used to study quantum many-body system. To find the quantum system corresponds to the tensor network form can lead to a bridge between quantum computation of PDEs. However, the nonlinearity in certain type of PDEs may cause problems in state preparation of quantum algorithms. To update the information of the nonlinearity, measurements have to be applied at each step. The projective measurements in the computational basis can destroy the coherent quantum state, which requires additional state preparations in quantum computation.

Bibliography

[1] D. Deutsch, "Quantum theory, the church–turing principle and the universal quantum computer," *Proceedings of the Royal Society of London A: Mathematical, Physical and Engineering Sciences*, vol. 400, no. 1818, pp. 97–117, 1985.

[2] R. P. Feynman, "Simulating physics with computers," *International Journal of Theoretical Physics*, vol. 21, no. 6, pp. 467–488, 1982.

[3] D. P. DiVincenzo, "Quantum computation," *Science*, vol. 270, no. 5234, pp. 255–261, 1995.

[4] M. A. Nielsen and I. L. Chuang, *Quantum Computation and Quantum Information.* Cambridge, UK: Cambridge University Press, 2000.

[5] J. I. Cirac and P. Zoller, "Goals and opportunities in quantum simulation," *Nature Physics*, vol. 8, pp. 264–266, 2012.

[6] T. H. Johnson, S. R. Clark, and D. Jaksch, "What is a quantum simulator?," *EPJ Quantum Technology*, vol. 1, no. 1, p. 10, 2014.

[7] B. P. Lanyon, C. Hempel, D. Nigg, M. Müller, R. Gerritsma, F. Zähringer, P. Schindler, J. T. Barreiro, M. Rambach, G. Kirchmair, M. Hennrich, P. Zoller, R. Blatt, and C. F. Roos, "Universal digital quantum simulation with trapped ions," *Science*, vol. 334, no. 6052, pp. 57–61, 2011.

[8] I. Bloch, J. Dalibard, and S. Nascimbène, "Quantum simulations with ultracold quantum gases," *Nature Physics*, vol. 8, pp. 267–276, 2012.

[9] M. Mller, S. Diehl, G. Pupillo, and P. Zoller, "Engineered open systems and quantum simulations with atoms and ions," in *Advances in Atomic, Molecular, and Optical Physics* (P. Berman, E. Arimondo, and C. Lin, eds.), vol. 61 of *Advances In Atomic, Molecular, and Optical Physics*, pp. 1 – 80, Academic Press, 2012.

[10] P. W. Shor, "Algorithms for quantum computation: Discrete logarithms and factoring," *Proceedings of the 35th Annual Symp. on Found. of Comp. Science*, vol. 35, pp. 124–124, 1994.

[11] L. P. Pitaevskii and S. Stringari, *Bose-Einstein Condensation.* Clarendon Press, 2003.

[12] C. J. Pethick and H. Smith, *Bose-Einstein Condensation in Dilute Gases.* Cambridge University Press, 2 ed., 2008.

[13] M. H. Anderson, J. R. Ensher, M. R. Matthews, C. E. Wieman, and E. A. Cornell, "Observation of bose-einstein condensation in a dilute atomic vapor," *Science*, vol. 269, no. 5221, pp. 198–201, 1995.

[14] A. E. Leanhardt, T. A. Pasquini, M. Saba, A. Schirotzek, Y. Shin, D. Kielpinski, D. E. Pritchard, and W. Ketterle, "Cooling bose-einstein condensates below 500 picokelvin," *Science*, vol. 301, no. 5639, pp. 1513–1515, 2003.

[15] H. J. Metcalf and P. van der Straten, *Laser Cooling and Trapping.* Springer-Verlag New York, 1999.

[16] W. Ketterle and N. V. Druten, "Evaporative cooling of trapped atoms," vol. 37 of *Advances In Atomic, Molecular, and Optical Physics*, pp. 181 – 236, Academic Press, 1996.

[17] M. Theis, G. Thalhammer, K. Winkler, M. Hellwig, G. Ruff, R. Grimm, and J. H. Denschlag, "Tuning the scattering length with an optically induced feshbach resonance," *Phys. Rev. Lett.*, vol. 93, p. 123001, 2004.

[18] C. Chin, R. Grimm, P. Julienne, and E. Tiesinga, "Feshbach resonances in ultracold gases," *Rev. Mod. Phys.*, vol. 82, pp. 1225–1286, 2010.

[19] D. Jaksch, C. Bruder, J. I. Cirac, C. W. Gardiner, and P. Zoller, "Cold bosonic atoms in optical lattices," *Phys. Rev. Lett.*, vol. 81, pp. 3108–3111, 1998.

[20] D. Jaksch and P. Zoller, "The cold atom hubbard toolbox," *Annals of Physics*, vol. 315, no. 1, pp. 52 – 79, 2005. Special Issue.

[21] M. Lewenstein, A. Sanpera, V. Ahufinger, B. Damski, A. Sende, and U. Sen, "Ultracold atomic gases in optical lattices: Mimicking condensed matter physics and beyond," *Adv. in Phys.*, vol. 56, pp. 243–379, 2007.

[22] I. Bloch, J. Dalibard, and W. Zwerger, "Many-body physics with ultracold gases," *Rev. Mod. Phys.*, vol. 80, pp. 885–964, 2008.

[23] M. Greiner, O. Mandel, T. Esslinger, T. W. Hansch, and I. Bloch, "Quantum phase transition from a superfluid to a mott insulator in a gas of ultracold atoms," *Nature*, vol. 415, no. 6867, pp. 39–44, 2002.

[24] S. Sachdev, *Quantum Phase Transitions*. Cambridge University Press, UK, 2001.

[25] T. Kinoshita, T. Wenger, and D. S. Weiss, "A quantum Newton's cradle," *Nature*, vol. 440, p. 900, 2006.

[26] M. Vojta, "Quantum phase transitions," *Reports on Progress in Physics*, vol. 66, no. 12, p. 2069, 2003.

[27] P. Jurcevic, H. Shen, P. Hauke, C. Maier, T. Brydges, C. Hempel, B. P. Lanyon, M. Heyl, R. Blatt, and C. F. Roos, "Direct observation of dynamical quantum phase transitions in an interacting many-body system," *Phys. Rev. Lett.*, vol. 119, p. 080501, 2017.

[28] L. Santos, M. A. Baranov, J. I. Cirac, H.-U. Everts, H. Fehrmann, and M. Lewenstein, "Atomic quantum gases in kagomé lattices," *Phys. Rev. Lett.*, vol. 93, p. 030601, 2004.

[29] S. Safaei, C. Miniatura, and B. Grémaud, "Triangular and honeycomb lattices of cold atoms in optical cavities," *Phys. Rev. A*, vol. 92, p. 043810, 2015.

[30] S. Peil, J. V. Porto, B. L. Tolra, J. M. Obrecht, B. E. King, M. Subbotin, S. L. Rolston, and W. D. Phillips, "Patterned loading of a bose-einstein condensate into an optical lattice," *Phys. Rev. A*, vol. 67, p. 051603, 2003.

[31] O. Mandel, M. Greiner, A. Widera, T. Rom, T. W. Hänsch, and I. Bloch, "Coherent transport of neutral atoms in spin-dependent optical lattice potentials," *Phys. Rev. Lett.*, vol. 91, p. 010407, 2003.

[32] W. S. Bakr, J. I. Gillen, A. Peng, S. Fölling, and M. Greiner, "A quantum gas microscope for detecting single atoms in a hubbard-regime optical lattice," *Nature*, vol. 462, pp. 74–77, 2009.

[33] J. F. Sherson, C. Weitenberg, M. Endres, M. Cheneau, I. Bloch, and S. Kuhr, "Single-atom-resolved fluorescence imaging of an atomic mott insulator," *Nature*, vol. 467, pp. 68–72, 2010.

[34] E. Haller, J. Hudson, A. Kelly, D. A. Cotta, B. Peaudecerf, G. D. Bruce, and S. Kuhr, "Single-atom imaging of fermions in a quantum-gas microscope," *Nature Physics*, vol. 11, pp. 738–742, 2015.

[35] L. W. Cheuk, M. A. Nichols, M. Okan, T. Gersdorf, V. V. Ramasesh, W. S. Bakr, T. Lompe, and M. W. Zwierlein, "Quantum-gas microscope for fermionic atoms," *Phys. Rev. Lett.*, vol. 114, p. 193001, 2015.

[36] S. Will, T. Best, U. Schneider, L. Hackermüller, D.-S. Lühmann, and I. Bloch, "Time-resolved observation of coherent multi-body interactions in quantum phase revivals," *Nature*, vol. 465, pp. 197–201, 2010.

[37] J. Schachenmayer, L. Pollet, M. Troyer, and A. J. Daley, "Spontaneous emission and thermalization of cold bosons in optical lattices," *Phys. Rev. A*, vol. 89, p. 011601, 2014.

[38] D. Clément, N. Fabbri, L. Fallani, C. Fort, and M. Inguscio, "Exploring correlated 1d bose gases from the superfluid to the mott-insulator state by inelastic light scattering," *Phys. Rev. Lett.*, vol. 102, p. 155301, 2009.

[39] N. Gemelke, X. Zhang, C.-L. Hung, and C. Chin, "In situ observation of incompressible mott-insulating domains in ultracold atomic gases," *Nature*, vol. 460, pp. 995–998, 2009.

[40] D. P. DiVincenzo, "The physical implementation of quantum computation," *Fortschritte der Physik*, vol. 48, no. 911, pp. 771–783, 2000.

[41] D. Jaksch, H.-J. Briegel, J. I. Cirac, C. W. Gardiner, and P. Zoller, "Entanglement of atoms via cold controlled collisions," *Phys. Rev. Lett.*, vol. 82, pp. 1975–1978, 1999.

[42] D. Jaksch, J. I. Cirac, P. Zoller, S. L. Rolston, R. Côté, and M. D. Lukin, "Fast quantum gates for neutral atoms," *Phys. Rev. Lett.*, vol. 85, pp. 2208–2211, 2000.

[43] G. K. Brennen, C. M. Caves, P. S. Jessen, and I. H. Deutsch, "Quantum logic gates in optical lattices," *Phys. Rev. Lett.*, vol. 82, pp. 1060–1063, 1999.

[44] O. Mandel, M. Greiner, A. Widera, T. Rom, T. W. Hänsch, and I. Bloch, "Controlled collisions for multi-particle entanglement of optically trapped atoms," *Nature*, vol. 425, pp. 937–940, 2003.

[45] P. Jessen, D. Haycock, G. Klose, G. Smith, I. Deutsch, and G. Brennen, "Quantum control and information processing in optical lattices," *Quantum Information and Computation*, vol. 1, no. SUPPL. 1, pp. 20–32, 2001.

[46] S. C. Benjamin and S. Bose, "Quantum computing with an always-on heisenberg interaction," *Phys. Rev. Lett.*, vol. 90, p. 247901, 2003.

[47] T. Calarco, U. Dorner, P. S. Julienne, C. J. Williams, and P. Zoller, "Quantum computations with atoms in optical lattices: Marker qubits and molecular interactions," *Phys. Rev. A*, vol. 70, p. 012306, 2004.

[48] H. J. Briegel, D. E. Browne, W. Dr, R. Raussendorf, and M. Van den Nest, "Measurement-based quantum computation," *Nature Physics*, vol. 5, p. 19, 2009.

[49] E. Farhi and S. Gutmann, "Analog analogue of a digital quantum computation," *Physical Review A (Atomic, Molecular, and Optical Physics)*, vol. 57, no. 4, pp. 2403–2406, 1998.

[50] C. Mochon, "Hamiltonian oracles," *Phys. Rev. A*, vol. 75, p. 042313, 2007.

[51] G. Brassard and P. Hoyer, "An exact quantum polynomial-time algorithm for simon's problem," in *Proceedings of the Fifth Israeli Symposium on Theory of Computing and Systems*, pp. 12–23, 1997.

[52] L. K. Grover, "Quantum computers can search rapidly by using almost any transformation," *Phys. Rev. Lett.*, vol. 80, pp. 4329–4332, 1998.

[53] L. K. Grover, "A fast quantum mechanical algorithm for database search," *Proceedings of the 28th Annual ACM Symposium on the Theory of Computing*, pp. 212–219, 1996.

[54] R. J. David Deutsch, "Rapid solution of problems by quantum computation," *Proceedings of the Royal Society of London A: Mathematical, Physical and Engineering Sciences*, vol. 439, no. 1907, pp. 553–558, 1992.

[55] R. Cleve, A. Ekert, C. Macchiavello, and M. Mosca, "Quantum algorithms revisited," *Proceedings of the Royal Society of London A: Mathematical, Physical and Engineering Sciences*, vol. 454, no. 1969, pp. 339–354, 1998.

[56] P. W. Shor, "Polynomial-time algorithms for prime factorization and discrete logarithms on a quantum computer," *SIAM Review*, vol. 41, no. 2, pp. 303–332, 1999.

[57] L. Hales and S. Hallgren, "An improved quantum fourier transform algorithm and applications," in *Proceedings 41st Annual Symposium on Foundations of Computer Science*, pp. 515–525, 2000.

[58] S. Barz, I. Kassal, M. Ringbauer, Y. O. Lipp, B. Dakić, A. Aspuru-Guzik, and P. Walther, "A two-qubit photonic quantum processor and its application to solving systems of linear equations," *Scientific Reports*, vol. 4, pp. 6115–6119, 2014.

[59] B. P. Lanyon, J. D. Whitfield, G. G. Gillett, M. E. Goggin, M. P. Almeida, I. Kassal, J. D. Biamonte, M. Mohseni, B. J. Powell, M. Barbieri, A. Aspuru-Guzik, and A. G. White, "Towards quantum chemistry on a quantum computer," *Nature Chemistry*, vol. 2, pp. 106–111, 2010.

[60] D. W. Berry, "High-order quantum algorithm for solving linear differential equations," *Journal of Physics A: Mathematical and Theoretical*, vol. 47, no. 10, p. 105301, 2014.

[61] A. Ambainis, "Quantum walk algorithm for element distinctness," *SIAM Journal on Computing*, vol. 37, no. 1, pp. 210–239, 2007.

[62] A. Ambainis, "Polynomial degree and lower bounds in quantum complexity: Collision and element distinctness with small range," *Theory of Computing*, vol. 1, no. 3, pp. 37–46, 2005.

[63] S. Kutin, "Quantum lower bound for the collision problem with small range," *Theory of Computing*, vol. 1, no. 2, pp. 29–36, 2005.

[64] D. W. Berry, A. M. Childs, R. Cleve, R. Kothari, and R. D. Somma, "Exponential improvement in precision for simulating sparse hamiltonians," *Forum of Mathematics, Sigma*, vol. 5, 2017.

[65] A. Das and B. Chakrabarti, "Quantum annealing and analog quantum computation," *Rev. Mod. Phys*, vol. 80, p. 1061, 2008.

[66] E. Farhi, J. Goldstone, S. Gutmann, and M. Sipser, "Quantum computation by adiabatic evolution," *quant-ph/0001106*, 2000.

[67] D. Aharonov, W. van Dam, J. Kempe, Z. Landau, S. Lloyd, and O. Regev, "Adiabatic quantum computation is equivalent to standard quantum computation," *SIAM Journal on Computing*, vol. 37, no. 1, pp. 166–194, 2007.

[68] W. van Dam, M. Mosca, and U. Vazirani, "How powerful is adiabatic quantum computation?," in *Proceedings 2001 IEEE International Conference on Cluster Computing*, pp. 279–287, 2001.

[69] H.-T. Chiang, G. Xu, and R. D. Somma, "Improved bounds for eigenpath traversal," *Phys. Rev. A*, vol. 89, p. 012314, 2014.

[70] E. Farhi, D. Gosset, I. Hen, A. W. Sandvik, P. Shor, A. P. Young, and F. Zamponi, "Performance of the quantum adiabatic algorithm on random instances of two optimization problems on regular hypergraphs," *Phys. Rev. A*, vol. 86, p. 052334, 2012.

[71] A. P. Young, S. Knysh, and V. N. Smelyanskiy, "Size dependence of the minimum excitation gap in the quantum adiabatic algorithm," *Phys. Rev. Lett.*, vol. 101, p. 170503, 2008.

[72] T. Kadowaki and H. Nishimori, "Quantum annealing in the transverse ising model," *Phys. Rev. E*, vol. 58, pp. 5355–5363, 1998.

[73] A. Finnila, M. Gomez, C. Sebenik, C. Stenson, and J. Doll, "Quantum annealing: A new method for minimizing multidimensional functions," *Chemical Physics Letters*, vol. 219, no. 5, pp. 343 – 348, 1994.

[74] I. Hen, "Realizable quantum adiabatic search," *EPL (Europhysics Letters)*, vol. 118, no. 3, p. 30003, 2017.

[75] R. Babbush, P. J. Love, and A. Aspuru-Guzik, "Adiabatic quantum simulation of quantum chemistry," *Scientific Reports*, vol. 4, pp. 6603–6613, 2014.

[76] P. J. J. O'Malley, R. Babbush, I. D. Kivlichan, J. Romero, J. R. McClean, R. Barends, J. Kelly, P. Roushan, A. Tranter, N. Ding, B. Campbell, Y. Chen, Z. Chen, B. Chiaro, A. Dunsworth, A. G. Fowler, E. Jeffrey, E. Lucero, A. Megrant, J. Y. Mutus, M. Neeley, C. Neill, C. Quintana, D. Sank, A. Vainsencher, J. Wenner, T. C. White, P. V. Coveney, P. J. Love, H. Neven, A. Aspuru-Guzik, and J. M. Martinis, "Scalable quantum simulation of molecular energies," *Phys. Rev. X*, vol. 6, p. 031007, 2016.

[77] L. Veis and J. Pittner, "Adiabatic state preparation study of methylene," *The Journal of Chemical Physics*, vol. 140, no. 21, p. 214111, 2014.

[78] S. R. White, "Density matrix formulation for quantum renormalization groups," *Phys. Rev. Lett.*, vol. 69, pp. 2863–2866, 1992.

[79] S. R. White, "Density-matrix algorithms for quantum renormalization groups," *Phys. Rev. B*, vol. 48, pp. 10345–10356, 1993.

[80] S. Rommer and S. Ostlund, "A class of ansatz wave functions for 1d spin systems and their relation to dmrg," *Phys. Rev. B*, vol. 55, p. 2164, 1997.

[81] F. Verstraete and J. I. Cirac, "Matrix product states represent ground states faithfully," *Phys. Rev. B*, vol. 73, p. 094423, 2006.

[82] G. Vidal, "Efficient classical simulation of slightly entangled quantum computations," *Phys. Rev. Lett.*, vol. 91, p. 147902, 2003.

[83] A. J. Daley, C. Kollath, U. Schollwöck, and G. Vidal, "Time-dependent density-matrix renormalization-group using adaptive effective hilbert spaces," *Journal of Statistical Mechanics: Theory and Experiment*, vol. 2004, no. 04, p. P04005, 2004.

[84] S. R. White and A. E. Feiguin, "Real-time evolution using the density matrix renormalization group," *Phys. Rev. Lett.*, vol. 93, p. 076401, 2004.

[85] A. J. Daley, "Quantum trajectories and open many-body quantum systems," *Advances in Physics*, vol. 63, no. 2, pp. 77–149, 2014.

[86] P. Kaye, R. Laflamme, and M. Mosca, *An Introduction to Quantum Computing.* Oxford University Press, USA, 2007.

[87] P. Dirac, "A new notation for quantum mechanics," *Math. Proc. Cambridge Phil. Soc.*, vol. 35, pp. 416–418, 1939.

[88] D. J. Griffiths, *Introduction to Quantum Mechanics.* UK: Pearson, 2014.

[89] A. Kitaev, "Quantum measurements and the abelian stabilizer problem," vol. 3, 1996.

[90] W. Nawrocki, *Introduction to Quantum Metrology.* Springer, 2015.

[91] V. Giovannetti, S. Lloyd, and L. Maccone, "Quantum-enhanced measurements: beating the standard quantum limit," *Science*, vol. 306, p. 1330, 2004.

[92] V. Giovannetti, S. Lloyd, and L. Maccone, "Quantum metrology," *Phys. Rev. Lett.*, vol. 96, p. 010401, 2006.

[93] E. Knill, G. Ortiz, and R. D. Somma, "Optimal quantum measurements of expectation values of observables," *Phys. Rev. A*, vol. 75, p. 012328, 2007.

[94] R. Cleve, A. Ekert, C. Macchiavello, and M. Mosca, "Quantum algorithms revisited," *Proceedings of the Royal Society A: Mathematical, Physical and Engineering Sciences*, vol. 454, no. 1969, pp. 339–354, 1998.

[95] G. Brassard, P. Høyer, M. Mosca, and A. Tapp, *Quantum Computation and Quantum Information: A Millennium Volume.* AMS Contemporary Mathematics Series, USA: Am. Math. Soc., 2000.

[96] D. Nagaj, P. Wocjan, and Y. Zhang, "Fast amplification of QMA," *Quant. Inf. Comp.*, vol. 9, p. 1053, 2009.

[97] A. Montanaro, "Quantum speedup of monte carlo methods," *Proc. Roy. Soc. Ser. A*, vol. 471, p. 20150301, 2015.

[98] D. Berry, A. Childs, R. Cleve, R. Kothari, and R. Somma, "Simulating hamiltonian dynamics with a truncated taylor series," *Phys. Rev. Lett.*, vol. 114, p. 090502, 2015.

[99] A. M. Childs, R. Kothari, and R. D. Somma, "Quantum algorithm for systems of linear equations with exponentially improved dependence on precision," *SIAM Journal on Computing*, vol. 46, no. 6, pp. 1920–1950, 2017.

[100] E. Farhi, J. Goldstone, S. Gutmann, and M. Sipser, "Quantum computation by adiabatic evolution," *quant-ph/0001106*, 2000.

[101] J. Roland and N. J. Cerf, "Quantum search by local adiabatic evolution," *Physical Review A*, vol. 65, no. 4, p. 042308, 2002.

[102] A. B. Finnila, M. A. Gomez, C. Sebenik, C. Stenson, and J. D. Doll, "Quantum annealing: A new method for minimizing multidimensional functions," *Chem. Phys. Lett.*, vol. 219, pp. 343–348, 1994.

[103] E. Farhi, J. Goldstone, and S. Gutmann, "Quantum adiabatic evolution algorithms versus simulated annealing," *quant-ph/0201031*, 2002.

[104] I. Hen, "Period finding with adiabatic quantum computation," *EPL (Europhysics Letters)*, vol. 105, no. 5, p. 50005, 2014.

[105] C.-P. Sun, "High-order quantum adiabatic approximation and berry's phase factor," *Journal of Physics A: Mathematical and General*, vol. 21, no. 7, p. 1595, 1988.

[106] P. Wocjan and A. Abeyesinghe, "Speed-up via quantum sampling," *Phys. Rev. A*, p. 042336, 2008.

[107] S. Boixo, E. Knill, and R. D. Somma, "Eigenpath traversal by phase randomization," *Quantum Inf. and Comp.*, vol. 9, pp. 833–855, 2009.

[108] S. Boixo, E. H. Knill, and R. Somma, "Fast quantum algorithms for traversing paths of eigenstates," *Quantum Information & Computation*, 2010.

[109] R. D. Somma, S. Boixo, H. Barnum, and E. Knill, "Quantum simulations of classical annealing processes," *Phys. Rev. Lett.*, vol. 101, pp. 130504–4, 2008.

[110] C. Gerry and P. Knight, *Introductory Quantum Optics*. Cambridge University Press, 2004.

[111] C. Orzel, A. K. Tuchman, M. L. Fenselau, M. Yasuda, and M. A. Kasevich, "Squeezed states in a bose-einstein condensate," *Science*, vol. 291, no. 5512, pp. 2386–2389, 2001.

[112] T. Stöferle, H. Moritz, C. Schori, M. Köhl, and T. Esslinger, "Transition from a strongly interacting 1d superfluid to a mott insulator," *Phys. Rev. Lett.*, vol. 92, p. 130403, 2004.

[113] I. M. Georgescu, S. Ashhab, and F. Nori, "Quantum simulation," *Rev. Mod. Phys.*, vol. 86, pp. 153–185, 2014.

[114] S. Lloyd, "Universal quantum simulators," *Science*, vol. 273, no. 5278, pp. 1073–1078, 1996.

[115] N. W. Ashcroft and N. D. Mermin, *Solid State Physics*. Thomson Learning, 1976.

[116] W. Kohn, "Analytic properties of bloch waves and wannier functions," *Phys. Rev.*, vol. 115, pp. 809–821, 1959.

[117] M. P. A. Fisher, P. B. Weichman, G. Grinstein, and D. S. Fisher, "Boson localization and the superfluid-insulator transition," *Phys. Rev. B*, vol. 40, pp. 546–570, 1989.

[118] J. Mun, "Bose-einstein condensates in optical lattices : the superfluid to mott insulator phase transition," 2009.

[119] W. Krauth, M. Caffarel, and J.-P. Bouchaud, "Gutzwiller wave function for a model of strongly interacting bosons," *Phys. Rev. B*, vol. 45, pp. 3137–3140, 1992.

[120] T. D. Kühner, S. R. White, and H. Monien, "One-dimensional bose-hubbard model with nearest-neighbor interaction," *Phys. Rev. B*, vol. 61, pp. 12474–12489, 2000.

[121] H. Pichler, J. Schachenmayer, J. Simon, P. Zoller, and A. J. Daley, "Noise- and disorder-resilient optical lattices," *Phys. Rev. A*, vol. 86, p. 051605, 2012.

[122] H. Pichler, J. Schachenmayer, A. J. Daley, and P. Zoller, "Heating dynamics of bosonic atoms in a noisy optical lattice," *Phys. Rev. A*, vol. 87, p. 033606, 2013.

[123] F. Verstraete, V. Murg, and J. Cirac, "Matrix product states, projected entangled pair states, and variational renormalization group methods for quantum spin systems," *Advances in Physics*, vol. 57, no. 2, pp. 143–224, 2008.

[124] U. Schollwck, "The density-matrix renormalization group in the age of matrix product states," *Annals of Physics*, vol. 326, no. 1, pp. 96 – 192, 2011. January 2011 Special Issue.

[125] G. Vidal, "Efficient classical simulation of slightly entangled quantum computations," *Phys. Rev. Lett.*, vol. 91, p. 147902, 2003.

[126] G. Vidal, "Efficient simulation of one-dimensional quantum many-body systems," *Phys. Rev. Lett.*, vol. 93, p. 040502, 2004.

[127] J. E. Gentle, *Numerical Linear Algebra for Applications in Statistics.* Springer-Verlag, 1998.

[128] M. Suzuki, "General theory of fractal path integrals with applications to many-body theories and statistical physics," *Journal of Mathematical Physics*, vol. 32, no. 2, pp. 400–407, 1991.

[129] G. Vidal, "Classical simulation of infinite-size quantum lattice systems in one spatial dimension," *Phys. Rev. Lett.*, vol. 98, p. 070201, 2007.

[130] G. Lindblad, "On the Generators of Quantum Dynamical Semigroups," *Commun. Math. Phys.*, vol. 48, p. 119, 1976.

[131] C. Gardiner, *Stochastic Methods: A Handbook for the Natural and Social Sciences.* Springer-Verlag Berlin Heidelberg, 2009.

[132] B. Apolloni, C. Caravalho, and D. de Falco, "Quantum stochastic optimization," *Stochastic Processes and their Applications*, vol. 33, p. 233, 1989.

[133] T. Kadowaki and H. Nishimori, "Quantum annealing in the transverse ising model," *Phys. Rev. E*, vol. 58, pp. 5355–5363, 1998.

[134] E. Farhi, J. Goldstone, S. Gutmann, J. Lapan, A. Lundgren, and D. Preda, "A quantum adiabatic evolution algorithm applied to random instances of an NP-complete problem," *Science*, vol. 292, pp. 472–476, 2001.

[135] G. Santoro and E. Tosatti, "Optimization using quantum mechanics: Quantum annealing through adiabatic evolution," *J. Phys. A*, vol. 39, p. R393, 2006.

[136] D. Perez-Garcia, F. Verstraete, J. I. Cirac, and M. Wolf, "Peps as unique ground states of local hamiltonians," *Quant. Inf. Comp.*, vol. 8, p. 0650, 2008.

[137] M. Schwarz, K. Temme, and F. Verstraete, "Preparing projected entangled pair states on a quantum computer," *Phys. Rev. Lett.*, vol. 108, p. 110502, 2012.

[138] M. Born and V. Fock, "Beweis des adiabatensatzes," *Zeitschrift für Physik*, vol. 3-4, p. 165, 1928.

[139] A. Messiah, *Quantum Mechanics*. Dover Publications, 1999.

[140] D. Aharonov, W. van Dam, J. Kempe, Z. Landau, S. Lloyd, and O. Regev, "Adiabatic quantum computation is equivalent to standard quantum computation," *SIAM J. Comp.*, vol. 37, no. 1, pp. 166–194, 2007.

[141] A. Mizel, D. A. Lidar, and M. Mitchell, "Simple proof of the equivalence between adiabatic quantum computation and the circuit model," *Phys. Rev. Lett.*, vol. 99, p. 070502, 2007.

[142] R. Oliveira and B. M. Terhal, "The complexity of quantum spin systems on a two-dimensional square lattice," *Quant. Inf. Comp*, vol. 8, p. 0900, 2008.

[143] D. Aharonov, D. Gottesman, S. Irani, and J. Kempe, "The power of quantum systems on a line," *Comm. Math. Phys.*, vol. 287, p. 41, 2009.

[144] A. Ganti and R. Somma, "On the gap of hamiltonians for the adiabatic simulation of quantum circuits," *International Journal of Quantum Information*, vol. 11, no. 07, p. 1350063, 2013.

[145] R. Cleve, D. Gottesman, M. Mosca, R. Somma, and D. Yonge-Mallo, "Efficient discrete-time simulations of continuous-time quantum query models," *Proceedings of the 41st Annual IEEE Symp. on Theory of Computing*, pp. 409–416, 2009.

[146] N. Wiebe, D. Berry, P. Hoyer, and B. C. Sanders, "Higher-order decompositions of ordered operator exponentials," *J. Phys. A: Math. Theor.*, vol. 43, p. 065203, 2010.

[147] A. Childs and R. Kothari, "Simulating sparse hamiltonians with star decompositions," *Theory of Quantum Computation, Communication, and Cryptography*, p. 94, 2011.

[148] D. Berry, R. Cleve, and R. D. Somma, "Exponential improvement in precision for hamiltonian-evolution simulation," *arXiv:1308.5424*, 2013.

[149] S. Jansen, M. Ruskai, and R. Seiler, "Bounds for the adiabatic approximation with applications to quantum computation," *J. of Math. Phys.*, vol. 48, no. 10, pp. 102111–15, 2007.

[150] S. Jordan, *Quantum computation beyond the circuit model*. Massachusetts Institute of Technology, 2008.

[151] K.-P. Marzlin and B. C. Sanders, "Inconsistency in the application of the adiabatic theorem," *Phys. Rev. Lett.*, vol. 93, p. 160408, 2004.

[152] M. H. S. Amin, "Consistency of the adiabatic theorem," *Phys. Rev. Lett.*, vol. 102, p. 220401, 2009.

[153] S. Kirkpatrick, C. Gelatt, and M. Vecchi, "Optimization by simulated annealing," *Science*, vol. 220, p. 671, 1983.

[154] A. Feiguin, R. D. Somma, and C. Batista, "Exact real-space renormalization method and applications," vol. 88, 2013.

[155] R. Somma, C. Batista, and G. Ortiz, "Quantum approach to classical statistical mechanics," *Phys. Rev. Lett.*, vol. 99, p. 030603, 2007.

[156] S. Bravyi and B. Terhal, "Complexity of stoquastic frustration-free hamiltonians," *SIAM J. Comput.*, vol. 39, p. 1462, 2009.

[157] N. de Beaudrap, M. Ohliger, T. Osborne, and J. Eisert, "Solving frustration-free spin systems," *Phys. Rev. Lett.*, vol. 105, p. 060504, 2010.

[158] R. D. Somma and S. Boixo, "Spectral gap amplification," *SIAM J. Comp*, vol. 42, pp. 593–610, 2013.

[159] F. Verstraete, M. Wolf, D. Perez-Garcia, and J. Cirac, "Criticality, the area law, and the computational power of projected entangled pair states," *Phys. Rev. Lett.*, vol. 96, p. 220601, 2006.

[160] F. Verstraete, V. Murg, and J. Cirac, "Matrix product states, projected entangled pair states, and variational renormalization group methods for quantum spin systems," *Advances in Physics*, vol. 57, no. 2, pp. 143–224, 2008.

[161] B. Hajek, "Cooling schedules for optimal annealing," *Mathematics of Operations Research*, vol. 13, no. 2, pp. 311–329, 1988.

[162] A. Ambainis and O. Regev, "An elementary proof of the quantum adiabatic theorem," *quant-ph/0411152*, 2004.

[163] D. A. Lidar, A. T. Rezakhani, and A. Hamma, "Adiabatic approximation with exponential accuracy for many-body systems and quantum computation," *J. Math. Phys.*, vol. 50, p. 102106, 2009.

[164] J. E. Avron, M. Fraas, G. M. Graf, and P. Grech, "Landau-zener tunneling for dephasing lindblad evolutions," *Communications in Mathematical Physics*, vol. 305, no. 3, pp. 633–639, 2011.

[165] M. Rigol, "Breakdown of thermalization in finite one-dimensional systems," *Phys. Rev. Lett.*, vol. 103, p. 100403, 2009.

[166] A. C. Cassidy, C. W. Clark, and M. Rigol, "Generalized thermalization in an integrable lattice system," *Phys. Rev. Lett.*, vol. 106, p. 140405, 2011.

[167] M. Rigol and M. Fitzpatrick, "Initial-state dependence of the quench dynamics in integrable quantum systems," *Phys. Rev. A*, vol. 84, p. 033640, 2011.

[168] D. C. McKay and B. DeMarco, "Cooling in strongly correlated optical lattices: prospects and challenges," *Reports on Progress in Physics*, vol. 74, no. 5, p. 054401, 2011.

[169] H. Pichler, A. J. Daley, and P. Zoller, "Nonequilibrium dynamics of bosonic atoms in optical lattices: Decoherence of many-body states due to spontaneous emission," *Phys. Rev. A*, vol. 82, p. 063605, 2010.

[170] J. Schachenmayer, L. Pollet, M. Troyer, and A. J. Daley, "Thermalization of strongly interacting bosons after spontaneous emissions in optical lattices," *EPJ Quantum Technology*, vol. 2, no. 1, p. 1, 2015.

[171] J. M. Deutsch, "Quantum statistical mechanics in a closed system," *Phys. Rev. A*, vol. 43, pp. 2046–2049, 1991.

[172] M. Srednicki, "Chaos and quantum thermalization," *Phys. Rev. E*, vol. 50, pp. 888–901, 1994.

[173] M. Rigol, V. Dunjko, and M. Olshanii, "Thermalization and its mechanism for generic isolated quantum systems," *Nature*, vol. 452, pp. 854–858, 2008.

[174] A. Montanaro, "Quantum algorithms: an overview," *Npj Quantum Information*, vol. 2, pp. 15023–15030, 2016.

[175] M. Szegedy, "Quantum speed-up of markov chain based algorithms," *Proceedings of the 45th Annual IEEE Symposium on Foundations of Computer Science*, pp. 32–41, 2004.

[176] F. Magniez, A. Nayak, J. Roland, and M. Santha, "Search via quantum walk," *Proceedings of the 39th Symposium on the Theory of Computing*, pp. 575–584, 2006.

[177] D. Poulin and P. Wocjan, "Preparing ground states of quantum many-body systems on a quantum computer," *Phys. Rev. Lett.*, vol. 102, p. 130503, 2009.

[178] A. Narayan Chowdhury and R. D. Somma, "Quantum algorithms for gibbs sampling and hitting-time estimation," vol. 17, pp. 41–64, 2016.

[179] J. Kelly, R. Barends, A. G. Fowler, A. Megrant, E. Jeffrey, T. C. White, D. Sank, J. Y. Mutus, B. Campbell, Y. Chen, Z. Chen, B. Chiaro, A. Dunsworth, I. C. Hoi, C. Neill, P. J. J. O/'Malley, C. Quintana, P. Roushan, A. Vainsencher, J. Wenner, A. N. Cleland, and J. M. Martinis, "State preservation by repetitive error detection in a superconducting quantum circuit," *Nature*, vol. 519, no. 7541, pp. 66–69, 2015.

[180] E. A. Martinez, C. A. Muschik, P. Schindler, D. Nigg, A. Erhard, M. Heyl, P. Hauke, M. Dalmonte, T. Monz, P. Zoller, and R. Blatt, "Real-time dynamics of lattice gauge theories with a few-qubit quantum computer," *Nature*, vol. 534, no. 7608, pp. 516–519, 2016.

[181] T. Monz, D. Nigg, E. A. Martinez, M. F. Brandl, P. Schindler, R. Rines, S. X. Wang, I. L. Chuang, and R. Blatt, "Realization of a scalable shor algorithm," *Science*, vol. 351, no. 6277, pp. 1068–1070, 2016.

[182] S. Debnath, N. M. Linke, C. Figgatt, K. A. Landsman, K. Wright, and C. Monroe, "Demonstration of a small programmable quantum computer with atomic qubits," *Nature*, vol. 536, no. 7614, pp. 63–66, 2016.

[183] R. Blatt and D. Wineland, "Entangled states of trapped atomic ions," *Nature*, vol. 453, no. 7198, pp. 1008–1015, 2008.

[184] J. Clarke and F. K. Wilhelm, "Superconducting quantum bits," *Nature*, vol. 453, no. 7198, pp. 1031–1042, 2008.

[185] M. H. Devoret and R. J. Schoelkopf, "Superconducting circuits for quantum information: An outlook," *Science*, vol. 339, no. 6124, pp. 1169–1174, 2013.

[186] D. D. Awschalom, L. C. Bassett, A. S. Dzurak, E. L. Hu, and J. R. Petta, "Quantum spintronics: Engineering and manipulating atom-like spins in semiconductors," *Science*, vol. 339, no. 6124, pp. 1174–1179, 2013.

[187] J. Yepez, "Quantum computation of fluid dynamics," in *Quantum Computing and Quantum Communications* (C. P. Williams, ed.), (Berlin, Heidelberg), pp. 34–60, Springer Berlin Heidelberg, 1999.

[188] H. L. Toor, "Mass transfer in dilute turbulent and nonturbulent systems with rapid irreversible reactions and equal diffusivities," *AIChE J.*, vol. 8, pp. 70–78, 1962.

[189] R. S. Brodkey, ed., *Turbulence in Mixing Operation*. New York, NY: Academic Press, 1975.

[190] P. A. Libby and F. A. Williams, eds., *Turbulent Reacting Flows*, vol. 44 of *Topics in Applied Physics*. Heidelberg: Springer-Verlag, 1980.

[191] S. B. Pope, "PDF methods for turbulent reactive flows," *Prog. Energ. Combust.*, vol. 11, pp. 119–192, 1985.

[192] P. Givi, "Model free simulations of turbulent reactive flows," *Prog. Energ. Combust.*, vol. 15, pp. 1–107, 1989.

[193] W. Kollmann, "The PDF approach to turbulent flow," *Theor. Comp. Fluid Dyn.*, vol. 1, pp. 249–285, 1990.

[194] P. A. Libby and F. A. Williams, eds., *Turbulent Reacting Flows*. London, England: Academic Press, 1994.

[195] S. B. Pope, *Turbulent Flows*. Cambridge, UK: Cambridge University Press, 2000.

[196] D. C. Haworth, "Progress in probability density function methods for turbulent reacting flows," *Prog. Energ. Combust.*, vol. 36, no. 2, pp. 168–259, 2010.

[197] C. Dopazo, "Recent developments in PDF methods," in Libby and Williams [194], ch. 7, pp. 375–474.

[198] R. O. Fox, *Computational Models for Turbulent Reacting Flows*. Cambridge, UK: Cambridge University Press, 2003.

[199] P. Givi, "Filtered density function for subgrid scale modeling of turbulent combustion," *AIAA J.*, vol. 44, no. 1, pp. 16–23, 2006.

[200] D. C. Haworth and S. B. Pope, "Transported Probability Density Function Methods for Reynolds-Averaged and Large-Eddy Simulations," in *Turbulent Combustion Modeling* (T. Echekki and E. Mastorakos, eds.), vol. 95 of *Fluid Mechanics and Its Applications*, pp. 119–142, Springer Netherlands, 2011.

[201] D. C. Haworth and S. B. Pope, "Monte Carlo solutions of a joint PDF equation for turbulent flows in general orthogonal coordinates," *J. Comput. Phys.*, vol. 72, no. 2, pp. 311–346, 1987.

[202] P. E. Kloeden, E. Platen, and H. Schurz, *Numerical Solution of Stochastic Differential Equations through Computer Experiments*. New York, NY: Springer-Verlag, corrected second printing ed., 1997.

[203] C. K. Madnia, F. A. Jaberi, and P. Givi, "Large eddy simulation of heat and mass transport in turbulent flows," in *Handbook of Numerical Heat Transfer* (W. J. Minkowycz, E. M. Sparrow, and J. Y. Murthy, eds.), ch. 5, pp. 167–189, New York, NY: John Wiley & Sons, Inc., second ed., 2006.

[204] J. Janicka, W. Kolbe, and W. Kollmann, "Closure of the transport equation for the probability density function of turbulent scalar field," *J. Non-Equil. Thermodyn.*, vol. 4, pp. 47–66, 1979.

[205] S. B. Pope, "An improved turbulent mixing model," *Combust. Sci. Technol.*, vol. 28, pp. 131–145, 1982.

[206] G. Kosály and P. Givi, "Modeling of turbulent molecular mixing," *Combust. Flame*, vol. 70, pp. 101–118, 1987.

[207] F. A. Jaberi, R. S. Miller, C. K. Madnia, and P. Givi, "Non-Gaussian scalar statistics in homogeneous turbulence," *J. Fluid Mech.*, vol. 313, pp. 241–282, 1996.

[208] E. E. O'Brien, "The probability density function (PDF) approach to reacting turbulent flows," in Libby and Williams [190], ch. 5, pp. 185–218.

[209] S. B. Pope, "The probability approach to modeling of turbulent reacting flows," *Combust. Flame*, vol. 27, pp. 299–312, 1976.

[210] H. Chen, S. Chen, and R. H. Kraichnan, "Probability distribution of a stochastically advected scalar field," *Phys. Rev. Lett.*, vol. 63, no. 24, pp. 2657–2660, 1989.

[211] S. B. Pope, "Mapping closures for turbulent mixing and reaction," *Theor. Comp. Fluid Dyn.*, vol. 2, pp. 255–270, 1991.

[212] L. Valiño and C. Dopazo, "A binomial langevin model for turbulent mixing," *Phys. Fluids A*, vol. 3, no. 12, pp. 3034–3037, 1991.

[213] R. S. Miller, S. H. Frankel, C. K. Madnia, and P. Givi, "Johnson-Edgeworth translation for probability modeling of binary scalar mixing in turbulent flows," *Combust. Sci. Technol.*, vol. 91, no. 1-3, pp. 21–52, 1993.

[214] S. Subramaniam and S. B. Pope, "A mixing model for turbulent reactive flows based on Euclidean minimum spanning trees," *Combust. Flame*, vol. 115, pp. 487–514, 1998.

[215] A. Y. Klimenko and S. B. Pope, "The modeling of turbulent reactive flows based on multiple mapping conditioning," *Phys. Fluids*, vol. 15, no. 7, pp. 1907–1925, 2003.

[216] S. B. Pope, "A Model for Turbulent Mixing Based on Shadow-Position Conditioning," *Phys. Fluids*, vol. 25, no. 11, p. 110803, 2013.

[217] S. B. Pope, "Small scales, many species and the manifold challenges of turbulent combustion," *Proc. Combust. Inst.*, vol. 34, no. 1, pp. 1–31, 2013.

[218] R. L. Curl, "Dispersed phase mixing: I. Theory and effects in simple reactors," *AIChE J.*, vol. 9, no. 2, pp. 175–181, 1963.

[219] K. T. Li and H. L. Toor, "Turbulent reactive mixing with a series-parallel reaction: Effect of mixing on yield," *AIChE Journal*, vol. 32, no. 8, pp. 1312–1320, 1986.

[220] A. Dutta and J. M. Tarbell, "Closure models for turbulent reacting flows," *AIChE Journal*, vol. 35, no. 12, pp. 2013–2027, 1989.

[221] C. K. Madnia and P. Givi, "Direct numerical simulation and large eddy simulation of reacting homogeneous turbulence," in *Large Eddy Simulations of Complex Engineering and Geophysical Flows* (B. Galperin and S. A. Orszag, eds.), ch. 15, pp. 315–346, Cambridge, England: Cambridge University Press, 1993.

[222] G. Xu, A. J. Daley, P. Givi, and R. D. Somma, "Turbulent mixing simulation via a quantum algorithm," *AIAA Journal*, pp. 1–13, 2017.

[223] M. Bachmayr, R. Schneider, and A. Uschmajew, "Tensor networks and hierarchical tensors for the solution of high-dimensional partial differential equations," *Foundations of Computational Mathematics*, vol. 16, no. 6, pp. 1423–1472, 2016.

[224] B. N. Khoromskij, "Tensor numerical methods for high-dimensional pdes: Basic theory and initial applications," 2014.